

UC Berkeley

UC Berkeley Electronic Theses and Dissertations

Title

Applications of Holography in Quantum Information Dynamics: Chaos, Teleportation, and Metrology

Permalink

<https://escholarship.org/uc/item/5m26g8h2>

Author

Kobrin, Bryce

Publication Date

2023

Peer reviewed|Thesis/dissertation

Applications of Holography in Quantum Information Dynamics:
Chaos, Teleportation, and Metrology

by

Bryce Kobrin

A dissertation submitted in partial satisfaction of the

requirements for the degree of

Doctor of Philosophy

in

Physics

in the

Graduate Division

of the

University of California, Berkeley

Committee in charge:

Professor Norman Y. Yao, Co-chair

Professor Joel E. Moore, Co-chair

Professor Raphael Bousso

Professor K. Birgitta Whaley

Fall 2023

Applications of Holography in Quantum Information Dynamics:
Chaos, Teleportation, and Metrology

Copyright 2023
by
Bryce Kobrin

Abstract

Applications of Holography in Quantum Information Dynamics:
Chaos, Teleportation, and Metrology

by

Bryce Kobrin

Doctor of Philosophy in Physics

University of California, Berkeley

Professor Norman Y. Yao, Co-chair

Professor Joel E. Moore, Co-chair

The eternal quest to reconcile quantum mechanics and general relativity has recently led to new insights at the interface between gravitational physics, condensed matter, and quantum information science. Much of this progress owes to the development of the holographic principle, a conjectured duality between gravitational systems and ordinary quantum mechanical systems. This opens up the possibility of translating gravitational phenomena into the language of microscopic quantum physics, and vice versa. This thesis explores several surprising connections that have emerged from a sharper understanding of this duality, with a particular emphasis on questions regarding the dynamics of quantum information. What general lessons can we draw from the physics of black holes about the propagation of quantum information in quantum many-body systems? How can we characterize this propagation and leverage it as a resource for performing tasks on large-scale quantum technologies? From a complementary perspective, how can we utilize quantum simulators to probe features of quantum gravity? By investigating these questions, this thesis sheds light on a rich variety of long-standing topics—including quantum chaos, teleportation, and metrology. More broadly, it demonstrates holography as a powerful theoretical framework for guiding our exploration of quantum many-body physics.

Contents

Contents	i
List of Figures	iv
List of Tables	xix
1 Introduction	1
1.1 Quantum information scrambling	5
1.2 The SYK model: a toy model of holography	9
1.3 Quantum teleportation and traversable wormholes	14
2 Many-body chaos in the Sachdev-Ye-Kitaev model	18
2.1 The SYK model and its gravity dual	20
2.2 Non-equilibrium dynamics in the SYK model	22
2.3 Lyapunov exponent of the SYK model	23
2.4 Discussion and outlook	25
3 Many-body quantum teleportation via operator spreading in the traversable wormhole protocol	26
3.1 Summary of results	28
3.2 Introduction to diagrammatic notation	35
3.3 General requirements for successful teleportation	38
3.4 Connection to operator size	40
3.5 Peaked-size teleportation	45
3.6 Peaked-size teleportation at late times	50
3.7 Peaked-size teleportation at intermediate times	53
3.8 Interplay between peaked-size and gravitational teleportation	66
3.9 Experimental proposals	77
3.10 Outlook	92
4 Comment on “Traversable wormhole dynamics on a quantum processor”	94
4.1 Thermalization and scrambling	96
4.2 Teleportation signal	98

4.3	Size winding	99
5	Butterfly metrology: a universal protocol for quantum-enhanced sensing	103
5.1	Butterfly metrology protocol	105
5.2	Global control	108
5.3	Experimental proposals	109
5.4	Robustness to errors	111
5.5	Conclusion	112
6	Adiabatic preparation of thermofield double states	113
6.1	Ground state of the coupled system	115
6.2	Theoretical framework and emergent dynamics	116
6.3	Adiabatic condition and shortcuts to adiabaticity	119
6.4	Discussion and outlook	121
A	Details on many-body chaos in the Sachdev-Ye-Kitaev model	124
A.1	Numerical methods	124
A.2	Characterizing the Lyapunov exponent	128
A.3	Large N solutions	135
A.4	Schwarzian action	140
B	Details on many-body quantum teleportation via operator spreading in the traversable wormhole protocol	145
B.1	Precise bound for the peaked size regime	145
B.2	The Hayden-Preskill recovery protocol	151
B.3	State teleportation fidelity	159
B.4	Rydberg numerical simulations	162
B.5	Random unitary circuit numerics	163
B.6	Random circuit calculations	168
B.7	Teleportation of fermions	171
B.8	Teleportation and inelastic scattering at infinite temperature	177
C	Details on comment on “Traversable wormhole dynamics on a quantum processor”	179
C.1	Other learned models	179
C.2	Four-point correlators with $i \neq j$	180
C.3	Teleportation at fixed injection time	181
C.4	Size-winding metrics	182
C.5	Other fully-commuting models	183
D	Details on butterfly metrology	185
D.1	Comparison to previous time-reversed sensing protocols	185
D.2	Haar-random evolution	186

D.3	Measuring the opposite quadrature	188
D.4	Stochastic growth model	190
D.5	Experimental proposals	193
D.6	Error analysis	200
E	Details on adiabatic preparation of thermofield double states	207
E.1	Thermofield double dynamics from the eigenstate thermalization hypothesis	207
E.2	Analysis of quantum adiabatic protocol	215
E.3	Analysis of semi-classical adiabatic protocol	216
	Bibliography	220

List of Figures

- 1.1 Schematic of two protocols for performing quantum teleportation: (a) the conventional protocol, and (b) the so-called traversable wormhole protocol (also referred to as many-body quantum teleportation). Both protocols send an unknown quantum state $|\psi\rangle$ between two parties, utilizing an entangled resource state, local measurement, and classical communication. The main distinction is that, in the traversable wormhole circuit, the unknown state is first “scrambled” under a many-body unitary U prior to measurement. Details on the two protocols and their connection to traversable wormhole physics are discussed in Chapter 3. . . . 15
- 2.1 Regularized OTOCs in the SYK model, $\tilde{F}(t) \equiv F(t)/F(0)$, as shown for $\beta J = 10$ and system sizes $N \in [12, 60]$. The early-time behavior is characterized by $1 - \tilde{F}(t) \sim e^{\lambda t}/N$ and different system sizes are approximately related by a time translation symmetry, $t \rightarrow t + 1/\lambda \log N$. (b) Applying a finite-size rescaling procedure to the data, we determine λ as a function of temperature (points). Our results exhibit excellent agreement with the theoretical predictions of the Schwinger-Dyson (SD) equations (dashed line), including in the regime where λ approaches the bound on chaos $2\pi/\beta$ (blue). 19
- 2.2 Regimes of analytic control for the SYK model as a function of system size, N , and inverse temperature, βJ . In the semiclassical limit (red and purple), the model is well-described by a dynamical mean-field solution (Schwinger-Dyson equations). At low temperatures, finite-size corrections can be calculated using the Schwarzian action (blue), which is dual to AdS₂ gravity. However, at sufficiently small sizes (gray), the dynamics are governed by the discreteness of the energy spectrum and neither effective theory provides a valid description. . . . 20

2.3 Two-point correlation functions in real and imaginary time. (a) Comparison of imaginary-time evolution between our numerics with 40 Majoranas (solid), the large N solution (dotted), and the Schwarzian action (dashed). At high temperatures, we observe quantitative agreement between our numerical results and the large N solution, while at low temperatures our numerics are well-described by the Schwarzian action. (b) Analogous comparison for real-time evolution with $\beta J = 56$. Our numerics show excellent agreement with the Schwarzian action for $tJ \gtrsim 10$. The disagreement at earlier times is attributed to the difference in high-energy modes, which are cut off at the energy scale J in the SYK model and are unbounded in the effective action. (inset) A salient feature in our real-time numerics is a non-monotonic trend with respect to temperature, as shown for $tJ = 20$. This behavior is captured by the Schwarzian action (dashed) and can be understood as a consequence of the square root edge of the energy spectrum.

22

3.1 (a) Teleportation protocol, proceeding from bottom to top. To teleport, a subset of the left qubits are measured in the \hat{O}_i basis, and operations $\hat{V}_i = e^{ig o_i \hat{O}_i / K}$ conditioned on the measurement results o_i are performed on the right (purple). (b) The protocol hosts two mechanisms of teleportation: peaked-size (red) and gravitational (blue). The channel capacity of peaked-size teleportation decreases with increasing time (dark to light red), while its fidelity decreases with decreasing temperature (dark to light red, again). At high temperature and late times, it is equivalent to teleportation in the HPR protocol (red diamond). Gravitational teleportation occurs at low temperatures in systems dual to semiclassical gravity (e.g. the SYK model), and exhibits the same channel capacity but *higher* fidelity compared to peaked-size teleportation. Increasing the strength of stringy corrections to the gravity theory interpolates between gravitational and peaked-size teleportation. (c) The two mechanisms display distinct time profiles for the teleportation fidelity at fixed coupling strength, g . In systems dual to gravity (top), the fidelity features a single $\mathcal{O}(1)$ peak near the scrambling time (gravitational, blue), and a late time revival (peaked-size, red) to a fidelity suppressed by the two-point function G_β [176]. In generic thermalizing systems (bottom), the fidelity oscillates between 0 and G_β with phase proportional to the operator size, may subsequently decay if sizes become not peaked, and revives at late times.

27

- 3.2 Numerical results for averaged operator size and teleportation fidelity of 1D, 2D, and 0D RUCs. **(a-b)** In 1D and 2D, sizes grow ballistically in time, while the size width grows with a slower power of t and matches predictions from the KPZ universality class (Section 3.7). Because of the separation between the size and size width, the teleportation fidelity for a single qubit exhibits an oscillatory behavior at intermediate times, with nearly perfect maximum fidelity. At late times, the teleportation fidelity saturates close to 1 for odd values of g/π , as expected for any scrambling system (Section 3.6). **(c)** In 0D all-to-all coupled RUCs, both the size and size width grow exponentially in time and obtaining a large separation between them requires encoding the initial state into p -body operators. With this encoding, the teleportation fidelity displays a distinct three-regime profile for $g \gg 1$. In particular, as in 1D and 2D, peaked-size teleportation succeeds *(i)* at early times, with an oscillating fidelity, and *(ii)* at late times, where the fidelity saturates close to 1 (for odd g/π). Between these regimes, no teleportation occurs because the size width has grown too large, $g\delta\mathcal{S}/N \gtrsim 1$ 53
- 3.3 Probing operator size width in a 1D RUC. **(top)** The size width initially grows as $t^{1/2}$ and reaches a peak at the scrambling time $t^* \sim N = 10000$. **(bottom)** We probe this behavior by measuring the teleportation fidelity of a single qubit with a large coupling $g = 57\pi \sim \sqrt{N}$. The fidelity exhibits a distinct decay-revival profile, controlled by whether the size width has exceeded the threshold $g\delta\mathcal{S}/N \approx 1$: nearly perfect fidelity initially, power law decay towards a trivial fidelity at intermediate times, and partial revival at late times. 57
- 3.4 Teleportation of multiple qubits in 0D RUCs. **(a)** Many-body teleportation fidelity, F_{EPR} , as a function of time for teleporting $n = 1, 3, 10$ qubits with fixed coupling strength ($g = 177\pi$). Compared to a single qubit, the decay-revival profile for multiple qubits is shifted to earlier times, since multi-qubit operators both have a larger size width and saturate the system size earlier. Moreover, multi-qubit teleportation is not possible at late times, resulting in a trivial late-time fidelity (Sec. 3.6). **(b)** Numerical results for the channel capacity n_{max} as function of the number of coupled qubits K , which exhibit a clear linear scaling. To determine the channel capacity, we compute the maximum *per qubit* fidelity $F_{\text{EPR}}^{(1)}$ for a fixed number of qubits, n , and couplings, K , while allowing the coupling strength, g , and evolution time to vary. For fixed K , $F_{\text{EPR}}^{(1)}$ decreases as the number of qubits n is increased, as depicted in the inset for $K = 9000$. The channel capacity n_{max} is defined as the maximum number of qubits for which the fidelity is above a fixed threshold (dashed line). 64

- 3.5 Schematic of the teleportation protocol from the bulk gravitational perspective in AdS₂, under both **(a)** semiclassical gravity, and **(b)** strong stringy corrections. The TFD state corresponds to a two-sided black hole. Local quantum mechanical operators, $\psi_{l/r}$, create or annihilate particles near the two boundaries, with wavefunctions $\Psi_{l/r}$ (red). The protocol begins by inserting a particle on the left side, with wavefunction Ψ_l (red, bottom left), at time $-t$, which then falls towards the interior of the geometry during time-evolution (red line). The two-sided coupling, $\frac{g}{N} \sum_i \psi_{i,l} \psi_{i,r}$, is then applied, producing a shock wave (blue) that interacts with the in-falling particle [90, 176]. **(a)** In the semiclassical limit, the shock wave shifts the position the in-falling particle outside of the right horizon (dashed), which enables the particle to reemerge near the right boundary (red, top right) [90, 176]. **(b)** When stringy effects are present, the scattering amplitude between the in-falling particle and the shock wave is modified according to Eq. (3.99) [176, 230]. In the highly stringy limit and at early times, the interaction results in an overall phase shift, $\theta = gG_N A_\epsilon (\Delta/2)^\epsilon e^{\epsilon t}$ [Eq. (3.101)]. The overlap between the in-falling particle and a particle at the right boundary is nevertheless non-zero (red, top right), and is given by the unperturbed two-point function, $G_\beta = i \langle \psi_l \psi_r \rangle$. [Note that stringy effects may also modify the initial wavefunctions of $\Psi_{l/r}$, as we discuss in the context of Eq. (3.103).] 74
- 3.6 One-sided implementation (right) of the original two-sided teleportation protocol (left), derived using repeated applications of Eq. (3.9) [replacing $U \rightarrow U^T$ for convenience, compared to Fig. 6.1(a)]. Blue arrows denote the sequence of operations in the one-sided protocol, the green band marks the teleported qubit and its corresponding component in the one-sided protocol, and the red band marks the initial EPR state and its corresponding component. 80
- 3.7 **(a)** In the proposed analog Rydberg teleportation protocol, qubits are encoded in a ground state $|g\rangle$ and a Rydberg state $|r\rangle$. Nearest-neighbor interactions (dark blue) can be time-reversed, but next-nearest neighbor interactions (light blue) cannot. **(b)** Numerical results comparing the average state teleportation fidelity for single-qubit teleportation with perfectly reversed time-evolution (solid) with the proposed, imperfect time-reversal (dashed). In particular, we implement the one-sided protocol using $N = 20$ total spins; $K = N - 1$ ‘measured’ spins (i.e. all except the spin encoding $|\psi\rangle$), whose single-qubit rotations are generated by $\hat{O}_i = \hat{Z}_i$; and time evolution under the analog Rydberg Hamiltonian [Eq.(3.104)] with parameters $\Omega_i = .9$, $\Delta_i = -1.5$, $J_0 = 1$ (for all i). **(c)** Implementation of U or U^\dagger in the digital protocol, consisting of alternating layers of controlled-phase gates (horizontal black lines) between nearest neighbor atoms and single-qubit rotations (red boxes). Here, qubits are encoded in two hyperfine ground states. Insets show possible pulse sequences to implement the controlled-phase gate and the single-qubit rotations [122]. The full TW protocol is obtained by inserting this gate sequence (and its Hermitian conjugate) in place of U , U^\dagger in Fig. 5. 82

- 3.8 Finite-size scaling of the Rydberg simulations **(a)** as a function of time with $g = \pi$, and **(b)** as a function of coupling strength g with $t = 12$. The system was evolved under the Rydberg Hamiltonian, Eq. (3.104), with the same system parameters as in Fig. 3.7. At late times, the fidelity increases for larger systems but decreases for larger values of g . This is consistent with our error analysis in Section 3.6; in particular, we expect the error to scale as $g^2\delta S^2/N^2$ and the size distribution to approach a binomial distribution for which $\delta S \sim \mathcal{S}/\sqrt{N}$. In contrast, at early times, smaller systems exhibit a larger fidelity not because of the size width but because the acquired phase is $\eta_d g \mathcal{S}(t)/N$, where $\eta_d g$ is fixed and $\mathcal{S}(t)$ is initially independent of size. The curves in (a) intersect near the scrambling time due to the transition between the early and late time regimes. 84
- 3.9 **(a-b)** Chain of atomic ions, with qubit states $|0\rangle, |1\rangle$ represented by hyperfine ground states. The states are coupled by a pair of laser beams, one with individual addressing (with strength g_1 , purple) and one applied globally (with strength g_2). Each beam is strongly detuned from an excited state $|e\rangle$ by an amount Δ . The coherent beatnote between the beams, at frequency ω_0 , drives stimulated Raman transitions between the qubit levels with an effective Rabi frequency $g_1 g_2 / 2\Delta$, and also modulates the Coulomb interaction between qubits to give rise to an effective Ising interaction. **(a)** A two-qubit entangling gate, $XX_{ij}(\theta)$, (red) is performed by addressing only ions i and j with the first beam. **(b)** Half of the qubits are addressed, which leads to analog time-evolution under the Hamiltonian Eq. (3.105) (blue) for all addressed spins. **(c)** Quantum circuit implementation of the teleportation protocol at finite temperature. EPR pairs are formed using two-qubit gates. The TFD state is then prepared via a QAOA approach by iterating multiple times between two-qubit gates coupling the sides and analog time-evolution on both sides individually [255, 271]. The state $|\psi\rangle$ is inserted either by projectively measuring the designated qubit and preparing the state, or by digitally swapping in an additional qubit (not shown). Finally, teleportation is implemented using similar ingredients as well as feed-forward measurements (purple dotted lines). 86

- 4.1 **Lack of thermalization in Model 1.** (a) Two-point correlation functions averaged over Majorana operators, $G_{\text{avg}}(t)$, for Model 1 (green; replicating Fig. 3b of [121]) and several disorder realizations of the $N = 10$ SYK model (orange). As observed in [121], the average correlation function displays similar behavior between the two models. For both models, $\beta = 4$, and, for the SYK model, the couplings are drawn from a normal distribution with mean zero and variance $6J^2/N^3$, where $J = 1.125$. (b) In Model 1, the *individual* two-point correlation functions, $G_i(t)$, display large oscillations. (c) In the SYK model (taking a single disorder instance), the individual correlation functions all exhibit decay. This behavior is independent of the disorder realization. (d-f) Analogous results for the average and individual four-point correlation functions, $F_{\text{avg}}(t)$ and $F_i(t)$, in Model 1 and the $N = 10$ SYK model. Again, the agreement between the two models holds only for the averaged correlation functions (d), and not for the individual correlation functions (e-f). 96
- 4.2 **Teleportation signal of Model 1.** (a) Teleportation circuit from [121]. The qubit to be teleported is swapped with a pair of Majorana operators in the left system L. The success of teleportation from L to R is measured by the mutual information between a reference qubit P and a readout qubit T. (b) Mutual information, I_{PT} , of the symmetric teleportation protocol with $\mu = -12$ for Model 1 (orange; replicating Fig. 2a of [121]) and several realizations of the $N = 10$ SYK model with $J = 1.25$ (grey). The machine-learning procedure in [121] trains Model 1 to reproduce the mutual information (as a function of time) of the SYK model for a specific pair of input operators, ψ^1 and ψ^2 . For this pair of operators, the mutual information indeed shows good agreement between the two models. (c) In Model 1, when the teleportation protocol is performed with input operators that were not involved in the training procedure, i.e. ψ^i and ψ^j where $i < j \in [3, 7]$, the mutual information as a function of time exhibits significant variations. (d) For comparison, in the $N = 10$ SYK model, the mutual information for all pairs of input operators is consistent. The dashed line indicates the mutual information at $t = 0$ for reference. 97

- 4.3 **Comparison of size winding behavior in Model 1 and other random small-size fully-commuting Hamiltonians.** (a) Scatter plots depicting the eight non-zero coefficients, c_P^2 , for ψ^1 of Model 1 at $t = 2.8$. The x-values are the coefficient magnitudes, $|c_P|^2$, and the y-values are the coefficient phases, $\phi_P \equiv \arg c_P^2 - \arg q(1)$. Perfect phase alignment occurs when the phase of all coefficients at a given size $|P|$ matches the phase of their sum (dashed line). This occurs trivially for the single coefficient with $|P| = 1$, and via the alignment of ~ 2 -3 coefficients for $|P| = 3, 5$. (b) A comparison of the phase alignment, \bar{r} , for each operator in: Model 1, Model 1 with random coefficients, Model 1 with random terms and coefficients, a random all-to-all Ising model, the $N = 10$ SYK model, Model 2, and Model 3. For Models 1,2,3, the phase alignment for the trained operators, ψ^1 and ψ^2 , is indicated with a star. As in [121], we take $\beta = 4$, and time $t = 2.8$ for Models 1,2 and $t = 2$ for Model 3. For the random models, three different disorder realizations are shown, with small horizontal offsets for clarity. (c) An analogous comparison for the linear slope metric, χ . (d) The size winding phase, $\arg q(|P|) - \arg q(1)$, as a function of the operator size, $|P|$, for Model 1 (top) and Model 1 with random coefficients (bottom). The size of each marker is scaled proportional to $|q(|P|)|$. The stars in Model 1 correspond to operators ψ^1 (replicating Fig. 3d in [121]) and ψ^2 99
- 4.4 (a) Two-point correlation functions, $G_i(t)$, for all Majorana operators in Model 2. (b) (left) Mutual information for the symmetric teleportation protocol with the trained operators, ψ^1 and ψ^2 , and $\mu = -12$ for: Model 2 (blue), and multiple instances of $N = 10$ SYK model (grey). (right) Mutual information for the symmetric teleportation protocol with all pairs of untrained operators, and $\mu = -12$. (c) Size-winding phase for each of the untrained operators at $t = 2.8$. (d-f) Depicts the analogous results for Model 3. As in [121], the teleportation protocol is performed with $\mu = -17$ for Model 3 (replicating Fig. S25 of [121]), and the size-winding phase is evaluated at $t = 2$ 102
- 5.1 (a) Butterfly metrology protocol with local control. The “butterfly state” is prepared by evolving forward and backward under a many-body unitary U , interleaved with a local rotation, $(\hat{1} + i\hat{V})/\sqrt{2}$. The signal ϕ is detected via oscillations in the local observable $\langle \hat{V} \rangle$. (b) The protocol performs interferometry between two trajectories. In the first (top), the forward and backward evolution cancel, yielding the polarized state $|\mathbf{0}\rangle$. In the second (bottom), the local perturbation yields a “scrambled” state, $i\hat{V}(t)|\mathbf{0}\rangle$. If U is scrambling, the two trajectories acquire macroscopically different phases under the signal, leading to a Heisenberg-enhanced sensitivity. 104

- 5.2 **(a)** Schematic of the polarization distribution $P(S_z)$ for (above) a GHZ state and (below) a butterfly state (Eq. 5.1), with evolution U corresponding to a Haar-random unitary. The butterfly state features a delta function at $S_z = N/2$ and bimodal distribution centered $S_z = 0$ with width $\sim \sqrt{N}$; the separation between the peaks is a factor of 2 away from the maximal separation exhibited by the GHZ state. **(b)** The sensing signal under Haar-random evolution features damped oscillations with a frequency $\omega = N$ (see Appendix D). **(c)** Metrological gain, $2N/\eta^2$, vs. N for (red) the Heisenberg limit, (black) the standard quantum limit, our sensing protocol with (blue solid) local and (dashed) global controls. For up to $N = 20$, the Haar-random prediction is in agreement with exact quantum dynamics of a 1D spin chain after the scrambling time (data points). **(d)** Improvement in sensitivity, η , as a function of evolution time, t , for a locally interacting system. The sensitivity initially as $\eta^{-1} \sim t^d$ owing to the ballistic operator growth and saturates at $\eta^{-1} \sim N$ at the scrambling time, t_s 106
- 5.3 Butterfly metrology with only global control. State preparation involves a global rotation $e^{i\epsilon\hat{S}_x}$. The signal is detected by measuring the total spin polarization $\langle\hat{S}_x\rangle$. 108
- 5.4 Numerical simulations for the sensing protocol under the dynamics of two experimental platforms. (a) The sensitivity of our protocol with *local* controls for a hybrid spin system, consisting of a single NV center surrounded by a cluster of P1 centers. The simulations are performed via exact diagonalization with $N \in [14, 20]$ total spins. After an initial growth period, the sensitivity saturates at $\eta = 2/N$ (dashed line), consistent with our expectation for fully scrambled dynamics. The inset displays the sensitivity for large-scale systems, $N \sim 10^4 - 10^5$, simulated via a stochastic growth model (Appendix D). (b) The metrological gain, $1/(N\eta^2)$, and sensitivity (inset) of our protocol with *global* controls implemented for a dense ensemble of NV centers. The total number of spins is $N \in [14, 20]$ spins. For both systems, the density of spin defects is 100 ppm, corresponding to an average nearest-neighbor interaction of ~ 1 MHz. 110
- 6.1 Adiabatic protocol to prepare the thermofield double (TFD) state. For couplings much greater than the interaction strength, $\mu \gg J$, the ground state of the coupled Hamiltonian, Eq. (6.1), resembles EPR pairs between the left and right system (left). For small couplings, $\mu \ll J$, the ground state is near the TFD state at a temperature set by μ (right). Our protocol prepares the TFD state by initializing EPR pairs and slowly decreasing the coupling along an adiabatic path $\mu(\lambda)$ 114

- 6.2 Comparison between the ground state of Eq. 6.1 (blue) and a TFD state with respect to Eq. 6.2 (orange). (a) Large- N numerical results for the left-right correlator, $i \langle \chi_L \chi_R \rangle$, in the two states as a function of single-side energy density, $\langle H_L \rangle$. The results are obtained by sweeping μ and β , respectively. (inset) By matching the left-right correlator in the two states, we obtain the effective temperature of the TFD state, β_{eff} as a function of μ . (b) Dynamical correlation function, $i \langle \chi_L(t) \chi(0) \rangle$ beginning in the ground-state at $mu = 0.2J$ (blue) and the TFD state (yellow) at the corresponding temperature, $\beta = \beta_{\text{eff}}(\mu) = 3.72J$. In both cases, the system is evolved under the uncoupled Hamiltonian, Eq. 6.2. Similar agreement holds for other values of μ within the range of numerical stability, i.e. $\mu \gtrsim 0.1J$ 116
- 6.3 Quenched dynamics of Eq. 6.1 simulated with large- N numerics for three types of protocols: (a) a sudden quench, (b) adiabatic cooling, and (c) a two-step non-adiabatic protocol. In all cases, the initial state is a low-temperature state of Eq. 6.1. (a) The coupling is suddenly reduced from $\mu = 0.4$ to $\mu = 0.38$ (above). This gives rise to oscillations in the single-side energy density, $\langle H_L \rangle / N$ (below). (Inset) The oscillation frequency as function of μ based on: (points) the quenched simulations, and (green) the predictions of the semi-classical framework using the mass and potential described in Appendix E. For comparison, the (off-diagonal) gap of Eq. 6.1 is also shown (purple), which was obtained by simulating Eq. 6.1 in imaginary time [94]. (b) The coupling is reduced in an adiabatic fashion; in particular, it follows an exponential decay profile, $\mu(t) = 0.5e^{-t/\tau}$ (above). As τ increases, the energy density of the final state decreases (below). The energy density of the ground state of Eq. 6.2 is shown as a dashed grey line. (Inset) The effective temperature of the final state, determined from the energy density, increases as a function of the decay time, τ . (c) The coupling is reduced suddenly under a single step (light red) and under two steps (dark red). The former shows analogous oscillations to the sudden quenches of (a). By timing the second step to minimum of the first oscillation, one can “catch” the system at this energy density. The resulting state has nearly the same energy density as the final state obtained via adiabatic cooling (dashed grey). The energy density, $\langle H_{\mu_f} \rangle / N$ is shown in terms of the final coupling, i.e. Eq. 6.1 with $\mu = 0.1$ 117

- 6.4 Finite-sized analysis of the ground state of Eq. 6.1 for systems with $N \in [8, 24]$ Majoranas per side. The overlap between the ground state and a TFD state is decomposed into two quantities: (a) the support within the diagonal sector, $\mathcal{N}_d = \sum_n |c_{nn}|^2$, and (b) the maximum overlap of the *normalized* diagonal wavefunction, $\mathcal{F}_d = \max_\beta \sum_n |c_{nn} e^{-\beta/2 E_n}|^2 / (\mathcal{N}_d Z_\beta)$. (c) For $N = 8$, the individual diagonal coefficients c_{nn} (points) are well-fit by a linear decay function, $A/(E_n - k)$, where k is a fitting parameter and A is constrained by normalization (solid lines). (d) For $N = 24$, the coefficients are fit by a different polynomial function, $A/(E_n - k)^p$, with $p \approx 4.5$ (inset). Despite the non-exponential behavior, the course-grained wavefunction, $\psi(E_n) \equiv \sqrt{\Omega(E_n)} c_{nn}$, where $\Omega(E_n)$ is the density of states is in reasonable agreement with the wavefunction for the best-fit TFD state (solid lines). Note that the number of coefficients has been subsampled for visual convenience. 122
- A.1 The numerical error of OTOCs computed with Krylov subspace methods compared to exact diagonalization. The error is quantified as the maximum difference in the OTOCs for timescales $tJ \leq 20$ (Eq. A.4). Error bars represent the standard deviation over 100 disorder realizations. 127
- A.2 Disorder fluctuations of the OTOCs, as measured by the standard deviation of t^* given by $1 - \tilde{F}(t^*) = 0.25$. Two sources of disorder contribute to the total fluctuations (solid): the Hamiltonian coefficients J_{ijkl} (dashed) and the initial random state (dot-dashed). (a-c) Fluctuations vs. system size for (a) $\beta J = 0.18$, (b) $\beta J = 1.8$, and (c) $\beta J = 18$. (d-f) Fluctuations vs. temperature for (d) $N = 16$, (e) $N = 24$, and (f) $N = 32$ 128
- A.3 Extracting λ by fitting to a simple exponential. (a) For each set of data, we apply least squares regression based on the fitting function, $a + b e^{\lambda_{\text{fit}} t}$, (dashed line) within a window $F_0 \leq F(t) \leq F_1$ (white area). (b) We then extrapolate λ_{fit} as a function of system size through quadratic function in $1/N$ (solid lines). The results are shown for $\beta J = 5.6$, $F_0 = 0.03$, and various values for F_1 . The dashed line represents the theoretical prediction for λ . (c) Extrapolated results for λ as a function of temperature for several values of F_1 ; these exhibit significant disagreement with the theoretical results (dashed line). (d) The theoretical curve for $\tilde{F}(t)$ at low temperatures, given by (A.6), (orange) compared to the leading-order simple exponential (purple). 130
- A.4 Extracting λ by fitting to the low-temperature, semiclassical solution, i.e. (A.6) with $\Delta = 1/4$. Analogous to Fig. A.3, we fit each set of data using least squares regression (a) and perform a $1/N$ extrapolation on the best-fit values for λ (b), as shown for $\beta J = 5.6$. (c) The extrapolated results for $\lambda(\beta)$ are compared with the theoretical prediction (dashed line); there is noticeable disagreement regardless of the fitting window specified by F_1 (in all cases $F_0 = 0.03$). 131

- A.5 Finite-size rescaling procedure for extracting λ . (a) For a fixed temperature, we numerically simulate OTOCs across a range of system sizes. At each system size, the time $t^*(N)$ is determined for which the (normalized) OTOC, $\tilde{F}(t) \equiv F(t)/F(0)$, reaches a fixed value, i.e. $\tilde{F}(t^*) = 1 - F_0$. Data shown correspond to $\beta J = 1.8$ and $F_0 = 0.25$. (b) The Lyapunov exponent λ is computed from the slope of $t^*(N)$ with respect to $\log N$ via an extrapolation procedure. (c) The extrapolation procedure is shown for each temperature and $F_0 = 0.16$ and 0.25 . We approximate $\lambda_{\text{fit}}(N)$ (data) by computing the finite difference $\Delta t^*(N)/\Delta(\log N)$ between successive system sizes. We then perform a $1/N$ extrapolation (solid lines) on the subset of system sizes (white area) whose first 20 eigenvalues are within $\Delta E = \beta J$ of the ground state. To avoid over-fitting, the extrapolation relies on a quadratic function for $\beta J \geq 5.6$ and a linear function for lower temperatures. 132
- A.6 Numerical data for unregularized (a) and regularized (b) OTOCs at various temperatures. (a) The unregularized data correspond to the real part of the OTOC normalized by the initial value and is shown for three different system sizes: $N = 12, 24$ and 40 . For $N = 12$ the lower temperature correlators grow faster than the high temperature correlators; this trend is reversed for $N \gtrsim 24$. (b) Compared to the unregularized data, the growth timescale for the regularized data increases significantly at low temperatures. This discrepancy is attributed to the difference in the scrambling time for the two types of correlators. In particular, the scrambling time for the unregularized OTOC is highly suppressed at low temperatures, implying that the observed growth in the numerics arises from dissipative dynamics rather than to chaos. (Inset) Schematic of the two configurations (unregularized and regularized), represented as a path in real (horizontal) and imaginary (vertical) time. 133
- A.7 The finite-size rescaling procedure applied to regularized (a) and unregularized (b) OTOCs. The data points corresponds to $\lambda_{\text{fit}}(N)$ for various size intervals and the dashed line is the theoretical prediction. The unregularized results exhibit a weaker temperature dependence, and there is a larger discrepancy from theoretical predictions at low temperatures. 134
- A.8 Schematic relationship between various theories describing the dynamics of the SYK model. The Schwinger-Dyson (SD) equations represent the large N solution at all temperatures (A.10), while the Schwarzian action (A.24) captures finite N behavior at low temperatures. In the limit $N \gg \beta \gg 1$, both theories approach the conformal limit (A.11). 135
- A.9 The normalized magnitude, C_1 , of the leading-order term in the OTOC, $C_1/Ne^{\lambda t}$, as a function of temperature. The magnitude is calculated numerically (black) for the regularized OTOC using (A.22); at high temperatures $C_1 \approx 1.4$ and at low temperatures $C_1 \approx 0.5\beta J$, in agreement with the semiclassical solution, (A.29) (blue). For the unregularized OTOC, the semiclassical solution predicts the low-temperature scaling $C_1 \sim (\beta J)^3$ (red). 139

- A.10 (a) Results for the imaginary-time Green’s function, $G(\tau)$, at $\beta J = 100$ from our numerics (left) and the solution of the Schwarzian action (right). (b) Finite-size scaling of $G(\tau = \beta/2)$. Our numerics (data) begin to agree with the Schwarzian solution (dashed line) at $N \approx 30$. For smaller sizes (gray area), we observe finite-size effects that cannot be accounted for by the Schwarzian action, which we attribute to the discreteness of the energy spectrum. 141
- A.11 The retarded Green’s function for the SYK model with 40 Majoranas (left), the Schwarzian action with $C_{\text{Sch}} = 0.4$ (middle), and the large N Schwinger-Dyson equations (right). The late-time behavior of the SYK results and the Schwarzian action is governed by the random-matrix-like form of the energy spectrum, which manifests as a non-monotonicity with respect to temperature. . . . 142
- B.1 Extended data for average operator size and size width in 1D **(a)** and 2D **(b)** RUCs. The average size grows ballistically $\sim t^d$ (dashed line) and saturates at $t_{\text{scr}} \sim L \sim N^{1/d}$. The size width matches the predictions from the KPZ universality class (dashed lines) and allows us to extract the prefactors in Eq. (3.56) and (3.57). In particular, we determine α_{bulk} and β_{bulk} from the saturation values (light gray), and α_{boundary} and β_{boundary} from the initial growth rate (dark gray). 165
- B.2 Teleporting multiple qubits ($n = 5$) in 1D, where the input qubits are evenly spaced in the system ($N = 10000$). **(a)** Teleportation is achieved with high fidelity for $t \leq 1300$ (Region I). This corresponds to the regime in which the light cones of the operators are non-overlapping. Interestingly, order-one fidelity can also occur for $1300 < t < 2600$ (Region II), when adjacent light cones have overlapped, but only for certain values of g . No multi qubit teleportation is possible for $t \geq 2600$ (Region III), as expected from the lack of size addition. **(b)** The three Regions can be detected by changes in the slope of the operator size as a function of time. In particular, the growth rate decreases when nearest neighbor light cones, then next nearest neighbor light cones, etc. begin to overlap. 166

- B.3 Procedure for determining the channel capacity in 0D RUCs. **(a-b)** For fixed n and K , we compute the per qubit fidelity while sweeping both the evolution time and coupling strength g . **(a)** The fidelity as a function of evolution time with coupling strength fixed is optimized at the first local maximum, which corresponds to $\eta_d g \mathcal{S} / N = \pi$. **(b)** After optimizing the evolution time, the fidelity as a function of the coupling strength g is maximal when g (and correspondingly the average operator size \mathcal{S}) is tuned to balance errors due to size addition and the finite number of couplings (see Section 3.7 for details). The data shown correspond to $n = 38$ and $K = 9000$. **(c)** The channel capacity is defined as the maximum number of qubits that can be teleported while maintaining the fidelity per qubit above a fixed threshold, i.e. $1 - F_{\text{EPR}}^{(1)} \leq 0.07$ (dashed line). To determine this number, we fit the optimal fidelity as a function of n (for each K) with a linear fit in log space and compute the intercept of the fit with the threshold fidelity. The fits approximately collapse with respect to n/K , indicating that the channel capacity is linear in K 167
- C.1 **(a)** Four-point correlation functions, $F_{ij}(t)$, for Model 1, shown for all pairs of Majorana operators, $i < j \in [1, 7]$. **(b)** The same correlation functions for a specific instance of the $N = 10$ SYK model with $J = 1.125$ and $i < j \in [1, 10]$. . . 181
- C.2 **(a)** Mutual information of the teleportation protocol with fixed injection time as a function of the readout time (i.e. $t_0 = 2.8$ and $t = t_1$). The mutual information for Model 1 and the trained operators, ψ^1 and ψ^2 , is in reasonable agreement with that of multiple instances of the $N = 10$ SYK model (grey). **(b)** The mutual information for Model 1 and all pairs of untrained operators, ψ^i and ψ^j with $i < j \in [2, 7]$, exhibits variations and revivals as a function of time. **(c)** The mutual information for all pairs of operators in the $N = 10$ SYK model exhibits a single consistent peak. 182
- C.3 Phase alignment, \bar{r} , of the random all-to-all Ising model as a function of the system size $N \in [4, 8]$, with $J = 0.17$ and $\beta = 4$. Three disorder realizations are shown at each system size, with small horizontal offsets for clarity. 184
- D.1 The general form of an echo protocol, which underlies previous time-reversal-based sensing proposals. In contrast to our protocol, time-reversed evolution is employed only in the detection stage, rather than during the state preparation. 186

- D.2 Global sensitivity as a function of $\bar{\epsilon}$ for the measurement operator (blue) S and (orange) $M = 2 \sin(\epsilon S)$. We observe excellent agreement between the analytic prediction for Haar-random evolution (solid line) and the late-time dynamics of a $N = 18$ spin system (points). The spin system consists of all-to-all, random two-body terms: $H = \sum_{i < j} \sum_{\mu, \nu} J_{ij}^{\mu\nu} \sigma_{\mu}^i \sigma_{\nu}^j$, where $\mu, \nu \in \{X, Y, Z\}$ and $J_{ij}^{\mu\nu}$ is drawn from a Gaussian distribution with standard deviation J/\sqrt{N} . The evolution time is $tJ = 10$. Similar results are obtained for generic Hamiltonians evolved past the scrambling time, though the agreement is not as precise as the disordered, all-to-all spin system at the accessible system sizes. 189
- D.3 Two protocols for measuring the real part of $\Phi(\phi)$. (a) The first protocol is identical to the original protocol with local controls [Fig. 1(a) of Chapter 5], except we replace the local rotation $e^{i\frac{\pi}{2}4\hat{V}} \sim \hat{1} + i\hat{V}$ with a local projection, e.g. $|0\rangle\langle 0| \sim \hat{1} + \hat{Z}$. (b) The second protocol, which we dub a “double echo”, involves applying the butterfly state preparation circuit and its inverse. The final state is measured in the computational basis, and either the return probability to the initial state or the average polarization is computed. This approach may be applied with either local or global controls to prepare the butterfly state. . . 191
- D.4 Comparison between the stochastic model (solid lines) and exact dynamics (dashed) for the two proposed spin models at small sizes. (a) The sensitivity for the local protocol using the hybrid spin system. (b) The metrological gain for the global protocol using an ensemble of NV centers. The stochastic model is plotted with respect to the number of discrete time steps, while the exact dynamics are plotted with respect to continuous time evolution. By comparing the results, we estimate the conversion factor between discrete steps and continuous evolution time. We average the stochastic model over $\sim 10^4$ realizations (i.e. different Clifford circuits) and the exact dynamics over ~ 10 positional configurations. 193
- D.5 A pulse sequence for engineering the hybrid spin Hamiltonian H (Eq. D.14) into \tilde{H}^+ (Eq. D.18). The sequence consists of two frame rotations with equal duration, τ . In the first, a $\pi/2$ pulse applied along the X direction brings P_z into P_y and P_y into $-P_z$. In the second, a $\pi/2$ pulse applied along the Y direction brings P_z into P_x and P_x into $-P_z$. By rotating in the opposite direction (i.e. switching $\pi/2$ into $-\pi/2$ and vice versa), the pulse sequence instead generates \tilde{H}^- 195

D.6 Numerical simulations of our protocol with four proposed experimental platforms: (a) Rydberg dipolar atoms in two-dimensions, i.e. Eq. D.13 with $a/r_{ij} = 1$ for nearest neighbors; (b) atoms in an optical cavity, i.e. Eq. (D.27-D.28), with (left) $s = -\frac{1}{2}$ and (right) $s = \frac{1}{2}$; (c) superconducting qubits with analog interactions, Eq. D.29; (d) trapped ions under a non-local, random unitary circuit. In (a),(c), and (d), the protocol with local controls is performed and the initial state is a random product state in the X basis (averaged over ~ 10 realizations). In (b), we implement the protocol with global controls and a fully polarized state initial state, $|\mathbf{0}\rangle = |+\rangle^{\otimes N}$. The circuit geometry for the trapped ion simulations is shown in (d). Each layer consists of $N/2$ two-qubit gates (yellow), acting on random pairs of qubits, and a random-qubit rotation on each of the qubits (blue). 205

D.7 Illustration of the effect of errors on our sensing protocol. Errors within the light-cone of \hat{V} (red dashed areas) suppress the coherence between the two trajectories of the butterfly state. Errors within the light-cone of a local polarization operator σ_i^z (blue dashed areas, shown for a representative polarization operator) suppress the polarization of the first trajectory of the butterfly state. The sensitivity of the protocol is affected by both types of errors, and is thus suppressed proportional to the local error rate γ multiplied by the space-time volume of the four light-cones. Note that initialization and readout errors can be included in this diagram as well; since they only act at times when the light-cones have size one, they have only an $\mathcal{O}(1)$ effect on the sensitivity. 206

List of Tables

3.1	Summary of our expectations for teleportation in a variety of physical models. For each model, we specify the associated teleportation mechanism, the optimal value of the coupling strength g , the optimal teleportation fidelity, and the channel capacity. Here G_β is the imaginary time two-point function (Section 3.5), $\mathcal{S}(t)$ is the size of a time-evolved operator, K is the number of measured qubits [Fig. 6.1(a)], $\eta_d = 1/(1 - 1/d^2)$ is an order one constant determined by the local qudit dimension d [Sec. 3.4], and G_N is Newton's constant. We refer to the Summary of Results and the cited sections for further details.	31
5.1	Summary of proposed implementations.	111
A.1	Summary of computational requirements for computing OTOCs using Krylov subspace methods [2]. All computations in this work were performed using matrix-free methods; for comparison, we also list the memory requirement for standard, full-matrix computations.	125
D.1	Summary of proposed experimental platforms.	195

Acknowledgments

It is often said that we are the average of the five people we spend the most time with. In my experience, this would be a significant underestimate for the number of inspiring individuals who have contributed to my formation as a scientist and left a lasting impact on my research trajectory. I can only hope to acknowledge here a small subset of these remarkable people.

First and foremost, I would like to thank my advisor, Norman Yao, for giving me the opportunity to pursue this research and looking after my development, both personally and academically, in countless ways. There are very few people I know whose character embodies the phrase “larger than life”, and Norm is undoubtedly one of them. Anyone who has worked with Norm will surely develop this impression, so there is hardly a need for further elaboration. Suffice it to say that I consider myself extremely fortunate to have joined Norm’s group early on and spent many of my happiest and most stimulating years basking in his infectiously positive and nurturing presence. I truly cannot imagine a more fulfilling PhD experience than under his mentorship.

My graduate years have also benefited from the wonderful scientific atmosphere created by the other members of the Yao group. I am especially amazed by the talents and determination of the first crop of experimentalists—Thomas Mittiga, Satcher Hsieh, Pra Bhattacharyya, and Chong Zu—who successfully built the group’s lab from scratch and within a few years turned it into an unstoppable scientific enterprise. I reflect with immense pride on my small role in the initial experiments and on our collective actions towards establishing sustainable working conditions for the group through our attempted coup. I am equally impressed by the creative and collaborative spirit of the theorists in the group, including Francisco Machado, Kamphol (Best) Akkaravarawong, Bingtian Ye, Tommy Schuster, Max Block, Chris Olund, Marcus Bintz, and Greg Kahanamoku-Meyer. It has been remarkable to “grow up together” as physicists, branch out and discover our own research niches, and, more recently, take our first tentative steps into the world beyond graduate school. I would especially like to acknowledge Tommy, my co-author—and *de facto* co-advisor—on essentially all the work presented in this thesis. I have time and time again been blown away by his pure brilliance and clarity of thought. It is an honor to have been his longterm collaborator and confidante, and I cannot imagine where the projects in this thesis would have ended up without his vital involvement.

I would like to thank many other collaborators whose insights and personalities are imprinted upon this body of research. I am particularly grateful to Zhenbin Yang for guiding me into my initial foray into holography and providing critical advice ever since. I thank Douglas Stanford and Ping Gao for providing invaluable feedback and for patiently sharing with me their knowledge of black holes. I thank Ben Nachman and Chris Bauer for teaching me about particle physics and involving me in our fully remote, “lockdown” project. I thank Vincent Su and Hugo Marrochio for our brainstorming and coffee sessions in the BCTP. I thank Jarrod McClean and Kostya Kechedzhi for mentoring me during my research stints

at Google and ensuring that my physics training will be put to good use after graduation. I am looking forward to building quantum computers with them for years to come!

My gratitude extends to the entire Berkeley physics department for providing a vibrant academic community and social atmosphere. I am particularly thankful for the wisdom and inspiration I have received from many former post-docs (and now professors), including Felix Flicker, Snir Gazit, Thomas Scaffidi, Soonwon Choi, Jack Kemp, and Emily Davis. I would like to thank Brad Mitchell, Nick Dale, Andy Bierkert, Nikola Maksimovic, Ven Chandrasekaran, and the other members of my graduate cohort for keeping my life balanced, navigating with me through Berkeley's volatile housing scene, and sharing innumerable deep dish pizzas from Zachary's.

Looking back, I would like to acknowledge many other encouraging figures from my undergraduate days at Cornell. I am indebted to Paul McEuen for providing me with my first taste for research and exemplifying for me what it means to be a great scientist. I thank the members of the McEueun group, especially Peter Rose, Alejandro Cortese, Jonathan Alden, and Melina Blees, for their patience and mentorship as I fumbled my way through the early stages of research. I thank my professors, Peter Wittich, Tom Hartman, and Yuval Grossman, for guiding me through my undergraduate years and giving me the confidence to pursue graduate school. I would also like to acknowledge my mentors at ICFO in Barcelona, Adrian Bachtold and Alexandros Tavernarakis, for expanding my research horizons and providing me with a blissful year full of personal development.

Above all, I am grateful for the loving support I have received from my family and friends, as I have spent many years chasing my dreams. Starting with my childhood fascinations with watches and origami, followed by my teenage determination to move first across the country and later even farther, my parents have consistently encouraged me to follow my heart and provided me with every conceivable opportunity for success. I am grateful to my big sister, Cassie, for keeping me grounded all these years and for looking after me from afar, and to my brother-in-law, Alex, for taking good care of her. Finally, I thank my life partner, Basak, for accompanying me on this long and wonderful journey and nurturing me with her love at every step of the way. Sensiz olmaz, tatlim.

Citations to previously published work

The work presented in this thesis is adapted from previously published work. In order of appearance:

Chapter 2 is adapted from:

B. Kobrin, Z. Yang, G. D. Kahanamoku-Meyer, C. T. Olund, J. E. Moore, D. Stanford, N. Y. Yao, “Many-body chaos in the Sachdev-Ye-Kitaev model.” *Physical review letters* 126.3 (2021): p. 030602.

Chapter 3 is adapted from:

T. Schuster*, B. Kobrin*, P. Gao, I. Cong, E. T. Khabiboulline, N. M. Linke, M. D. Lukin, C. Monroe, B. Yoshida, N. Y. Yao, “Many-body quantum teleportation via operator spreading in the traversable wormhole protocol”. *Physical Review X* 12.3 (2022), p. 031013.

Chapter 4 is adapted from:

B. Kobrin, T. Schuster, N. Y. Yao, “Comment on ‘Traversable wormhole dynamics on a quantum processor’ ”. arXiv:2302.07897 (2023).

Chapter 5 is in preparation for publication as:

B. Kobrin*, T. Schuster*, M. Block, B. Mitchell, E. Davis, N. Y. Yao, “Butterfly Metrology: A Universal Protocol for Quantum-Enhanced Sensing" (in preparation, 2023).

Chapter 6 is in preparation for publication as:

B. Kobrin*, T. Schuster*, V. P. Su, H. C. Marrochio, N. Y. Yao, “Adiabatic preparation of thermofield double states" (in preparation, 2023).

Chapter 1

Introduction

Modern physics rests upon two pillars developed in the early twentieth century: quantum mechanics and general relativity. Quantum mechanics is the framework that describes the behavior of microscopic particles, encompassing everything from the elementary particles probed at the large Hadron collider to the electronic devices that enrich our everyday lives. General relativity is the theory that governs the universe on cosmological scales, offering insights into the formation of galaxies and making predictions regarding the existence and behavior of enigmatic celestial phenomena, such as black holes. At the core of fundamental physics lies the persistent quest to reconcile these two theoretical frameworks, which have, for generations, appeared to be fundamentally incompatible with each other.

In the past few decades, tremendous progress has been made towards laying the foundation for a unified quantum theory of gravity. This endeavor has not only advanced our fundamental understanding of the universe but has also generated a surprising collision between the traditionally independent disciplines of atomic physics and high-energy physics. The work in this thesis explores recent developments that have emerged as a by-product of this collision, centering around the topic of *quantum information dynamics*. But, before getting there, let us start with a brief historical background.

From black holes to quantum computers

The seeds of a quantum theory of gravity can be traced to Stephen Hawking's seminal calculations on black hole radiation in the 1970s [110]. By adding small quantum corrections to classical general relativity, Hawking showed that matter does, in fact, escape a black hole in the form of radiation, eventually leading to the complete evaporation of the black hole itself. This immediately raised a question: Can one recover information swallowed by a black hole during its formation? Hawking's calculation unambiguously predicted a negative answer. However, this conclusion violated the central principle of unitarity in quantum mechanics—which implies that information can never truly be destroyed—resulting in the famous black hole information paradox.

In the 1990s, a major step was taken towards developing a more precise formulation of quantum gravity with the introduction of the *holographic principle* and its specific realization in the AdS/CFT correspondence [114, 169, 240]. This correspondence posits an exact mapping between two physical systems: a “bulk” system which is governed by a theory of quantum gravity, and a “boundary” system that is governed by ordinary quantum mechanics (without gravity). The notion of holography refers to the fact that the bulk system features one extra spatial dimension compared to the boundary, as in a hologram. Notably, only certain types of theories are known to satisfy this correspondence; anti de-Sitter (AdS) space refers to a specific type of spacetime (the opposite of the one we live in), and conformal field theory (CFT) refers to a special quantum field theory which possesses a high degree of symmetry. Nevertheless, among these theories, all features could in principle be mapped from the bulk to the boundary; in other words, gravitational phenomena could be explained from the perspective of pure quantum mechanics, and vice versa.

Over the last decade, accelerated progress has occurred towards fleshing out this holographic “dictionary” and applying it to resolve long-standing puzzles about quantum gravity. Two major trends stand out among the recent developments. First, motivated by the original black hole information paradox and subsequent variations, there has been a strong emphasis on quantum information theory to understand the structure and dynamics of gravity. An important early breakthrough was the formulation of a relationship linking the area of a region to the amount of entanglement, or quantum information, encoded in that region [214]. Recently, an application of this relationship provided the first evidence for a correction to Hawking’s calculation and supported the conclusion that information can, indeed, be recovered from the radiation of a black hole [7, 8, 193, 194]. In other scenarios, the dynamics of quantum information can be viewed as particles traveling through spacetime geometries, such as traversable wormholes [90, 176]. What unifies these examples and numerous others is the ability to interpret quantum information, a seemingly abstract property, from a geometric perspective.

The second noteworthy development was the discovery of a “toy model” of holography. In 2015, Alexei Kitaev demonstrated a holographic duality between a simple quantum system of interacting fermions, now known as the Sachdev-Ye-Kitaev (SYK) model, and a low-dimensional theory of gravity [133, 173, 218]. Owing to their relative simplicity, both systems admit a large degree of analytical control and have enabled calculations that reveal subtle properties about the nature of quantum gravity. Additionally, unlike prior examples of the AdS/CFT correspondence, the SYK model constitutes a *microscopic* quantum system (represented as a many-body Hamiltonian) rather than a quantum field theory. Consequently, discoveries in the realm of gravity can be seamlessly translated into the language of discrete, many-body systems. This presents novel prospects for reinterpreting and generalizing gravitational phenomena from a microscopic perspective, leveraging the tools of atomic many-body physics. Coupled with the emergence of large-scale quantum technologies, it also suggests a new *experimental* possibility: By implementing protocols on a controllable quantum device, such as a quantum computer, one could hope to validate and discover features about the nature of quantum gravity.

Motivation and overview of this thesis

This thesis focuses on quantum information dynamics, a topic which lies at the intersection of the above recent trends. Our central questions are: How does locally encoded quantum information spread across a complex quantum system under unitary dynamics? And how can this information be recovered? The original motivation for these questions owes much to the study of black hole thermalization. Indeed, the special nature of quantum information dynamics in black holes provided a key signature for the holographic interpretation of the SYK model and remains one of the sharpest diagnostics of gravitational behavior. Yet, the ideas and tools that emerged in this context extend to more general quantum systems, forming the basis for new perspectives on several widespread topics in quantum many-body physics, including quantum thermalization, chaos, and metrology.

The work in this thesis aims to build upon these connections. Specifically, we utilize the powerful framework of holography, and its concrete realization in the SYK model, to draw general lessons about quantum many-body systems and inspire novel protocols for characterizing and leveraging quantum information dynamics. Along the way, we provide a microscopic interpretation for several gravitational phenomena, and we demonstrate how these phenomena generalize as one perturbs away from the gravitational limit. In turn, this understanding provides a foundation for the long-term goal of designing and interpreting experimental protocols to probe aspects of quantum gravity on a quantum computer.

The rest of the thesis is organized as follows:

- In the remainder of this Chapter, we provide a brief pedagogical introduction to the relevant topics of this work. We first define the notion of quantum information scrambling, as characterized by out-of-time-order correlators (OTOCs), and draw connections with operator size distributions and semiclassical chaos. We next introduce the SYK model and its relation to extremal black holes. Lastly, we discuss quantum teleportation and its role in understanding the recovery of information from a black hole.
- In Chapter 2, we present an in-depth study of thermalization and scrambling in the SYK model. Our key results include the first numerical verification of maximal quantum chaos, as well as the direct observation of quantum fluctuations in gravity. More broadly, our work highlights the importance of finite-temperature and finite-size effects in the study of holography in microscopic systems.
- The subsequent three Chapters are related to a novel quantum communication protocol motivated by the recent discovery of traversable wormholes. In Chapter 3, we show that the same protocol can succeed via two distinct mechanisms: the gravitational mechanism and a “peaked-size” mechanism. We show that the peaked-size regime occurs across a diverse landscape of quantum systems, ranging from the SYK model at high temperatures to random quantum circuits, and is related to “stringy” corrections in gravity. We discuss how the traversable wormhole protocol can be utilized to distinguish between generic and intrinsically gravitational scrambling dynamics.

- In Chapter 4, we comment on a recent experiment that implements the traversable wormhole protocol on Google’s quantum processor. Our discussion underscores the subtleties that arise in interpreting experimental observations in small-sized systems as signatures of gravity.
- In Chapter 5, we propose a novel scheme for quantum metrology based on a modification of the traversable wormhole protocol, which we refer to as “butterfly metrology”. This protocol allows us to establish an explicit relation between quantum information scrambling and quantum-enhanced sensing. We demonstrate that Heisenberg-like sensitivity can be achieved in a wide variety of quantum architectures which feature time-reversed interactions.
- In Chapter 6, we propose and analyze an adiabatic scheme to efficiently prepare the thermofield double (TFD) state in the SYK model. This state corresponds to a geometry of a two-sided black hole and forms the backbone for the teleportation protocol discussed above. Our scheme is motivated by the physics of *eternal* traversable wormholes and hinges on a microscopic interpretation of a gravitational mode known as the boundary graviton.

Before we dive in, I would like to briefly mention another set of directions I explored during my graduate studies. Motivated by the experimental efforts of the Yao research lab, I became interested in applications of quantum sensing and analog quantum simulation using spin defects in diamond—in particular, nitrogen-vacancy (NV) centers. For the former, I contributed to the development of a theoretical model for the charge environment of the NV centers [182], a proposal for optically enhanced electric-field sensing [34], and the development of the sensing capabilities of NV centers under high pressure [30, 117]. For the latter, I provided theoretical support for understanding the dynamics of strongly interacting dipolar spins, with a focus on the emergence of anomalous spin diffusion [278] and the nature of many-body spin noise [67]. These studies, although not directly related to holography, helped cultivate my interests in quantum sensing and simulation, which are common threads throughout this work.

Note on author contributions—The main body of this thesis is adapted from collaborative efforts on behalf of many authors. Although it is difficult to distinguish the roles of each author, I would like to highlight several particularly important contributions. In Chapter 2, Zhenbin Yang advised the numerical analysis and performed the gravitational calculations; Greg Kahanamoku-Meyer developed the numerical software for performing the large-scale simulations and provided numerical support; and Chris Olund laid the groundwork with preliminary simulations and analysis. Building upon these contributions, I performed the large-scale simulations, developed the fitting methodology, and performed the data analysis. The remaining Chapters are devoted to collaborations led by Thomas Schuster and myself, in which both of us contributed extensively to all aspects of the work. In addition, in Chapter 3, Ping Gao contributed to the theoretical calculations and gravitational interpretation; in

Chapter 5, Maxwell Block contributed to the development of the protocol; and, in Chapter 6, Vincent Su contributed to developing and performing the numerical simulations.

1.1 Quantum information scrambling

Quantum information scrambling describes the process by which initially local information becomes increasingly non-local under quantum dynamics. While this process is ubiquitous among interacting quantum systems, the *way* in which it occurs depends on the specific nature of the system. Indeed, scrambling dynamics provided an early clue of the special microscopic structure of black holes and remains a key signature for understanding and identifying holographic systems.

Let us first illustrate the concept of information scrambling with a simple microscopic example. Consider a collection of N qubits, in which one of the qubits is initialized in a pure state and the rest of the system is in a fully mixed state. We can describe the initial state of the system as $\rho = \frac{1}{2^N}(\mathbb{1} + \hat{V}) \otimes \mathbb{1}_{N-1}$, where \hat{V} is a local operator acting on the first qubit. For example, $\hat{V} = \hat{Z}$ implies that the first qubit is initialized in the state $|0\rangle$. The system evolves under an interacting Hamiltonian, H , for time t . A key question is: How easily can one determine the original state?

An intuitive way to address this question is by considering the evolution of the local operator in the Heisenberg picture. At time t , the operator becomes $\hat{V}(t) = e^{-iHt}\hat{V}e^{iHt}$. We can detect the extent of this operator by taking a commutator with a local operator on a different qubit, \hat{W} , i.e. $[\hat{V}(t), \hat{W}]$. Initially, this commutator is zero, but over time, $\hat{V}(t)$ will become more complex, and the operators will cease to commute. To quantify the degree to which they fail to commute, we can measure the square of the commutator:

$$C(t) = \text{tr} \left[[\hat{V}(t), \hat{W}]^2 \right]. \quad (1.1)$$

Note that taking the square is important; if one were to measure commutator itself, the trace would involve the sum over complex eigenvalues, which would generally lead to large destructive interference. A simple expansion of the above expression yields

$$C(t) = 2\text{tr} \left[\hat{V}(t)\hat{W}\hat{V}(t)\hat{W} \right] + 2. \quad (1.2)$$

The correlators that appear here are known as *out-of-time-order* correlators (OTOCs) [133, 150, 228].

The behavior of such correlators is dependent on the system's dynamics. For example, consider a system with local interactions in one dimension. At early times, the time-evolved operator $\hat{V}(t)$ is constrained to a relatively small region localized at the initial site. But as time passes this region grows, typically with a wavefront that travels ballistically. By measuring OTOCs, one can detect the extent of the growth, e.g. the OTOC with respect to \hat{X}_i decays once $\hat{V}(t)$ has spread to site i . When the OTOCs for all operators have decayed,

it indicates that the wavefront has reached the edge of the system. This timescale is known as the *scrambling time*, t_s . For a spatially local system in d dimensions, owing to the ballistic growth, one expects the scrambling time to scale as $t_s \sim N^{1/d}$.

Over the past two decades, the scrambling behavior of black holes, and its specific characterization via OTOCs, has been a central topic in holography. There are two key features that characterize black hole dynamics:

1. The scrambling time for black holes is $t_s = \frac{1}{\lambda} \log N$, where λ is the so-called Lyapunov exponent. Such systems are known as *fast scramblers* [226]. From a microscopic perspective, this behavior indicates that the interactions are non-local, e.g. all-to-all interactions.
2. The Lyapunov exponent is given by $\lambda \approx 2\pi T/\hbar$, where T is the temperature of the system. This rate saturates a universal upper bound and is thus referred to as *maximal chaos* [171].

Satisfying these two properties is generally considered a necessary condition for a quantum system to be dual to a black hole. The latter requirement, in particular, remains one of the sharpest indicators of gravitational behavior.

In the next section, we show that the SYK model (at low temperatures) indeed satisfies both properties and possesses a well-defined gravitational dual. Subsequently, we discuss the close relationship between information scrambling and quantum teleportation. This was an integral part of the original motivation for considering the nature of scrambling in black holes and lays the foundation for understanding the traversable wormhole protocol.

Before proceeding, however, let us discuss two important perspectives on OTOCs, which help elucidate their role as a diagnostic tool and their behavior under different physical settings.

Relation to operator size

We begin by introducing the notion of *operator size* and outlining its connection to OTOCs. A formal way to describe the dynamics of a time-evolved operator $\hat{V}(t)$ is to decompose $\hat{V}(t)$ into a complete operator basis. For bosonic qubits, the natural basis is strings of Pauli operators, e.g. $\hat{X} \otimes Z \otimes \hat{1} \otimes \hat{Y} \otimes \hat{1}$. As discussed in Chapter 3, generalizations of this basis exist for high-dimensional qudits or fermionic operators. Explicitly, we write $\hat{V}(t)$ as

$$\hat{V}(t) = \sum_R c_R(t) \hat{R} \tag{1.3}$$

where the sum is over all 4^N Pauli strings in an N -qubit system, and c_P are real coefficients satisfying $\sum_R |c_R(t)|^2 = 1$. We now show that individual OTOCs, and sums over OTOCs, allow us to probe various properties of the distribution $|c_R(t)|^2$.

Let us start with an individual OTOC between $\hat{V}(t)$ and a Pauli operator \hat{W} . Expanding in the Pauli basis, we have

$$\frac{1}{d} \text{tr} \left[\hat{V}(t) \hat{W} \hat{V}(t) \hat{W} \right] = \sum_R |c_R(t)|^2 \eta_{R,W}, \quad (1.4)$$

where $d = 2^N$ accounts for normalization, and

$$\eta_{R,W} = \begin{cases} 1, & \text{if } [\hat{R}, \hat{W}] = 0 \\ -1, & \text{otherwise.} \end{cases} \quad (1.5)$$

Thus, the OTOC simply measures the probability that $\hat{V}(t)$ commutes with \hat{W} .

Next, consider the average OTOC between $\hat{V}(t)$ and the four Pauli operators on site i (including the identity). Taking the sum explicitly, we have

$$\sum_{W \in \{X_i, Y_i, Z_i, \mathbb{1}_i\}} \frac{1}{4d} \text{tr} \left[\hat{V}(t) \hat{W} \hat{V}(t) \hat{W} \right] = \sum_R |c_R(t)|^2 \delta_{R, \mathbb{1}_j}, \quad (1.6)$$

where

$$\delta_{R, \mathbb{1}_j} = \begin{cases} 1, & \text{if } \hat{R} \text{ is the identity on site } i \\ 0, & \text{otherwise.} \end{cases} \quad (1.7)$$

This has a simple interpretation: the average OTOC measures the probability that $\hat{V}(t)$ has support on site i .

Following this logic, we can sum over local OTOCs on all sites to measure the average number of sites that $\hat{V}(t)$ has support on. Explicitly, we have:

$$\sum_{i, W \in \{X_i, Y_i, Z_i, \mathbb{1}_i\}} \frac{1}{4d} \text{tr} \left[\hat{V}(t) \hat{W} \hat{V}(t) \hat{W} \right] = \sum_R |c_R(t)|^2 \mathcal{S}[\hat{R}], \quad (1.8)$$

where $\mathcal{S}[\hat{R}]$ counts the number of non-identity operators in \hat{R} . For example, for $\hat{R} = \hat{X} \otimes Z \otimes \hat{\mathbb{1}} \otimes \hat{Y} \otimes \hat{\mathbb{1}}$, we have $\mathcal{S}[\hat{R}] = 3$. The above relation establishes a precise connection between the decay of OTOCs and the average *operator size* of $\hat{V}(t)$ [202]. For example, in a local one-dimensional system, one typically finds that number of local OTOCs that have decayed increases linearly in time, indicating the linear growth in the size of $\hat{V}(t)$. Alternatively, in a fast scrambling system, the exponential decay of all local OTOCs implies that the operator size of $\hat{V}(t)$ grows exponentially in time.

More generally, we can describe the growth of the operator $\hat{V}(t)$ in terms of an *operator size distribution* [202, 208]. This (normalized) distribution $P(\mathcal{S})$ is defined as

$$P(\mathcal{S}) = \sum_{R: \mathcal{S}[R]=\mathcal{S}} |c_R(t)|^2. \quad (1.9)$$

While the sum over local OTOCs probes the first moment of this distribution, the full distribution contains much more information about the operator growth dynamics. For example, generic local interacting systems feature tightly peaked distributions, whereas all-to-all interacting systems feature broad distributions. In Chapter 3, we discuss measurements that probe the full operator size distribution, its characteristic behavior in different physical settings, and its consequences for performing teleportation.

We note that the discussion so far has been restricted to characterizing the dynamics at infinite temperature. Generalizing operator growth dynamics and information scrambling to finite-temperature dynamics leads to subtleties related to thermal regularization (see Chapter 2 for a detailed discussion). In the context of traversable wormholes, the natural generalization is to consider the time-evolved operator [202],

$$\rho_\beta^{1/2} \hat{V}(t) = \sum_R c_R(t) \hat{R} \quad (1.10)$$

where $\rho_\beta = e^{-\beta H} / \text{tr}[e^{-\beta H}]$ is the thermal Gibbs ensemble at inverse temperature β for the many-body Hamiltonian H . The coefficients $c_R(t)$ are now complex. They can be described by a (real) size distribution defined above, as well as a (complex) winding size distribution, defined as [44]

$$f(\mathcal{S}) = \sum_{R: \mathcal{S}[R]=\mathcal{S}} c_R^2(t). \quad (1.11)$$

For the SYK model, the complex phase of $f(\mathcal{S})$ exhibits a subtle property known as “size-winding”. This behavior provides a microscopic interpretation for the gravitational mechanism of traversable wormholes [44]. It forms a central part of the discussions in Chapters 3 and 4.

Relation to semiclassical chaos

A second perspective on OTOCs is via the lens of semiclassical chaos. To begin, consider a classical system with a single degree of freedom characterized by p and q . For concreteness, one can imagine p and q as the position and momentum of a billiard ball in a stadium. Chaos implies that two nearby trajectories will deviate exponentially in time—the so-called butterfly effect. An indication of this deviation is given by $\partial q(t) / \partial q(0) = \{q(t), p(0)\} \sim e^{\lambda t}$, where $\{\cdot, \cdot\}$ is a Poisson bracket.

Let us now translate this behavior to a quantum system in the semiclassical limit, $\hbar \rightarrow 0$. At early times, we can describe the quantum dynamics by quantizing q and p and replacing the Poisson bracket with a commutator: $\{q(t), p(0)\} \rightarrow \frac{1}{i\hbar} [\hat{q}(t), \hat{p}(0)]$. We then take the thermal average and, before doing so, square the commutator to avoid phase cancellation. This leads to [171]

$$C(t) = \text{Tr} [[\hat{q}(t), \hat{p}(0)]^2] \approx \hbar^2 \langle \{q(t), p(0)\}^2 \rangle, \quad (1.12)$$

where $\langle \cdot \rangle$ is the phase space average. Classical chaos thus implies $C(t) \sim \hbar^2 e^{2\lambda t}$, and the scrambling time is $t_s \sim 1/\lambda \log \hbar^{-1}$.

We emphasize that this perspective on OTOCs only applies to systems in the semiclassical limit ¹. Such systems can generally be divided into two categories:

1. Conventional semiclassical systems, for which the system’s action is much greater than \hbar . These systems include the aforementioned semiclassical billiard balls (for which $\hbar \rightarrow 0$), as well as large-spin models (for which $S \gg 1$).
2. *Large-N* systems, for which the semiclassical limit is $1/N \rightarrow 0$. For such systems, the effective Plank constant $\hbar_{\text{eff}} = 1/N$, and the scrambling time is $t_s \sim 1/\lambda \log N$.

We observe a direct correspondence between fast scramblers, described in the previous section, and large-N chaotic systems.

In a seminal paper, Maldacena, Shenker, and Stanford showed that *any* quantum system whose OTOCs exhibit exponential growth is characterized by a Lyapunov exponent that is universally bounded [171]:

$$\lambda \leq \frac{2\pi T}{\hbar} \quad (1.13)$$

Prior holographic calculations demonstrated that black holes saturate the upper bound, $\lambda \approx 2\pi T/\hbar$ [171, 209, 228]. In fact, the exponent comes from a simple, universal effect in which the energy of infalling particles is “blue-shifted” as they approach the black hole horizon. This indicates that the dynamics of black holes is very special: They are the most chaotic systems in nature!

In Chapter 2, we study the behavior of OTOCs in the SYK model and provide the first direct numerical evidence for the saturation of the above bound. We also discuss a subtlety regarding the regularization of finite-temperature OTOCs. To be precise, the derivation of the chaos bound considered “regularized” OTOCs of the form [171]

$$\text{Tr} \left[\rho_\beta^{1/4} \hat{V}(t) \rho_\beta^{1/4} \hat{W} \rho_\beta^{1/4} \hat{V}(t) \rho_\beta^{1/4} \hat{W} \right]. \quad (1.14)$$

Much debate followed about the importance of regularization and whether “unregularized” OTOCs, e.g. $\text{Tr} \left[\rho \hat{V}(t) \hat{W} \hat{V}(t) \hat{W} \right]$, could violate the bound [161, 212]. In Chapter 2, we resolve aspects of this debate by showing analytically that the Lyapunov exponent is independent of regularization for a large class of large-N systems, including the SYK model.

1.2 The SYK model: a toy model of holography

We are now ready to introduce the lead actor in our story: the SYK model. Although first introduced by Sachdev and Ye in 1993, the model was rediscovered by Alexei Kitaev

¹Even in such systems, there are many subtleties equating the exponential growth of OTOCs and the presence of classical chaos [118, 257].

in 2015, who provided a simpler microscopic form and demonstrated the first evidence for a gravitational interpretation [133, 218]. In what follows, we briefly summarize the key features of the SYK model and its relation to low-dimensional gravity. A more comprehensive introduction can be found in many sources, including [14, 173, 198].

In its conventional form, the SYK model consists of N Majorana fermions χ_i , which interact via random all-to-all four-body interactions:

$$H = \sum_{i < j < k < l} J_{ijkl} \chi_i \chi_j \chi_k \chi_l, \quad (1.15)$$

where J_{ijkl} are random coefficients drawn from a Gaussian distribution with mean zero and variance $\overline{J_{ijkl}^2} = 6J^2/N^6$. Note that Majorana fermions obey the commutation relation $\{\chi_i, \chi_j\} = \delta_{ij}$, and two Majorana fermions can be constructed from a single ordinary fermion via

$$\chi_{2i} = \frac{1}{\sqrt{2}}(c_i + c_i^\dagger), \quad \chi_{2i+1} = \frac{-i}{\sqrt{2}}(c_i - c_i^\dagger). \quad (1.16)$$

From a microscopic perspective, one can view Eq. 6.2 as a system of ordinary fermions where the single-particle terms (e.g. $c_i^\dagger c_j$) have been eliminated, and the two-particle terms have been completely randomized (including particle-number conserving terms, e.g. $c_i^\dagger c_j^\dagger c_k c_l$, and non-conserving terms, e.g. $c_i^\dagger c_j^\dagger c_k^\dagger c_l$). A more general class of SYK models consists of random q -body interactions, rather than the 4-body interactions above. While $q = 2$ model is a simple free-fermionic system, all versions of the model with $q \geq 4$ exhibit qualitatively similar physics as the standard $q = 4$ model shown in Eq. 6.2 [173].

Before delving into details, let us highlight two ways in which the SYK model is special from a many-body physics standpoint. The first important feature is the presence of random all-to-all interactions². At a technical level, this implies that the dynamics in the large- N limit can be captured by a form of dynamical mean-field theory. As described below, this provides analytic tractability despite being a strongly interacting system. At a more physical level, all-to-all interactions suggest that the model will be a fast scrambler, i.e. scramble in $\sim \log N$ time. Notably, these properties, on their own, are not difficult to satisfy: Other systems with all-to-all interactions, including bosonic and spin systems, can also be described with mean-field theory and exhibit fast scrambling behavior (at least at high temperatures)[22, 134]³.

A second, and much more unique, feature of the model is the absence of either spin glass ordering or quasiparticle excitations at arbitrarily low temperatures [56]. Spin-glass ordering would imply the break down of the (replica-symmetric) mean-field treatment and,

²More specifically, the interactions are random and k -local (meaning contain a finite number of operators). The physics of random, *non-local* systems like GUE Hamiltonians is distinct; for example, such systems can scramble in $O(1)$ time.

³It is important to point out a distinction between systems with *uniform* all-to-all interactions and systems with generic all-to-all interactions (including random interactions). The former are described by large-spin collective degrees of freedom and effectively become classical spin systems in the large- N limit.

most likely, hinder the fast-scrambling behavior [260]. This situation generally occurs for spin or bosonic systems with all-to-all interactions below a certain critical temperature [16]. This explains the necessity of fermionic operators. At the same time, the absence of quasiparticle excitations is crucial for achieving maximal chaos, i.e. $\lambda \approx 2\pi T$. Indeed, systems that feature quasiparticles may exhibit fast-scrambling behavior, but their Lyapunov exponent is parametrically separated from the chaos bound [103, 234]. A sufficient requirement for the absence of quasiparticles is an extensive zero-temperature entropy, which indeed occurs in the SYK model for $q \geq 4$ [56, 173]⁴. As an alternative perspective, one can say that the SYK model at low temperatures is in a critical regime, analogous to a quantum system near a quantum critical point. It is only within this regime that the physics of the SYK model has a clear gravitational interpretation.

Large- N analysis

Let us now describe the formal techniques for solving for the properties of the SYK model in the limit $N \gg 1$ [133, 173]. This approach applies at any temperature and relies on the fact that the SYK model is a so-called large- N system. Schematically, we begin by defining the single-particle Green's function in imaginary time τ :

$$G(t) = \langle \mathcal{T} \chi_i(\tau) \chi_i(0) \rangle_\beta. \quad (1.17)$$

At leading order in $1/N$, we identify a set of Feynman diagrams that contribute to the Green's function (the “iterated watermelon” diagrams). These diagrams can be resummed using a simple recursion relation, yielding a set of self-consistent classical equations, known as the Schwinger Dyson equations⁵:

$$G(\omega) = \frac{1}{-i\omega - \Sigma(\omega)}, \quad \Sigma(\tau) = J^2 [G(\tau)]^3 \quad (1.18)$$

Note that the first equation is expressed in the frequency domain, while the second equation is in the time domain. One can numerically solve these equations at any temperature to obtain the equilibrium Green's function in imaginary time. Analogous equations can also be determined via analytical continuation for the real-time Green's function under equilibrium conditions, as well as for quenched dynamics [75].

In the low-temperature limit, $\beta J \gg 1$, one can simplify the Schwinger Dyson equations by setting $\omega \rightarrow 0$. In this form, we observe that the Schwinger Dyson equations are invariant

⁴By zero-temperature entropy, we mean taking the large- N limit before taking $T \rightarrow 0$. If the limits are taken in the opposite order, then the zero-temperature entropy is *not* extensive; e.g., for a finite-sized system, there is generally a non-degenerate ground state.

⁵These equations can also be determined through a path integral approach [14]. In particular, one writes down the action for the system and integrates over the disorder. This leads to a large- N action (i.e. whose prefactor is $\sim N$), such that, in the large- N limit, it is justified to take the saddle-point solution. This solution exactly corresponds to the Schwinger-Dyson equations.

under any continuous time reparameterizations, $f(\tau)$:

$$G(\tau) \rightarrow [f'(\tau)]^\Delta G(f(\tau)), \quad \Sigma(\tau) \rightarrow [f'(\tau)]^{\Delta(q-1)} \Sigma(f(\tau)) \quad (1.19)$$

with $\Delta = 1/q$. This indicates an emergent *conformal symmetry*. An ansatz that satisfies the simplified Schwinger Dyson equations is [173]

$$G_c(\tau) = \frac{b}{|\tau|^{2\Delta}} \text{sgn}(\tau), \quad (1.20)$$

with $\Delta = 1/q$ and $b = 1/(\sqrt{2}\pi^{1/4})$. This corresponds to the zero-temperature, imaginary-time Green's function. The finite-temperature solution is obtained via the reparameterization, $f(\tau) = \tan \frac{\pi\tau}{\beta}$, which yields:

$$G(\tau) = b \left[\frac{\pi}{\beta \sin \frac{\pi\tau}{\beta}} \right]^{2\Delta}. \quad (1.21)$$

At leading order in $1/N$, we can utilize similar techniques to solve for the out-of-time-order correlators (OTOCs),

$$F(t) \equiv \langle \chi_i(t) \chi_j \chi_i(t) \chi_j \rangle_\beta. \quad (1.22)$$

The analysis consists of identifying the relevant set of diagrams (the ‘‘ladder’’ diagrams) and performing the sum recursively [133, 173]. This results in a classical, eigenvalue equation. One can solve this equation numerically at all temperatures, obtaining the Lyapunov exponent, as well as the prefactor C in $F(\tau) \sim C/N e^{\lambda t}$ which determines the exact scrambling time [104]. At low temperature, one can again utilize the emergent conformal symmetry to perform the calculation analytically. This resulted in the first evidence that the Lyapunov exponent saturated the bound on chaos, $\lambda \approx 2\pi/\beta$, for $\beta J \gg 1$ [133, 173].

We note that additional analytical control is obtained by taking the large- q limit, $q \rightarrow \infty$ [173]⁶. In this limit, the large- N dynamics becomes analytically tractable at all temperatures, avoiding the need for numerical computations. This limit is often useful for building intuition about the larger class of SYK models. In Chapters 2, 3, and 6, we utilize a combination of these two large- N techniques when exploring the dynamics of the SYK model.

Low-energy effective action and its gravitational dual

We observed above that a conformal symmetry emerges in the Schwinger Dyson equations, Eq. 1.18, when we set $i\omega \rightarrow 0$. In particular, this leads to an infinite set of solutions related by time reparameterizations. However, the conformal symmetry is explicitly broken by finite $i\omega$. This implies that the manifold of time reparameterizations acquires a non-zero action. The resulting mode, referred to as the ‘‘soft mode’’, dominates the physics at low

⁶Specifically, we are considering taking $q \rightarrow \infty$ after $N \rightarrow \infty$. Another tractable limit is $N \rightarrow \infty, q \rightarrow \infty$ with N/q^2 fixed [27].

temperatures. Physically, this situation is somewhat analogous to a simple system with a continuous symmetry—say, a Heisenberg magnet—in a symmetry-broken phase, where one applies a small field to explicitly break the symmetry. The original spontaneous symmetry breaking gives rise to a Goldstone mode, while the explicit symmetry-breaking leads to a low-energy action for this mode.

In the SYK model, the low-energy action is known as the Schwarzian action and is given by [173]:

$$S = -\frac{N\alpha_S}{J} \int_0^\beta d\tau \text{Sch}(f(\tau), \tau), \quad \text{Sch}(f(\tau), \tau) \equiv \frac{f'''}{f'} - \frac{3}{2} \left(\frac{f''}{f'} \right)^2 \quad (1.23)$$

where $f(\tau)$ is a time reparameterization (relative to $G_c(\tau)$ in Eq. 1.20) described above and $\alpha_S \approx 0.01$ for $q = 4$. At inverse temperature β , the action is minimized by $f(\tau) = \tan \frac{\tau\pi}{\beta}$, the transformation that takes a circle to a line. This justifies the finite-temperature correlation function we gave in Eq. 1.21. Intuitively, one can think of the action as penalizing transformations that deviate from a circle.

Crucially, the Schwarzian action establishes a direct link with gravitational physics: It is derived from the universal gravitational action that governs near-extremal black holes, i.e. a black hole whose charge is near-maximal relative to its mass⁷. Indeed, the gravitational action provides an effective description near the black hole horizon for near-extremal black holes in any dimension, including the ones in our universe!⁸

Owing to this connection, explicit gravitational calculations can be translated to properties in the SYK model at low temperatures, and vice versa. As we have already discussed, maximal chaos has a natural origin in gravitational physics and thus also occurs in the SYK model in the low temperature regime. In Chapter 2, we discuss more subtle properties about the SYK dynamics, which can be exactly described by gravitational calculations. In Chapter 3, we further show that phenomena related to traversable wormhole physics can be readily seen in the SYK model at low temperatures. In the opposite direction, there have been a number of features that were first seen in the SYK model and later described within the gravitational framework. A seminal example is related to the spectral form factor, which quantifies how close a system is to a random matrix theory [60]. Numerical observations in the SYK model were subsequently explained by detailed, and highly nontrivial, calculations in AdS₂ gravity [215].

A few additional comments are in order. First, we note that, in dimensionless units, the prefactor of the Schwarzian action is $\sim N/(\beta J)$. This implies that the classical, saddle-point approximation, e.g. described by Eq. 1.21, is applicable only in the limit $N \gg \beta J$. Nevertheless, the action itself governs the system across the wider range of parameters; it only requires low temperatures $\beta J \gg 1$ and large sizes $N \gg 1$. In other words, the Schwarzian

⁷Specifically, the gravitational action, known as JT gravity, consists of AdS₂ spacetime with an additional dilaton field.

⁸In higher dimensions, the relevant spatial dimension is the radial dimension; the transverse spatial dimensions are factored out.

action describes *quantum fluctuations* in the low-temperature regime. Such fluctuations are relevant for describing the SYK dynamics at finite sizes (see Chapter 2), as well as at long timescales [60, 215].

Second, we emphasize that the Schwarzian action describes SYK dynamics only at low temperatures, $\beta J \gg 1$. At higher temperatures, the SYK model is governed by a more complicated action. If one attempts to interpret this action as a bulk theory, one finds that it is no longer a local, gravitational theory, but rather a theory with non-local, or “stringy”, features [135]. While exact calculations can no longer be performed with this bulk theory, some properties can be described in a phenomenological way. For example, “stringy” corrections have been shown to reduce the Lyapunov exponent away from the chaos bound, suggesting a bulk explanation for a non-maximal Lyapunov exponent in SYK at high temperatures [230]. In Chapter 3, we discuss similar “stringy” effects in the context of the traversable wormhole protocol.

To summarize, the SYK model in a particular limit— $\beta J \gg 1$ and $N/(\beta J) \gg 1$ —can be accurately described in terms of a simple gravitational dual. Furthermore, we can perturb away from this limit in two ways: by reducing the system size or increasing the temperature. We can then ask how features present in the original limit are modified, from the perspective of both the microscopic theory (the SYK model) and the bulk theory. In this way, we can hope to understand the interpolation between systems with a gravitational dual and more general quantum systems.

1.3 Quantum teleportation and traversable wormholes

We have seen how local quantum information becomes inaccessible under many-body quantum evolution. However, assuming the evolution is unitary, the initial information is never truly lost. Thus, it is natural to ask: How can one recover the initial information? In this section, we discuss recent developments on addressing this question which have revealed surprising connections between quantum teleportation, quantum scrambling, and traversable wormholes.

Conventional quantum teleportation

We begin by reviewing the standard form of quantum teleportation, which allows the transmission of quantum information between two parties without the physical movement of quantum particles [189]. Let us illustrate the protocol with a simple example. Alice contains an unknown quantum state $|\psi\rangle$ encoded in a quantum particle, say the polarization of a photon. She wishes to send this state to her friend, Bob. Of course, the most straightforward method would be to send the photon itself through a physical quantum network (e.g. a fiber optic cable). However, let’s assume that this network is not available.

Remarkably, Alice can still send the state to Bob through a more indirect scheme, which we depict in Fig. 1.1(a). In particular, Alice and Bob first share an entanglement resource in

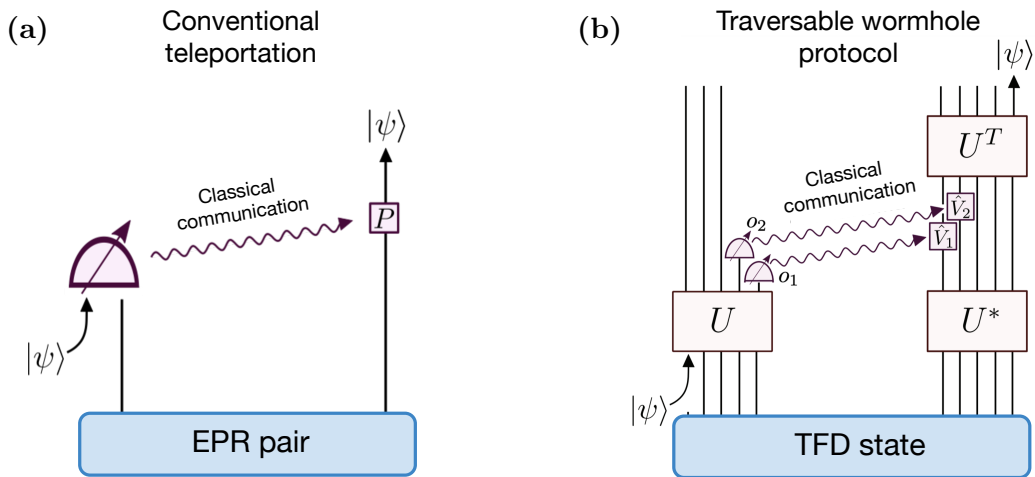


Figure 1.1: Schematic of two protocols for performing quantum teleportation: (a) the conventional protocol, and (b) the so-called traversable wormhole protocol (also referred to as many-body quantum teleportation). Both protocols send an unknown quantum state $|\psi\rangle$ between two parties, utilizing an entangled resource state, local measurement, and classical communication. The main distinction is that, in the traversable wormhole circuit, the unknown state is first “scrambled” under a many-body unitary U prior to measurement. Details on the two protocols and their connection to traversable wormhole physics are discussed in Chapter 3.

the form of a maximally entangled EPR pair, $|\text{EPR}\rangle = 1/\sqrt{2}(|0\rangle_A|0\rangle_B + |1\rangle_A|1\rangle_B)$. Alice performs a measurement involving this resource state and transmits the measurement outcome to Bob in the form of a classical bit. Based on this information, Bob performs a simple operation on his end of the entangled state and recovers the initial state $|\psi\rangle$. Thus, the transfer of an unknown quantum state is enabled by shared entanglement, local measurement, and classical communication.

Hayden-Prekill thought experiment

In a seminal 2007 paper, Hayden and Preskill laid the foundation for a connection between quantum teleportation and the recovery of information from a black hole [111]. In particular, they imagined a quantum state $|\psi\rangle$ falling into a black hole and scrambling under the black hole dynamics. The black hole then emits particles in the form of Hawking radiation, which are collected by an external observer outside of the black hole horizon. They were interested in understanding how much Hawking radiation would be necessary to recover the initial state.

To this end, they modeled the black hole as a generic, random quantum system and

assumed that enough time had passed that the initial quantum state had become fully scrambled. Utilizing quantum information theoretic arguments, they calculated that at least half of the black hole would need to radiate before the initial state could be recovered. However, they also showed a twist: If the external observer has access to an *entangled* copy of the black hole, then only a very small amount of radiation would be needed to recover the state.

This situation is reminiscent of the simple form of quantum communication described above. Under conventional teleportation, Alice is able to utilize an entangled resource to transfer an unknown quantum state. In the Hayden-Preskill setup, the interior of the black hole represents one side of the entangled resource state, and an external observer has access to the other side. According to Hayden and Preskill's calculations, an external observer can leverage this entanglement to recover the initial quantum state. However, unlike the simple form of quantum teleportation, the recovery would *only* work if the unknown state is first scrambled under quantum dynamics. Thus, somewhat paradoxically, while scrambling implies that local information becomes increasingly difficult to access, it also enables that information to be transmitted to a distant observer!

Recovery of scrambled quantum information

While Hayden and Preskill provided a proof of existence for the information recovery, only in the past few years have specific protocols been developed that realize this procedure. The first protocol was proposed by Yoshida and Kitaev and applies to generic quantum evolution [263]. As in the Hayden-Preskill setup, the resource state is a collection of fully entangled EPR pairs, and the initial quantum state $|\psi\rangle$ is scrambled on one side of the EPR state under a many-body unitary. Yoshida and Kitaev's recovery protocol relies on collecting a few particles from the initial side of the EPR state and performing an operation with these particles and the opposite side of the entangled state. Notably, the success of their protocol is directly related to how much $|\psi\rangle$ has been scrambled, as measured by a sum over OTOCs.

At around the same time, a second protocol was discovered in the context of traversable wormholes [90, 176]. A wormhole geometry consists of two connected black holes. In classical general relativity, two observers can jump into opposite sides of the wormhole and meet in the middle, but they are subsequently forbidden from leaving the interior; in other words, the wormhole cannot be traversed. In 2017, a surprising discovery by Gao, Jafferis, and Wall showed that quantum corrections could change this situation and render the wormhole traversable. From the perspective of the boundary quantum mechanical system, one can view the traversable wormhole as a protocol for sending a quantum state from one observer to another. Much like the Hayden-Preskill recovery protocol described above, this so-called traversable wormhole protocol relies on an entangled state and scrambling dynamics. In contrast, however, it was thought to only succeed if the dynamics were generated by a system dual to gravity, such as the SYK model at low temperatures.

In Chapter 3, we show that these two recovery protocols are, in fact, closely related⁹. As depicted in Fig. 1.1(b), both protocols can be viewed as a form of *many-body teleportation*, in which entanglement, scrambling, and classical communication are combined to transfer an unknown quantum state. Nevertheless, there exist two distinct mechanisms for which protocol succeeds, which are most naturally understood from the perspective of operator growth dynamics (see discussion above). The gravitational mechanism relies on a microscopic property known as *size winding*, while the more generic mechanism which applies to general quantum systems relies on having a *peaked-size* operator size distribution. Interestingly, these two mechanisms are smoothly connected to each other; for example, one can interpolate between them in the SYK model as a function of temperature.

Building on this framework, we show that the traversable wormhole protocol provides a powerful experimental tool for probing operator growth dynamics in a quantum simulator and identifying signatures of gravitational dynamics. Indeed, a recent experiment executed on Google’s quantum processor utilized the protocol to study a highly simplified version of the SYK model [121]. In Chapter 4, we comment on this experiment, highlighting the challenges involved in the long-term goal of probing quantum gravity with microscopic quantum systems.

At the same time, the physics of traversable wormholes can also provide inspiration for new forms of quantum algorithms. In Chapter 5, we demonstrate that a modification of the traversable wormhole protocol leads to a universal scheme for quantum sensing, which we dub “butterfly metrology”. In Chapter 6, we propose an adiabatic algorithm based on *eternal* traversable wormholes [170], which allows for the efficient preparation of *thermofield double (TFD) states*—the entanglement resource needed in the traversable wormhole protocol.

⁹More specifically, we focus on the deterministic version of Yoshida and Kitaev’s protocol involving a single step of Grover’s search. See Chapter 3 for details.

Chapter 2

Many-body chaos in the Sachdev-Ye-Kitaev model

Characterizing thermalization in strongly interacting quantum systems is a goal that spans across multiple disciplines ranging from condensed matter and quantum information to quantum gravity. Recent developments toward this goal have revealed striking insights into the relationship between quantum chaos and the delocalization, or scrambling, of quantum information. This unification is partly provided by the notion of out-of-time-order correlators (OTOCs), which take the general form $\langle W(t)V(0)W(t)V(0) \rangle$ for local operators V and W [132, 149, 229]. From an information theoretic perspective, these correlators determine the degree to which local information becomes hidden in nonlocal degrees of freedom, leading to the effective memory loss of initial conditions [116, 229]. From the perspective of chaos, OTOCs measure the sensitivity of one operator towards a small perturbation induced by another operator at an earlier time [172, 231]. In particular, for semiclassical chaotic systems, OTOCs are expected to exhibit a period of exponential growth analogous to the classical butterfly effect [155, 161].

At the intersection between these two perspectives lies the discovery of a new form of quantum chaos in strongly interacting systems, known as many-body chaos. This phenomenon is characterized by OTOCs whose leading order behavior is given by $e^{\lambda t}/N$, where λ is the Lyapunov exponent and N is related to the number of degrees of freedom per site [172, 225]. While such behavior was first anticipated in [225] and confirmed using holographic duality in [229], the first concrete Hamiltonian model to exhibit many-body chaos was introduced by Kitaev following previous work by Sachdev and Ye [133, 135, 174, 219]. Remarkably, at low temperatures, the Lyapunov exponent of this so-called SYK model saturates a universal bound, $\lambda \leq 2\pi T$, where T is the temperature of the system [172]. The saturation of this bound is known to occur in theories of quantum gravity and their holographic duals [231], and indeed a direct correspondence has since been established between the low temperature dynamics of the SYK model and a universal theory of near extremal black holes (i.e. Jackiw-Teitelboim gravity) [80, 123, 135, 175]. More recently, a number of other models that exhibit many-body chaos have been studied; however, their rate of chaos

is parametrically slower than the thermodynamic bound [55, 234]. In parallel, there have also been numerous proposals to directly measure OTOCs in coherently controlled quantum simulators [25, 74, 126, 148, 155, 156, 242, 259, 264, 273], as well as a number of experimental demonstrations in small-scale systems [35, 107, 146, 156].

A major hurdle in benchmarking these experiments/proposals and in identifying novel models that exhibit many-body chaos, is the lack of a reliable numerical toolset. Indeed, in order to observe a period of clear exponential growth, the scrambling time must be well-separated from other effects related to local relaxation that occur at early times [13, 172, 259]

In this Chapter, we take steps to overcome these challenges by employing massively parallelized Krylov subspace methods and developing new extrapolation tools to characterize many-body chaos. Specifically, we compute correlation functions for the SYK model for systems of up to $N = 60$ Majorana fermions and leverage the model's correspondence with quantum gravity to interpret finite-size effects. We present two main results. First, we demonstrate that our numerical results for two-point functions, $G(t) = \langle W(t)W(0) \rangle$, agree quantitatively with analytic predictions in two distinct regimes: (i) at high temperatures, our results match the mean-field solution of the microscopic model, and (ii) at low temperatures, our results are consistent with the full quantum dynamics of near extremal black holes. These latter results represent, to the best of our knowledge, the first direct numeri-

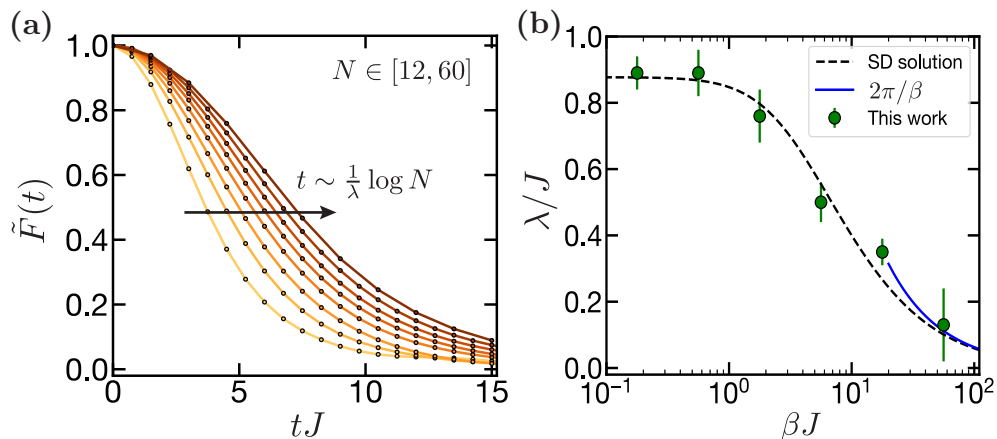


Figure 2.1: Regularized OTOCs in the SYK model, $\tilde{F}(t) \equiv F(t)/F(0)$, as shown for $\beta J = 10$ and system sizes $N \in [12, 60]$. The early-time behavior is characterized by $1 - \tilde{F}(t) \sim e^{\lambda t}/N$ and different system sizes are approximately related by a time translation symmetry, $t \rightarrow t + 1/\lambda \log N$. (b) Applying a finite-size rescaling procedure to the data, we determine λ as a function of temperature (points). Our results exhibit excellent agreement with the theoretical predictions of the Schwinger-Dyson (SD) equations (dashed line), including in the regime where λ approaches the bound on chaos $2\pi/\beta$ (blue).

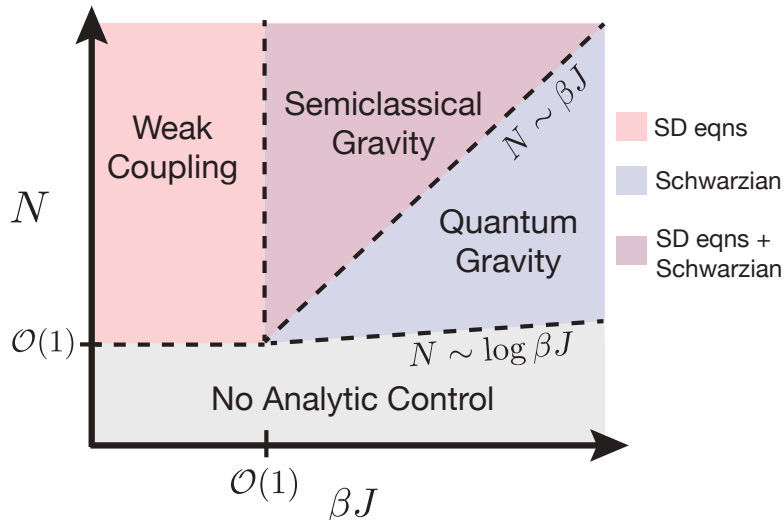


Figure 2.2: Regimes of analytic control for the SYK model as a function of system size, N , and inverse temperature, βJ . In the semiclassical limit (red and purple), the model is well-described by a dynamical mean-field solution (Schwinger-Dyson equations). At low temperatures, finite-size corrections can be calculated using the Schwarzian action (blue), which is dual to AdS_2 gravity. However, at sufficiently small sizes (gray), the dynamics are governed by the discreteness of the energy spectrum and neither effective theory provides a valid description.

cal verification of quantum gravity correlators, and highlight the close connection between finite-size corrections and gravitational fluctuations.

Second, we introduce an extrapolation procedure for determining the Lyapunov exponent that explicitly takes into account higher-order terms in the OTOCs. We verify that this procedure accurately determines λ as a function of temperature, including at low temperatures where $\lambda \approx 2\pi T$ (Fig. 5.1).

2.1 The SYK model and its gravity dual

Consider the SYK Hamiltonian given by [133, 174]:

$$H = \sum_{i < j < k < l} J_{ijkl} \chi_i \chi_j \chi_k \chi_l. \tag{2.1}$$

Here χ_i ($i = 1, \dots, N$) are Majorana fermions which obey the anti-commutation relation, $\{\chi_i, \chi_j\} = \delta_{ij}$, and J_{ijkl} are random (real) coefficients sampled from a Gaussian distribution with zero mean and variance $\overline{J_{ijkl}^2} = 6J^2/N^3$.

In order to probe the system’s non-equilibrium dynamics, we will compute two different types of correlators. In-time correlators reveal how excitations in the system relax towards equilibrium. In particular, we will consider the average imaginary-time Green’s function, $G(\tau)$, and its real-time cousin, $G_R(t)$, given by

$$G(\tau) \equiv \overline{\langle \chi_i(\tau) \chi_i(0) \rangle_\beta} \quad (2.2)$$

$$G_R(t) \equiv 2\text{Re} \left[\overline{\langle \chi_i(t) \chi_i(0) \rangle_\beta} \right] \quad (2.3)$$

where $\tau(t) > 0$ is imaginary (real) time, $\langle \dots \rangle_\beta = \frac{1}{Z} \text{Tr} [\dots e^{-\beta H}]$ is a thermal average at inverse temperature $\beta = 1/T$, and the overline denotes the (quenched) average over disorder realizations. On the other hand, to probe chaos and the scrambling of quantum information, we will consider out-of-time-order correlators. We will primarily focus on the regularized OTOC,

$$F^{(r)}(t) \equiv \overline{\langle \chi_i(t) \rho^{\frac{1}{4}} \chi_j(0) \rho^{\frac{1}{4}} \chi_i(t) \rho^{\frac{1}{4}} \chi_j(0) \rho^{\frac{1}{4}} \rangle} \quad (2.4)$$

where $i \neq j$, and $\rho = e^{-\beta H}$, the imaginary-time evolution associated with the thermal ensemble, is distributed evenly among the four operators. In the supplemental materials, we provide a detailed discussion regarding the key differences between this correlator and the unregularized version ¹ [1].

In the large N , semiclassical limit, both in-time and out-of-time correlators can be exactly computed via a diagrammatic approach [133, 174]. The average Green’s functions are determined by the self-consistent Schwinger-Dyson equations. For the OTOCs, the leading order term in $1/N$ is computed by summing a series of ladder diagrams.

Beyond the semiclassical limit, the dynamics at low temperature (i.e. $\beta J \gg 1$) are captured by an effective theory known as the “Schwarzian theory” (Fig. 2.2) [14, 135, 174, 258]. The same theory also describes Jackiw-Teitelboim gravity, a simple quantum gravity description of two-dimensional Anti-de-Sitter space.

Crucially, correlators in the Schwarzian theory are exactly computable [144, 258], which will enable us to perform quantitative, finite-size-scaling comparisons for two-point functions $G(\tau)$ and $G_R(t)$ *outside* of the semiclassical limit. However, for the four-point function, the expressions are more complicated, and we will compare numerics to the ansatz: $F(t) = C_0 + C_1 \left(\frac{e^{\lambda t}}{N}\right) + C_2 \left(\frac{e^{\lambda t}}{N}\right)^2 + \dots$, which is valid for large N and $t \lesssim 1/\lambda \log N$ [144, 175, 258]. An analogous series expansion is expected to characterize OTOCs for the SYK model at high temperatures (and any other model described by ladder diagrams) ² [104, 234].

¹Of course, the unregularized OTOC, $F^{(u)}(t) = \langle W(t)V(0)W(t)V(0)\rho \rangle$, is often more relevant for experiments and we provide a detailed discussion of the differences in the supplemental materials [1]. In particular, we discuss the importance of the magnitude C_1 of the leading exponentially growing term in the OTOC, $(C_1/N)e^{\lambda t}$ [104].

²We note that the series expansion of $F(t)$ in terms of $e^{\lambda t}/N$ relies on the fact that the SYK model contains a single positive Lyapunov exponent [133, 135, 174]. For a chaotic system with multiple Lyapunov exponents, $F(t)$ would have additional terms corresponding to each exponent, though at late times the terms with the largest Lyapunov exponent would remain dominant.

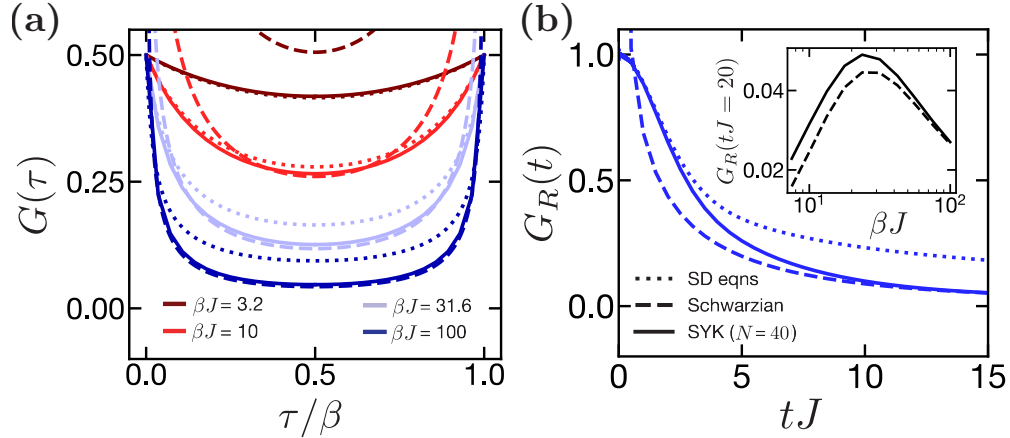


Figure 2.3: Two-point correlation functions in real and imaginary time. (a) Comparison of imaginary-time evolution between our numerics with 40 Majoranas (solid), the large N solution (dotted), and the Schwarzian action (dashed). At high temperatures, we observe quantitative agreement between our numerical results and the large N solution, while at low temperatures our numerics are well-described by the Schwarzian action. (b) Analogous comparison for real-time evolution with $\beta J = 56$. Our numerics show excellent agreement with the Schwarzian action for $tJ \gtrsim 10$. The disagreement at earlier times is attributed to the difference in high-energy modes, which are cut off at the energy scale J in the SYK model and are unbounded in the effective action. (inset) A salient feature in our real-time numerics is a non-monotonic trend with respect to temperature, as shown for $tJ = 20$. This behavior is captured by the Schwarzian action (dashed) and can be understood as a consequence of the square root edge of the energy spectrum.

2.2 Non-equilibrium dynamics in the SYK model

Our central numerical tool is a massively-parallelized implementation of a class of iterative methods known as Krylov subspace methods [1, 2, 216]. These methods approximate the time evolution of an initial state, $|\psi(t)\rangle = e^{-iHt} |\psi\rangle$, within a subspace formed by successive applications of the Hamiltonian. Since this requires an initial pure state, we approximate thermal averages by taking the expectation value with respect to a Haar-random state $|\tilde{\psi}\rangle$ [101, 165, 235]:

$$\text{Tr} \left[\hat{O} e^{-\beta H} \right] \approx \left\langle \tilde{\psi} \left| e^{-\frac{\beta}{2} H} \hat{O} e^{-\frac{\beta}{2} H} \right| \tilde{\psi} \right\rangle. \quad (2.5)$$

Owing to quantum typicality, the error in this approximation scales inversely with the number of states in the thermal ensemble and, thus, decreases exponentially with N for arbitrary systems and temperatures (above the spectral gap) [235]. In practice, we further reduce the error by averaging over initial states [1].

To begin probing the thermalizing dynamics of the SYK model, we compute the aver-

age Green's functions for both real- and imaginary-time evolution in the temperature range, $0 < \beta J \leq 100$. At high temperatures, the imaginary-time Green's function, $G(\tau)$, shows excellent agreement with the semiclassical solution given by the Schwinger-Dyson equations [Fig. 2.3(a)]. At lower temperatures, the difference between our numerics and the semiclassical solutions widens. To understand the origin of these corrections, we plot the full solution predicted by the Schwarzian action. This exhibits close quantitative agreement with our data at temperatures corresponding to $\beta J \gtrsim 50$. Crucially, this confirms that the Schwarzian action, or its corresponding gravity dual, accurately captures finite-size corrections away from the semiclassical regime.

A few remarks are in order. First, we note that the agreement with the Schwarzian action is only valid for system sizes larger than $N \approx 30$ [1]. For smaller sizes, we observe additional finite-size corrections that are attributed to the discreteness of the energy spectrum. Such non-Schwarzian corrections are expected to dominate when the temperature approaches the energy of the level spacings (i.e. $N \sim \log \beta J$ in Fig. 2.2) [97, 106]. Second, the agreement between the Schwarzian and our numerics does not hold at timescales shorter than the inverse of the microscopic coupling strength (i.e. $\tau J \lesssim 1$); specifically, the Schwarzian dynamics diverge as $\tau J \rightarrow 0$ while our numerics approach a finite value. This difference arises from the fact that the Schwarzian action is the effective theory only at low energies (compared to J); for higher energies, the SYK dynamics are governed by the microscopic nature of the model.

Much like the imaginary-time case, we find that the retarded Green's function, $G_R(t)$, agrees with the semiclassical solutions at high temperatures and with the full dynamics of the Schwarzian action at low temperature [Fig. 2.3(b)]. We note, however, that the early-time discrepancy with the Schwarzian action is extended to later times (i.e. $\beta J \sim 10$). This can be attributed to the longer timescale required for the phase cancellation of the high-energy modes in real time, as opposed to the direct suppression that occurs in imaginary time.

Working with real-time dynamics also allows us to probe a rather non-trivial prediction of the Schwarzian action. In particular, one expects the late-time dynamics to be governed by the functional form of the spectral density at low energies, $\rho(E) \sim E^{\frac{1}{2}}$ [14, 60, 95]. This square-root singularity leads to a power-law decay of the Green's function, with a power that depends on both the temperature and the timescale. Intriguingly, it predicts a *non-monotonic* temperature dependence for the decay of the Green's function, in stark contrast to the monotonic dependence predicted by the semiclassical solution. This non-trivial temperature dependence, consistent with only the full Schwarzian solution, is indeed borne out by the numerics [inset, Fig. 2.3(b)].

2.3 Lyapunov exponent of the SYK model

To probe many-body chaos in the SYK model, we now compute regularized OTOCs [Eqn. A.9] for temperatures in the range $0 < \beta J \leq 56$ and for system sizes up to $N = 60$. In the large N limit, one expects a well-defined period of exponential growth, starting from

the timescale at which the two-point functions decay and persisting until the scrambling time [172]. However, for conventional exact diagonalization studies, there is little separation between these timescales, owing to the limited system sizes that are numerically accessible; indeed, prior studies actually observed an increase in the extracted Lyapunov exponent as a function of decreasing temperature — the opposite behavior of what is expected [1, 86]. By scaling to larger system sizes using Krylov subspace methods, we observe a direct turnover in this trend. Moreover, we introduce a novel extrapolation method, which provides a robust way of extracting the Lyapunov exponent.

The intuition behind our method is as follows: For a large class of many-body chaotic systems, the full form of the OTOC in the semiclassical limit is given by a series in $e^{\lambda t}/N$. Crucially, this series exhibits a rescaling symmetry, wherein $N \rightarrow rN$ amounts to shifting the full curve by $t \rightarrow t + 1/\lambda \log r$. This symmetry can be shown explicitly for the Schwarzian action, which governs low-temperature dynamics of the SYK model, and is also expected to hold at high temperatures [104, 234].

This suggests that we can determine λ at a given temperature by attempting to collapse our data [Fig. 5.1(a)] through finite-size rescaling of the form $t \rightarrow t + 1/\lambda \log N$. More specifically, we first interpolate our data to find the time, t_* , at which each curve crosses a fixed value, i.e. $F(t_*)/F(0) = 1 - F_0$ [1]. Next, we estimate $\lambda_{\text{fit}}(N)$ as $1/\lambda_{\text{fit}} = dt_*/d(\log N)$, where N corresponds to the system size about which we take the numerical derivative. Finally, we fit our results to a $1/N$ series, $\lambda_{\text{fit}}(N) = \lambda_0 + \lambda_1/N + \lambda_2/N^2 + \dots$; the leading order term λ_0 corresponds to the extrapolated value for λ as $N \rightarrow \infty$.

In Fig. 5.1(b), we present our results for λ_0 as a function of temperature. We observe excellent agreement with analytic predictions for all temperatures in the range $0 < \beta J \leq 56$. Crucially, our protocol works at *low-temperatures* where the $2\pi/\beta$ scaling (saturating the bound on chaos) becomes apparent.

An important question to ask is over what range of temperatures we expect our procedure to remain valid. There are three relevant considerations. First, the temperature must be high compared to the energy associated with the level spacing; we account for this requirement by considering only system sizes where at least 20 eigenstates, on average, lie within $\Delta E = 1/\beta$ of the ground state. Second, the system must be sufficiently close to the semiclassical limit for the rescaling symmetry to hold. It is known from the Schwarzian action that this condition corresponds to $\beta J \lesssim N$. Asymptotically this is a much stronger requirement than the first condition; however, for the system sizes relevant for our study ($N \lesssim 60$) both requirements imply a low temperature limit of $\beta J \approx 60$.

Third, there must sufficient separation between the scrambling time and the short-time dissipative dynamics. In the case of the regularized correlator, this condition is given by $\beta J \lesssim N$, leading to the same temperature range as the semiclassical requirement. However, in the case of unregularized correlators, the corresponding condition is $(\beta J)^3 \lesssim N$; this implies that the unregularized correlator is subject to stronger finite-size effects, which we corroborate through our numerics [1].

2.4 Discussion and outlook

By employing massively parallelized Krylov subspace methods and developing novel extrapolation tools, we have demonstrated that one can utilize numerics to accurately capture the thermalizing and chaotic dynamics of the SYK model. Our results for two-point Green's functions represent a direct verification of the dynamics of quantum black holes in a highly fluctuating regime. Moreover, our finite-size rescaling procedure for extracting Lyapunov exponents leads to the first numerical evidence that the SYK model saturates the theoretical bound on chaos, $\lambda \approx 2\pi T$.

We anticipate that the numerical tools demonstrated here will open the door to a number of intriguing future directions. First, our numerical tools can be applied to variations of the SYK model (i.e. large q limit) for which the effective action (i.e. Liouville action) is known for all temperatures [28, 60, 81]. This will enable quantitative studies of finite-size corrections in the high-temperature regime, where the Schwarzian action is not valid. Second, our procedure for characterizing Lyapunov exponents can diagnose many-body chaos in other models beyond the SYK model; this is of particular relevance for experimental platforms which have constraints on the types of interactions and disorder that can be realized [25, 35, 53, 65, 146]. Finally, we envision future numerical simulations to test more complex gravitational phenomena, including traversable wormholes [91, 177], and the possible emergence of SYK dynamics in transport experiments of quantum materials [9, 48, 140].

Chapter 3

Many-body quantum teleportation via operator spreading in the traversable wormhole protocol

Quantum teleportation leverages entanglement to transmit quantum information between distant locations [21, 23, 190, 206, 207]. Typically, one thinks about teleportation in the context of a few, well-controlled degrees of freedom. For example, two distant observers might share a pair of maximally entangled qubits (i.e. an Einstein-Podolski-Rosen (EPR) pair [189]), enabling a measurement by one observer to teleport an unknown quantum state to the other.

Recently, a confluence of seminal results has unveiled several novel instances of teleportation in strongly-interacting, *many-body* systems [18, 35, 44, 88, 90, 147, 170, 176, 188, 263, 265]. Similar to conventional quantum teleportation, these protocols utilize shared entanglement as well as measurement and classical communication. However, they differ from conventional quantum teleportation in a few key aspects. Most notably, prior to teleportation, the initial quantum state is *scrambled* by the application of a many-body unitary. At first glance, this coexistence of scrambling—broadly speaking, the increasing complexity of initially simple quantum information under many-body time dynamics [116, 171, 209, 226, 228]—and teleportation might seem counterintuitive. Indeed, one often thinks of teleportation as a directed quantum channel moving information between two specific locations; in contrast, scrambling disperses quantum information across all of the degrees of freedom in a system. The most natural way to reconcile these two perspectives is through the language of quantum error correction [111]: by encoding, via scrambling, one observer’s local information into non-local correlations across a many-body system, one can in fact teleport this information with access only to any few of the system’s qubits.

The most notable example of many-body teleportation is the so-called traversable wormhole (TW) protocol, discovered in the context of quantum gravity [18, 44, 88, 90, 176, 188]. From the bulk gravitational perspective, this protocol consists of a particle traveling from one side of a wormhole geometry to the other; the wormhole is rendered traversable by the

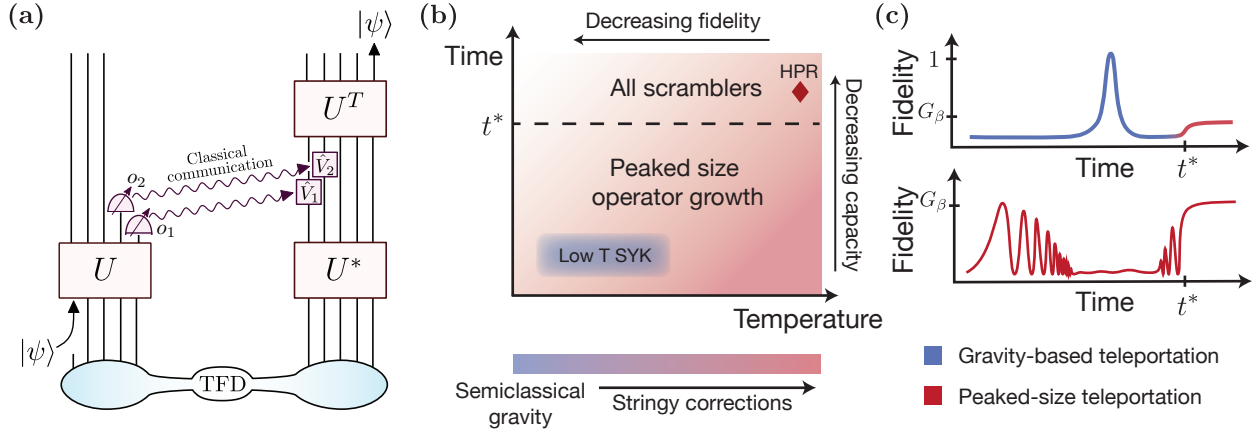


Figure 3.1: **(a)** Teleportation protocol, proceeding from bottom to top. To teleport, a subset of the left qubits are measured in the \hat{O}_i basis, and operations $\hat{V}_i = e^{ig o_i \hat{O}_i / K}$ conditioned on the measurement results o_i are performed on the right (purple). **(b)** The protocol hosts two mechanisms of teleportation: peaked-size (red) and gravitational (blue). The channel capacity of peaked-size teleportation decreases with increasing time (dark to light red), while its fidelity decreases with decreasing temperature (dark to light red, again). At high temperature and late times, it is equivalent to teleportation in the HPR protocol (red diamond). Gravitational teleportation occurs at low temperatures in systems dual to semiclassical gravity (e.g. the SYK model), and exhibits the same channel capacity but *higher* fidelity compared to peaked-size teleportation. Increasing the strength of stringy corrections to the gravity theory interpolates between gravitational and peaked-size teleportation. **(c)** The two mechanisms display distinct time profiles for the teleportation fidelity at fixed coupling strength, g . In systems dual to gravity (top), the fidelity features a single $\mathcal{O}(1)$ peak near the scrambling time (gravitational, blue), and a late time revival (peaked-size, red) to a fidelity suppressed by the two-point function G_β [176]. In generic thermalizing systems (bottom), the fidelity oscillates between 0 and G_β with phase proportional to the operator size, may subsequently decay if sizes become not peaked, and revives at late times.

application of a coupling between the two sides. In the boundary theory, the wormhole geometry corresponds to a highly entangled thermofield double (TFD) state shared between two copies of a many-body system, and the coupling is implemented via measurement and feed-forward operations [Fig. 6.1(a)]. Crucially, for this bulk-boundary correspondence to hold, the Hamiltonian describing the boundary system must exhibit “coherent”, gravitational scrambling dynamics—this is realized, most notably, in the Sachdev-Ye-Kitaev (SYK) model at low temperatures [133, 173].

Interestingly, recent work has uncovered a number of instances of many-body teleportation *without* gravitational dynamics. For example, teleportation in the TW protocol was recently demonstrated analytically in the SYK model at *high* temperatures [88], and numerically in chaotic spin chains at late times [44, 188]; in both cases, the microscopic mechanism for teleportation remains an outstanding puzzle. In addition to the TW protocol, an alternate many-body teleportation protocol was introduced in the context of the Hayden-Preskill variant of the black hole information paradox [111, 263]. This so-called Hayden-Preskill recovery (HPR) protocol allows for many-body teleportation via *generic* scrambling dynamics. Although the two protocols bear some structural similarity, the HPR protocol is exponentially less efficient for teleporting multiple qubits. To this end, understanding the precise relationship between these protocols remains an essential open question.

In this Chapter, we present a unified framework for many-body teleportation from the perspective of the growth of operators under scrambling time-evolution. Most significantly, this framework leads to the identification of a new teleportation mechanism—dubbed *peaked-size teleportation*—which succeeds for a wide variety of physical systems and encapsulates all known examples of many-body teleportation outside of the gravitational regime. We emphasize that peaked-size teleportation represents a *distinct* teleportation mechanism compared to “gravitational” teleportation. Although the same TW protocol can host either mechanism, the features of peaked-size teleportation differ markedly from those of gravitational teleportation [Fig. 6.1(c), Table I]. Crucially, this distinction implies that the TW protocol can act as a litmus test for identifying intrinsically gravitational dynamics. More broadly, our results pave the way towards utilizing the TW protocol as a powerful experimental tool for characterizing the growth of operators in strongly interacting systems.

3.1 Summary of results

We now provide a technical overview of our main results and the organization of our manuscript. This summary is intended to introduce the overarching concepts of our work, such that the remaining sections are self-contained and can be read according to individual preference. A more detailed, section-by-section guide to the reader is included at the end of this summary.

In **Section 3.2**, we begin with a general description of the TW protocol [Fig. 1(a)]. In this protocol, locally encoded quantum information is inserted into one side of an entangled thermofield double (TFD) state and teleported to the other side through a combination of

(i) unitary evolution of each side individually, and (ii) a simple two-sided coupling that acts on a large subsystem of each side. The coupling is quite flexible in form, and corresponds to unitary evolution, e^{igV} , under a two-sided interaction

$$V = \frac{1}{K} \sum_{i=1}^K O_{i,l} O_{i,r}^*, \quad (3.1)$$

where $\{O_i\}$ are *any* set of K local, non-identity operators applied to the left (l) and right (r) side of the system. This coupling can be performed as either a quantum gate, or through local measurements of O_i on the left side, followed by classical communication and feed-forward operations on the right side [Fig. 1(a)].

In **Section 3.3**, we discuss the general requirements for successful teleportation in the TW circuit. In particular, we relate the teleportation fidelity to the following correlation functions of the two-sided system [176]:

$$C_Q(t) \equiv \langle \text{TFD} | Q_r(-t) e^{igV} Q_l(t) | \text{TFD} \rangle \quad (3.2)$$

where $Q(\pm t)$ is a time-evolved operator initially acting on the qubit(s) to be teleported. Our analysis leads to two conditions on these correlators that, when combined, are necessary and sufficient for teleportation to succeed with unit fidelity:

1. The magnitudes of the correlators must be maximal for every Q .
2. The phases of the correlators must be the same for every Q .

Here, Q runs over a complete basis of operators on the qubits to be teleported. We show that Condition 1 is naturally satisfied, even without the coupling V , if the TFD state is at infinite temperature, in which case it reduces to an extensive set of maximally entangled EPR pairs. On the other hand, Condition 2 requires that the coupling acts non-trivially on the operators Q .

In **Section 3.4**, we describe the relation between the coupling, V , and the growth of time-evolved operators, $Q(t)$. For the purposes of teleportation, this growth is characterized by the *size distribution* of the operators [202, 203, 208], which provides a finer-grained measure of quantum information scrambling compared to more conventional quantities such as out-of-time-ordered correlators (OTOCs) [150, 171, 228]. Specifically, writing $Q(t)$ as a sum over Pauli strings, $Q(t) = \sum_R c_R(t) R$, we define the size distribution as:

$$P(\mathcal{S}) = \sum_{\mathcal{S}[R]=\mathcal{S}} |c_R(t)|^2, \quad (3.3)$$

where the sum is over Pauli strings, R , of size, \mathcal{S} (equal to the string's number of non-identity components). By probing correlations between the two sides of the doubled Hilbert space, the coupling V directly measures the operator size [202].

In **Section 3.5**, we introduce the *peaked-size* mechanism for many-body teleportation. This mechanism is possible whenever the size distributions of time-evolved operators, $Q(t)$, are tightly peaked about their average size. In this scenario, the exponentiated coupling, e^{igV} , applies approximately the same phase, proportional to the size, to each coefficient, c_R , and therefore to the entire operator, $Q(t)$. We show that these applied phases are sufficient to align the correlators' phases for all operators Q , thereby achieving Condition 2. We also demonstrate that the magnitudes of the correlators are unchanged by the coupling when size distributions are tightly peaked. This implies that peaked-size teleportation achieves perfect fidelity at infinite temperature, where Condition 1 is automatically satisfied; at finite temperature, peaked-size teleportation can still occur, but with a reduced fidelity (Table I).

In **Sections 3.6-3.7**, we analyze examples of peaked-size teleportation across a wide variety of interacting, many-body dynamics. We demonstrate that the capabilities of peaked-size teleportation—most notably, the fidelity and the number of qubits that can be sent (i.e. the channel capacity)—depend on the temperature, coupling strength, evolution time, and the specific scrambling dynamics of the model under study (Table I).

More specifically, in **Section 3.6**, we provide general arguments that all scrambling systems exhibit peaked-size teleportation at *late times*, after the system's scrambling time ($t \gtrsim t_s$). In this regime, operators have become fully delocalized across the system, so that their size distributions are peaked about a typical, extensive value. We also show that late time peaked-size teleportation is limited to transmitting only a single qubit.

In **Section 3.7**, we show that many scrambling quantum systems also feature peaked-size teleportation at *intermediate times*, i.e. after the local thermalization time but before the scrambling time ($t_{th} \lesssim t \lesssim t_s$). We begin with ergodic short-range interacting systems in $\geq 1D$, which we show naturally possess peaked-size distributions due to thermalization within the bulk of a time-evolved operator's light cone. In contrast, the size distributions of operators in all-to-all coupled (0D) systems are not intrinsically peaked; nevertheless, peaked sizes can be engineered by non-locally encoding the quantum information before insertion into the teleportation circuit. Interestingly, in both of these classes of dynamics, we find that multiple ($\sim \mathcal{O}(K)$) qubits can be teleported simultaneously via the peaked-size mechanism, in contrast with the unit channel capacity of late time teleportation. We substantiate these claims through extensive numerical and analytic studies on a variety of physical models: random unitary circuits (RUCs) in dimensions $d = 0, 1$, and 2 [187], the SYK model, and (in Section 3.9) experimentally relevant spin chain Hamiltonians [29].

In **Section 3.8**, we discuss the interplay between peaked-size and gravitational teleportation. Notably, we expect gravitational teleportation to occur only at low temperatures, where certain quantum mechanical models (e.g. the SYK model) are known to possess a dual description in terms of conformal matter coupled to gravitational dynamics. From the perspective of operator growth, the unique feature of gravitational teleportation is the presence of non-trivial phase *winding* in a variant of the size distribution [44]. Crucially, this effect enables gravitational teleportation to satisfy Condition 1, and thereby achieve high teleportation fidelity at low temperatures, in sharp contrast with peaked-size teleportation (Table I).

Model	Teleportation mechanism	Protocol parameters	Maximum per qubit fidelity	Channel capacity
All scrambling systems at late times (Refs. [176, 263], Section 3.6)	peaked-size	$g = \pi \bmod 2\pi$	$\sim G_\beta$	1 qubit
≥ 1 D RUCs & chaotic spin systems (Sections 3.5,3.7,3.9)	peaked-size	$\eta_d g \mathcal{S}(t)/N = \pi \bmod 2\pi$	$\sim G_\beta$	$\sim K$ qubits
0D RUCs, with encoding (Section 3.7)	peaked-size	$\eta_d g \mathcal{S}(t)/N = \pi \bmod 2\pi$	~ 1	$\sim K$ qubits
High- T SYK, with encoding (Ref. [88], Sections 3.7)	peaked-size	$\eta_d g \mathcal{S}(t)/N = \pi \bmod 2\pi$	~ 1	$\sim K$ qubits
Low- T SYK / AdS ₂ gravity (Refs. [44, 88, 90, 176], Fig. 6.1)	gravitational	$g e^t/N \sim 1$ (SYK) $g G_N e^t \sim 1$ (AdS ₂)	~ 1	$\sim K$ qubits
AdS ₂ gravity with strong stringy corrections, with encoding (Section 3.8)	peaked-size	$g \mathcal{S}(t)/N \sim \pi \bmod 2\pi$	$\sim G_\beta$	—

Table 3.1: Summary of our expectations for teleportation in a variety of physical models. For each model, we specify the associated teleportation mechanism, the optimal value of the coupling strength g , the optimal teleportation fidelity, and the channel capacity. Here G_β is the imaginary time two-point function (Section 3.5), $\mathcal{S}(t)$ is the size of a time-evolved operator, K is the number of measured qubits [Fig. 6.1(a)], $\eta_d = 1/(1 - 1/d^2)$ is an order one constant determined by the local qudit dimension d [Sec. 3.4], and G_N is Newton’s constant. We refer to the Summary of Results and the cited sections for further details.

Intriguingly, while it may seem that there is a sharp distinction between peaked-size and gravitational teleportation, we find that this is not always this case. In particular, we show that varying the temperature of the SYK model provides a continuous interpolation between gravitational teleportation at low temperature and peaked-size teleportation at high temperature. In the dual picture, perturbing away from the low temperature limit corresponds to adding *stringy* corrections to the gravity theory [103, 173, 230]. Following this intuition, we show that teleportation in a gravity theory with strong stringy corrections [176] bears a remarkable qualitative similarity to peaked-size teleportation, thus providing a first step towards a bulk understanding of this phenomenon.

Finally, in **Section 3.9**, we discuss experimental applications of the TW protocol for probing many-body dynamics. In particular, we demonstrate that the protocol can function as a diagnostic tool for scrambling dynamics in near-term quantum simulators, enabling one to starkly distinguish between generic thermalizing systems and gravitational dynamics. To this end, we provide detailed blueprints for realizing the protocol in two complementary experimental platforms—Rydberg atom arrays [29, 102, 143, 167, 178, 252] and trapped ions [17, 32, 47, 87, 184]. Specifically, the observation of a high teleportation fidelity at low

temperatures would be a tantalizing experimental indicator of gravitational scrambling dynamics. In addition, gravitational dynamics exhibit unique qualitative features as a function of both evolution time and protocol parameters [Fig. 6.1(c), Table 3.1]. More broadly, our analysis suggests that the TW protocol can provide insights into many-body dynamics outside the gravitational regime. In particular, we demonstrate that the fidelity of peaked-size teleportation probes higher moments of operator size distributions [203].

Guide to the reader—Considering the wide scope of results presented in this work, we encourage readers to skip to sections that align with their specific interests and refer to the above summary for context. To this end, we highlight below the nature of each section and provide recommendations for readers of different backgrounds. Sections 3.2-3.4 introduce the formal tools and derivations necessary for rigorously understanding our results. These sections will be of interest to readers with a background in quantum information who wish to understand the precise connection between teleportation and operator sizes. Sections 3.5-3.7 introduce peaked-size teleportation and analyze its realization in several example systems. Since many these systems are experimentally accessible, these sections will be most relevant to members of the quantum simulation and many-body physics communities. Section 3.8 focuses on the interplay of peaked-size teleportation and gravitational physics, both in the SYK model and from a bulk gravitational perspective. For brevity, background material on gravitational physics is relegated to references, making this section best suited for experts at the intersection of quantum information and quantum gravity. Finally, Section 3.9 contains a summary of the experimental signatures of the TW protocol, detailed blueprints for Rydberg atom and trapped ion implementations, and a discussion of the protocol’s behavior under experimental error. This section will be of interest to AMO experimentalists and all readers interested in near-term realizations of many-body quantum teleportation [200].

Relation to previous works

To further elaborate on the broad context of our results, a brief summary of the relevant prior studies and their relation to our work is provided as follows.

Gravitational teleportation in the TW protocol—Traversable wormhole teleportation was originally introduced in Refs. [90, 176] in the context of gravitational physics, where it was realized that a coupling of the form V enables a traversable channel between the boundaries of a two-sided black hole. The explicit quantum mechanical circuit implementing this teleportation [Fig. 6.1(a)] was later introduced in Refs. [44, 88], alongside exact calculations for the teleportation fidelity in the large- q SYK model [88]. While the emphasis of our work is not on the bulk interpretation of gravitational teleportation—indeed, the peaked-size teleportation mechanism is intended to *contrast* with the gravitational mechanism—it will be helpful to recall the main results from the gravitational perspective.

We focus on the specific case of two-dimensional anti-de Sitter space, which is the bulk dual of the SYK model at low temperatures [134, 176]. In the simplest case (ignoring gravitational backreaction), the two-sided correlator, Eq. 3.2, can be explicitly calculated

and is given by [176]:

$$C_Q(t) = \left(\frac{1}{2 - g \frac{\Delta_O}{2^{\Delta_O+1}} G_N e^{2\pi t/\beta}} \right)^{2\Delta_Q}. \quad (3.4)$$

Here, G_N is Newton's constant, $\beta = 1/T$ is the inverse temperature of the black hole, Δ_O is the conformal dimension of the coupling operators O_i [Eq. (3.1)], and Δ_Q is the conformal dimension of the operator Q . In the context of the SYK model, G_N is inversely proportional to the number of Majorana fermions, N , and the black hole temperature is equal to the temperature of the TFD state [88, 176].

For our purposes, the most notable feature of the correlator is that it exhibits a sharp peak at time $t \approx G_N \log(g)$ [Fig. 6.1(c)], corresponding to the moment a particle inserted on one side of the black hole emerges on the other side. While in the above formula [Eq. (3.4)], the correlator diverges at this time, in the large- q SYK model, this divergence is regularized and the correlator peaks at its maximal value of unity [88]. Thus, at time $t \approx G_N \log(g)$, the correlator satisfies Condition 1 for successful teleportation; in Ref. [88], it was shown that Condition 2 is also satisfied for certain conformal dimensions of the operators Q . In combination, this leads to unit teleportation fidelity.

Another notable feature of gravitational teleportation is the ability to teleport multiple qubits simultaneously, as discussed in Ref. [176]. In the gravitational picture, multi-qubit teleportation has an intuitive explanation: particles corresponding to different qubits pass through the black hole in parallel, without interacting with one another. However, for sufficiently many qubits, the effects of gravitational backreaction become important, leading to a predicted channel capacity of $\mathcal{O}(K)$.

HPR teleportation—An independent, but closely related, set of protocols for many-body teleportation was introduced in Ref. [263] for the recovery of information in the Hayden-Preskill thought experiment [111]. Unlike previous works on traversable wormholes, in Ref. [263] teleportation succeeds for any fully scrambling unitary dynamics (i.e. at late times, $t \gtrsim t_s$), with no reliance on gravitational physics. However, the channel capacity of HPR teleportation is fundamentally limited: multi-qubit teleportation requires a protocol whose circuit depth grows exponentially in the number of qubits to be teleported [263].

In Appendix B.2, we show that a deterministic variant of the HPR protocol (for single-qubit teleportation) is in fact *equal* to the TW protocol in Fig. 6.1(a), restricted to infinite temperature and with a particular choice of the coupling operators, O_i . Furthermore, in Section 3.6 we show that teleportation at *late times* via the peaked-size mechanism is equivalent to this variant of HPR teleportation. However, peaked-size teleportation is more powerful than HPR teleportation in the sense that: (i) it succeeds for a much larger class of couplings, V , (ii) it can succeed at intermediate times, and (iii) at such times, it is capable of sending multiple qubits with no change in the protocol's complexity, an exponential improvement over the HPR protocol.

Previous many-body teleportation experiments—Many-body quantum teleportation has recently been demonstrated in both trapped ion [147] and superconducting qutrit [35] experiments. Both Refs. [35, 147] implement a probabilistic variant of the HPR protocol, which

differs slightly from the TW protocol, while Ref. [147] also implements the deterministic variant discussed above. In all cases, the scrambling dynamics, U , are generated by digital quantum gates acting on a small number of qubits. Teleportation is performed for a single qubit and a fully scrambling unitary, placing the experiments in the same physical regime as late-time, peaked-size teleportation.

Our work demonstrates that experiments in the *TW protocol* at *intermediate times* can access new regimes of many-body quantum teleportation, with the potential to provide more information about the scrambling dynamics under study. Most notably, such experiments can distinguish between teleportation in generic many-body systems (via the peaked-size mechanism) versus systems with a gravity dual (via the gravitational mechanism), which is not possible in the HPR protocol.

SYK teleportation in the TW protocol—In Ref. [88], the two-sided correlator of the TW protocol [Eq. (3.2)] was calculated exactly for the large- q SYK model (defined in Section 3.7). As anticipated in Ref. [176], the correlator at low temperatures—where the model is dual to gravity—agrees with the gravitational result [Eq. (3.4)] up to the previously mentioned regularization. More surprisingly, it was shown that teleportation with unit fidelity is also possible at high temperatures—where the model is not dual to gravity. As we will see in Section 3.7, all features of high temperature teleportation in the SYK model are in precise agreement with the peaked-size mechanism; our work thus provides a microscopic understanding for this previously unexplained result.

Gravity in the lab—Ref. [44] discusses various instances of teleportation in the TW protocol. The authors distinguish two teleportation mechanisms: (i) an “operator transfer” mechanism, which occurs at intermediate times in gravitational systems and is capable of teleporting multiple qubits, and (ii) a “state transfer” mechanism, which occurs at late times in all scrambling systems, and is capable of sending only a single qubit. Moreover, they introduce a microscopic interpretation for the teleportation mechanism in gravitational systems, termed “size winding”, which we connect to in Section 3.8.

In our terminology, the first teleportation mechanism corresponds to gravitational teleportation, while the second mechanism corresponds to peaked-size teleportation at late times¹. In our work, we provide a microscopic interpretation for late time teleportation (i.e. the peaked-size mechanism) and demonstrate that it is equivalent to teleportation in the HPR protocol. In addition, we demonstrate that peaked-size teleportation is a more general phenomenon that also occurs at intermediate times in many systems, where we show that it is capable of teleporting multiple qubits.

In a follow-up work, Ref. [188], whose pre-print was posted concurrently with that of this work, the same authors elaborate on their previous results and provide more detailed examples and calculations. These agree with our own results in areas of overlap.

¹The terminology of Ref. [44] can be understood using our two Conditions for teleportation. Specifically, operator transfer corresponds to situations that satisfy Condition 1, but not necessarily Condition 2, as occurs in gravitational teleportation [see Eq. (3.4)]. State transfer corresponds to situations that satisfy both Conditions.

3.2 Introduction to diagrammatic notation

We begin by introducing a diagrammatic “tensor network” notation for depicting the teleportation circuit. Adapted from Ref. [263], this notation provides a precise visual framework for analyzing teleportation in Section 3.3 and will be convenient for deriving rigorous results on the teleportation fidelity in Section 3.5.

To begin, we represent a quantum ket $|\psi\rangle$ and bra $\langle\psi|$ as:

$$|\psi\rangle = \begin{array}{|c} | \\ \hline |\psi\rangle \end{array}, \quad \langle\psi| = \begin{array}{|c} \langle\psi| \\ \hline | \end{array} \quad (3.5)$$

Note that time proceeds upwards—an initial state $|\psi\rangle$ terminates the bottom of a leg, while a final projection $\langle\psi|$ terminates the top. Similarly, much as in Fig. 6.1(a), we represent an operator, for instance the many-body unitary U , as a box with input (bottom) and output (top) legs:

$$U = \begin{array}{|c} \text{C} & \text{C} \\ \hline U \\ \hline \text{A} & \text{A} \end{array} \quad (3.6)$$

Here we have decomposed the input and output into two subsystems, A and its complement for the input, C and its complement for the output, in reference to the teleportation protocol. Specifically, comparing to Fig. 6.1(a), subsystem A consists of the qubits supporting the input state $|\psi\rangle$, while subsystem C consists of the coupled qubits.

The diagrammatic notation is particularly useful when working with EPR states. The EPR state on two qubits is defined as $|\text{EPR}\rangle = (|00\rangle + |11\rangle)/\sqrt{2}$; for a system of N d -dimensional qudits, this is generalized to $\frac{1}{\sqrt{d^N}} \sum_{i=1}^{d^N} |i\rangle_l |i\rangle_r^*$. Here $\{i\}$ is an arbitrary d^N -dimensional basis, $*$ denotes time-reversal (i.e. complex conjugation), and l and r denote the left and right system, respectively. In the diagrammatic notation, we represent this as:

$$|\text{EPR}\rangle = \frac{1}{\sqrt{d^N}} \sum_{i=1}^{d^N} |i\rangle_l |i\rangle_r^* \equiv \begin{array}{|c} \text{A} & \bar{\text{A}} & \bar{\text{A}} & \text{A} \\ \hline \text{---} & \text{---} & \text{---} & \text{---} \\ \hline \bullet & & & \end{array} \quad (3.7)$$

We have again decomposed each system into two subsystems, A and its complement, $\bar{\text{A}}$, for convenience (subsystem A is chosen to be identical between the left and right sides). Each dot represents a normalization factor given by the inverse square root of the subsystem’s dimension.

To see the utility of the diagrammatic notation, recall that a fundamental property of the EPR state is that an operator acting on the left side is equivalent to its transpose acting

on the right:

$$\begin{aligned}
 O_l |\text{EPR}\rangle &= \frac{1}{\sqrt{d^N}} \sum_{i,j} O_{ij} |i\rangle_l |j^*\rangle_r \\
 &= \frac{1}{\sqrt{d^N}} \sum_{i,j} O_{ij}^T |j\rangle_l |i^*\rangle_r = O_r^T |\text{EPR}\rangle
 \end{aligned} \tag{3.8}$$

where the middle equality swaps the i, j indices of the sum. In diagrammatic notation, this becomes simply

$$\begin{aligned}
 O_l |\text{EPR}\rangle &= \text{Diagram 1} \\
 &= \text{Diagram 2} = O_r^T |\text{EPR}\rangle
 \end{aligned} \tag{3.9}$$

i.e. the operator O “slides” from the left to right side of the EPR pairs, with its input and output indices correspondingly transposed. Similarly, expectation values in the EPR state can be easily computed in terms of the trace of (one-sided) operators, e.g.

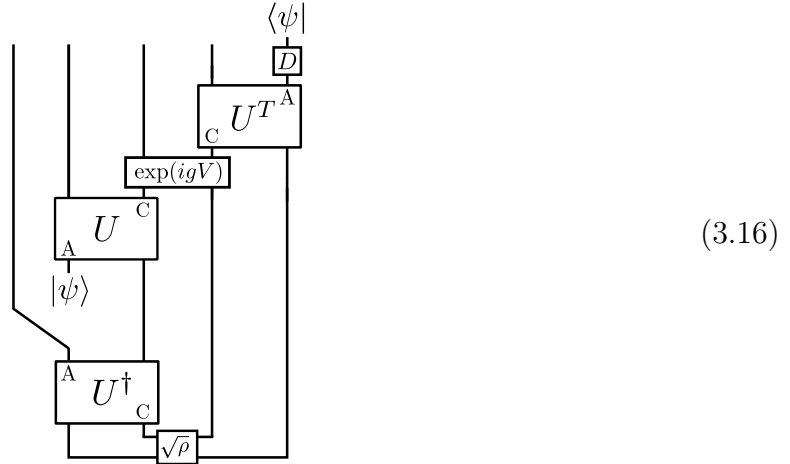
$$\begin{aligned}
 \langle \text{EPR} | A_l B_r | \text{EPR} \rangle &= \text{Diagram 1} \\
 &= \text{Diagram 2} = \frac{1}{d^N} \text{tr}(BA^T)
 \end{aligned} \tag{3.10}$$

where the final equality follows from $\langle \text{EPR} | B_l A_l^T | \text{EPR} \rangle = (1/d^N) \sum_{ij} \langle i^* | j^* \rangle \langle i | B A^T | j \rangle = (1/d^N) \sum_i \langle i | B A^T | i \rangle$.

The EPR state is closely related to the thermofield double (TFD) state, $\text{TFD} \equiv \sum_i e^{-\beta E_i/2} |E_i\rangle_l |E_i^*\rangle_r / \text{tr}(e^{-\beta H})^{1/2}$. Here H is a time-reversal symmetric Hamiltonian, $H = H^*$, with eigenstates $|E_i\rangle$, and eigenvalues E_i . The TFD state is parameterized by an effective “temperature” $1/\beta$. At infinite effective temperature ($\beta = 0$), the TFD and EPR states are equal. At finite temperature, the TFD state is obtained by applying the square root of the density matrix, $\rho^{1/2} \equiv e^{-\beta H/2} / \text{tr}(e^{-\beta H})^{1/2}$, to either side of the EPR state, which

This circuit proceeds as follows: (i) prepare the TFD state, (ii) insert the state $|\psi\rangle$ on subsystem A of the left side, (iii) time-evolve the two sides by U, U^* , (iv) couple the two sides via the unitary operator e^{igV} , with V as in Eq. (3.1), (v) evolve the right side by U^T , (vi) apply a ‘decoding’ operator D , and (vii) measure the output state of subsystem A on the right side. Compared to Fig. 6.1(a), we have made two modifications. First, we have replaced the measurement and classical communication with a quantum coupling e^{igV} , as described in Section 3.1. Second, we now include a simple decoding operator, D , applied at the end of the circuit before state recovery. We will find that $D = Y \otimes \dots \otimes Y$ for peaked-size teleportation of a multi-qubit subsystem, where Y is the single-qubit Pauli Y operator (Section 3.5).

Finally, we note that a straightforward application of Eq. (3.12) allows us to re-express the circuit as



This equivalent version of the protocol was introduced in Refs. [44, 88] and will be more convenient for analysis from here on.

3.3 General requirements for successful teleportation

We now introduce heuristic arguments for when teleportation succeeds in this protocol. This will culminate in the two requirements for teleportation listed in Section 3.1. In Section 3.5, we derive these conditions more formally by providing exact relations between the two-sided correlators in Eq. (3.2) and the teleportation fidelity.

We begin with the protocol in Eq. (3.16). To proceed, we insert a resolution of the

identity $\mathbb{1} = \sum_{\phi} |\phi\rangle\langle\phi|$ on the “swapped out” subsystem A (the output of U_l^\dagger)²:

(3.17)

This reformulation makes it clear that teleportation depends on the action of the coupling on states of the form $Q_{A,l}(t) |\text{TFD}\rangle$, where $Q_A = |\psi\rangle\langle\phi|$ and³ $Q_A(t) \equiv U Q_A U^\dagger$.

Teleportation succeeds when the coupling “transfers” $|\psi(t)\rangle\langle\phi(t)|$ from the left to right side of the TFD state. More precisely, the following identity, if true for *all* operators Q_A on A, would guarantee successful teleportation for all states:

(3.18)

Here θ_Q is an overall phase and we represent conjugation by the decoding operator as $\tilde{Q}_A \equiv D^\dagger Q_A D$. One can verify this explicitly by plugging the RHS of the above equality into Eq. (3.17): the topmost applications of $D U^T$ and $U^* D^\dagger$ cancel, leaving $Q_A \rightarrow |\psi\rangle\langle\phi|$ as the topmost operator on the right side, i.e. subsystem A is in the state $|\psi\rangle$.

To quantify whether this equality holds, we measure the inner product between the two

²At infinite temperature, using Eq. (3.9), $|\phi\rangle$ can be understood as the counterpart of $|\psi\rangle$, to be teleported from right to left instead of left to right. To see this, use Eqs. (3.9, 3.12) to re-express $\langle\phi|_l U_l^\dagger \rightarrow U_l^\dagger |\phi\rangle_r$, and apply $D_l U_l^\dagger$ after coupling to recover $|\phi\rangle$.

³Traditionally, this would be considered reverse time-evolution, and denoted $Q_A(-t)$. For brevity, we have flipped the sign of t throughout the text.

states⁴:

$$C_Q = \langle \text{TFD} | \tilde{Q}_{A,r}^\dagger(-t) e^{igV} Q_{A,l}(t) | \text{TFD} \rangle$$
(3.19)

This is precisely the two-sided correlation function introduced in Eq. (3.2), now modified to include the decoding operator. In particular, if the correlation function is maximal for all operators Q_A , then Eq. (3.18) holds and teleportation succeeds with perfect fidelity for all initial states.

In practice, it is sufficient to evaluate the correlators for a complete basis of operators on subsystem A (e.g. the Pauli operators). In this case, we now have *two* requirements on the operator correlators, as listed in Section 3.1: (i) all correlators must have maximal magnitude, i.e. equal to 1, and (ii) all correlators must have the *same phase*—if two operators both individually obey Eq. (3.18) but with different phases, their sum will not.

At infinite temperature, owing to Eq. (3.9), we will see that the first requirement is satisfied even in the absence of the coupling, for any symmetric or antisymmetric operator. To satisfy the second requirement, the role of the coupling e^{igV} must be to apply a Q_A -dependent overall phase. In the following section, we analyze the action of the coupling and show precisely when such an overall phase occurs.

3.4 Connection to operator size

In this section, we outline the connection between the coupling V and the operator size when V is acted on states of the form:

$$Q_{A,l}(t) | \text{TFD} \rangle = Q_{A,l}(t) \rho_l^{1/2} | \text{EPR} \rangle. \quad (3.20)$$

This connection was discovered in a number of previous works, focusing primarily on a specific bilinear coupling in fermionic systems [44, 162, 163, 188, 202, 208, 238]. In the

⁴For simplicity of notation and consistency with previous works [88, 90, 176], from here on we have assumed that the unitary is symmetric, $U^T = U$, $U^\dagger = U^*$.

following, we introduce this connection in the context of bosonic systems and argue that it applies to a good approximation for any generic, local couplings. From this, we then show that the action of the exponentiated coupling, e^{igV} , is particularly simple—it applies an overall phase—whenever operator size distributions are tightly peaked.

Coupling measures size

In bosonic qudit systems, we define the size of a Pauli string as its number of non-identity elements [208]. For instance, the Pauli string

$$\mathbb{1} \otimes X \otimes \mathbb{1} \otimes \mathbb{1} \otimes Z \otimes X \otimes \mathbb{1} \quad (3.21)$$

has size 3. A more general operator can be written as a sum of Pauli strings, R :

$$Q_A(t)\rho^{1/2} = \sum_R c_R(t)R, \quad (3.22)$$

and possesses a corresponding *size distribution* [202, 208]⁵:

$$P(\mathcal{S}) = \sum_{\mathcal{S}[R]=\mathcal{S}} |c_R(t)|^2. \quad (3.23)$$

The distribution is normalized to 1 if Q_A is unitary,

$$\sum_{\mathcal{S}} P(\mathcal{S}) = \sum_R |c_R(t)|^2 = \text{tr}(Q_A^\dagger Q_A \rho) = 1. \quad (3.24)$$

One can naturally characterize the size distribution via its moments—for instance, the average size, $\mathcal{S}[Q_A(t)\rho^{1/2}] \equiv \sum_{\mathcal{S}} P(\mathcal{S})\mathcal{S}$ (when context is clear, we denote this simply as \mathcal{S}), and the size width, $\delta\mathcal{S}$.

We will now show that the coupling V approximately measures the operator size, in the sense that it acts on states of the form Eq. (3.20) as:

$$VQ_{A,l}(t) |\text{TFD}\rangle \approx d^{N/2} \sum_R \left(1 - \eta_d \frac{\mathcal{S}[R]}{N}\right) c_R(t) R_l |\text{EPR}\rangle, \quad (3.25)$$

where $\eta_d \equiv 1/(1 - 1/d^2)$ is an order one constant determined by the local qudit dimension, d . Expectation values of V thus measure the average size, while higher powers of V measure higher moments of the size distribution [202, 208]. In particular, the exponentiated coupling in the teleportation protocol applies a *size-dependent phase* to each Pauli string of $Q_A(t)\rho^{1/2}$:

$$e^{igV} Q_{A,l}(t) |\text{TFD}\rangle \approx d^{N/2} e^{ig} \sum_R e^{-in_d g \mathcal{S}[R]/N} c_R(t) R_l |\text{EPR}\rangle, \quad (3.26)$$

⁵We note that, at finite temperature, the coefficients $c_R(t)$ will generally be complex. Their phases thus carry information beyond that captured by the size distribution, which we discuss in Section 3.8.

We derive this connection by first introducing an *exact* measure of operator size in bosonic qudit systems, generalizing previous measures for Majorana fermionic systems [202, 208]. We then argue that successively more generic couplings display approximately the same behavior, when acted on time-evolved operators in generic many-body scrambling dynamics.

In bosonic qudit systems, we find that the operator size is precisely measured by a sum of individual EPR projectors on each qudit i :

$$V_s = \frac{1}{N} \sum_{i=1}^N P_{\text{EPR},i} = \frac{1}{Nd^2} \sum_{i=1}^N \sum_{P_i} P_{i,l} P_{i,r}^*, \quad (3.27)$$

where d is the local qudit dimension, N is the number of qudits, and P_i form a complete basis of single-qudit operators (e.g. for qubits $P_i \in \{\mathbb{1}, X, Y, Z\}$). To see this, let us first analyze the action of a single EPR projector, $P_{\text{EPR},i}$. Writing a given Pauli string as a tensor product of single-qudit Paulis, $R = \bigotimes_{j=1}^N R_j$, we find

$$P_{\text{EPR},i} R_l |\text{EPR}\rangle = \delta_{R_i, \mathbb{1}} R_l |\text{EPR}\rangle, \quad (3.28)$$

using Eq. (3.10) and $\text{tr}_i(R_i)/d_i = \delta_{R_i, \mathbb{1}}$. A single EPR projector thus acts as a binary variable, giving eigenvalue 1 or 0 if a given Pauli string is, or is not, the identity on the designated qudit. The full coupling is a sum of these binary variables over all qudits and therefore counts the total number of non-identity elements in the Pauli string, i.e. the operator size. Its eigenvectors are the states $R_l |\text{EPR}\rangle$ with eigenvalues $1 - \mathcal{S}[R]/N$, as in Eq. (3.25).

We now turn to more general local couplings. First, as a trivial but useful modification, we can remove the identity operators from V_s , since these are not included our original definition of the coupling, V [Eq. (3.1)]. These constitute a fraction $1/d^2$ of the complete basis, P_i , summed in Eq. (3.27). Removing these terms renormalizes the eigenvalues of the coupling:

$$\begin{aligned} & \left(\frac{1}{N(d^2 - 1)} \sum_{i=1}^N \sum_{P_i \neq \mathbb{1}} P_{i,l} P_{i,r}^* \right) R_l |\text{EPR}\rangle \\ & = \left[1 - \eta_d \frac{\mathcal{S}[R]}{N} \right] R_l |\text{EPR}\rangle, \end{aligned} \quad (3.29)$$

which now match those quoted in Eq. (3.25). Note that the left side sum is now over $N(d^2 - 1)$ non-identity operators and normalized accordingly.

Second, we consider omitting some of the *non-identity* P_i at each site. Intuitively, under thermalizing dynamics, if an operator has spread to some qudit i it should not matter which Pauli operator we use to probe the operator's presence. For example, for qubits, we could omit the $O_j = X_i, Y_i$ couplings and keep only $O_j = Z_i$. A random Pauli string has equal probability to commute with Z_i as it would with X_i and Y_i ; thus, coupling using only Z_i operators is sufficient for measuring a thermalized operator's size.

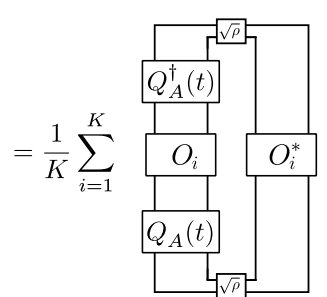
Third, we expect even more general couplings, composed of O_i that are local but not necessarily Pauli operators, to behave similarly. Specifically, each individual coupling, $O_{i,l}O_{i,r}$, will asymptote to two different expectation values before and after the time-evolved operator has spread to the support of O_i . Before, the coupling will maintain its expectation value in the unperturbed TFD state, $\text{tr}(O_i\rho^{1/2}O_i^\dagger\rho^{1/2})$. After, the spread of $Q_A(t)$ will disrupt the two-sided correlations in the TFD state that give rise to this initial expectation value, and the coupling will instead asymptote to its value in two thermal states, $\text{tr}(O_i\rho) \cdot \text{tr}(O_i\rho)$. As before, the sum of many terms, each behaving as above, leads to an approximate measure of operator size.

Lastly, we consider the case where the coupling is restricted to act only on some subsystem C , consisting of K qudits⁶. The coupling now measures the number of non-identity elements of a Pauli string within C —we denote this as the K -size, \mathcal{S}_K , of the Pauli string. The eigenvalues of the coupling are the same as those in Eq. (3.29), with the replacement $\mathcal{S}/N \rightarrow \mathcal{S}_K/K$. For a typical Pauli operator, we expect the K -size distribution of an operator to be similar to its full size distribution when K is large and the coupled qubits are distributed randomly. In particular, in this scenario we expect the average K -size, \mathcal{S}_K , to be proportional to the average size, \mathcal{S} ,

$$\frac{\mathcal{S}_K}{K} \approx \frac{\mathcal{S}}{N}. \quad (3.30)$$

For simplicity, we will make this substitution in the remainder of the work. However, if C is a spatially local subsystem (instead of a random subsystem), then this replacement will be modified depending on the spatial extent of the operator.

As a final remark, we note that the operator size distribution is directly related to out-of-time-order correlators (OTOCs), a more familiar quantity for probing operator growth [150, 171, 228]. In particular, the average size is equal to a sum of OTOCs between Q_A and O_i [202, 208],

$$\begin{aligned} \text{OTOC}_1 &= \langle V \rangle_Q \equiv \langle \text{TFD} | Q_{A,l}^\dagger(t) V Q_{A,r}(t) | \text{TFD} \rangle \\ &= \frac{1}{K} \sum_{i=1}^K \text{tr} \left(\rho^{1/2} Q_A(t) O_i Q_A^\dagger(t) \rho^{1/2} O_i^\dagger \right) \end{aligned} \quad (3.31)$$


using Eqs. (3.9-3.14). Higher moments of the size distribution can also be probed by OTOCs, now between Q_A and various products of the O_i , e.g. $O_i O_j$ for the size width. We discuss

⁶For simplicity, this assumes that there is a single coupling per qudit in C .

these relations further, paying particular attention to subtleties that arise at finite temperature, in Section 3.8.

Peaked-size distributions

The exponentiated coupling [Eq. (3.26)] has a particularly action when the size distribution of $Q_A(t)\rho^{1/2}$ is *tightly peaked* about its average size. In this regime, each Pauli string gains approximately the same phase, and so the action of the coupling reduces to applying a Q_A -dependent overall phase,

$$e^{igV} Q_{A,l}(t) |\text{TFD}\rangle \approx e^{ig\langle V \rangle_Q} Q_{A,l}(t) |\text{TFD}\rangle, \quad (3.32)$$

where the applied phase is proportional to the average K -size [see Eq. (3.29, 3.30)],

$$\begin{aligned} g \langle V \rangle_Q &= g \langle \text{TFD} | Q_{A,l}^\dagger(t) V Q_{A,l}(t) | \text{TFD} \rangle \\ &\approx g - \eta_d g \frac{\mathcal{S}_K [Q_A(t)\rho^{1/2}]}{K}, \end{aligned} \quad (3.33)$$

defining $\eta_d \equiv 1/(1 - 1/d^2)$ for convenience.

Corrections to this behavior are controlled by higher moments of the size distribution. Focusing on the overlap of the coupled and uncoupled states, the leading order correction is equal to the K -size variance, $\delta\mathcal{S}_K^2/K^2 = \langle V^2 \rangle_Q - \langle V \rangle_Q^2$, multiplied by g^2 :

$$\begin{aligned} \langle e^{igV} \rangle_Q &= \left\langle 1 + igV - \frac{1}{2}g^2V^2 + \dots \right\rangle_Q \\ &= \left(1 + ig \langle V \rangle_Q - \frac{1}{2}g^2 \langle V \rangle_Q^2 + \dots \right) \\ &\quad - \frac{1}{2}g^2 \left(\langle V^2 \rangle_Q - \langle V \rangle_Q^2 \right) + \dots \\ &= \exp \left(ig \langle V \rangle_Q \right) - \frac{1}{2}(\eta_d g)^2 \delta\mathcal{S}_K^2/K^2 + \dots \end{aligned} \quad (3.34)$$

The K -size variance receives contributions from two sources: the variance of the full size distribution, $\delta\mathcal{S}^2$, and a statistical error from sampling only K of N qubits for the K -size. If the K qubits are distributed randomly, these errors scale as $\delta\mathcal{S}_K \sim \delta\mathcal{S} \cdot (K/N)$ and $\delta\mathcal{S}_K \sim \sqrt{\mathcal{S}_K} \approx \sqrt{\mathcal{S}K/N}$, respectively (see Appendix B.6 for a detailed derivation of the latter). These are small compared to the average K -size whenever $\delta\mathcal{S} \ll \mathcal{S}$ and $1 \ll \mathcal{S}_K$.

In Appendix B.1, we go beyond these leading order corrections and provide quantitative bounds on when the peaked-size approximation in Eq. (3.32) is valid. In general, we can strictly prove that this approximation holds whenever there is a parametric separation between an asymptotic size width, defined in the appendix, and the average size.

3.5 Peaked-size teleportation

Having established general conditions for successful teleportation (Section 3.3) as well as the connection between the coupling in the TW protocol and operator size distributions (Section 3.4), we are now ready to introduce the peaked-size mechanism for teleportation. In this section, we first demonstrate peaked-size teleportation in its simplest context: teleportation of a single qubit at infinite temperature. We then show that the fidelity of peaked-size teleportation is necessarily suppressed at finite temperature. For ease of reading, we relegate rigorous results supporting each of the above arguments to the end of the section. We turn to specific physical systems realizing peaked-size teleportation in the following sections: in Section 3.6 we show that peaked-size teleportation of a single qubit occurs in all scrambling systems at late times, while in Section 3.7 we show that peaked-size teleportation of multiple qubits occurs in certain systems at intermediate times.

Single-qubit teleportation

To analyze teleportation of a single qubit, we turn to the two-sided correlators in Eq. (3.19), with $Q_A \in \{\mathbb{1}, X, Y, Z\}$ running over the single-qubit Pauli operators. We recall that the requirements for teleportation are for all C_Q to have (i) maximal magnitude and (ii) the same phase.

The first requirement is naturally satisfied at infinite temperature even *before coupling and decoding* but the second requirement is not. In particular, the four correlators with $D = \mathbb{1}$, $g = 0$ are:

Q_A	C_Q
$\mathbb{1}$	+1
X	+1
Y	-1
Z	+1

($D = \mathbb{1}$)
($g = 0$)

where the left entries are qubit operators, Q_A , and the right entries are the correlators, C_Q . The correlators have maximal magnitude because each operator can be transferred perfectly from left to right using Eq. (3.9). However, the Y operator picks up an overall minus sign during this process, since $Y^T = -Y$, and so the correlator phases are not aligned. One can verify the resulting teleportation fidelity is indeed trivial. Our goal will be to show that the action of the coupling in Eq. (3.32), as well as a simple decoding operation, are sufficient to align the four phases.

To begin, we assume that all time-evolved Pauli operators have a tightly peaked size distribution and that the average size \mathcal{S} is the same for all non-identity operators. From Eqs. (3.32-3.33), we have that the coupling applies a total phase difference $\eta_d g \mathcal{S} / N$ between

the thermofield double state (the identity operator; size zero) and all perturbed states (time-evolved Pauli operators; size \mathcal{S}). Our table of correlator phases is thus modified to:

$$\begin{array}{c}
 \begin{array}{|c|c|} \hline Q_A & C_Q \\ \hline \mathbb{1} & +1 \\ X & +1 \\ Y & -1 \\ Z & +1 \\ \hline \end{array} \\
 (D = \mathbb{1}) \\
 (g = 0)
 \end{array}
 \longrightarrow
 \begin{array}{c}
 \begin{array}{|c|c|} \hline Q_A & C_Q \\ \hline \mathbb{1} & e^{-i\eta_{dg}\mathcal{S}/N} \\ X & +1 \\ Y & -1 \\ Z & +1 \\ \hline \end{array} \\
 (D = \mathbb{1}) \\
 (g \neq 0)
 \end{array}$$

We again do not achieve perfect phase alignment. However, we can now correct the misaligned phases using the decoding operator, $D = Y$. This applies an additional minus sign to the X and Z correlators:

$$\begin{array}{c}
 \begin{array}{|c|c|} \hline Q_A & C_Q \\ \hline \mathbb{1} & +1 \\ X & +1 \\ Y & -1 \\ Z & +1 \\ \hline \end{array} \\
 (D = \mathbb{1}) \\
 (g = 0)
 \end{array}
 \longrightarrow
 \begin{array}{c}
 \begin{array}{|c|c|} \hline Q_A & C_Q \\ \hline \mathbb{1} & e^{-i\eta_{dg}\mathcal{S}/N} \\ X & +1 \\ Y & -1 \\ Z & +1 \\ \hline \end{array} \\
 (D = \mathbb{1}) \\
 (g \neq 0)
 \end{array}
 \longrightarrow
 \begin{array}{c}
 \begin{array}{|c|c|} \hline Q_A & C_Q \\ \hline \mathbb{1} & e^{-i\eta_{dg}\mathcal{S}/N} \\ X & -1 \\ Y & -1 \\ Z & -1 \\ \hline \end{array} \\
 (D = Y) \\
 (g \neq 0)
 \end{array}$$

The correlator phases are now aligned whenever

$$\eta_{dg} \frac{\mathcal{S}}{N} = \pi \pmod{2\pi}, \tag{3.35}$$

leading to perfect teleportation at these values.

Peaked-size teleportation at finite temperature

There are two important modifications to peaked-size teleportation at finite temperature. First, the relevant notion of operator size is modified [202]. In particular, in the peaked-size regime, the difference in phase applied between the identity and non-identity Pauli operators is modified to

$$\mathcal{S}[Q_A(t)] \rightarrow \mathcal{S}[Q_A(t)\rho^{1/2}] - \mathcal{S}[\rho^{1/2}]. \tag{3.36}$$

Second, the maximal fidelity of peaked-size teleportation is reduced at finite temperature. In particular, when sizes are tightly peaked, the two-sided correlators factorize into a constant magnitude multiplied by an overall phase:

$$\begin{aligned}
 C_Q &= \langle \text{TFD} | \tilde{Q}_{A,r}^\dagger Q_{A,l} | \text{TFD} \rangle e^{i(g - \eta_{dg}\mathcal{S}_K[Q_A(t)\rho^{1/2}]/K)} \\
 &= G_\beta(Q_A) \cdot e^{i\theta_Q}
 \end{aligned} \tag{3.37}$$

where θ_Q combines the effects of transposition, coupling, and decoding, and the correlator magnitude corresponds to an imaginary-time Green’s function,

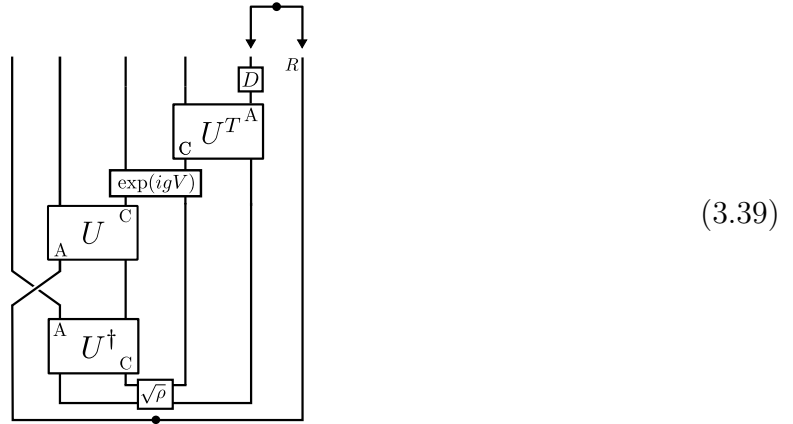
$$G_\beta(Q_A) \equiv \text{tr}(Q_A^\dagger \rho^{1/2} Q_A \rho^{1/2}) \leq 1. \quad (3.38)$$

This Green’s function is unity at infinite temperature and generically decreases at finite temperatures, due to the reduced entanglement of the TFD state. This violates the maximal magnitude requirement for teleportation, and therefore leads to a corresponding decrease in the teleportation fidelity.

The astute reader will recall that finite temperature teleportation is known to succeed with $\mathcal{O}(1)$ fidelities (i.e. higher than G_β) in theories with a gravity dual [88, 90, 176]; this is a signature of physics outside the peaked-size regime, which we connect to in Section 3.8.

Rigorous expressions for teleportation fidelity

We now derive formal expressions of the teleportation fidelity for n teleported qubits as a function of the correlator phases. To do so, we consider a variant of the protocol where instead of teleporting a quantum state we attempt to distill an EPR pair:



Here state insertion is replaced by swapping in one “half” of an EPR pair with a reference subsystem R (far right) into subsystem A of the left side. When subsystem A is teleported from left to right, the circuit results in an EPR pair between the reference subsystem R and subsystem A of the right (top arrows). The fidelity of EPR distillation is precisely related to the average fidelity of state teleportation [265], $F_{\text{EPR}} = [(d_A + 1)\langle F_\psi \rangle - 1]/d_A$, where $d_A = 2^n$ is the dimension of subsystem A when teleporting n qubits.

We calculate the teleportation fidelity by Pauli decomposing the SWAP operator as

SWAP = $\sum_{Q_A} Q_A \otimes Q_A^\dagger / d_A$. This gives:

$$F_{\text{EPR}} = \text{[Diagram 1]} = \frac{1}{d_A^2} \sum_{Q_1, Q_2} \text{[Diagram 2]} = \frac{1}{d_A^4} \sum_{Q_1, Q_2} \text{[Diagram 3]} = \frac{1}{d_A^4} \sum_{Q_1, Q_2} \text{[Diagram 4]}. \quad (3.40)$$

where the third equality utilizes the diagrammatic identities Eqs. (3.9, 3.10), and the fourth equality inserts the identity, $\mathbb{1} = D_r U_r U_r^\dagger D_r^\dagger$, in the center of the right side (recall our notation $\tilde{Q}_{1/2} = D^\dagger Q_{1/2} D$). Writing the rightmost diagram as an equation, we have:

$$F_{\text{EPR}} = \frac{1}{d_A^4} \sum_{Q_1, Q_2} \langle \text{TFD} | Q_{2,l}^\dagger(t) e^{-igV} \tilde{Q}_{2,r}(-t) \times \tilde{Q}_{1,r}^\dagger(-t) e^{igV} Q_{1,l}(t) | \text{TFD} \rangle. \quad (3.41)$$

Similar expressions for teleportation of quantum states are contained in Appendix B.3.

In general, the teleportation fidelity and two-sided correlators are related only by a lower bound,⁷

$$F_{\text{EPR}} \geq \left| \frac{1}{d_A^2} \sum_{Q_A} C_Q \right|^2. \quad (3.42)$$

This is obtained diagrammatically by inserting the projector, $|\text{TFD}\rangle\langle\text{TFD}|$, into the center

⁷Under special circumstances, namely large- N models, one may be able to factorize the above expression in terms of correlators of the form Eq. (3.19) [88].

of Eq. (3.40):

$$\frac{1}{d_A^4} \sum_{Q_1, Q_2} \geq \frac{1}{d_A^4} \sum_{Q_1, Q_2} \quad (3.43)$$

A similar bound was obtained in Ref. [44, 188], conditional on certain assumptions about operators' size distributions.

At infinite temperature *in the peaked-size regime*, we have $C_Q = e^{i\theta_Q}$ and the fidelity is equal to the lower bound:

$$F_{\text{EPR}} = \frac{1}{d_A^4} \sum_{Q_1, Q_2} e^{i(\theta_{Q_1} - \theta_{Q_2})} = \left| \frac{1}{d_A^2} \sum_{Q_A} e^{i\theta_Q} \right|^2. \quad (3.44)$$

The sum is over d_A^2 terms, and is unity only when all the operators' phases are the same. In the case of a single-qubit teleportation at infinite temperature in the peaked-size regime, plugging the final table of Section 3.5 into the above equation gives a fidelity:

$$F_{\text{EPR}} = \frac{5}{8} - \frac{3}{8} \cos(\eta dg \mathcal{S}/N), \quad (3.45)$$

which oscillates between trivial fidelity ($F_{\text{EPR}} = 1/4$) and unity as a function of the operators'

size. At finite temperature in the peaked-size regime, we instead find

$$\begin{aligned}
 F_{\text{EPR}} &= \frac{1}{d_A^4} \sum_{Q_1, Q_2} e^{i(\theta_{Q_1} - \theta_{Q_2})} \text{tr} \left(Q_2^\dagger Q_1 \rho^{1/2} Q_1^\dagger Q_2 \rho^{1/2} \right) \\
 &\leq \frac{1}{d_A^4} \sum_{Q_1, Q_2} \text{tr} \left(Q_2^\dagger Q_1 \rho^{1/2} Q_1^\dagger Q_2 \rho^{1/2} \right) \\
 &= \frac{1}{d_A^2} \sum_{Q_A} \text{tr} \left(Q_A \rho^{1/2} Q_A^\dagger \rho^{1/2} \right) \\
 &= \frac{1}{d_A^2} \sum_{Q_A} G_\beta(Q_A).
 \end{aligned} \tag{3.46}$$

where the maximum fidelity is again achieved when the correlator phases align. However, its value is now less than unity, and instead is equal to a sum of various imaginary time Green's functions, i.e. the correlator magnitudes [Section 3.5, Eq. (3.38)].

3.6 Peaked-size teleportation at late times

We now introduce the simplest physical example of peaked-size teleportation: teleportation in any scrambling system at late times (after the scrambling time). There are two distinguishing features of this regime: (i) the circuit can only teleport a single qubit, i.e. the channel capacity is one, and (ii) as for all peaked-size teleportation, the teleportation fidelity is suppressed at low temperatures. We also demonstrate that this regime of peaked-size teleportation, as well as the full quantum circuit implementing the TW protocol, are equivalent to HPR teleportation of a single qubit. In Section 3.7, we will demonstrate that the single-qubit late time channel capacity can be overcome at intermediate times in many scrambling systems.

Teleportation at late times

At late times, the dynamics of a scrambling system can be approximated by a Haar random unitary⁸ [111, 210]. In this case, each time-evolved operator, $Q_A(t)$, becomes a sum of random Pauli strings, each with probability $1/d^2$ to be the identity at any individual site. As a result, time-evolved operators have an average size,

$$\mathcal{S} \approx (1 - 1/d^2)N, \tag{3.47}$$

⁸This approximation is modified in systems with a conserved quantity. Size distributions in such systems have been considered in Refs. [130, 204, 205]; at late times (after conserved quantities have diffused across the entire system), they are expected to be similar to size distributions without a conserved quantity, up to corrections $\sim 1/N$.

and a size width,

$$\delta\mathcal{S} \sim \sqrt{N}, \quad (3.48)$$

where the scaling is based on the central limit theorem. The K -size distribution takes the same form, replacing N with K , and is tightly peaked as long as K is large (specifically, $g\delta\mathcal{S}_K/K \approx g/\sqrt{K} \ll 1$).

For simplicity, we will focus on late time teleportation at infinite temperature; finite temperature modifications follow according to Section 3.5. Using Eqs. (3.32-3.33), we find that the coupling applies a relative phase e^{ig} between the identity operator (size zero) and all non-identity Pauli operators (size above) [176]:

$$\begin{aligned} e^{igV} |\text{EPR}\rangle &= e^{ig} |\text{EPR}\rangle \\ e^{igV} Q_{A,l}(t) |\text{EPR}\rangle &= Q_{A,l}(t) |\text{EPR}\rangle. \end{aligned} \quad (3.49)$$

The lack of an applied phase for non-identity Pauli operators corresponds to the vanishing of $\langle V \rangle_Q$ at late times, when OTOCs have decayed to zero [see Eq. (3.33)]. From Section 3.5, we see that whenever

$$g = \pi \pmod{2\pi}, \quad (3.50)$$

single-qubit teleportation succeeds.

A brief argument shows that late time teleportation of higher dimensional quantum states is not possible. Consider teleportation of a d -dimensional qudit, with a basis of states $|i\rangle$, $i = 0, \dots, d-1$. The qudit Pauli operators are generated by the ‘clock’ and ‘shift’ operators: $Z|i\rangle = e^{i\omega}|i\rangle$, with $\omega = 2\pi/d$, and $X|i\rangle = |i+1\rangle$. The two generators obey the commutation relation, $XZ = e^{-i\omega}ZX$. After transposition, each Pauli operator, $X^p Z^q$, becomes

$$(X^p Z^q)^T = Z^{T,q} X^{T,p} = Z^q X^{-p} = e^{-ipq\omega} X^{-p} Z^q. \quad (3.51)$$

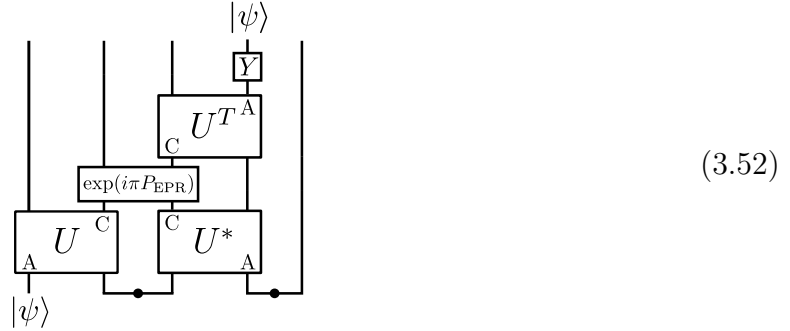
Meanwhile, late time dynamics ensure that the coupling applies an overall phase only to the identity operator. For teleportation to be successful, we would therefore require a decoding operation, D , that acts as $DX^{-p}Z^qD^\dagger \sim X^pZ^q$. Suppose there was such a unitary operator⁹, and consider its action on the generators: $DXD^\dagger = X^{-1}$ and $DZD^\dagger = Z$. The above action implies that commuting the two generators gives a different phase before and after decoding: $DXZD^\dagger = e^{-i\omega}DZXD^\dagger = e^{-i\omega}ZX^{-1}$ and $DXZD^\dagger = X^{-1}Z = e^{+i\omega}ZX^{-1}$. This is a contradiction whenever $e^{+i\omega} \neq e^{-i\omega}$, i.e. whenever $d > 2$.

Equivalence to HPR protocol

We now turn to the equivalence between peaked-size teleportation and teleportation in the HPR protocol. The latter was originally introduced to recover information in the Hayden-Preskill thought experiment [111, 263], and is reviewed in detail in Appendix B.2.

⁹The astute reader may note that this operation is in fact implemented by the *anti-unitary* operator, $D|i\rangle = |-i \pmod{d}\rangle^*$. However, if one decomposes state insertion in terms of Pauli operators as $|\psi\rangle\langle\phi| = \sum_{Q_A} c_Q Q_A$ (see Section 3.3), one desires that the entire operator $|\psi\rangle\langle\phi|$ be transferred from left to right for all possible $\langle\phi|$. The preceding anti-unitary operator will complex conjugate the coefficients c_Q , thus spoiling teleportation for any $\langle\phi|$ where these are complex.

Here, we restrict our attention to teleportation in the deterministic variant of the protocol, of a single qubit at infinite temperature [147, 263]. The protocol takes the form:



where P_{EPR} projects onto an EPR pair between subsystems C on the left and right sides.

The equivalence between this protocol and the TW protocol [Eq. (3.15)] is manifest, with the only difference being the locality of the coupling. Specifically, the HPR coupling is of the same general form as the TW coupling [Eq. (3.1)]:

$$gV \equiv \pi P_{\text{EPR}} = \frac{\pi}{d_C^2} \sum_{P_C} P_{C,l} P_{C,r}^*, \quad (3.53)$$

where the sum is over a complete basis of d_C^2 Pauli operators on C. However, the operators P_C are typically non-local across C, whereas the coupling considered in the TW protocol was restricted to local operators. As a consequence, the HPR coupling functions as a binary variable measuring whether or not an operator has support on subsystem C (see Section 3.4). In contrast, the TW coupling measures the operator size within C, which takes an approximately continuous range of values when C is large. Crucially, at late times under scrambling dynamics, the effect of both couplings will be the same: to apply an overall phase to non-identity operators.

A few additional remarks are in order. First, while the leading order effect of the HPR and TW couplings is the same, they lead to different finite-size corrections. In particular, in a fully scrambled system, the variance in the phases applied by the HPR coupling is equal to the probability of a random Pauli string not having support on C, which is suppressed exponentially in the size of C, i.e. $1/d_C^2$. On the other hand, the variance in phases applied by the TW coupling is suppressed only polynomially, by $\sim g^2 \delta \mathcal{S}_K^2 / K^2 \sim g^2 \mathcal{S}_K / K^2 \sim g^2 / K$ [see Eq. (3.48) and the discussion below Eq. (3.34)]. These enhanced phase fluctuations are relevant for finite-size implementations of the TW protocol, as discussed further in Section 3.9.

Second, it has previously been shown that an extended version of the HPR protocol allows for teleportation of *multiple* qubits at late times [263]. Because of the equivalence between the protocols, this extension would also allow for multi-qubit teleportation via the peaked-size mechanism. However, the enhanced channel capacity comes with a trade-off: the circuit complexity (measured by the number of applications of the unitary U) grows exponentially in the number of qubits to be teleported. As we will see in the following

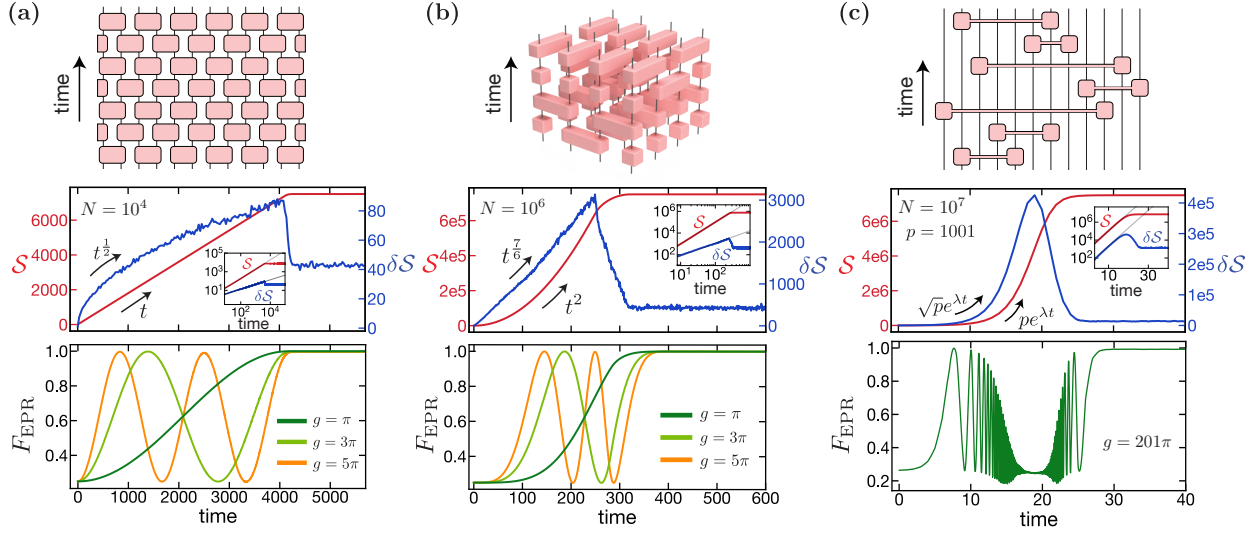


Figure 3.2: Numerical results for averaged operator size and teleportation fidelity of 1D, 2D, and 0D RUCs. **(a-b)** In 1D and 2D, sizes grow ballistically in time, while the size width grows with a slower power of t and matches predictions from the KPZ universality class (Section 3.7). Because of the separation between the size and size width, the teleportation fidelity for a single qubit exhibits an oscillatory behavior at intermediate times, with nearly perfect maximum fidelity. At late times, the teleportation fidelity saturates close to 1 for odd values of g/π , as expected for any scrambling system (Section 3.6). **(c)** In 0D all-to-all coupled RUCs, both the size and size width grow exponentially in time and obtaining a large separation between them requires encoding the initial state into p -body operators. With this encoding, the teleportation fidelity displays a distinct three-regime profile for $g \gg 1$. In particular, as in 1D and 2D, peaked-size teleportation succeeds *(i)* at early times, with an oscillating fidelity, and *(ii)* at late times, where the fidelity saturates close to 1 (for odd g/π). Between these regimes, no teleportation occurs because the size width has grown too large, $g\delta S/N \gtrsim 1$.

section, this limitation can be overcome by peaked-size teleportation in the TW protocol at intermediate times, owing to the locality of the TW coupling.

3.7 Peaked-size teleportation at intermediate times

We now turn to analyzing the behavior of peaked-size teleportation at intermediate times, i.e. before the scrambling time. In this regime, multiple qubits can be teleported given a certain condition on the growth of time-evolved operators, namely when the overlap of the operators' support is sufficiently small.

We explicitly demonstrate that this condition is satisfied, and multi-qubit teleporation is possible, in a wide variety of physical systems at infinite temperature. These include random unitary circuits (RUCs) in $\geq 1D$, for which peaked sizes naturally occur due to local thermalization within each operator’s light cone, and time-evolved operators are non-overlapping due to spatial locality. More surprisingly, we show that multi-qubit peaked-size teleportation can also be achieved in ‘fast scrambling’, all-to-all coupled systems, including 0D random unitary circuits and the SYK model (at infinite temperature) [111, 226]. In this case, operators are *not* spatially separated at any nonzero time; nonetheless, the overlap of their size distributions remains *probabilistically* small at sufficiently early times. Furthermore, we demonstrate that while size distributions of local operators are generically *not* tightly peaked in all-to-all systems, peaked size distributions can be engineered in the TW protocol by *encoding* one’s initial state into large p -body operators.

Finally, we consider the channel capacity—i.e. the maximum number of qubits that can be teleported (allowing both g and t to vary)—of peaked-size teleportation in all-to-all coupled systems. This is an essential question for comparing the capabilities of peaked-size teleportation with those of gravitational teleportation in traversable wormholes [176]. Remarkably, we provide analytic and numerical evidence that the channel capacity of peaked-size teleportation in 0D RUCs, a quite simple microscopic system, is asymptotically equivalent to that of the gravitational mechanism! Namely, the number of qubits n that can be teleported scales with the number of couplings in the protocol, $n \sim K$.

Multi-qubit teleportation: additive operator sizes

We begin with a few simple examples of multi-qubit teleportation to build intuition. First, consider a unitary U that factorizes as $U = U_1 \otimes \cdots \otimes U_n$, where each U_i acts on a disjoint subsystem. If we insert n qubits individually into the n different subsystems, then the entire protocol decouples into n independent channels and there is no restriction on sending multiple qubits. This trivial example relies on the fact that U does not scramble information across the entire system but only within each disjoint subsystem. We see that full scrambling of information by U in fact *inhibits* the teleportation protocol’s channel capacity (considered for a fixed set of qubits and dynamics).

A similar situation occurs even when the dynamics are not factorizable, as long as the teleported qubits are in causally separated regions. For example, consider a ($\mathcal{D} \geq 1$)-dimensional system with short-range interactions, where the inserted qubits are spatially separated. At intermediate times, the time-evolved qubit operators will have support within a local ‘light cone’ about their initial location, but will continue to act on disjoint subsystems. This scenario is therefore no different from the previous example and multi-qubit teleportation remains possible, as long as (i) the size distributions of each operator is tightly peaked, (ii) the coupling V has support within each qubit’s light cone, and (iii) the light cones of each qubit are non-overlapping. This final requirement constrains the number of qubits that can be sent at a given time t . In particular, the light cone of each operator will have a radius $v_B t$ where v_B is the butterfly velocity. The maximum number of non-overlapping light cones—

equal to the total number of qubits n that can be teleported—is therefore $n \lesssim N/(v_B t)^D$, where N is the total system volume.

More formally, we can analyze the success of n -qubit teleportation using the two-sided correlators, C_Q . We are concerned with n -qubit operators $Q(t) = Q_1(t) \dots Q_n(t)$, where each $Q_i \in \{I, X, Y, Z\}$ is a single-qubit Pauli on the i^{th} teleported qubit. We work at infinite temperature and assume that sizes are tightly peaked. Teleportation therefore succeeds whenever all correlators have the same phase.

Inspired by the example of n decoupled protocols, we will take the decoding operator to be the tensor product, $D = Y \otimes \dots \otimes Y$. The combination of transposition and conjugation by D thus applies a minus sign to every single-qubit non-identity Pauli operator. An additional phase is applied by coupling proportional to the size of each operator. For example, for $n = 2$ qubits, we have:

Q_A	C_Q
$\mathbb{1} \otimes \mathbb{1}$	1
$Q_1 \otimes \mathbb{1}$	$-1 \times e^{-i\eta_{dg}\mathcal{S}_1/N}$
$\mathbb{1} \otimes Q_2$	$-1 \times e^{-i\eta_{dg}\mathcal{S}_2/N}$
$Q_1 \otimes Q_2$	$(-1)^2 \times e^{-i\eta_{dg}\mathcal{S}_{12}/N}$

where \mathcal{S}_i and \mathcal{S}_{ij} are shorthand for $\mathcal{S}[Q_i(t)]$ and $\mathcal{S}[Q_i(t)Q_j(t)]$. In order for all correlators to have the same phase, we require that $\eta_{dg}\mathcal{S}_1/N = \eta_{dg}\mathcal{S}_2/N = \pi \bmod 2\pi$, and that the operator sizes *add*, such that $e^{-i\eta_{dg}\mathcal{S}_{12}/N} \approx e^{-i\eta_{dg}(\mathcal{S}_1+\mathcal{S}_2)/N} = e^{i(\pi+\pi)} = 1$.

This requirements generalize straightforwardly to n qubits. Specifically, teleportation succeeds whenever the single-qubit operator sizes obey $\eta_{dg}\mathcal{S}_i/N = \pi \bmod 2\pi$ and the multi-qubit operator sizes *add* under operator multiplication:

$$\begin{aligned} \mathcal{S}[Q_1(t)Q_2(t) \dots Q_n(t)] \\ \approx \mathcal{S}[Q_1(t)] + \mathcal{S}[Q_2(t)] + \dots + \mathcal{S}[Q_n(t)]. \end{aligned} \quad (3.54)$$

This latter requirement implies that the phases applied by the coupling, e^{igV} , factorize, and allows the n qubits to be teleported ‘in parallel’ as in the previous simple examples.

The size addition requirement naturally bounds the channel capacity in terms of the number of couplings, K . Specifically, the K -size takes integer values between 1 and K . However, the requirement that all three single-qubit Pauli operators have the same K -size increases the minimum K -size to 2. From Eq. (3.54), this implies that an n -qubit operator has a K -size of at least $2n$, which is only possible if

$$2n \leq K. \quad (3.55)$$

Indeed, this strict upper bound can also be understood from an information theoretic perspective: teleporting n qubits requires an increase of $2n$ in the mutual information between the left and right sides of the system. Each of the K classical bits sent from left to right in Fig. 6.1(a) increases the mutual information by at most 1, so at least $2n$ bits are required.

≥ 1 D random unitary circuits

As a first concrete example of intermediate time peaked-size teleportation, we consider a random unitary circuit (RUC) applied to a lattice of N qubits in one or higher dimensions. At each time step, pairs of neighboring qubits are evolved via independent Haar random unitaries arranged in a ‘brick-layer’ fashion, with periodic boundary conditions [Fig. 3.2(a,b)]. Operator growth in such systems has been studied at great length, and is believed to be a good model for many aspects of information scrambling under Hamiltonian dynamics [130, 159, 187, 205, 232, 249]. We extend these previous studies by demonstrating new results on the behavior of the operator size *width*—i.e. power-law scaling at intermediate times and suppression at late times—which we show can be detected by the teleportation fidelity (Fig. 3.3).

A key property of Haar random unitary circuits is that the expectation values of many circuit quantities can be computed by replacing the Haar random unitaries with randomly chosen *Clifford* unitaries, thereby enabling efficient classical simulation [64, 187]. Generally, this equivalence holds for any quantity that contains no more than *two* copies each of U and U^\dagger (e.g. the Renyi-2 entropy, or the OTOC); however, for systems of qubits, this property holds for up to three copies [142, 250, 274]. From Eq. (3.41), we see that the teleportation fidelity contains three copies of U and U^\dagger , so the average fidelity is efficiently simulable¹⁰. Moreover, by definition, the size distributions of operators under Clifford dynamics are perfectly tightly-peaked, since a Pauli operator Q_A evolved under a Clifford unitary remains a single Pauli string. Hence, the teleportation fidelity can be computed using the simplified expression given in Eq. (3.44).

In more detail, we calculate the average EPR fidelity for teleporting n qubits through the following procedure. First, we choose a particular realization of U by sampling each 2-qubit unitary from a uniform distribution of 2-qubit Clifford unitaries. Second, we determine the K -size of UQ_AU^\dagger for each n -qubit Pauli operator, Q_A , or, if n is large, for a random subset of these operators; such simulations can be performed efficiently with a time cost that scales linearly with the circuit depth. Third, we compute the fidelity for a given coupling g using Eq. (3.44), with the phases $\theta_Q = \eta_d g \mathcal{S}_K / K + \pi \mathcal{S}[Q_A(0)]$, where the latter term captures the fact that decoding and transposition apply a minus sign for each non-identity element of the initial Q_A . Finally, we average the EPR fidelity over multiple realizations of U .

The results of these simulations for $n = 1$ qubit in 1D and 2D are shown in Fig. 3.2(a,b). As expected, the average operator size grows ballistically, $\mathcal{S} \propto t^D$, until the operator’s light cone reaches the edge of the system, at which point the size saturates to $3/4N$. While the behavior of the size width is more complex, in both dimensionalities it grows more slowly than the average size. This implies that the size distribution is tightly-peaked and the teleportation fidelity can be approximated by $F = \frac{5}{8} - \frac{3}{8} \cos(\eta_d g \mathcal{S} / N)$ [Eq. (3.45)]. We verify that the time profile of the fidelity follows this prediction, and nearly perfect fidelity is achieved when $\eta_d g \mathcal{S} / N = \pi \pmod{2\pi}$. In Appendix B.5, we also demonstrate that

¹⁰For higher-dimensional qudits, while we cannot efficiently simulate the teleportation fidelity, we can still calculate the correlators Eq. (3.19), which lower bound the fidelity via Eq. (3.42).

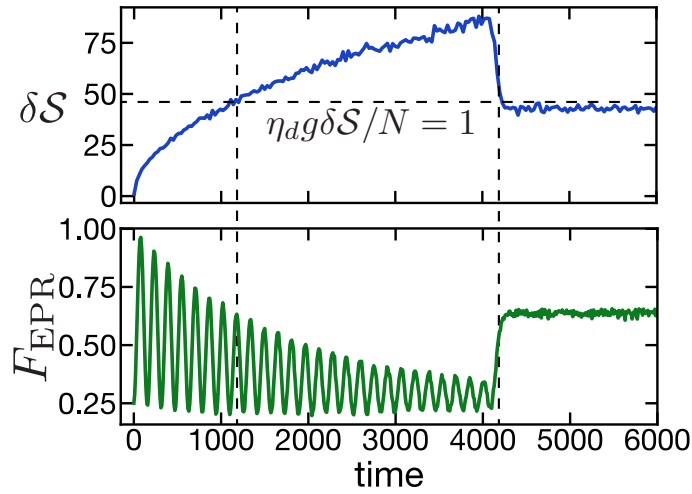


Figure 3.3: Probing operator size width in a 1D RUC. (top) The size width initially grows as $t^{1/2}$ and reaches a peak at the scrambling time $t^* \sim N = 10000$. (bottom) We probe this behavior by measuring the teleportation fidelity of a single qubit with a large coupling $g = 57\pi \sim \sqrt{N}$. The fidelity exhibits a distinct decay-revival profile, controlled by whether the size width has exceeded the threshold $g\delta\mathcal{S}/N \approx 1$: nearly perfect fidelity initially, power law decay towards a trivial fidelity at intermediate times, and partial revival at late times.

teleportation of $n > 1$ qubits is also possible at intermediate times, as long as their light cones do not overlap.

Probing the size width—Let us now turn to the time profile of the size width, which exhibits a *peak* near the scrambling time in both 1D and 2D. Qualitatively, this behavior arises from fact that the size width receives contributions from two sources: the interior of the light cone, and the boundary of the light cone. Within the light cone, we expect a ≥ 1 D system with a small local Hilbert space to ‘locally thermalize’ as the operator spreads. This implies that the bulk’s contribution to the size width scales as $\delta\mathcal{S}_{\text{bulk}} \propto \sqrt{\mathcal{S}} \propto t^{D/2}$ and saturates at the scrambling time. Second, the size width also receives contributions from the light cone’s boundary, which has not yet thermalized. At late times, the boundary of the light cone reaches the edge of the system and these additional contributions subside, leading to the peak in the size width at the scrambling time.

To quantify these effects, we note that the growth of operators in ≥ 1 D RUCs is predicted to fall in the Kardar–Parisi–Zhang (KPZ) universality class [127, 187]. In 1D, fluctuations in the light cone boundary have been verified numerically to have a growing width $\sim t^\alpha$ with the KPZ growth exponent $\alpha = 1/2$ [187]. This implies that the contribution of the boundary

to the size width is $\delta S_{\text{boundary}} \propto t^{1/2}$, and the full width is

$$\delta S = \begin{cases} (\alpha_{\text{bulk}} + \alpha_{\text{boundary}})t^{1/2}, & t \lesssim t_{\text{scr}} \\ \alpha_{\text{bulk}}t_{\text{scr}}^{1/2}, & t \gtrsim t_{\text{scr}} \end{cases} \quad (3.56)$$

We note that the maximum size width relative to the late-time size width is a constant set by $(\alpha_{\text{bulk}} + \alpha_{\text{boundary}})/\alpha_{\text{bulk}}$. Comparing the size width of multiple system sizes, we observe excellent agreement with predicted scalings over a wide range of system sizes (Appendix B.5).

The time profile of the size width is directly observable in the peaked-size teleportation fidelity if we scale $g \sim t_{\text{scr}}^{1/2} \sim N^{1/2}$. In particular, by setting N/g to lie between the maximum size width and the late time size width, we observe a distinct decay-revival profile for the teleportation fidelity (Fig. 3.3). At early times, we observe successful teleportation with an oscillating fidelity. The fidelity decays slowly, as a power law in time, as it receives corrections proportional to the growing size variance $\sim g^2 \delta \mathcal{S}^2 / N^2$. After the scrambling time, we see a revival in the teleportation fidelity as the size width narrows. The lack of a parametric separation between the maximum and late time size widths means that late time teleportation will also have some finite error for this value of g .

In 2D, we find that the scaling of the size width also matches predictions from the KPZ universality class. In this case, the width of the boundary scales as $\sim t^\alpha$, with $\alpha = 1/3$ [187]. However, to calculate the boundary's contribution to the size width, one must take into account two additional considerations. First, the boundary is 1-dimensional, so its length trivially grows in time as $\sim t$. Second, fluctuations of the boundary are expected to have a finite correlation length, $\xi \sim t^{1/z}$, where $z = 3/2$ is the KPZ dynamic exponent [59]. Thus, the boundary can be modeled as $n_\xi \sim t/\xi = t^{1/3}$ uncorrelated regions, each of length ξ . Each region contributes $\sim \xi t^\alpha$ to the size width; adding the uncorrelated contributions from all regions yields a total size width $\delta \mathcal{S} \sim \sqrt{n_\xi} \xi t^\alpha = t^{1/6+2/3+1/3} = t^{7/6}$.

The time profile of the size width in 2D is thus given by

$$\delta S = \begin{cases} \beta_{\text{bulk}}t + \beta_{\text{boundary}}t^{7/6}, & t \lesssim t_{\text{scr}} \\ \beta_{\text{bulk}}t_{\text{scr}}, & t \gtrsim t_{\text{scr}} \end{cases} \quad (3.57)$$

We confirm these scalings in our numerics (Fig. 3.2(b) and Appendix B.5). Notably, the size width is now dominated by the boundary contribution at intermediate times, such that the ratio of the maximum size width to the late time size width scales as $t_{\text{scr}}^{1/6} \sim N^{1/12}$. As in 1D, one can probe this behavior using the peaked-size teleportation fidelity, now with $g \sim N/t_{\text{scr}}^{7/6} \sim N^{5/12}$. We emphasize that in 2D, the scaling of the size width is determined by *correlations* between different points on the light-cone boundary. This goes beyond the behavior studied in previous works on RUCs, which focus on quantities probed by local OTOCs.

0D random unitary circuits

We now turn to random unitary circuits in zero dimensions, a prototypical model for ‘fast scramblers’ [111, 226]. These circuits are constructed as follows: at each time-step,

we partition the N qubits into randomly chosen pairs, and apply independent Haar random 2-qubit unitaries to each pair.

Below we analyze such circuits using theoretical arguments, in combination with numerical simulations via Clifford circuits. As the later parts of our analysis are rather technical, we briefly summarize the main results: (i) peaked size teleportation remains possible but only if the input state is initially encoded in non-local, p -body operators; (ii) even though there is no complete separation of operator light cones, size addition still occurs at intermediate times in a probabilistic sense and enables multi-qubit teleportation; and (iii) the maximum channel capacity is linear in the number of coupled qubits, K . These results are depicted numerically in Fig. 3.2(c) and 3.4.

Peaked sizes—In all-to-all coupled systems, operators are generally expected to grow exponentially in time, $\mathcal{S} \sim e^{\lambda t}$, where λ is the Lyapunov exponent [226]. The reason is simple: at each time step, every term in an operator—rather than just those on a ‘light-cone’ boundary—has a fixed probability of spreading under random pairwise unitaries. A somewhat less intuitive expectation is that the size width also generally grows exponentially [202]. One way of understanding this is by imagining two realizations of the dynamics: in one realization the initial operator doubles at the first time and in the other it does not. In effect, the latter system now lags behind the former by one time step, Δt , and the difference in their sizes at later times will be exponentially magnified, to $e^{\lambda t}(1 - e^{-\lambda \Delta t})$.

The lack of separation between the size and size width seems to preclude the possibility of peaked-size teleportation at intermediate times. Nevertheless, we can engineer such a separation by *encoding* the information of each input qubit into p -body operators, with $p \gg 1$ [88]. As an example, consider encoding a single qubit into $p = 5$ qubit operators via

$$\begin{aligned}
 E(X \otimes \mathbb{1} \otimes \mathbb{1} \otimes \mathbb{1} \otimes \mathbb{1})E^\dagger &= Z \otimes X \otimes X \otimes Y \otimes Z \\
 E(Y \otimes \mathbb{1} \otimes \mathbb{1} \otimes \mathbb{1} \otimes \mathbb{1})E^\dagger &= Y \otimes Z \otimes Z \otimes X \otimes Y \\
 E(Z \otimes \mathbb{1} \otimes \mathbb{1} \otimes \mathbb{1} \otimes \mathbb{1})E^\dagger &= X \otimes Y \otimes Y \otimes Z \otimes X,
 \end{aligned} \tag{3.58}$$

Here, E is a Clifford unitary encoding operation that conjugates state insertion and decoding [explicitly, replacing $U \rightarrow UE, U^* \rightarrow U^*E^*$, and $U^T \rightarrow E^T U^T$ in Fig. 6.1(a)]. The success of teleportation is now dependent on the size distributions of time-evolved p -body operators, $Q_A(t) = UEP E^\dagger U^\dagger$, where P runs over the initial unencoded single-qubit Pauli operators. As we will soon verify explicitly, before the scrambling time the support of each of the p operators composing Q_A will be approximately non-overlapping, so that their size distributions will convolve. Thus, the total operator size is multiplied by a factor of p but, through the central limit theorem, the size width is multiplied only by \sqrt{p} .

In more detail, consider the size growth of an operator, Q_A , with initial size $\mathcal{S}_0 = p$. During a single time step, each qubit i in the support of $Q_A(t)$ is paired with another random qubit; for simplicity, we assume the second qubit is outside the support of $Q_A(t)$, which should be valid at times well before the scrambling time. Under random two-qubit Clifford time-evolution, $Q_A(t)$ grows to have support on both qubits with probability $\nu = 1 - 2(d^2 - 1)/(d^4 - 1)$ (9/15 for qubits). The operator size, \mathcal{S}_t , therefore grows stochastically

in time, according to

$$\begin{aligned}
 \mathcal{S}_{t+1} &= \mathcal{S}_t + \sum_{i=0}^{\mathcal{S}_t} s_i \\
 &= \mathcal{S}_t + \text{Bi}_t(\mathcal{S}_t, \nu) \\
 &\approx (1 + \nu)\mathcal{S}_t + \sqrt{\mathcal{S}_t\nu(1 - \nu)} \mathcal{N}_t(0, 1)
 \end{aligned} \tag{3.59}$$

where each s_i is a binary random variable that increases the size by 1 with probability ν and 0 with probability $1 - \nu$, and $\text{Bi}_t(\mathcal{S}_t, \nu)$ denotes the binomial distribution with \mathcal{S}_t trials and probability ν , which we can approximate as a normal distribution, $\mathcal{N}_t(\nu\mathcal{S}_t, \sqrt{\mathcal{S}_t\nu(1 - \nu)})$. The size at time t can thus be written as a sum of random variables drawn at each time step:

$$\begin{aligned}
 \mathcal{S}_t &\approx (1 + \nu)^t p \\
 &+ \sqrt{\nu(1 - \nu)} \sum_{t'=0}^{t-1} (1 + \nu)^{t-t'-1} \sqrt{\mathcal{S}_{t'}} \mathcal{N}_{t'}(0, 1)
 \end{aligned} \tag{3.60}$$

from which we see that the average size grows exponentially in time with Lyapunov exponent $e^\lambda = 1 + \nu$. Deviations arise at each time step t' , with typical magnitude $(1 + \nu)^{t-t'-1} \sqrt{\mathcal{S}_{t'}} \approx (1 + \nu)^{t-1-t'/2} \sqrt{p}$. Since this decays exponentially in t' , we can approximate the total variation, $\delta\mathcal{S}_t$, as the largest term in the sum ($t' = 0$), which has magnitude

$$\delta\mathcal{S}_t \sim (1 + \nu)^{t-1} \sqrt{p} \approx \frac{\mathcal{S}_t}{\sqrt{p}}. \tag{3.61}$$

As anticipated, the size width is dominated by early time errors that have exponentially grown in time, so that the ratio of the size width to the size remains constant at $\sim 1/\sqrt{p}$ (after some period of growth from its initial value, 0).

To support these claims, we numerically simulate the time-evolved size distribution of operators with an initial size $p \approx 1000$ [Fig. 3.2(c)]. As expected, we observe that the average size grows exponentially as $\sim pe^{\lambda t}$ and saturates at a timescale $t^* \sim \log(N/p)$. Moreover, the size width grows at the same exponential rate but its magnitude is suppressed by a factor of \sqrt{p} compared to the average size.

To verify that this allows for teleportation, we next compute the fidelity for teleporting a single qubit, in the regime $g \gg 1$. As shown in Fig. 3.2(c), teleportation occurs with near perfect fidelity beginning at $t \approx t^* - \log(gp)$, corresponding $g\mathcal{S}/N \approx 1$. Thereafter, the teleportation fidelity decreases exponentially in time, consistent with the increase of the size width. At time $t \approx t^* - \log(g\sqrt{p})$, teleportation stops succeeding entirely, since the size width has reached the limit $\delta\mathcal{S}/N \sim 1$. Finally, at late times $t \approx t^* - \log(p)$, the fidelity revives as the system becomes fully scrambled and the operator size width narrows to $\delta\mathcal{S} \sim \sqrt{\mathcal{S}}$.

Size addition—We now turn to the possibility of teleporting multiple qubits in 0D RUCs. Within the peaked-size regime, this reduces to the question of whether operator sizes add according to Eq. (3.54). Satisfying this requirement in all-to-all coupled systems is not as

trivial as in $\geq 1D$, since time-evolved operators typically act on overlapping subsystems at any finite time. Nevertheless, we now provide a simple argument for why size addition holds despite this.

To do so, we model each time-evolved Pauli operator $Q_i(t)$ as an independent random Pauli string of size $\mathcal{S}[Q_i]$. Consider two such strings, P_1 and P_2 , with support on regions A_1 and A_2 and sizes $\mathcal{S}[P_1] = |A_1|$ and $\mathcal{S}[P_2] = |A_2|$. The size of the product, P_1P_2 , is the size of the union $A_1 \cup A_2$, minus the number of sites where the two strings overlap and have the same single-qubit Pauli operator. This occurs with probability $1/(d^2 - 1) = 1/3$ at each site in the region $A_1 \cap A_2$, giving

$$\begin{aligned} \mathcal{S}[P_1P_2] &\approx |A_1 \cup A_2| - \frac{1}{3}|A_1 \cap A_2| \\ &= \mathcal{S}[P_1] + \mathcal{S}[P_2] - \frac{4}{3}|A_1 \cap A_2|. \end{aligned} \tag{3.62}$$

The deviation from the simple additive rule $\mathcal{S}[P_1P_2] = \mathcal{S}[P_1] + \mathcal{S}[P_2]$ is thus controlled by $|A_1 \cap A_2|$. If the Pauli strings P_1, P_2 have independently random areas of support, the size of this intersection scales as:

$$|A_1 \cap A_2| \sim \mathcal{S}[P_1]\mathcal{S}[P_2]/N, \tag{3.63}$$

which is subleading to $\mathcal{S}[P_i]$ at intermediate times (when $\mathcal{S}/N \ll 1$). To derive this, note that the probability for *both* strings to have support on a given qubit is $\sim (\mathcal{S}[P_1]/N)(\mathcal{S}[P_2]/N)$; summing over N qubits gives the above result.

For n -qubit teleportation, one must consider the combined size, $\mathcal{S}[P_1 \dots P_m]$, of m independent Pauli strings, where m takes a typical value $m \approx 3n/4$ (a typical n -qubit operator has non-identity support on $3n/4$ qubits). In general, this quantity will receive corrections from $\binom{m}{k}$ different k -way intersections of the strings, for all $2 \leq k \leq m$. For random Pauli strings, the expected size of these intersections scales as $N|A_1 \cap \dots \cap A_k| = \prod_{i=1}^k \frac{|A_i|}{N} \sim \mathcal{S}^k/N^{k-1}$, where $\mathcal{S} \sim |A_i|$ is the typical size of a single Pauli string [see Eq. (3.63) above]. For a given k , the correction to size addition will be the sum of $\binom{m}{k} \sim m^k$ different intersections and therefore scales as $m\mathcal{S}(m\mathcal{S}/N)^{k-1}$. These corrections can be neglected if they are small compared to the total size; this occurs when $m\mathcal{S} \ll N$, which corresponds to a timescale much less than the scrambling time.

To demonstrate this claim, we numerically simulate the teleportation protocol with $n > 1$ qubits in the regime $1 \ll p, np \ll K$ [Fig. 3.4]. Analogous to single-qubit teleportation, the teleportation fidelity exhibits oscillations beginning at $t \approx t^* - \log(gp)$, and vanishes at $t \approx t^* - \log(g\sqrt{pn})$ due to the growth of the combined size width. However, in contrast to the single-qubit case, teleportation of multiple qubits is not possible at late times, $t \gtrsim t^* - \log(gpn)$, as predicted in Section 3.6. Interestingly, between these two regimes, we observe a partial revival of the fidelity: this indicates that the operator size widths begin to narrow before the additive condition is completely invalidated.

Error analysis—While we have confirmed that multi-qubit teleportation can be achieved in certain ideal limits, a key question remains: how does the maximum number of qubits that

can be teleported scale as a function of K , i.e. what is the protocol's channel capacity? To answer this question, we now estimate how deviations from these ideal limits lead to errors in peaked-size teleportation and ultimately constrain the channel capacity. Throughout this discussion, we assume that the size, \mathcal{S} , is extensive, but K is not; this is the natural regime for probing the channel capacity of the protocol at intermediate times, and is the physical scenario in the context of traversable wormholes [176]. The details of this and the following subsection are quite technical in nature, and may be skipped by most readers.

In summary, we identify four distinct sources of error in the multi-qubit teleportation fidelity, $F = 1 - \epsilon$:

1. Errors due to finite p : $\epsilon \sim ng^2\mathcal{S}_K^2/K^2p$
2. Errors due to finite K : $\epsilon \sim ng^2\mathcal{S}_K/K^2$
3. Errors due to imperfect size addition: $\epsilon \sim [n^2g^2\mathcal{S}_K^4/K^4 + \dots]$, where ellipses indicate higher orders in $(n\mathcal{S}_K/K)^2$
4. Errors due to fluctuations in size addition: $\epsilon \sim [n^2g^2\mathcal{S}_K^2/K^3 + \dots]$, where ellipses indicate higher orders in $n\mathcal{S}_K/K$

We discuss each of these errors in detail below.

The first and second sources of error are due to imperfectly peaked K -size distributions. The K -size width receives contributions from finite- p corrections, $\sim \mathcal{S}_K/\sqrt{p}$, and finite- K corrections, $\sim \sqrt{\mathcal{S}_K}$ [see the discussion below Eq. (3.34)]. To translate these into errors in the teleportation fidelity, we multiply the size width by g/K and take the square. This gives fidelity errors $\sim g^2\mathcal{S}_K^2/pK^2$ and $\sim g^2\mathcal{S}_K/K^2$ per teleported qubit.

The third and fourth sources of error arise from imperfect size addition. This leads both to 'systematic' errors, due to the average overlap of operators, as well as 'sampling' errors, due to random fluctuations in this overlap. We begin with the systematic errors: as we recall, the size addition of m time-evolved operators receives corrections from k -way overlaps of the operators, each scaling as $\sim m\mathcal{S}_K(m\mathcal{S}_K/K)^{k-1}$, for $2 \leq k \leq m$ (rescaling our previous results to the K -size instead of the size). The nonlinear dependence on m indicates that sizes do not add perfectly. Nevertheless, when teleporting an n -qubit initial state for large n , we can correct for the above effect at leading order by using a linear approximation for m^k about its typical value, $(3n/4)^k$. This leads to an effectively smaller operator size, which can be observed in the reduced frequency of the fidelity oscillations for 10-qubit teleportation compared to 1-,3-qubit teleportation in Fig. 3.4(a). The leading errors after this shift are quadratic in $\delta m \equiv m - 3n/4$, which has a typical magnitude $\delta m \sim \sqrt{n}$. Multiplying by g/K and taking the square, we therefore find multi-qubit fidelity errors $\sim (g\mathcal{S}_K/K)^2(n\mathcal{S}_K/K)^{2k-2}$; at leading order $k = 2$, this gives $\sim n^2g^2\mathcal{S}_K^4/K^4$.

Finally, each intersection above is subject to additional random fluctuations about its average value. When operator sizes are much smaller than the system size, we can treat each intersection as arising from a binomial process, in which case fluctuations are proportional to the square root of the intersection's average size (see Appendix B.6 for a detailed

accounting). These add in quadrature for $\sim n^k$ overlaps, producing a total fidelity error $\sim (g^2/K)(n\mathcal{S}_K/K)^k$.

Channel capacity— To define the channel capacity of the teleportation protocol, we fix a per qubit error threshold ϵ_{th} , and determine the maximum number of qubits that can be sent while maintaining a multi-qubit fidelity above this threshold¹¹, i.e. $F \geq 1 - n\epsilon_{\text{th}}$. We are interested in how the channel capacity scales with the number of couplings, K , while allowing both g and \mathcal{S}_K (determined by the evolution time) to vary.

In 0D RUCs, all errors increase with g , so it is optimal to set g to its minimal value, $\eta_{\text{dg}}\mathcal{S}/N = \pi$. This gives a per qubit error

$$\frac{\epsilon}{n} \sim \frac{1}{p} + \frac{1}{\mathcal{S}_K} + \left[\frac{n\mathcal{S}_K^2}{K^2} + \dots \right] + \left[\frac{n^2}{K} + \dots \right]. \quad (3.64)$$

The first term is negligible in the large p limit and so we will neglect it from here on.

We minimize the remaining terms with respect to \mathcal{S}_K . There are two relevant regimes. For $n \lesssim \sqrt{K}$, the minimum is determined entirely by the leading order contributions in $n\mathcal{S}_K/K$ to the error (i.e. neglecting the ellipses). Taking the derivative and setting to zero, we have the minimum at $\mathcal{S}_K^{(1)} \sim K^{2/3}/n^{1/3}$. As we increase n , the optimal size approaches the value $\mathcal{S}_K^{(2)} \sim K/n$. At this point, size addition errors of all orders (i.e. the ellipses) become large, and so the true minimum becomes fixed just below $\mathcal{S}_K^{(2)}$. This crossover between these two minima occurs at $n \sim \sqrt{K}$, at which $\mathcal{S}_K^{(1)} \sim \mathcal{S}_K^{(2)}$.

The above minima give two distinct scalings for the per qubit error and thus the channel capacity. The first minimum has a per qubit error $\epsilon^{(1)}/n \sim (n/K^2)^{1/3}$, which gives rise to a superlinear channel capacity, $n \lesssim \epsilon_{\text{th}}^3 K^2$. However, as we increase K , this capacity eventually surpasses the value \sqrt{K} . Above this, the optimal size is given by the second minimum, which has an error $\epsilon^{(2)}/n \sim n/K$, and thus the channel features an asymptotically linear capacity,

$$n \lesssim \epsilon_{\text{th}} K. \quad (3.65)$$

This is a stronger instance of the strict general bound Eq. (3.55). Intuitively, this channel capacity arises because the individual K -sizes must be large, $\mathcal{S}_K \gg 1$, for the K -size to be tightly peaked, while at same time the combined K -size must be much smaller than K , $n\mathcal{S}_K \ll K$, for the K -sizes to add; hence $n \ll K$.

We test this scaling numerically by simulating the teleportation protocol and measuring the per qubit fidelity, $F_{\text{EPR}}^{(1)}$, as a function of n and K . Specifically, for each value of K , we sweep the number of qubits n and determine the maximum qubits that can be sent before the infidelity exceeds a threshold, $1 - F_{\text{EPR}}^{(1)} = \epsilon_{\text{th}}$. These results are shown in Fig. 3.4(b) and exhibit a clear linear trend across two orders of magnitude, confirming our prediction of a linear channel capacity.

¹¹We note that this definition of channel capacity differs from more conventional definitions [189]; we do not expect this difference to qualitatively affect the scaling of the channel capacity with K , as the fidelity drops off steeply above the capacity [Fig. 3.4(b)].

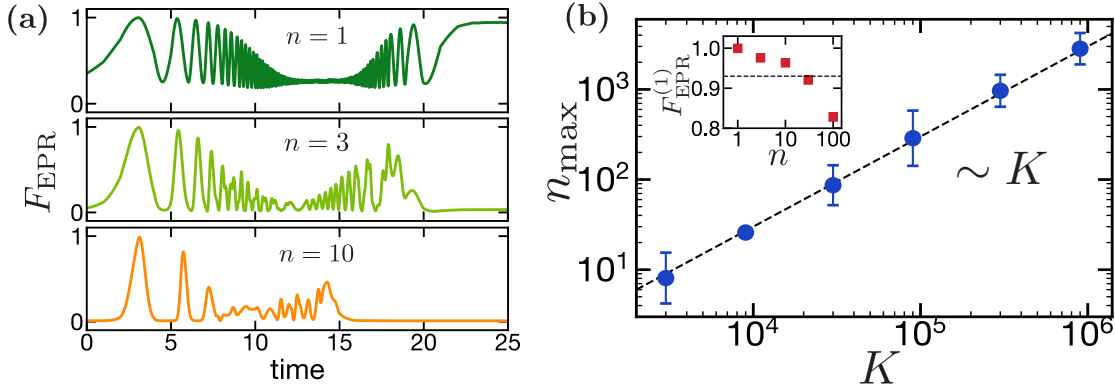


Figure 3.4: Teleportation of multiple qubits in 0D RUCs. **(a)** Many-body teleportation fidelity, F_{EPR} , as a function of time for teleporting $n = 1, 3, 10$ qubits with fixed coupling strength ($g = 177\pi$). Compared to a single qubit, the decay-revival profile for multiple qubits is shifted to earlier times, since multi-qubit operators both have a larger size width and saturate the system size earlier. Moreover, multi-qubit teleportation is not possible at late times, resulting in a trivial late-time fidelity (Sec. 3.6). **(b)** Numerical results for the channel capacity n_{max} as function of the number of coupled qubits K , which exhibit a clear linear scaling. To determine the channel capacity, we compute the maximum *per qubit* fidelity $F_{\text{EPR}}^{(1)}$ for a fixed number of qubits, n , and couplings, K , while allowing the coupling strength, g , and evolution time to vary. For fixed K , $F_{\text{EPR}}^{(1)}$ decreases as the number of qubits n is increased, as depicted in the inset for $K = 9000$. The channel capacity n_{max} is defined as the maximum number of qubits for which the fidelity is above a fixed threshold (dashed line).

A few final remarks are in order. First, while in principle the per qubit fidelity can be calculated by taking the n^{th} root of the full n -body fidelity, this approach is numerically unstable for large n . Thus, we instead compute the fidelity of a *single* qubit, while trying to send multiple qubits, using an approach derived in Appendix B.5. This amounts to performing a sum analogous to Eq. (3.44), but only including pairs of Q_1 and Q_2 that are equal on all sites except for one.

Second, the range of system parameters that lie within the linear scaling regime is ultimately constrained by the finite total system size, $N = 10^8$. In particular, to maximize the linear scaling regime, we choose $p = 101$ and $\epsilon_{\text{th}} = 0.07$. The former ensures that finite- p errors are negligible, while the latter allows the number of qubits at the threshold to be large enough to access the $n \gtrsim \sqrt{K}$ regime but small enough that the operators are initially dilute, i.e. $n \ll N/p$.

Large- q SYK model: infinite temperature

We now demonstrate peaked-size teleportation in a 0D Hamiltonian system, the large- q SYK model, at infinite temperature. While teleportation at low temperatures in the SYK model is known to succeed via the gravitational mechanism, teleportation at infinite temperature was discovered only recently [88]. In addition to showing that this mechanism is in fact peaked-size teleportation, we also find that, remarkably, *all* qualitative aspects of this teleportation match those of 0D RUCs.

The large- q SYK model is defined by the Hamiltonian [173, 202]:

$$H = i^{q/2} \sum_{1 \leq j_1 \leq \dots \leq j_q} J_{j_1, \dots, j_q} \psi_{j_1} \dots \psi_{j_q}, \quad (3.66)$$

where ψ_i are Majorana fermions, $\{\psi_i, \psi_j\} = 2\delta_{ij}$, and the couplings are drawn independently from a Gaussian distribution with zero mean and a variance $\langle J_{j_1, \dots, j_q}^2 \rangle = J^2/2q \binom{N-1}{q-1}$. This model is exactly solvable at all temperatures in the large- q , large- N limit [173, 202].

To construct the teleportation protocol for the SYK model, we first define the N -fermion EPR state,

$$\psi_{j,l} |\text{FEPR}\rangle \equiv -i\psi_{j,r} |\text{FEPR}\rangle, \quad \forall j = 1, \dots, N \quad (3.67)$$

From this, the TFD state is obtained as before,

$$|\text{TFD}\rangle \equiv e^{-\beta H_l/2} |\text{FEPR}\rangle. \quad (3.68)$$

For the two-sided coupling, we consider the simple bilinear interaction,

$$V = \frac{1}{2qN} \sum_{j=0}^N i\psi_{j,l}\psi_{j,r}, \quad (3.69)$$

which measures the size of operators in the Majorana string basis, divided by qN [202, 208].

As in 0D RUCs, the size and size width of time-evolved operators in the SYK model increase exponentially in time, and exhibit a large separation only when initially encoded in p -body operators. To see this, we can generalize previous computations of size distributions in the large- q SYK model [202] to initial p -body operators, $\psi = \psi_1\psi_2 \dots \psi_p$; this relies on the factorization of SYK correlation functions in the large- N limit [88]. After the relaxation time ($t \gtrsim 1/J$), but before the scrambling time ($t \lesssim \log(N/p)/J$), the size and size width are:

$$\mathcal{S} \approx \frac{p}{2} e^{2Jt}, \quad \delta\mathcal{S} \approx \frac{\sqrt{2qp}}{4} e^{2Jt}. \quad (3.70)$$

The scaling $\delta\mathcal{S} \sim \mathcal{S}/\sqrt{p}$ matches that found for 0D RUCs; in particular, ensuring a large separation between the size and size width requires $p \gg q$. Note that our condition for peaked size distributions depends on the (large) parameter q , through the size width.

This large separation suggests that peaked-size teleportation is possible at early times in the large- p limit. To verify this, we analyze the two-sided correlator, which is given by [90]

$$\begin{aligned} C_\psi(t) &= \langle e^{-igV} \psi_r(-t) e^{igV} \psi_l(t) \rangle \\ &= \left(\frac{1}{1 + i \frac{g}{N} \frac{1}{4} e^{2Jt}} \right)^{2p/q} \end{aligned} \quad (3.71)$$

at infinite temperature before the scrambling time¹². For large p and early times, we can approximate the correlator as

$$C_\psi(t) \approx \exp\left(-i \frac{g}{qN} \frac{p}{2} e^{2Jt}\right), \quad (3.72)$$

using $(1 + ix)^m \approx e^{imx}$, valid when $mx^2 \equiv \frac{2p}{q} \left(\frac{g}{N} \frac{1}{4} e^{2Jt}\right)^2 \ll 1$. We refer to this regime as the “early time regime”, and analyze its analog in large- N systems at finite temperature in Section 3.8.

Crucially, as expected for peaked-size teleportation, the early time correlator consists of an overall phase equal the average operator size, Eq. (3.70), multiplied by g/qN . This indicates that teleportation succeeds with nearly maximal fidelity beginning when $g\mathcal{S}/qN \approx 1$. Based on its similarity with 0D RUCs, we expect that teleportation in this regime is capable of teleporting $\mathcal{O}(K)$ qubits (Table 3.1); however, we do not calculate this explicitly. Teleportation continues to succeed until the above approximation breaks down, which occurs when the size width, $\delta\mathcal{S}$, becomes of order $(g/qN)^{-1}$. As for all scrambling systems, the two-sided correlator is expected to revive at late times, $t \gtrsim \log(N/p)/J$, at which point the sizes saturate the entire system [90, 176] (see Section 3.6); this is not reflected in Eq. (3.71), which is valid only before the scrambling time.

3.8 Interplay between peaked-size and gravitational teleportation

In this section, we seek to understand the interplay between peaked-size and gravitational teleportation. A central theme in this understanding is a comparison between the size distribution introduced in Section 3.4, and the *winding size distribution* introduced in Ref. [44, 188].

To illustrate the distinction between these distributions, consider a time-evolved Majorana fermion operator, decomposed in a basis of Majorana strings, χ [202, 208]:

$$\psi(t)\rho^{1/2} = \sum_{\chi} c_{\chi}\chi. \quad (3.73)$$

¹²The inclusion of e^{-igV} in the correlator applies a phase e^{-ig} to the bra on the left side, which conveniently subtracts off the constant term in V 's relation to operator size [Eq. (3.25)].

From this decomposition, one defines the size distribution [202, 208],

$$P(\mathcal{S}) = \sum_{\chi: \mathcal{S}[\chi]=\mathcal{S}} |c_\chi|^2, \quad (3.74)$$

and the winding size distribution [44, 188],

$$f(\mathcal{S}) = \sum_{\chi: \mathcal{S}[\chi]=\mathcal{S}} c_\chi^2, \quad (3.75)$$

where $\mathcal{S}[\chi]$ is the size of the string χ . Note that the size distribution is real-valued, while the winding size distribution may be complex.

The teleportation correlators [under coupling Eq. (3.69)] are, in fact, directly related to the winding size distribution [44, 188]:

$$C_\psi(t) = -i \sum_{\mathcal{S}=0}^{\infty} e^{-ig\mathcal{S}/qN} f(\mathcal{S}), \quad (3.76)$$

which can be derived by explicitly plugging Eq. (3.73) into the teleportation correlator. The size distribution, by contrast, is related to “one-sided” correlation functions, e.g. Eq. (3.31), where both instances of the time-evolved operator appear on the same side of the TFD state [202].

Despite this distinction, we have so far been able to analyze teleportation using the size distribution, as opposed to the winding size distribution, because the two are equal in two circumstances. The first is at infinite temperature, where the coefficients c_χ are real because $\psi(t)$ is Hermitian. The second has been precisely our focus: when size distributions are perfectly tightly peaked, in which case both distributions approach a delta function.

In what follows, we describe several scenarios in which the distinction between the two distributions becomes relevant. First we begin in large- N systems, where large- N factorization provides a precise relation between the teleportation correlator and the OTOC at early times. We find that, even in the presence of the large- p encoding, the correlator deviates from the peaked-size prediction whenever the OTOC contains an imaginary part. Large- N systems encompass both peaked-size and gravitational teleportation—our results suggest that the former occurs in systems where the OTOC is real (e.g. at infinite temperature with large- p encoding, see Section 3.7), while the latter occurs where the OTOC is imaginary (e.g. at low temperature in SYK) [103, 134]. Second, we review recent results showing that this deviation eventually leads an $\mathcal{O}(1)$ correlator magnitude when the winding size distribution takes a particular form, thereby enabling teleportation with unit fidelity (see Section 3.3). This is conjectured to be the microscopic origin of gravitational teleportation [44, 188], and so we expect it to occur only in low temperature models with a gravity dual. Third, we return to teleportation in the large- q SYK model and show that this model interpolates between gravitational teleportation at low temperatures and peaked-size teleportation at high temperatures. Surprisingly, this interpolation occurs despite the fact that the large- p

encoding ensures a large separation between the size and size width, i.e. the size distribution naively appears tightly peaked, even at low temperatures. Finally, motivated by this smooth interpolation, we conclude this section by searching for a ‘dual’ description of peaked-size teleportation in a bulk gravitational theory. In particular, we argue that strong stringy effects lead to the same qualitative features as peaked-size teleportation.

Early time teleportation in large- N systems

In Section 3.4, we saw that for peaked-size operators the teleportation correlator depends only on the first moment of the size distribution, i.e. the average size [Eq. (3.31)]. We will now show that a more general relationship holds for large- N systems at early times, where we substitute the average size with the first moment of the *winding* size distribution. Specifically, using Eqs. (3.9-3.14), the first moment of the winding size is given by a two-sided OTOC:

$$\text{OTOC}_2 = i \langle \text{TFD} | \psi_{1,r}(-t) V \psi_{1,l}(t) | \text{TFD} \rangle$$

$$\begin{aligned}
 &= \frac{-1}{K} \sum_{i=1}^K \text{Diagram} \\
 &= \frac{1}{K} \sum_{i=1}^K \text{tr} \left(\rho^{1/2} \psi_1(t) \psi_i \rho^{1/2} \psi_1(t) \psi_i \right)
 \end{aligned} \tag{3.77}$$

using Eqs. (3.9-3.14). This differs from the one-sided OTOC, for probing the average size [Eq. (3.31)], in terms of the placement of the thermal density matrix.

To relate the OTOC and the teleportation fidelity, we consider two simplifying assumptions. First, we focus on 0D large- N systems, e.g. the SYK model, with a p -body initial encoding. In such systems, the teleportation correlator in fact factorizes into a product of single-body correlators (up to $1/N$ corrections) [88]:

$$\begin{aligned}
 C_\psi(t) &= \langle e^{-igV} \psi_r(-t) e^{igV} \psi_l(t) \rangle \\
 &\approx \left[\langle e^{-igV} \psi_{1,r}(-t) e^{igV} \psi_{1,l}(t) \rangle \right]^p,
 \end{aligned} \tag{3.78}$$

where ψ_1 is a single-body operator.

Second, generalizing Eqs. (3.34, 3.72), we consider sufficiently early times to work at leading order in g ¹³:

$$\begin{aligned}
 C_\psi(t) &\approx e^{-igp\langle V \rangle} \left[\langle \psi_{1,r} \psi_{1,l} \rangle + ig \langle \psi_{1,r} V \psi_{1,l} \rangle + \dots \right]^p \\
 &\approx e^{-igp\langle V \rangle} \langle \psi_{1,r} \psi_{1,l} \rangle^p \left[\exp \left(igp \frac{\langle \psi_{1,r} V \psi_{1,l} \rangle}{\langle \psi_{1,r} \psi_{1,l} \rangle} \right) + \dots \right] \\
 &= (-iG_\beta)^p \exp \left(-i \frac{gp}{2q} \left[\frac{\text{OTOC}_2}{G_\beta} - G_\beta \right] \right) + \dots \\
 &= (-iG_\beta)^p \exp \left(-i \frac{gp}{2qN} G_\beta \mathcal{F}_2(t) \right) + \dots
 \end{aligned} \tag{3.79}$$

where $G_\beta = i \langle \psi_{1,r} \psi_{1,l} \rangle = \text{tr}(\rho^{1/2} \psi_1 \rho^{1/2} \psi_1)$ is the imaginary time Green's function, and $\mathcal{F}_2(t)$ is the first-order, connected component of the two-sided OTOC [Eq. (3.77)],

$$\text{OTOC}_2 \approx G_\beta^2 \left(1 + \frac{1}{N} \mathcal{F}_2(t) + \dots \right). \tag{3.80}$$

Similar to Eq. (3.34), the leading correction to Eq. (3.79) is $\sim pg^2[\langle V^2 \rangle_\psi - \langle V \rangle_\psi^2 / G_\beta]$, and the approximation holds when this is small.

Let us now consider the behavior of the teleportation correlator, Eq. (3.79), under different physical scenarios. We focus on chaotic systems during the so-called Lyapunov regime, which occurs between the thermalization time, $t \sim \mathcal{O}(1)$, and the scrambling time, $t \sim \mathcal{O}(\log N)$. In this regime, the connected OTOC is characterized by a simple exponential $\mathcal{F}_2(t) \sim e^{\lambda t}$ with a prefactor that is generally complex. As a result, we expect the teleportation correlator to exhibit two distinct effects: (i) the real part of $\mathcal{F}_2(t)$ causes rapid phase oscillations in the teleportation correlator, while (ii) the imaginary part increases/decreases the teleportation correlator magnitude, depending on the sign of the coupling g .

At infinite temperature, $\mathcal{F}_2(t)$ is strictly real and thus only effect (i) can occur. Indeed, in this case, the two-sided OTOC directly measures the operator size and Eq. (3.79) is equivalent to Eq. (3.34). It follows that peaked-size teleportation can be achieved with perfect fidelity: the teleportation correlator magnitudes are equal to one due to the infinite temperature, and their phases can be aligned by tuning g or t . More generally, at finite temperature, $\mathcal{F}_2(t)$ contains both a real and imaginary part, and the real part—which leads to effect (i)—is formally distinct from the first moment of the size distribution. Rather, recent work has shown that $\text{Re}\{\mathcal{F}_2(t)\}$ is computable via a ladder diagram identity and is physically interpreted as a ‘branching time’ [103, 268]. Here teleportation is similarly possible by tuning g or t to align the correlator phases, however the teleportation fidelity is bounded from above if the correlators do not have magnitude one (Section 3.3).

¹³In the first line, we use the fact that the thermofield double state has peaked size [202] to pull e^{-igV} outside the correlator. In the second line we use the expansion $(1 + ix)^m \approx e^{imx}$. In the third line we use $\langle V \rangle = i \langle \psi_{1,l} \psi_{1,r} \rangle / 2q = -G_\beta / 2q$.

At the opposite extreme, effect (ii) is dominant in systems with a gravity dual [103, 134] (as well as other maximally chaotic systems, e.g. maximally chaotic 2D CFTs with a large central charge [92]). In such cases, $\mathcal{F}_2(t)$ is mostly imaginary and leads to the growth (or decay) in the magnitude of the correlator. This opens the door to magnitudes *greater* than the two-point function, $|C_\psi(t)| > G_\beta$, which is not possible in peaked-size teleportation (Section 3.5). Interpolating between the two above limits, it has been conjectured that the prefactor of $\mathcal{F}_2(t)$ is proportional to $e^{i\lambda\beta/4\pi}$ [103, 134]. This would imply that the imaginary part is dominant if and only if $\lambda \approx 2\pi\beta$, i.e. the system approaches the bound on chaos [171].

Gravitational teleportation and the size-winding mechanism

We now move beyond early times and provide a brief review of how the correlator can achieve its maximal magnitude, 1, at finite temperatures. This occurs via the ‘size winding’ phenomenon introduced in Ref. [44, 188] as the microscopic mechanism for gravitational teleportation [90, 176]. We refer the reader to Ref. [188] for a complete discussion of this mechanism, including its connection to physical quantities in the bulk gravity theory. As we emphasize in Section 3.3, maximizing the magnitude of the correlators is necessary for high fidelity teleportation, but it is not sufficient: we must also align the correlator phases, for every operator on the subspace to be teleported.

To begin, note that the winding size distribution is normalized to the two-point function, $G_\beta \leq 1$, in contrast to the size distribution, which is normalized to 1. From Eq. (3.75), we see that this norm being less than one implies that the phases of the coefficients c_χ are not perfectly aligned for different strings χ . It is convenient to separate this misalignment into two classes: first, when coefficients of strings of the same size \mathcal{S} are misaligned, which manifests in the magnitude of $f(\mathcal{S})$ being less than maximal for a given \mathcal{S} , and second, when the phases of $f(\mathcal{S})$ for different sizes \mathcal{S} do not align with each other.

We focus on the latter case and, more specifically, consider an ansatz in which the coefficients’ phases *wind* with the size [44, 188]:

$$c_\chi = e^{-i\alpha\mathcal{S}[\chi]/q}|c_\chi|, \quad (3.81)$$

In this case, the coupling of the teleportation protocol, by applying a phase that is also proportional to the size, can serve to unwind the phases of $f(\mathcal{S})$ at the value $g/N = -2\alpha$ [see Eq. (3.76)]. This increases the teleportation correlator magnitude from its initial value, G_β , to unity. Although seemingly artificial, in the following subsection we show that this ansatz holds exactly for the SYK model at low temperatures.

Large- q SYK model: finite temperature

We now turn to explore the interplay between peaked-size and gravitational teleportation in an explicit example: the large- q SYK model at finite temperature and large- p encoding [202]. Despite the fact that this model features a large separation between the size

and size width, we show that teleportation is *not* governed by the peaked-size mechanism at low temperatures, due to the presence of strong size winding.

To begin, let us consider the finite-temperature teleportation correlator, given by [88]:

$$C_\psi(t) = (-iG_\beta)^p \left(\frac{1}{1 - \frac{g}{N} \frac{J}{2\lambda} e^{\lambda t} \sin(\lambda\beta/4) + i \frac{g}{N} \frac{1}{4} e^{\lambda t}} \right)^{2p/q}, \quad (3.82)$$

where $(G_\beta)^p = i^p \langle \psi_r \psi_l \rangle = (\lambda/2J)^{2p/q}$ is the p -body two-point function, and the Lyapunov exponent λ corresponds to the solution of

$$\beta\lambda = 2\beta J \cos(\lambda\beta/4) \quad (3.83)$$

and interpolates between $2\pi/\beta$ at low temperatures and $2J$ at high temperatures. At infinite temperature, the correlator reduces to Eq. (3.71), and follows our expectations for peaked-size teleportation (see Section 3.7). At low temperatures, where the model is known to possess a gravitational dual [133, 134, 173], the correlator behaves substantially differently; most notably, its magnitude increases from G_β^p at time zero to unity when $gJe^{\lambda t}/2\lambda N = 1$ [illustrated in Fig. 6.1(c)].

From this correlator, we can verify the two predictions made in Sections 3.8 and 3.8: (i) the early time behavior is governed by the two-sided OTOC, and (ii) the size winding mechanism is responsible for the $\mathcal{O}(1)$ peak in the correlator magnitude at low temperatures. To see the former, we expand the correlator in the early time regime:

$$C_\psi(t) \approx (-iG_\beta)^p \exp\left(-\frac{igp}{2qN} \left[i \frac{2J}{\lambda} e^{\lambda t} \sin(\lambda\beta/4) + e^{\lambda t} \right]\right). \quad (3.84)$$

Indeed, the term in the exponent is directly proportional to the connected piece of the two-sided OTOC [103],

$$\mathcal{F}_2(t) = i \frac{2J}{\lambda} e^{\lambda t} \sin(\lambda\beta/4) + e^{\lambda t}, \quad (3.85)$$

matching Eq. (3.79)¹⁴. At high temperatures this OTOC is equal to two times the operator size [Eq. (3.70)], resulting in phase oscillations, whereas at low temperatures the OTOC rotates to become predominantly imaginary, leading to an exponential growth in the correlator magnitude.

Next, to understand the role of size winding, we must analyze the full winding size distribution. We can derive this distribution by expanding the teleportation correlator in powers of $e^{-ig/qN}$ to match Eq. (3.76) [44, 188, 202]. To do so, it is convenient to consider the exact correlator (before a $g/N \ll 1$ approximation) [88, 202]:

$$C_\psi(t) = (-iG_\beta)^p \left(\frac{e^{-ig/2N}}{1 + i(1 - e^{-ig/N}) \left[\frac{J}{2\lambda} \sin(\lambda\beta/4) - \frac{i}{4} \right] e^{\lambda t}} \right)^{2p/q} \quad (3.86)$$

¹⁴More precisely, the correlator in Eq. (3.84) is missing a factor of G_β^p compared to Eq. (3.79). This same mismatch is noted in Ref. [202], and is attributed to the large- q limit utilized for the calculation, since in this limit G_β approaches 1.

Rewriting this correlator using Eq. (3.83) and the Taylor expansion,

$$\begin{aligned} & \left(\frac{1}{1 + (1 - e^{-\mu})x} \right)^{2p/q} \\ &= \frac{1}{(1+x)^{2p/q}} \sum_{n=0}^{\infty} e^{-n\mu} \binom{n + \frac{2p}{q} - 1}{n} \frac{1}{(1 + 1/x)^n}, \end{aligned} \quad (3.87)$$

and identifying the n^{th} coefficient with the winding size distribution, we have:

$$\begin{aligned} f(qn + p) &= - \frac{(-iG_\beta)^p}{\left(1 + \frac{J}{2\lambda} e^{\lambda t} e^{i\lambda\beta/4}\right)^{2p/q}} \\ &\quad \times \binom{n + \frac{2p}{q} - 1}{n} \frac{1}{\left(1 + \frac{2\lambda}{J} e^{-\lambda t} e^{-i\lambda\beta/4}\right)^n}. \end{aligned} \quad (3.88)$$

At intermediate times and large p , the distribution takes a particularly simple form,

$$f(qn + p) \approx (-iG_\beta)^p \frac{(\gamma + i2\alpha)^{2p/q}}{\Gamma(\frac{2p}{q})} n^{\frac{2p}{q}-1} e^{-\gamma n} e^{-i2\alpha n} \quad (3.89)$$

where we define the size decay rate, γ , as

$$\gamma = \frac{2\lambda}{J} e^{-\lambda t} \cos(\lambda\beta/4) = \left(\frac{\lambda}{J}\right)^2 e^{-\lambda t}, \quad (3.90)$$

using Eq. (3.83), and the size winding coefficient, α , as

$$2\alpha = -\frac{2\lambda}{J} e^{-\lambda t} \sin(\lambda\beta/4). \quad (3.91)$$

The above expression holds when $(2p/q)^2 \ll n \ll 1/\gamma^2, 1/\alpha^2$. Crucially, the distribution follows the size winding ansatz, $f(n) = |f(n)|e^{-i2\alpha n}$. Thus, we recognize that the maximum in the correlator magnitude occurs when the coupling has unwound the phases of $f(n)$, at $g/N = -2\alpha$, as expected from Section 3.8 [44, 188].

The fact that the correlator magnitude increases in time, and moreover reaches an $\mathcal{O}(1)$ value at low temperatures, is a hallmark of gravitational teleportation and signals physics outside the peaked-size regime. Naively, this result is surprising, as we expect the p -body encoding to ensure a peaked size distribution. Indeed, the average size and size width remain separated by \sqrt{p} at all temperatures [202]:

$$\mathcal{S}[\psi(t)\rho^{1/2}] - \mathcal{S}[\rho^{1/2}] \approx \frac{p}{2} \left(\frac{2J}{\lambda}\right)^2 e^{\lambda t} = \frac{2p}{\gamma}, \quad (3.92)$$

$$\delta\mathcal{S}[\psi(t)\rho^{1/2}] \approx \frac{\sqrt{2qp}}{4} \left(\frac{2J}{\lambda}\right)^2 e^{\lambda t} = \frac{\sqrt{2qp}}{\gamma}. \quad (3.93)$$

This demonstrates that our simple intuition, of judging a size distribution to be tightly peaked if the ratio between the size width and average size is small, is not always correct. Rather, in Appendix B.1, we provide a more precise condition for when peaked-size teleportation holds, and explicitly show that this condition breaks down for the SYK model at finite temperature (but remains satisfied at infinite temperature).

Let us now provide intuition for *how* peaked-size teleportation is modified by size winding at low temperatures. To this end, we express the SYK correlator in terms of the winding size distribution parameters:

$$\begin{aligned}
 C_\psi(t) &\approx (-iG_\beta)^p \frac{(\gamma + i2\alpha)^{2p/q}}{\Gamma(\frac{2p}{q})} \\
 &\times \int_0^\infty dn n^{\frac{2p}{q}-1} \exp(-\gamma n) \exp(-i[g/N + 2\alpha]n). \quad (3.94) \\
 &= (-iG_\beta)^p \left[\frac{\gamma + i2\alpha}{\gamma + i2\alpha + ig/N} \right]^{2p/q}
 \end{aligned}$$

At early times, this integral can be solved using a saddle-point approximation. At infinite temperature, the saddle point, n_s , occurs precisely at the average size, $n_s = (2p/q)/\gamma = \mathcal{S}/q$, giving the peaked-size correlator, $C_\psi = (-iG_\beta)^p \cdot \exp(-ig\mathcal{S}/qN)$. In contrast, at finite temperature, the size winding α shifts the saddle point in the imaginary direction of the complex plane, giving $n_s = (2p/q)/(\gamma + 2i\alpha)$ and a correlator $C_\psi = (-iG_\beta)^p \cdot \exp(-ign_s/qN)$. From this, we recognize the saddle point as precisely the two-sided OTOC, $n_s = \frac{p}{2q} \mathcal{F}_2(t)$.

The inclusion of the size winding in the low temperature saddle point thus has two effects. First, it contributes an imaginary part to the OTOC and thereby increases the magnitude of the teleportation correlator. More subtly, it also alters the *real* part of the OTOC. At low temperatures, $\alpha/\gamma \approx \beta J \gg 1$, and we can approximate the saddle as $n_s \approx (2p/q)/(2i\alpha) + (2p/q\gamma)(\gamma/2\alpha)^2$. Recognizing $\mathcal{S} = 2p/\gamma$, we see that the real part of the OTOC now corresponds to the average size suppressed by two factors of the ratio $(\alpha/\gamma)^2$.

Gravity with stringy effects

While the bulk of this paper approaches teleportation firmly through the lens of quantum mechanics, we would be remiss not to explore the analog of peaked-size teleportation in gravitational physics. Specifically, we would like to ask: is there a teleportation mechanism in gravitational systems that shares the same features as peaked-size teleportation? Such a connection might seem surprising, given the prevalence of peaked-size teleportation in quantum mechanical models with no apparent connection to gravity. Nonetheless, the smooth blending between gravitational teleportation and peaked-size teleportation in the SYK model suggests a positive answer.

Here, we demonstrate—in a particular gravitational geometry, AdS_2 —that an analog of peaked-size teleportation indeed occurs when strong stringy corrections [176, 230] are in-

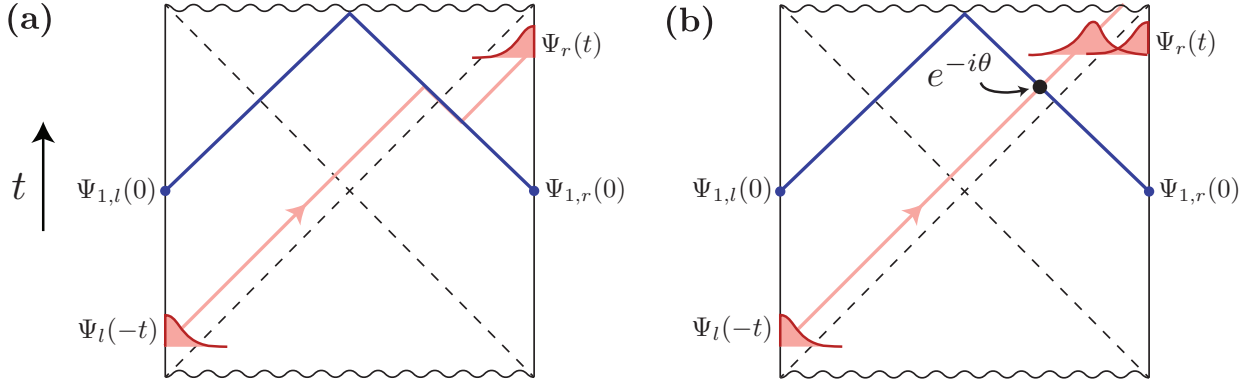


Figure 3.5: Schematic of the teleportation protocol from the bulk gravitational perspective in AdS_2 , under both **(a)** semiclassical gravity, and **(b)** strong stringy corrections. The TFD state corresponds to a two-sided black hole. Local quantum mechanical operators, $\psi_{l/r}$, create or annihilate particles near the two boundaries, with wavefunctions $\Psi_{l/r}$ (red). The protocol begins by inserting a particle on the left side, with wavefunction Ψ_l (red, bottom left), at time $-t$, which then falls towards the interior of the geometry during time-evolution (red line). The two-sided coupling, $\frac{g}{N} \sum_i \psi_{i,l} \psi_{i,r}$, is then applied, producing a shock wave (blue) that interacts with the in-falling particle [90, 176]. **(a)** In the semiclassical limit, the shock wave shifts the position the in-falling particle outside of the right horizon (dashed), which enables the particle to reemerge near the right boundary (red, top right) [90, 176]. **(b)** When stringy effects are present, the scattering amplitude between the in-falling particle and the shock wave is modified according to Eq. (3.99) [176, 230]. In the highly stringy limit and at early times, the interaction results in an overall phase shift, $\theta = gG_N A_\epsilon (\Delta/2)^\epsilon e^{\epsilon t}$ [Eq. (3.101)]. The overlap between the in-falling particle and a particle at the right boundary is nevertheless non-zero (red, top right), and is given by the unperturbed two-point function, $G_\beta = i \langle \psi_l \psi_r \rangle$. [Note that stringy effects may also modify the initial wavefunctions of $\Psi_{l/r}$, as we discuss in the context of Eq. (3.103).]

cluded in the gravitational theory¹⁵. Intuitively, our results are consistent with our previous analysis of the SYK model, where, in the dual gravitational theory, increasing the temperature is known to add stringy effects [134].

Our derivation closely follows that of Ref. [176] and assumes a background familiarity with the gravitational description of teleportation in AdS_2 (a thorough summary of which can be found in the seminal works of Refs. [90, 176]). In this setting, the teleportation correlator can be calculated explicitly by considering gravitational scattering in a wormhole geometry [Fig. 3.5]. We will maintain our SYK notation, so that V consists of K single-body fermion operators, ψ_i , and our input operator is a p -body fermion, ψ . The correlator can

¹⁵We are grateful to Zhenbin Yang and Douglas Stanford for discussions leading to this connection.

be solved for by decomposing the fermion operators in a momentum basis and applying the scattering matrix:

$$\begin{aligned}
 C_\psi^{\text{sc}}(t) &= e^{-ig\langle V \rangle} \int dk \Psi_r(k, t) \Psi_l^*(k, -t) \\
 &\times \exp \left(ig \int ds e^{i\delta(k, s)} i \Psi_{1,r}(s, 0) \Psi_{1,l}^*(s, 0) \right)
 \end{aligned}
 \tag{3.95}$$

where $\Psi_{l/r}(k, t)$ is the wavefunction for the p -body operator inserted on the left/right boundary with in-falling momentum k (and similarly $\Psi_{1,l/r}(s, 0)$ for any single-body operator in V), and $e^{i\delta(k, s)}$ is the scattering matrix element between $\psi(t)$ and $\psi_1(0)$. In pure gravity, i.e. in the absence of stringy effects, these quantities take the form [176]:

$$\Psi_r(k, t) \Psi_l^*(k, -t) = \frac{(2ike^{-t})^{2\Delta} e^{-4ike^{-t}}}{i\Gamma(2\Delta)(-k)} \Theta(-k)
 \tag{3.96}$$

$$\delta(k, s) = G_N ks
 \tag{3.97}$$

where we have set $\beta = 2\pi$ for convenience, $\Theta(x)$ is the Heavyside function, and $\Delta = p/q$ is the conformal weight of ψ . The single-body wavefunction, $\Psi_1(s, 0)$, is obtained by setting $t = 0$ and replacing $\Delta \rightarrow \Delta_1 = 1/q$ (i.e. the conformal weight of a single fermion).

In the semiclassical limit, we can evaluate the correlator by expanding $e^{i\delta}$ to linear order in G_N [176]. We find:

$$\begin{aligned}
 C_\psi^{\text{sc}}(t) &= \langle \psi_l \psi_r \rangle \frac{(-i)4^{2\Delta}}{\Gamma(2\Delta)} \\
 &\times \int_0^\infty dk (-ik)^{2\Delta-1} \exp(-i(\tilde{g}G_N e^t - 4)k),
 \end{aligned}
 \tag{3.98}$$

where $\tilde{g} \equiv g4^{-\Delta_1}\Delta_1/2$. This expression is almost identical to the large- q SYK correlator of Eq. (3.94), setting the size decay rate to zero, $\gamma = 0$, and identifying the momentum k in the gravitational calculation with the size n in the SYK model [241]. Notably, the correlator diverges at the teleportation time, $4 = \tilde{g}G_N e^t$. In bulk gravity, this divergence is exactly the light-cone pole between the left and right sides of the traversable wormhole, and is regulated by including higher order terms in G_N or stringy corrections [176].

While the full effects of stringy scattering in an AdS background are not known, we will take a phenomenological treatment as in Ref. [176, 230]. Here, the total effect of stringy corrections is to change the scattering amplitude to

$$\delta(k, s) = iG_N(-iks)^\varepsilon, \quad 0 \leq \varepsilon \leq 1,
 \tag{3.99}$$

where ε controls the strength of stringy effects, and varies from 1 in pure gravity to 0 in the highly stringy limit.

Again expanding $e^{i\delta}$ to leading order in G_N , and Wick rotating $k \rightarrow -ik$, we can write the correlator as

$$C_\psi^{\text{stringy}}(t) = \langle \psi_l \psi_r \rangle \frac{4^{2\Delta}}{\Gamma(2\Delta)} \times \int dk k^{2\Delta-1} e^{-4k} \exp(-i^{1+\varepsilon} g G_N A_\varepsilon k^\varepsilon e^{\varepsilon t}) \quad (3.100)$$

where A_ε is a constant of order 1. Note that the k -dependence in front of exponential is a Poisson distribution with a saddle point at $k_s \approx \Delta/2$ in the heavy particle limit, $\Delta = p/q \gg 1$. At early times, $e^{\varepsilon t} G_N \ll 1$, and for strong stringy effects, $\varepsilon \rightarrow 0$, the change in this saddle point from the scattering, g , is negligible. In these limits, the saddle point approximation thus gives the correlator:

$$C_\psi^{\text{stringy}}(t) \approx \langle \psi_l \psi_r \rangle \exp(-ig G_N A_\varepsilon (\Delta/2)^\varepsilon e^{\varepsilon t}), \quad (3.101)$$

which has exactly the same form as in peaked-size teleportation [Eq. (3.37)]¹⁶! Specifically, the correlator is equal to the two-point function, $G_\beta = i\langle \psi_l \psi_r \rangle$, multiplied by a pure phase. Tentatively, this suggests interpreting the phase as the operator size in a dual boundary theory. This size,

$$S/N \sim G_N A_\varepsilon (\Delta/2)^\varepsilon e^{\varepsilon t}, \quad (3.102)$$

grows exponentially in time with a non-maximal Lyapunov exponent, $2\pi\varepsilon/\beta$.

A few remarks are in order. First, while in the above treatment the strength of stringy effects depends on a ‘free’ parameter ε , we expect that in a UV complete theory ε would in turn depend on the temperature (and other physical parameters). In particular, we expect $\varepsilon \rightarrow 1$ at low temperature in theories that are dual to pure gravity, and $\varepsilon \rightarrow 0$ at high temperature, where stringy, UV effects should play an important role. This statement also follows from the point of view of the boundary field theory, since the scattering matrix is proportional to an OTOC of the boundary theory, which is real at infinite temperature.

Second, if we would like to recover the infinite temperature SYK correlator, Eq. (3.71), from the scattering computation, choosing a proper ε as a function of β is not enough. One also needs to modify the *wavefunction* of ψ , to:

$$\Psi_r(k, t) \Psi_l^*(k, -t) = \frac{\varepsilon (2ik^\varepsilon e^{-\varepsilon t})^{2\Delta} e^{-4ik^\varepsilon e^{-\varepsilon t}}}{i\Gamma(2\Delta)(-k)} \Theta(-k) \quad (3.103)$$

Such a wavefunction modification due to UV data should be model dependent, and it would be interesting to understand how to derive this ‘stringy-corrected’ wavefunction from the bulk point of view. Nevertheless, one particular feature of the modified wavefunction has a clear motivation from the boundary perspective. Specifically, Wick rotating Eq. (3.103),

¹⁶Note that the phase in Eq. (3.101) becomes order-one within the Lyapunov regime, i.e. $t \lesssim 1/\varepsilon \log(1/G_N)$, but at sufficiently early times to satisfy $G_N e^{\varepsilon t} \ll 1$. These conditions are consistent as long as $\Delta = p/q$ is sufficiently large to ensure $A_\varepsilon (\Delta/2)^\varepsilon \gg 1$.

$k \rightarrow -ik$, leads to a distribution whose width, $\delta k \sim \Delta^{1/\varepsilon}$, broadens as $\varepsilon \rightarrow 0$. This broadening increases the phase variations in the exponential of Eq. (3.100) and results in the decay of the correlator at the timescale $e^{\varepsilon t} G_N / \sqrt{\Delta} \approx 1$ for small ε . From the boundary point of view, this decay corresponds to the requirement that the size width must be small, $g\delta\mathcal{S}/N \lesssim 1$, for peaked-size teleportation, as we saw for 0D RUCs and infinite temperature SYK (Section 3.7). We expect this decay to be common to many 0D quantum systems at high temperatures, which suggests that the broadening of the bulk stringy wavefunction as $\varepsilon \rightarrow 0$ might also be a general feature.

Finally, the most obvious effect of a non-unity ε is to change the scattering phase, $\delta(k, s)$, from being real-valued to complex. Indeed, in the strong stringy limit, $\delta(k, s)$ becomes purely imaginary. In general scattering theory, a complex δ means that the scattering matrix, $e^{i\delta}$, is no longer normalized, and implies the existence of inelastic scattering [230]. Since peaked-size teleportation is replicated in the limit $\varepsilon \rightarrow 0$, this suggests a more general relationship between peaked sizes and inelastic scattering. In Appendix B.8, we demonstrate that these two phenomena also coincide at infinite temperature, for arbitrary wavefunctions and scattering amplitudes.

3.9 Experimental proposals

Having illustrated the wide breadth of physics that enters into the TW protocol, in this section we outline explicitly how one can probe this physics in the laboratory. We begin with a summary of the key signatures of teleportation, and how they can be applied towards (i) characterizing operator size distributions in generic scrambling dynamics, and (ii) distinguishing generic vs. gravitational scrambling dynamics. For (i), we show that the TW protocol can be simplified dramatically at infinite temperature, where an equivalent ‘one-sided’ protocol eliminates the need to experimentally prepare the thermofield double state. We next present two near-term experimental realizations of the protocol: first with neutral atoms and second with trapped ions. The fundamental requirement is the ability to time-evolve forwards and backwards under many-body scrambling dynamics; recent experimental progress has demonstrated this in a number of quantum simulation platforms [11, 96, 157, 180, 251]. We conclude with a discussion of the effect of experimental error, and a comparison of the TW protocol with other diagnostics of scrambling physics.

Signatures of the TW protocol

We begin by reviewing the key signatures of the TW protocol, as discussed in the previous sections and summarized in Table 3.1. We first recall that the simplest experimental signal—that is, any non-trivial teleportation fidelity of a single qubit—has already been demonstrated experimentally in the closely-related HPR protocol [35, 147]. As discussed in Section 3.6, this signifies that the implemented unitary is scrambling but does not distinguish between

peaked-size or gravitational teleportation. In what follows, we discuss two more refined applications of the TW protocol.

Characterizing size distributions in generic scrambling dynamics—The dynamics of the teleportation fidelity within the TW protocol can be used to probe the size distributions of time-evolved operators. This approach relies on the peaked-size teleportation mechanism and thus applies to generic scrambling systems, including the examples analyzed in Section 3.7 (e.g. RUCs, spin chains, high T SYK).

Specifically, the teleportation fidelity as a function of time exhibits three relevant features. First, since peaked-size teleportation relies on the *width* of the size distribution being small, $g\delta\mathcal{S}/N \lesssim 1$, its success or failure indicates whether the width has surpassed the tunable value, N/g . Depending on the model and the value of g , this leads to a temporal profile that exhibits three regimes: initial teleportation when the size width is small, no teleportation when $\delta\mathcal{S} \gtrsim N/g$, and late time teleportation once the size width converges to its small final value in a finite-size system [as depicted schematically in Fig. 6.1(c) and observed numerically in 0D RUCs in Fig. 3.2(c)].

Second, within the peaked-size regime, oscillations in the teleportation fidelity as a function of time, $F = \frac{5}{8} - \frac{3}{8} \cos(\eta_d g \mathcal{S}(t)/N)$ [Eq. (3.45)], provide a direct measurement of the growth in operator size. In particular, setting $g = 2\pi n + \pi$, one expects to see n oscillations in the teleportation fidelity before it reaches its late time plateau. The peaks in these oscillations give the operator size as a function of time: $\mathcal{S} = (m/n)(1 - 1/d^2)N$ at the m^{th} peak.

Third, the teleportation of multiple qubits demonstrates the equivalent channel capacities of peaked-size and gravitational teleportation (Section 3.7). Formally, multi-qubit teleportation probes whether the sizes of time-evolved operators *add* under operator composition. While this is trivial when the operators are causally separated, determining the requirements for size addition under more general dynamics—e.g. all-to-all or power-law interactions—remains an open question¹⁷.

Distinguishing gravitational scrambling dynamics—The TW protocol can also be used as an experimental litmus test for gravitational dynamics. To this end, we propose to use two experimental signatures that distinguish between gravitational and peaked-size teleportation: (i) the teleportation fidelity at low temperature, and (ii) the behavior of the teleportation fidelity as a function of time, t , and the coupling strength, g . For (i), the observation of a high teleportation fidelity, $\sim \mathcal{O}(1)$, at low temperatures strongly suggests the occurrence of gravitational teleportation, since the fidelity of peaked-size teleportation is limited at such temperatures by the (small) two-point function, G_β . For (ii), one observes that the qualitative profile of the teleportation fidelity as a function of time differs between the two mechanisms (see Fig. 6.1(c) for a comparison between the two, and Figs. 3.2, 3.3 for additional examples of peaked-size teleportation). Namely, keeping g fixed, the fidelity of gravitational teleportation is expected to display a single peak as a function of time,

¹⁷Indeed, recent work has indicated that, in theories with a gravitational dual, the lack of size addition is related to a scattering event among infalling particles [108].

whereas the fidelity of peaked-size teleportation is highly oscillatory in time. Furthermore, gravitational teleportation works only for a specific *sign* of the coupling, $g > 0$, while the peaked-size teleportation fidelity is an even function of g [44, 90, 176, 188].

Contrasting with finite-size effects—Finally, we would like to distinguish many-body teleportation from spurious effects that may be seen in the TW protocol at small-size systems. The most effective way to avoid such signals is by utilizing a coupling gV [Eq. (3.1)] whose individual terms have a small magnitude, i.e. $g/K \ll 1$; this is most naturally achieved by including many couplings—which requires a sufficiently large system—and setting $g \sim \mathcal{O}(1)$. In this limit, the action of the coupling is negligible unless local operators have grown significantly under many-body dynamics, i.e. $\mathcal{S} \sim K/g \gg 1$ (see Section 3.4); any teleportation signal is thus necessarily a result of scrambling dynamics. Furthermore, we expect large-size operators to generically exhibit smooth size distributions, justifying our approximation (Section 3.4) that the teleportation fidelity is governed by the distributions’ first few moments.

Away from this limit, our general framework relating the teleportation fidelity to operator size distributions remains valid [e.g. Eq.(3.26)]. However, for $g/K \lesssim 1$, we expect the fidelity to be sensitive to the discrete nature of the size distributions, and our predictions based on the first few moments may no longer apply. Fortunately, as we show in the following subsections, none of these complications are evident for experimentally relevant system sizes (e.g. $K \sim N \sim 20$) and $g \sim \mathcal{O}(1)$ coupling strengths; indeed, our finite-size numerical results agree very well with predictions from the peaked-size teleportation framework [Fig. 3.7(b) and 3.8].

Lastly, in the case where $g/K \sim 1$, operator growth is no longer necessary for the coupling to have a strong effect, leading to the possibility of a teleportation signal unrelated to scrambling. Indeed, for $g/K = \pi$, the coupling effectively ‘swaps’ the left and right qubits. This is made precise for the coupling V_s [Eq. (3.27)], where $\exp(i\pi NV_s) = (\text{SWAP})Y_l Y_r$. In this case, one would observe perfect teleportation fidelity even without many-body time evolution, i.e. $U = \mathbb{1}$; in fact, if U is perturbed away from the identity via scrambling dynamics, the teleportation fidelity would actually become suppressed. The simplest way to see this is via Fig. 6.1(a)—in particular, any subsequent time-evolution on the right side of the system is in the wrong direction to refocus the time-evolved state (one would want to apply U^\dagger after the coupling, not U^T). To achieve a large teleportation fidelity, the combined time-evolution, $U^T U$, would therefore need to preserve the “teleported” state, $\langle \psi | U^T U | \psi \rangle \sim 1$, a situation that is only likely to occur if the dynamics are non-scrambling ($U = \mathbb{1}$ is a special case of this) or undergo a late-time, fine-tuned, Poincare-type recurrence.

One-sided implementation of teleportation circuit

Before proceeding to the experimental blueprints, we first introduce a simpler implementation of the teleportation protocol that works at infinite temperature (Fig. 3.6). The outcome of this protocol is equivalent to that of the two-sided protocol (up to experimental errors), yet it eliminates the need to prepare EPR pairs and requires half as many degrees

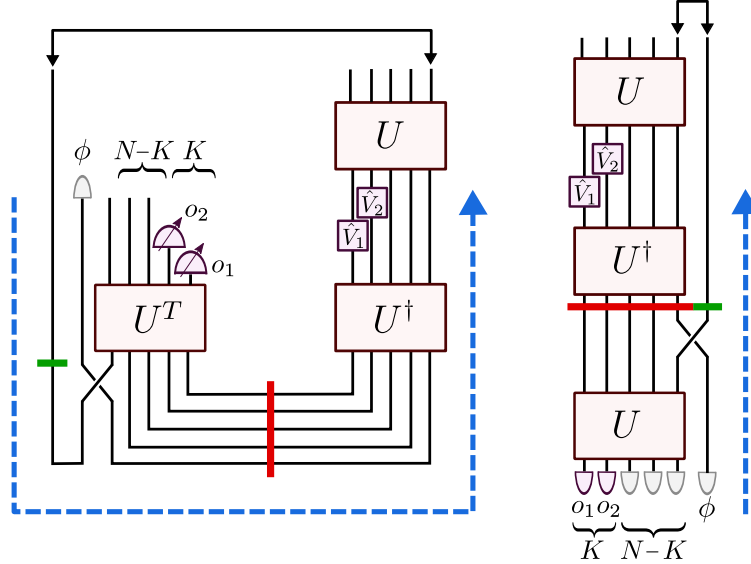


Figure 3.6: One-sided implementation (right) of the original two-sided teleportation protocol (left), derived using repeated applications of Eq. (3.9) [replacing $U \rightarrow U^T$ for convenience, compared to Fig. 6.1(a)]. Blue arrows denote the sequence of operations in the one-sided protocol, the green band marks the teleported qubit and its corresponding component in the one-sided protocol, and the red band marks the initial EPR state and its corresponding component.

of freedom. The cost of this simplification is two-fold: (i) it is restricted to simulating an infinite temperature TFD state, and (ii) it requires a higher depth quantum circuit.

We derive the one-sided implementation from the ‘two-sided’ implementation [copied in Fig. 3.6 from Fig. 6.1(a)] by sliding all operations from the left side of the many-body EPR pairs to the right side, using Eq. (3.9). The initial state of the one-sided circuit thus corresponds to the top left of the two-sided implementation. Namely, we initialize the K ‘measured’ qubits of subsystem C in a definite outcome state, $|o_1 \cdots o_K\rangle$ (purple). These states should be drawn from the distribution of measurement outcomes, but when teleporting an EPR pair at infinite temperature they will be uniformly distributed. For the $N - K$ ‘unmeasured’ qubits, we use the resolution of the identity $\mathbb{1} \propto \sum_s |s\rangle \langle s|$ to replace the unterminated legs with an initial product state in the computational basis, $|o_{K+1} \cdots o_N\rangle$ (gray). This state should be sampled from shot-to-shot over all 2^{N-K} basis states, in effect preparing a maximally mixed state on these qubits. Finally, we include one ancillary qubit for each qubit to be teleported, whose initial state is sampled over a complete basis $|\phi\rangle$ for the teleported subsystem (i.e. subsystem A in Section 3.2). Similar to the unmeasured qubits, this corresponds to the unterminated leg of the thermofield double state when we insert the teleported qubit $|\psi\rangle$ in the two-sided implementation.

Having defined an initial pure state, we now implement the circuit starting from the top left of the two-sided implementation and proceeding counter-clockwise (Fig. 3.6). The circuit consists of three successive applications of U or U^\dagger , interspersed with a swap gate exchanging subsystem A with the ancillary qubit(s), and operations $\hat{V}_i = e^{ig\sigma_i \hat{O}_i/K}$ determined by the initial state of the ‘measured’ qubits. The outcome of the circuit is an EPR measurement between the ancilla qubit and subsystem A (black arrows).

As one can see in Fig. 3.6, the one-sided implementation no longer performs teleportation, but rather prepares an EPR pair from an otherwise scrambled, many-body system. Specifically, we know that upon swapping out, subsystem A is maximally entangled with the remaining qubits whenever the unitary, U , is scrambling; the one-sided circuit distills this entanglement into an output EPR pair. This connection has been noted in gravity, where similar one-sided protocols can be interpreted as distilling the partner operators of emitted Hawking radiation [261, 262] or observing behind the horizon in the SYK model [139].

Preparing the thermofield double state

In the previous subsection, we introduced a one-sided protocol that obviates the need to prepare the highly entangled TFD state. However, this approach was restricted to infinite temperature; at *finite temperature*, one must implement the original two-sided protocol, which necessitates preparing a finite temperature TFD state. A number of recent works have explored the preparation of TFD states variationally using quantum approximate optimization algorithms (QAOA) [236, 255, 271]; we note that these preparation strategies require no additional experimental capabilities beyond those already necessary for the TW protocol. The optimization step within a QAOA-based TFD preparation relies on a cost function that requires one to measure the entanglement entropy between the two sides [255, 271]. While challenging, this can in principle be experimentally realized by either using several copies of the system [5, 63, 125] or via randomized measurements [77], both of which have been demonstrated in small-scale trapped ion experiments [46, 164].

Implementation with neutral Rydberg atoms

One particularly promising platform for implementing the traversable wormhole protocol is a quantum simulator based on neutral alkali or alkaline-earth atoms held in a reconfigurable and controllable array of optical dipole traps. Recent experiments have already achieved near-deterministic trapping and loading of atoms into arbitrary geometries in one, two, and three dimensions [19, 178, 256]. By leveraging the strong dipole coupling between atomic Rydberg states, high-fidelity analog quantum simulations and digital gates have also recently been demonstrated [29, 102, 143, 167, 178, 252]. These demonstrations have primarily used two natural schemes of encoding qubits into neutral atoms:

1. A qubit can be encoded by choosing an atomic ground state $|g\rangle$ to be the $|0\rangle$ state, and a highly excited Rydberg state $|r\rangle$ with principal quantum number $n \gg 1$ as the

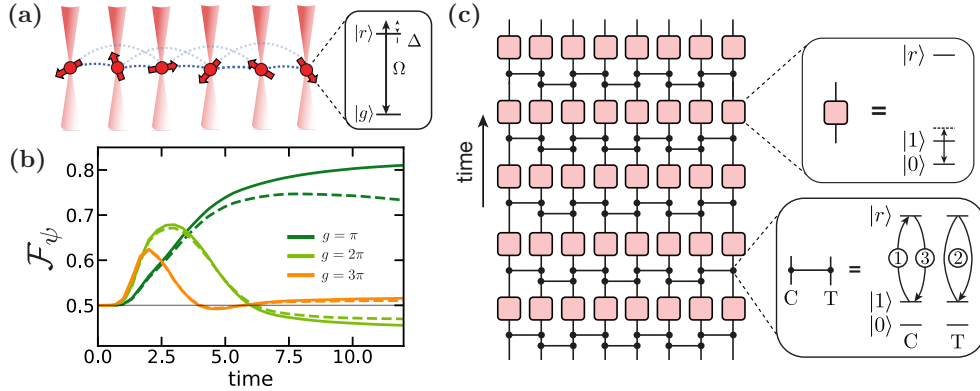


Figure 3.7: **(a)** In the proposed analog Rydberg teleportation protocol, qubits are encoded in a ground state $|g\rangle$ and a Rydberg state $|r\rangle$. Nearest-neighbor interactions (dark blue) can be time-reversed, but next-nearest neighbor interactions (light blue) cannot. **(b)** Numerical results comparing the average state teleportation fidelity for single-qubit teleportation with perfectly reversed time-evolution (solid) with the proposed, imperfect time-reversal (dashed). In particular, we implement the one-sided protocol using $N = 20$ total spins; $K = N - 1$ ‘measured’ spins (i.e. all except the spin encoding $|\psi\rangle$), whose single-qubit rotations are generated by $\hat{O}_i = \hat{Z}_i$; and time evolution under the analog Rydberg Hamiltonian [Eq.(3.104)] with parameters $\Omega_i = .9$, $\Delta_i = -1.5$, $J_0 = 1$ (for all i). **(c)** Implementation of U or U^\dagger in the digital protocol, consisting of alternating layers of controlled-phase gates (horizontal black lines) between nearest neighbor atoms and single-qubit rotations (red boxes). Here, qubits are encoded in two hyperfine ground states. Insets show possible pulse sequences to implement the controlled-phase gate and the single-qubit rotations [122]. The full TW protocol is obtained by inserting this gate sequence (and its Hermitian conjugate) in place of U , U^\dagger in Fig. 5.

$|1\rangle$ state [see Fig. 3.7(a)].

2. Alternatively, the qubit states can also be chosen as two long-lived hyperfine ground states (for alkali atoms or fermionic alkaline earth atoms) or a ground state and a metastable clock state (for bosonic alkaline earth atoms), such that the $|1\rangle$ state can be coupled to a Rydberg state to perform entangling gates [see Fig. 3.7(c)].

We will show how both encodings can be used to realize the teleportation protocol in feasible near-term experiments. We find that the first encoding is naturally suited to ‘analog’ time-evolution under the native (Ising-type) Hamiltonian for a Rydberg setup, but is limited to system sizes of $\lesssim 30 - 35$ qubits (in one spatial dimension) due to the inability to perfectly time-reverse long-range interactions. On the other hand, the second encoding is more flexible and allows for digital time-evolution including RUCs and Floquet dynamics. This time-evolution can be reversed exactly and is limited only by qubit and gate fidelities. While we

will primarily consider realizations of our protocol in experimental setups where the neutral atoms are individually trapped in optical tweezers and undergo (near-)resonant excitation to Rydberg states, we also conclude by discussing how similar physics can be seen in an optical lattice setup where the atoms are primarily in ground states $|0\rangle$ and $|1\rangle$, but one of these states is ‘dressed’ by an off-resonant laser field which couples it to a Rydberg state [99, 199, 266].

Analog implementation—We first consider the encoding where the qubit states $|0\rangle$ and $|1\rangle$ correspond to a ground state $|g\rangle$ and a highly excited Rydberg state $|r\rangle$. While neutral atoms are effectively non-interacting in their ground states, nearby atoms interact strongly via van der Waals interactions $\propto n^{11}/R^6$ if they are both in the Rydberg state, where R is the distance between the atoms. If one drives the transition $|g_i\rangle \leftrightarrow |r_i\rangle$ at each site i with tunable Rabi frequency Ω_i and detuning Δ_i [see Fig. 3.7(b)], the system will undergo analog time evolution under the Hamiltonian

$$H = \sum_i \frac{\Omega_i}{2} X_i + \sum_i \frac{\Delta_i}{2} (1 - Z_i) + \sum_{i \neq j} \frac{J_{ij}}{4} (1 - Z_i)(1 - Z_j) \quad (3.104)$$

where $X_i = |g_i\rangle\langle r_i| + |r_i\rangle\langle g_i|$, $Z_i = |g_i\rangle\langle g_i| - |r_i\rangle\langle r_i|$, and $J_{ij} = J_0/|i-j|^6$ is the van der Waals interaction strength between two atoms at positions i and j .

The Hamiltonian in Eq. (3.104) is scrambling and exhibits a scrambling time limited by the smaller of J_0 and Ω_i , $t^* \sim N/\min(J_0, \Omega_i)$. To minimize the total evolution time, we set $|\Omega_i| \sim J_0$, so that evolution under H for a time $\sim N/J_0$ implements a fully scrambling unitary U in the teleportation protocol. To implement U^\dagger , we reverse the nearest-neighbor interactions by conjugating time-evolution via Pauli operators X_i (i.e. applying π -pulses) on every other site. The tunable single-site parameters Ω_i and Δ_i are then adjusted to ensure that each single-site term is also reversed. We note that this simple scheme does *not* reverse the (much weaker) next-nearest-neighbor interactions.

In a one-dimensional array, the errors in our implementation will arise from two main sources: (i) the finite lifetime of the Rydberg state, which gives rise to a nonzero decoherence rate at each of the N sites, and (ii) the weak next-nearest neighbor interactions $\sim J_0/2^6 = J_0/64$, which cannot be time-reversed simultaneously with nearest neighbor interactions. To estimate the effect of the former, let us consider the specific case of ^{87}Rb atoms excited to the $70S$ Rydberg state [29, 143], which has a lifetime $\tau \approx 150 \mu\text{s}$. Realistically achievable Rabi frequencies and interaction strengths are of order $\sim 2\pi \times 10 - 100$ MHz. The total time to implement the three scrambling unitaries of the teleportation protocol is thus $\sim 3N/|\Omega_i|$; when summed over N qubits and compared to the Rydberg lifetime, this gives an estimated many-body error $\sim 3N^2/|\Omega_i|\tau$.

In order to precisely characterize the effects of imperfect backwards time-evolution, we perform large-scale numerical simulations of the teleportation protocol with the Rydberg Hamiltonian, Eq. (3.104) [2]. Our results are depicted in Fig. 3.7(b) for a one-dimensional chain of $N = 20$ atoms and three values of the coupling g . Analogous to our 1D RUC numerics [Fig. 3.2(a)], the fidelity increases monotonically in time for $g = \pi$; while, for

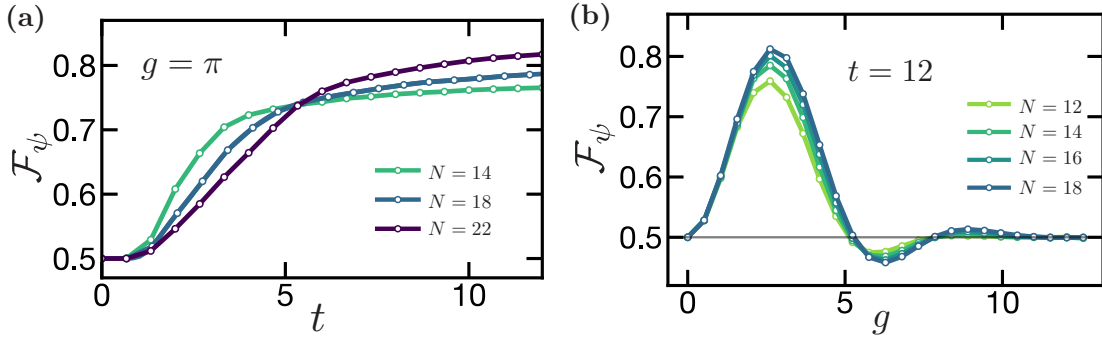


Figure 3.8: Finite-size scaling of the Rydberg simulations (a) as a function of time with $g = \pi$, and (b) as a function of coupling strength g with $t = 12$. The system was evolved under the Rydberg Hamiltonian, Eq. (3.104), with the same system parameters as in Fig. 3.7. At late times, the fidelity increases for larger systems but decreases for larger values of g . This is consistent with our error analysis in Section 3.6; in particular, we expect the error to scale as $g^2 \delta S^2 / N^2$ and the size distribution to approach a binomial distribution for which $\delta S \sim \mathcal{S} / \sqrt{N}$. In contrast, at early times, smaller systems exhibit a larger fidelity not because of the size width but because the acquired phase is $\eta_d g \mathcal{S}(t) / N$, where $\eta_d g$ is fixed and $\mathcal{S}(t)$ is initially independent of size. The curves in (a) intersect near the scrambling time due to the transition between the early and late time regimes.

$g = 2\pi$ and $g = 3\pi$, the fidelity oscillates in time, reaching a local maximum whenever the average size satisfies the phase-matching condition [Eq.(3.35)]. Notably, even with *perfect* time reversal, the overall fidelity is reduced from unity due to the finite width of the size distribution. This is a general feature of peaked-size teleportation in finite-size systems, since the relative size width scales as $\delta \mathcal{S} / \mathcal{S} \sim 1 / \sqrt{N}$ (Section 3.6). Indeed, in Fig. 3.8, we confirm that the fidelity improves with increasing system size and is consistent with our peaked-size error analysis [e.g. see Eq. (3.34)].

With *imperfect* time reversal, we observe an additional $\sim 10\%$ reduction in the fidelity compared to the ideal case at the scrambling time [Fig. 3.7(b)]. We can estimate the magnitude of this effect by assuming errors due to the next-nearest-neighbor interactions add coherently over time-intervals $\delta t \sim 1 / J_0$ (the local thermalization time), and incoherently at larger time-scales. Within each δt , each atom accumulates an error $\sim (\delta t J_0 / 64)^2$; summed over N atoms and total time $3t^* \approx 3N\delta t$, this gives a total many-body error $\sim 3N^2 / 64^2$. Thus, the error due to imperfect time reversal is magnified at larger system sizes and will eventually outweigh the improvement in fidelity from the narrowing of the size distribution.

Combined with the Rydberg lifetime error, this suggests that near-term experiments should be able to implement peaked-size teleportation in systems of $N \sim 35$ qubits. We note that in higher dimensions, the smaller relative distance of next-nearest neighbor atoms gives rise to a larger error contribution from imperfect time-reversal.

Digital implementation—To implement the protocol in larger systems, higher dimensions, and at finite temperature, we propose a digital scheme, using the second type of qubit encoding (i.e. hyperfine ground states) [Fig. 3.7(c)]. In this approach, we envision time-evolution to be formed from alternating layers of nearest-neighbor controlled-phase gates and single-qubit rotations. Here, the controlled-phase gates can be implemented by applying a simple pulse sequence to excite and de-excite qubits from the $|1\rangle$ state to the $|r\rangle$ state, so that the wavefunction acquires a phase of -1 if either of the two qubits are in the $|1\rangle$ state, but not if both qubits are in the $|0\rangle$ state [see Fig. 3.7(c) insets] [122]. As demonstrated in recent experiments [154], these Rydberg-mediated controlled-phase gates can be performed in parallel for sufficiently well-separated pairs of qubits, and non-nearest neighbor interactions can be avoided by slightly reducing the parallelism within each layer of controlled-phase gates. Single-qubit rotations can be performed with sufficiently high fidelity such that the overall circuit fidelity is primarily limited by the entangling gates [153, 256].

For a generic choice of gates, the circuit will be fully scrambling when U is composed of $\sim N$ layers of controlled-phase gates. The fidelity of the overall implementation is limited by the finite lifetime of the Rydberg state, which is populated for time $\sim 1/J_0$ during each controlled-phase gate. Assuming the same experimental parameters as in the analog case, one expects to be able to perform approximately $\Omega\tau \sim 10^3 - 10^4$ controlled-phase gates within the decoherence time-scale. Thus, in the digital approach, one expects that the teleportation protocol can naturally be implemented for $N \sim 200$ qubits.

The digital approach can also be adapted to experiments using Rydberg-dressed neutral atoms in an optical lattice [99, 199, 266]. In such a setup, qubits are again encoded in hyperfine ground states and strong Ising-like interactions are generated by coupling the qubit state $|1\rangle$ to a Rydberg state with a far-detuned laser field. In this way, the Rydberg interaction gives rise to an energy shift for two neighboring atoms both in the $|1\rangle$ state. Analogous to our previous discussion, a simple scrambling unitary could consist of alternating layers of Rydberg-dressed interactions and single-qubit rotations. While the total accumulated error in the Rydberg-dressing approach is comparable to the gate-based protocol, one potential advantage is an increased tunability of the interactions [31, 152].

In addition to scrambling time evolution, there are three ingredients to implement the one-sided teleportation circuit (Fig. 3.6): (i) the ability to ‘swap’ in the qubit $|\phi\rangle$, (ii) single-qubit rotations, $V_i = e^{\pm igZ_i/K}$, and (iii) the final measurement in the EPR basis. In both digital setups, these are easily accomplished by combining controlled-phase gates, arbitrary single-qubit rotations, and local measurements. In the analog setup, we propose to temporarily ‘turn off’ the Hamiltonian by transferring each Rydberg state $|r\rangle$ to a hyperfine ground state (e.g. the state used as $|1\rangle$ in the *digital* protocol) using a resonant laser pulse. Once this is done, all of the above operations can be performed identically as in the digital setup. Afterwards, an additional resonant laser pulse returns the system to the analog encoding. The ancillary qubit can be decoupled from the system qubits during Hamiltonian time-evolution in two ways: (i) by physically positioning the ancillary qubit far from the system, or (ii) by encoding the ancillary qubit in the hyperfine subspace throughout time-evolution.

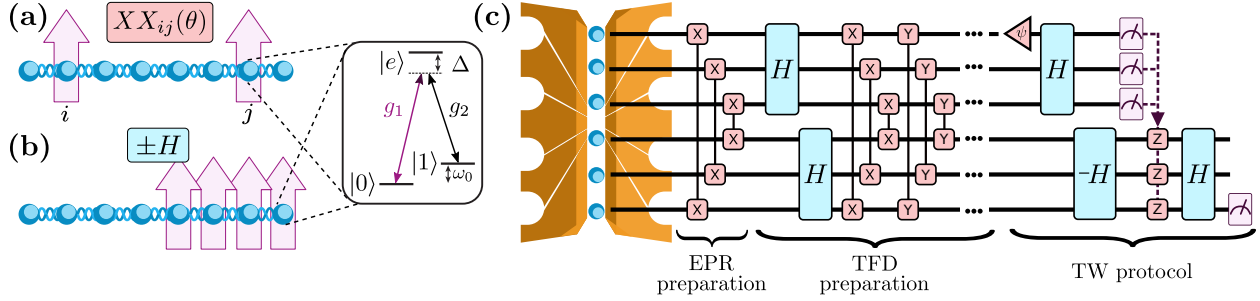


Figure 3.9: **(a-b)** Chain of atomic ions, with qubit states $|0\rangle$, $|1\rangle$ represented by hyperfine ground states. The states are coupled by a pair of laser beams, one with individual addressing (with strength g_1 , purple) and one applied globally (with strength g_2). Each beam is strongly detuned from an excited state $|e\rangle$ by an amount Δ . The coherent beatnote between the beams, at frequency ω_0 , drives stimulated Raman transitions between the qubit levels with an effective Rabi frequency $g_1g_2/2\Delta$, and also modulates the Coulomb interaction between qubits to give rise to an effective Ising interaction. **(a)** A two-qubit entangling gate, $XX_{ij}(\theta)$, (red) is performed by addressing only ions i and j with the first beam. **(b)** Half of the qubits are addressed, which leads to analog time-evolution under the Hamiltonian Eq. (3.105) (blue) for all addressed spins. **(c)** Quantum circuit implementation of the teleportation protocol at finite temperature. EPR pairs are formed using two-qubit gates. The TFD state is then prepared via a QAOA approach by iterating multiple times between two-qubit gates coupling the sides and analog time-evolution on both sides individually [255, 271]. The state $|\psi\rangle$ is inserted either by projectively measuring the designated qubit and preparing the state, or by digitally swapping in an additional qubit (not shown). Finally, teleportation is implemented using similar ingredients as well as feed-forward measurements (purple dotted lines).

The two-sided, finite temperature TW protocol can be achieved by combining the above techniques with TFD preparation as in Section 3.9. A particularly natural geometry for such a realization would be two parallel chains of Rydberg atoms, with each chain forming one side of the TFD state. The coupling between the two sides is naturally realized by the atoms' Ising interactions. This coupling can be applied independently from the one-sided Hamiltonian using either full digital control or by manipulating the inter- vs. intra-chain atomic distance.

Implementation with trapped ions

A second experimental platform that naturally enables the implementation of the TW protocol is arrays of individual trapped atomic ions [37, 248, 267]. Trapped ion qubits feature near-perfect replicability, negligible idle errors, and the ability to implement both a universal set of reconfigurable quantum gates [47] as well as analog long-range spin Hamiltonians [32,

184]. Entangling quantum gates have been demonstrated between isolated pairs of trapped ions with fidelities exceeding 99.9% [17, 87]. Teleportation protocols—including the HPR protocol [147]—involving gate operations, partial measurement and feedforward operations, have been experimentally realized in a number of contexts [20, 147, 190, 207].

Compared to Rydberg atom arrays, trapped ions offer two new regimes for exploring many-body teleportation. First, trapped ions naturally interact via a long-range analog Hamiltonian, whose time-evolution can be fully reversed within certain experimental regimes [138, 244]. Implementing the TW protocol in this setting would provide a window into operator spreading and size distributions under such long-range dynamics [79, 270]. Second, when operated digitally, the same long-range interaction has already been demonstrated to enable the preparation of thermofield double states [179, 236, 255, 271], a crucial step towards realizing the two-sided TW protocol at finite temperature (see Section 3.9).

We begin by outlining the analog and digital forms of time-evolution that are possible in trapped ion systems. Interactions between qubits typically stem from state-dependent optical dipole forces that off-resonantly drive motional sidebands of the qubit [57, 186]. These sideband operations mediate entanglement and give rise to an effective Ising coupling. When the optical forces are symmetrically detuned far from the upper and lower sidebands, the motion is only virtually excited, resulting in a long-range Ising Hamiltonian [Fig. 3.9(b)]:

$$H = \sum_{i < j} J_{ij} X_i X_j + B_z \sum_i Z_i, \quad (3.105)$$

where $J_{ij} \approx J_0/|i-j|^\alpha$, with $0 < \alpha < 3$ and $J_0 \lesssim 1$ kHz, and the effective magnetic field B_z can be realized by slightly asymmetrically detuning the driving field [183]. The sign of the couplings can be reversed by changing the detuning of the optical forces from the motional sidebands [138, 244].

On the other hand, when the optical dipole forces are closer to resonances of the motional modes, one can mediate interactions significantly faster, allowing for the execution of rapid, entangling quantum gates between pairs of illuminated ion qubits [Fig. 3.9(a)] [69, 276]. The native entangling gates are based upon Ising interactions between any selected pair of ions with a tunable interaction angle; in particular, both $XX_{ij}(\theta) = e^{-i\theta X_i X_j/2}$ and $YY_{ij}(\theta) = e^{-i\theta Y_i Y_j/2}$ gates are available and $\theta = \pi/2$ naturally creates an EPR pair [145, 254]. Typical entangling operations have duration $1/J_{\text{ent}} \sim 100 \mu\text{s}$, while decoherence time-scales are on the order of $\tau \sim 400$ ms [70]. Following the estimates of Section 3.9 and requiring $3N^2/J_{\text{ent}}\tau \lesssim 1$, we estimate that near-term state-of-the-art experiments can support high-fidelity many-body teleportation for up to $N \sim 35$ qubits.

Let us now describe an implementation of the one-sided TW protocol (Fig. 3.6). We first focus on the ability to implement both U and its inverse U^\dagger . For analog time-evolution [Eq. (3.105)], U^\dagger can be implemented by changing the sign of the detuning [96], while for digital time-evolution, one can directly invert and reverse the ordering of the quantum gates.

The one-sided protocol also requires the ability to locally address a sub-extensive number of individual qubits. In particular, a subset K of the qubits must be initially prepared in

a product state, $|o_1, \dots, o_K\rangle$ and later rotated by $\hat{V}_i = e^{igo_i \hat{O}_i/K}$. These rotations can be achieved by taking $\hat{O}_i = \hat{Z}_i$ and individually addressing the target ions using an auxiliary “poke” laser beam [233, 267].

Following the first application of U , one must swap out the qubit(s) corresponding to the teleported subsystem. This swap can be implemented either digitally by applying a SWAP-gate, or physically, by exchanging the two ions via a modulation of the ion trap’s axial fields [112, 128, 184].

Extending this implementation to the two-sided protocol [Fig. 6.1(a)] is straightforward. Initialization into EPR pairs (for infinite temperature) can be accomplished via simple Ising gates at the input of the circuit [Fig. 3.9(a,c)], while the TFD state (for finite temperature) can be prepared via variational methods (Section 3.9). Time-evolution can again take the form of either digital quantum gates [Fig. 3.9(a)] or analog Hamiltonian dynamics. To separately implement analog dynamics on the two sides of the system, one would illuminate only *half* of the ion chain at any given time [Fig. 3.9(b)]; this has the added benefit of avoiding unwanted coupling between the left and right sides, but implies that the time-evolution must be performed serially [Fig. 3.9(c)].

Finally, in the two-sided protocol, one must perform projective measurements on K qubits that feed-forward to the conditional rotations, \hat{V}_i . These partial measurements can be accomplished by using multiple ion species (i.e. different elements or isotopes) [20], or alternatively, this entire procedure can be replaced with a specific interaction, e^{igV} , between the two sides; this interaction is naturally realized via an $XX_{ij}(\theta)$ gate with $\theta = 2g/K$.

Effects of experimental error and relation to quantum error correction

We now turn to the effect of experimental error on the TW protocol. We find that teleportation is robust to nearly all errors that occur on the left side of the TFD state after time-evolution by U , but is strongly sensitive to errors at nearly all other locations in the protocol. These two extremes are emblematic of two different relations between scrambling and error: the former corresponds to interpretations of scrambling as an error-correcting code [111], while the latter reflects recent results showing that the effect of errors on scrambling measurements is enhanced proportional to the size, \mathcal{S} , of time-evolved operators [222]. In the following discussion, we demonstrate each of these points through simple but representative examples of experimental error.

We begin with the first case: consider errors occurring on the left side of the TFD state after application of U but before measurement/coupling. Recall that, in the absence of error, one can perform teleportation by using any $K \sim \mathcal{O}(1)$ qubits of the left side. This implies that teleportation is robust to *any* errors that affect only $N - K$ qubits: as long as one has knowledge of at least K qubits that are unaffected, measuring these qubits performs teleportation identically to the error-free case.

This robustness reflects previously noted connections between scrambling and quantum

error correction [111]. In particular, we note that many-body teleportation can be understood as an especially generic example of entanglement-assisted quantum error correction (EAQEC) [45]. Indeed, the setup for EAQEC is identical to that of the teleportation protocol: two parties, Alice and Bob, share entanglement (the TFD state), Alice applies an encoding circuit to her share of qubits (the left unitary, U), and decoding is achieved by teleporting Alice's quantum state to Bob's share of qubits (via the coupling, V , and unitaries on the right). Previous schemes for EAQEC have focused primarily on encodings via Clifford unitaries. In contrast, many-body teleportation, and more specifically peaked-size teleportation, succeeds for a *vastly* broader class of encoding procedures—i.e. scrambling many-body time dynamics—indicating that naturally occurring, strongly interacting systems offer novel methods of EAQEC.

On the other hand, errors that occur *during* encoding or decoding—i.e. during the application of U on the left side or at any point on the right side—strongly inhibit teleportation. As a first example, consider a single local error, W_1 , occurring with probability ε on the right side after coupling but before U^T (i.e. just before decoding). If the error, W_1 , grows to have a size, \mathcal{S} , after U^T is applied, one estimates that it will decrease the teleportation fidelity by an amount, $1 - F \sim \varepsilon\mathcal{S}/N$, proportional to the probability that W_1 has support on the teleported qubit after time-evolution. If we sum over such errors on all N qubits, we have $1 - F \sim \varepsilon\mathcal{S}$.

As a second example, consider a local error, W_2 , occurring with probability ε on the left side simultaneously with state insertion (e.g. a damaged TFD state in Fig. 6.1). In effect, this error shifts the correlator operators [Eq. (3.2)], $Q \rightarrow Q \otimes W_2$; following the arguments of Section 3.7, one then requires that the sizes add for teleportation to succeed, $\mathcal{S}[QW_2] = \mathcal{S}[Q] + \mathcal{S}[W_2]$. In a 1D short-range system (Section 3.7), this condition holds if and only if the light cones of W_2 and Q do not overlap. For $\mathcal{O}(\varepsilon N)$ randomly distributed errors, we expect this to hold as long as the spacing between errors, $1/\varepsilon$, is much larger than the size of the light cone, $\varepsilon\mathcal{S} \ll 1$. A similar scaling holds in 0D (Section 3.7). Here, we expect size addition to hold as long as the size of the total error (corresponding to a time-evolved product of $\sim \varepsilon N$ initially local operators), is much smaller than the system size, N . Once again, this requires $\varepsilon N\mathcal{S} \ll N$, or $\varepsilon\mathcal{S} \ll 1$.

The two previous examples are straightforwardly generalized to errors that accumulate continuously throughout time-evolution. To do so, we replace the error probability with an error rate, ε (now with units of inverse time). The total effect of the error is then given by the integral of the error rate multiplied by the size over time, $\varepsilon \int_0^t dt' \mathcal{S}(t')$ [222]. In one-dimensional systems evolved up to the scrambling time, i.e. $\mathcal{S} \sim Jt$ and $t_s \sim N/J$ for a local interaction strength J , we thus estimate a total error, $\varepsilon \int_0^{t_s} dt' Jt' \sim \varepsilon\mathcal{S}t_s \sim \varepsilon N^2/J$, in agreement with our rough estimates in Sections 3.9 and 3.9.

Finally, we consider a particular form of error that may be relevant for analog time-evolution: mismatches between the evolution times of U , U^* , and U^T . We denote these three evolution times as t_1, t_2, t_3 , respectively, and their mismatches as $\Delta t_{12} = t_2 - t_1$ and $\Delta t_{13} = t_3 - t_1$. We can characterize the mismatches' effect on the teleportation fidelity using the correlators, $C_Q(t_1, t_2, t_3) = \langle U_r^*(t_3) Q_r U_r^T(t_3) e^{igV} U_l(t_1) Q_l U_l^\dagger(t_2) \rangle$ (Section 3.3). From this,

we anticipate that the protocol is relatively insensitive to mismatches between t_3 and t_1, t_2 : teleportation succeeds as long as the mismatch is small compared to the local interaction strength, J , i.e. $J\Delta t_{13} \lesssim 1$. To estimate this, we set $g = 0$ and $t_1 = t_2$ in which case the correlator magnitude is given by an autocorrelation function, $C_Q = \langle Q(t_1)Q(t_3) \rangle = G(\Delta t_{13})$. The teleportation fidelity is bounded above by this expression, which decays on a time-scale $\sim 1/J$. On the other hand, teleportation is more strongly sensitive to the mismatch between t_1 and t_2 . To estimate this, we treat the difference in time-evolution between U and U^* as a product of $\sim (J\Delta t_{12})^2 N$ local errors occurring simultaneous with state insertion (to motivate this scaling, note that one can approximate $U(\Delta t_{12})$ as a product of $\sim N$ local unitaries for small Δt_{12} , and we expect the error to be an even function of Δt_{12}). Following our previous analysis, teleportation is successful as long as $\mathcal{S}(J\Delta t_{12})^2 N \ll N$, or $\mathcal{S}(J\Delta t_{12})^2 \ll 1$.

Directly measuring the size distribution

In Section 3.9, we discussed that the time profile of the teleportation fidelity reveals important features of the operators' size distributions, including the average operator size and the size width. We now demonstrate that a more precise characterization of the operator size distribution can be obtained by sweeping the coupling strength, g , at a fixed time, t .

For simplicity, we restrict to infinite temperature¹⁸ and the coupling V_s in Eq. (3.27), which precisely measures the operator size. In this case, the two-sided correlator [Eq. (3.2)] is equal to the characteristic function, $\Phi_{\mathcal{S}}(g)$, of the size:

$$C_Q(t) = e^{ig} \sum_{\mathcal{S}} P(\mathcal{S}) e^{-ig\mathcal{S}/N} \equiv e^{ig} \Phi_{\mathcal{S}}(g) \quad (3.106)$$

from which the size distribution can be obtained by a Fourier transform in g .

More precisely, to measure the *real part* of the characteristic function (i.e. the teleportation correlator), we perform the teleportation protocol with two small modifications: (i) we replace state insertion with the specific projection operator, $(1 + Q)/2$, and (ii) we measure the expectation value of Q applied to the right side, instead of the teleportation fidelity. This yields the quantity:

$$\begin{aligned} & \langle \text{EPR} | \frac{1 + Q_l(t)}{2} e^{-igV_s} Q_r(-t) e^{igV_s} \frac{1 + Q_l(t)}{2} | \text{EPR} \rangle \\ &= \text{Re} [\langle \text{EPR} | e^{-igV_s} Q_r(-t) e^{igV_s} Q_l(t) | \text{EPR} \rangle] \\ &= \text{Re} [\varphi_{\mathcal{S}}(g)], \end{aligned} \quad (3.107)$$

where in the second line we use that the ‘‘diagonal’’ terms between the two copies of $(1 + Q)/2$ vanish at infinite temperature. The imaginary part of the characteristic function can be

¹⁸At finite temperature, a similar procedure to what follows determines the winding size distribution discussed in Section 3.8 [188]. The size distribution can be determined by moving the final measurement of the TW protocol to the left side.

obtained similarly, by replacing state insertion, $(1+Q)/2$, with an application of the unitary operator, $(1+iQ)/\sqrt{2}$. Analogous to Fig. 3.6, both of these measurement schemes can be adapted into one-sided protocols using Eq. (3.9) whenever the coupling V is classical (i.e. composed of terms $O_{i,l}O_{i,r}^*$, where $\{O_i\}$ mutually commute). While such couplings do not measure the exact size distribution, we expect their behavior to be similar in most cases (Section 3.4).

For completeness, we also note an alternate method to measure the size distribution: one prepares the state $Q_l(t)|\text{EPR}\rangle$ and directly measures the two-sided coupling V_s . The probability distribution of the measurement results gives the size distribution [see the discussion below Eq. (3.27)].

Let us now compare these two protocols to other schemes for characterizing the size distribution of operators. First, we recall that a sum of local OTOCs yields the average operator size [Eq. (3.31)]. Hence, many existing protocols for measuring local OTOCs [243, 260] can be straightforwardly adapted to measuring the average size. Higher order moments of the size distribution can similarly be obtained from local OTOCs, using Eq. (3.27):

$$\begin{aligned} \langle(1-\mathcal{S}/N)^n\rangle &= \langle V_s^n \rangle_Q \\ &= \frac{1}{N^n} \sum_{P_{i_1}, \dots, P_{i_n}} \text{tr} \left(Q(t) \prod_{k=1}^n P_{i_k} Q^\dagger(t) \prod_{k=n}^1 P_{i_k}^\dagger \right). \end{aligned} \quad (3.108)$$

where the sum is over every possible combination of n single-qubit Pauli operators P_{i_1}, \dots, P_{i_n} . Based on this approach, however, the number of measurements required to determine the n^{th} moment scales as $\mathcal{O}(N^n)$. In certain situations, this scaling may be reduced through sampling, though this depends on the nature of the size distribution and the desired degree of precision. Furthermore, reconstructing the full profile of the size distribution from a finite number of moments is generally a difficult numerical task [124]. In contrast to these limitations, our proposal directly yields the full size distribution, and can recover its moments with a number of measurements independent of the system size¹⁹.

We can also compare our proposal to an independent protocol for measuring the size distribution introduced in Ref. [203]. The protocol of Ref. [203] is experimentally simpler than our own, and in particular involves only a single application of time-evolution by U (and no backwards time-evolution). However, this simplicity comes at a cost: resolving high-size components of the distribution requires a number of measurements that scales *exponentially* with size.

¹⁹This is simplest to see in the protocol which measures the two-sided coupling V_s . Here, the error in one's measurement of the n^{th} moment is equal to the expectation value of the moment's variance divided by the number of measurements, $(\delta\langle\mathcal{S}^n\rangle)^2 = (\langle\mathcal{S}^{2n}\rangle - \langle\mathcal{S}^n\rangle^2)/M$. If one wishes to resolve the moment to within a relative error ε , i.e. $\delta\langle\mathcal{S}^n\rangle < \varepsilon\langle\mathcal{S}^n\rangle$, one requires $M \sim \frac{\langle\mathcal{S}^{2n}\rangle - \langle\mathcal{S}^n\rangle^2}{\varepsilon^2\langle\mathcal{S}^n\rangle^2}$ measurements. This number does not scale with N since it contains the same powers of \mathcal{S} in the numerator and denominator.

3.10 Outlook

In this work, we developed a unified framework for understanding many-body teleportation from the perspective of operator growth under scrambling dynamics. The unifying concept within this framework is the size distribution of time-evolved operators [44, 188, 202, 203, 208]: these form the backbone of peaked-size teleportation, and provide a more fine-grained measure of operator growth compared to the average operator size (as given by the expectation value of OTOCs).

Our work suggests several future directions for applying and building upon this framework. First, while we have studied the size distributions in 0D and ≥ 1 D RUCs, it would be interesting to extend this analysis to a multitude of other physical systems, where one expects to find qualitatively distinct behavior. These include long-range interacting systems [78, 246], interacting and non-interacting integrable systems [203], ≥ 1 D systems with a large on-site Hilbert space [105], 0D systems with sparse couplings [24], and systems with conserved quantities [130].

Another set of open questions concerns the notion of operator size at finite temperature. In systems with peaked size distributions, we found that the phase of the two-sided teleportation correlator was directly proportional to the conventional definition of operator size [202]. Surprisingly, we observed that this relationship did not hold in the finite temperature SYK model; rather, the phase was given by the real part of the two-sided OTOC. Unlike the conventional size, this OTOC is not UV divergent, and is thus expected to be inherently independent of the microscopic Hilbert space. Recent work has shown that its real part isolates an incoherent component of operator spreading in large- N models [103]; further work is needed to establish and expand this framework. Related to these considerations, one may hope to better understand the bulk analogue of operator size in theories dual to gravity with strong stringy effects. While we have seen that stringy effects can mimic peaked-size teleportation, developing a physical interpretation of this correspondence would be extremely exciting.

Third, we have shown that a promising application of the teleportation protocol is to distinguish between different classes of scrambling dynamics. In particular, we have focused on two classes of scramblers—generic thermalizing systems and those with gravitational duals—and demonstrated that the key distinction between them is their teleportation fidelity at low temperatures. It is intriguing to ask whether the fidelity increase associated with gravitational teleportation may also occur in other systems, without a gravitational dual. For instance, recently the teleportation correlator magnitude was observed to increase slightly above G_β in non-local random Hamiltonian systems [44, 188]; generalizing this to other physical models would be of tremendous interest.

One may also wonder what role an extensive low temperature entropy—a key feature of the SYK model [173]—plays in the teleportation process. In particular, how well can systems with extensive low temperature entropy but no known gravitational dual teleport [6, 220]? We conjecture that an extensive entropy would allow one to *locally* encode each qubit into low-energy degrees of freedom (i.e. operators with an $\mathcal{O}(1)$ two-point function), since one

would only require $\mathcal{O}(1)$ qubits on the left side of the TFD in order to have one qubit of mutual information with the right side. Such an encoding would allow low temperature teleportation with perfect fidelity if operator sizes were peaked, naturally motivating the study of operator size distributions in such models.

Finally, we would like to discuss the relation between our results on the TW protocol and the eternal traversable wormhole (ETW) introduced in Ref. [170]. In the latter, the coupling, V , has an $\mathcal{O}(1)$ coefficient and, moreover, is applied *simultaneously* with single-sided Hamiltonian evolution (i.e. the full system evolves under a Hamiltonian, $H_l + H_r + g \sum_j O_{j,l} O_{j,r}^*$). Under these conditions, Refs. [170, 196] find that the ETW teleportation fidelity oscillates in time under gravitational dynamics, indicating that information is transmitted back and forth between the two boundaries. Intriguingly, unlike the TW protocol, the ETW oscillations occur at a time-scale given by the single-sided thermalization time ($\sim \beta$, the inverse effective temperature), and *not* the scrambling time. Developing a microscopic understanding of the ETW in terms of operator spreading, as well as exploring analogous physics in more generic many-body systems, remains an exciting open direction.

Chapter 4

Comment on “Traversable wormhole dynamics on a quantum processor”

The holographic principle posits that certain quantum mechanical Hamiltonians are dual to quantum theories of gravity [114, 169, 240]. Recently, there has been tremendous interest towards *experimentally* realizing such quantum mechanical models on a quantum processor. To this end, an important development was the discovery of a quantum teleportation protocol that is related to traversable wormholes (Fig. 4.2a) [44, 89, 90, 176, 188, 224]. Specifically, when the teleportation protocol is implemented using a Hamiltonian that is holographically dual to gravity, successful teleportation is described from the dual perspective as a particle traveling through a traversable wormhole.

A recent article [121] claims to observe traversable wormhole dynamics in an experimental setting. The most direct way to observe traversable wormhole dynamics would be to experimentally implement the SYK model, which is dual to gravity [133, 218]. However, it is extremely challenging to experimentally implement even a small-size version of the SYK model. To this end, [121] uses a machine-learning procedure to construct a sparse Hamiltonian that aims to preserve gravitational physics. More specifically, the machine-learning procedure is based upon reproducing the teleportation behavior of the SYK model (at system size $N = 10$) with only a small number of Hamiltonian terms. The result is the following Hamiltonian, henceforth “Model 1”,

$$\begin{aligned}
 H = & -0.36\psi^1\psi^2\psi^4\psi^5 + 0.19\psi^1\psi^3\psi^4\psi^7 - 0.71\psi^1\psi^3\psi^5\psi^6 \\
 & + 0.22\psi^2\psi^3\psi^4\psi^6 + 0.49\psi^2\psi^3\psi^5\psi^7.
 \end{aligned}
 \tag{4.1}$$

Here, ψ^i are Majorana fermions satisfying $\{\psi^i, \psi^j\} = \delta_{ij}$.

The authors claim that Model 1 “is consistent with gravitational dynamics of the dense SYK Hamiltonian” and demonstrates “gravitational teleportation...by means of an emergent wormhole”. They analyze five key properties of traversable wormhole physics:

- (i) scrambling and thermalization dynamics
- (ii) a teleportation signal that is consistent with a negative energy shockwave
- (iii) perfect size winding

- (iv) causal time-ordering of teleported signals
- (v) a Shapiro time delay

These claims are surprising given that:

Model 1 is fully-commuting. Each of the five Hamiltonian terms commutes with every other term.

which is alluded to in the Supplemental Material of [121]. This property is distinct from the SYK model, and fully-commuting models are known to exhibit markedly different dynamics from non-commuting models.

Given the interest in realizing non-trivial models of quantum gravity in experiment, it seems worthwhile to investigate the extent to which the model and strategy in [121] indeed capture the stated features of gravitational physics. Our central findings are:

- In contrast to the claims of [121], Model 1 does not thermalize. It exhibits strong oscillations in the correlation functions that characterize scrambling and thermalization (Fig. 4.1). The observation of thermalization in [121] is an artifact of averaging over these oscillations.
- In order to generate Model 1, the machine-learning procedure in [121] trains on teleportation involving two specific operators, ψ^1 and ψ^2 . The authors characterize the teleportation signal [properties (ii, iv, v)] and size winding [property (iii)] only for those operators that were trained on. We find that the teleportation signal only resembles that of the SYK model for the specific operators that were trained on, and not for general operators that were not involved in the training (Fig. 4.2).
- The observed perfect size winding in Model 1, is in fact, a widespread property of fully-commuting Hamiltonians at small system sizes (Fig. 4.3). Putting random numerical coefficients in front of the terms in Eq. (4.1) or taking random commuting terms, also produces perfect size winding. In the cases that we have examined, perfect size winding does not persist to larger system sizes or to non-commuting models at equivalent system sizes.

We emphasize an inherent tension between the first and third observations: Small-size, fully-commuting Hamiltonians do not thermalize but generally exhibit perfect size winding, while the opposite is true for larger or non-commuting systems. None of the systems considered in [121] satisfy both properties simultaneously. Nevertheless, both thermalization [110, 115] and size winding [44, 188] are central to the holographic correspondence and are known to occur in the SYK model at large system sizes [188].

Before proceeding, we note that two additional Hamiltonians are numerically studied in the Supplemental Material of [121]. We address these in Appendix C.1. The Hamiltonian Eq. (S16) in [121], henceforth “Model 2”, is produced by the same machine-learning procedure as Model 1. We find that Model 2 is nearly fully-commuting, and that the above observations

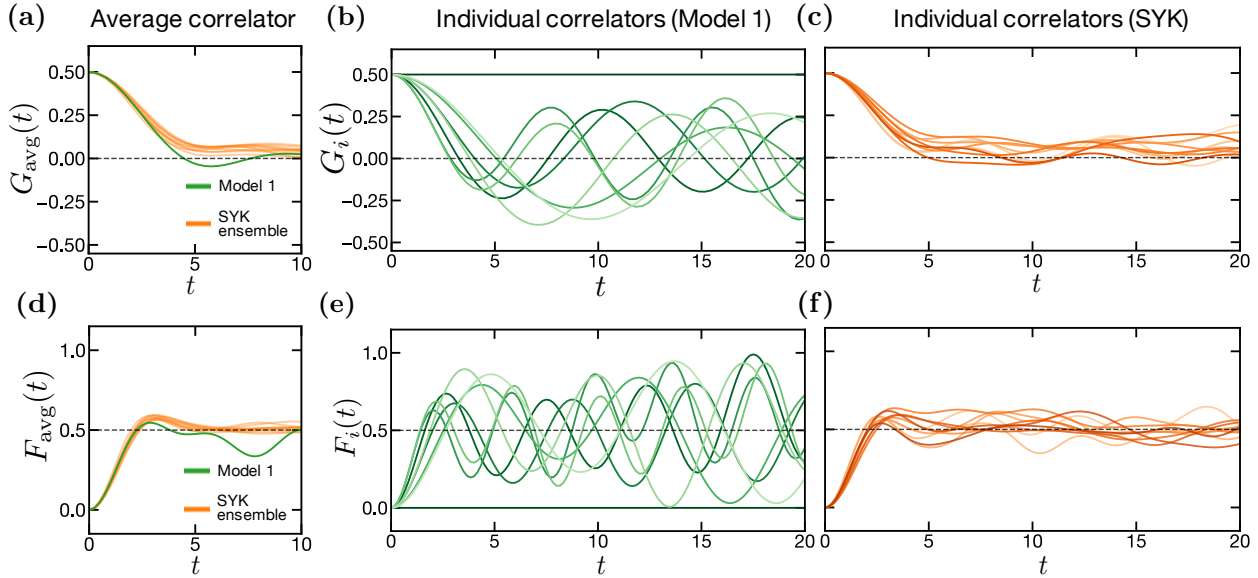


Figure 4.1: **Lack of thermalization in Model 1.** (a) Two-point correlation functions averaged over Majorana operators, $G_{\text{avg}}(t)$, for Model 1 (green; replicating Fig. 3b of [121]) and several disorder realizations of the $N = 10$ SYK model (orange). As observed in [121], the average correlation function displays similar behavior between the two models. For both models, $\beta = 4$, and, for the SYK model, the couplings are drawn from a normal distribution with mean zero and variance $6J^2/N^3$, where $J = 1.125$. (b) In Model 1, the *individual* two-point correlation functions, $G_i(t)$, display large oscillations. (c) In the SYK model (taking a single disorder instance), the individual correlation functions all exhibit decay. This behavior is independent of the disorder realization. (d-f) Analogous results for the average and individual four-point correlation functions, $F_{\text{avg}}(t)$ and $F_i(t)$, in Model 1 and the $N = 10$ SYK model. Again, the agreement between the two models holds only for the averaged correlation functions (d), and not for the individual correlation functions (e-f).

similarly hold. In contrast, the Hamiltonian Eq. (S17) in [121], henceforth “Model 3”, is produced by an alternate machine-learning procedure designed to maximize the difference in the teleportation signal between negative and positive couplings. Model 3 is not fully-commuting and exhibits clearer signatures of thermalization. However, as noted in [121], it does not exhibit perfect size winding.

4.1 Thermalization and scrambling

Ref. [121] claims that Model 1 “scrambles and thermalizes similarly to the original SYK model as characterized by the four- and two-point correlators.” To support this, they plot

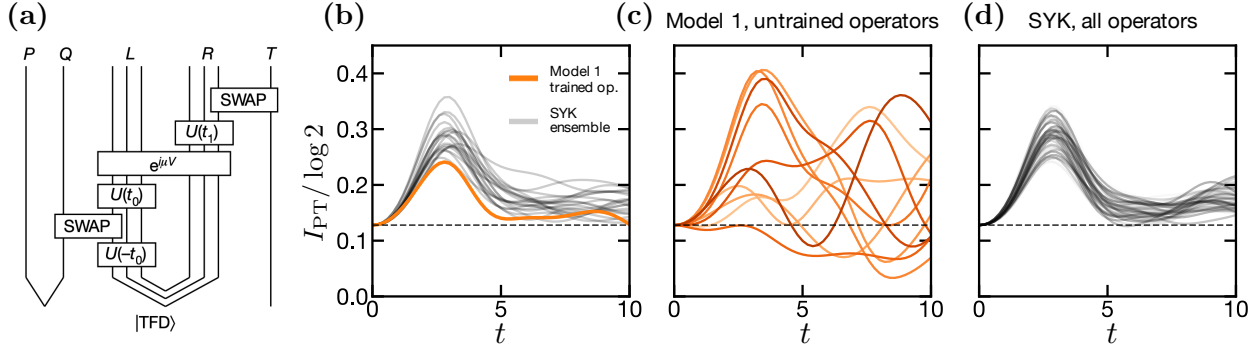


Figure 4.2: **Teleportation signal of Model 1.** (a) Teleportation circuit from [121]. The qubit to be teleported is swapped with a pair of Majorana operators in the left system L. The success of teleportation from L to R is measured by the mutual information between a reference qubit P and a readout qubit T. (b) Mutual information, I_{PT} , of the symmetric teleportation protocol with $\mu = -12$ for Model 1 (orange; replicating Fig. 2a of [121]) and several realizations of the $N = 10$ SYK model with $J = 1.25$ (grey). The machine-learning procedure in [121] trains Model 1 to reproduce the mutual information (as a function of time) of the SYK model for a specific pair of input operators, ψ^1 and ψ^2 . For this pair of operators, the mutual information indeed shows good agreement between the two models. (c) In Model 1, when the teleportation protocol is performed with input operators that were not involved in the training procedure, i.e. ψ^i and ψ^j where $i < j \in [3, 7]$, the mutual information as a function of time exhibits significant variations. (d) For comparison, in the $N = 10$ SYK model, the mutual information for all pairs of input operators is consistent. The dashed line indicates the mutual information at $t = 0$ for reference.

the *average* of each correlator over local Majorana operators. For example, they plot (Fig. 3b of [121]) the two-point correlator $G_{\text{avg}}(t) = \frac{1}{8} \sum_{i=1}^8 G_i(t)$, where $G_i(t) = \text{Re} [\langle \psi^i(t) \psi^i(0) \rangle_\beta]$ and the sum is over the seven operators in Eq. (4.1) and an additional operator ψ^8 that does not enter the Hamiltonian (reproduced in Fig. 4.1a). Here, $\langle \cdot \rangle_\beta = \text{Tr}[(\cdot) \rho_\beta]$ with $\rho_\beta = e^{-\beta H} / \text{Tr}[e^{-\beta H}]$.

The decay of two-point correlation functions is indicative of thermalization [62]. We note that it is not typical to average over a system’s two-point correlation functions when exploring thermalization, since this averaging can lead to a decay that is not representative of the individual correlation functions. As shown in Fig. 3b of [121] and we reproduce in Fig. 4.1a above, for both the SYK model and Model 1, the averaged correlation function, $G_{\text{avg}}(t)$, indeed exhibits decay. For the SYK model, this decay is consistent with the behavior of individual two-point correlation functions, and thus, thermalization (Fig. 4.1c). However, for Model 1, the individual two-point correlators, $G_i(t)$, exhibit strong revivals as a function of time (Fig. 4.1b). This indicates that the agreement in the thermalization behavior between the SYK model and Model 1 observed in Fig. 3b of [121] is an artifact of averaging over the

two-point correlation functions, and that in fact, Model 1 does not thermalize.

In Fig. 4.1d-f, we turn to the behavior of four-point correlation functions, $F_i(t) = -\text{Re} \left[\langle [\psi^i(t), \psi^i(0)]^2 \rangle_\beta \right]$, as well as their average, $F_{\text{avg}}(t) = \sum_{i=1}^8 F_i(t)$. Much like the two-point correlators, the agreement between the four-point correlation functions of Model 1 and the SYK model (Fig. 3b of [121]), is an artifact of averaging.

In the holographic correspondence, the persistent decay of the two- and four-point correlators corresponds to a perturbation falling toward a black hole [115, 228]. The strong revivals in the correlators of Model 1 contrast with this physics.

4.2 Teleportation signal

We now explore the claim that Model 1 “is consistent with gravitational dynamics of the dense SYK Hamiltonian beyond its training data”. Specifically, the authors claim that the teleportation signal of Model 1 demonstrates behavior compatible with a qubit emerging from a traversable wormhole. These claims are based upon analyzing the teleportation signal for the pair of operators, ψ^1 and ψ^2 , that were involved in the machine-learning training (Fig. 2 of [121]). To further test whether Model 1 is consistent with the gravitational dynamics of the dense SYK model, we examine the teleportation signal for operators that were not involved in the training procedure.

Fig. 2 of [121] presents the mutual information of the teleportation protocol as a function of two times: the injection time, t_0 , and the readout time, t_1 (see e.g. the circuit in Fig. 4.2a). For the symmetric teleportation protocol, with $t = t_0 = t_1$, traversable wormhole dynamics lead to the presence of a single peak in the mutual information as a function of time [121]. We note that Model 1 is trained to reproduce the symmetric teleportation signal of the SYK model for a specific pair of input Majorana operators, ψ^1 and ψ^2 . As depicted in Fig. 2a in [121] and in Fig. 4.2b above, the mutual information indeed exhibits a single peak for the trained operators in Model 1 and for various instances of the SYK model. However, for a generic pair of untrained operators in Model 1, the mutual information does not exhibit single-peak behavior, but rather, displays large oscillations as a function of time that strongly vary for different input operators (Fig. 4.2c). This sharply contrasts with teleportation in the SYK model, where the mutual information exhibits a single consistent peak in time for any pair of input operators (Fig. 4.2d).

We note that Ref. [121] also examines the teleportation protocol at a fixed injection time, while varying the readout time (Fig. 2b in [121]); our analysis of this protocol is shown in Appendix C.3. At short times, for Model 1, the mutual information exhibits a single peak for all pairs of operators, albeit with large variations in peak height. At longer times, generic pairs of operators exhibit multiple peaks in the mutual information, which are not observed in the SYK model.

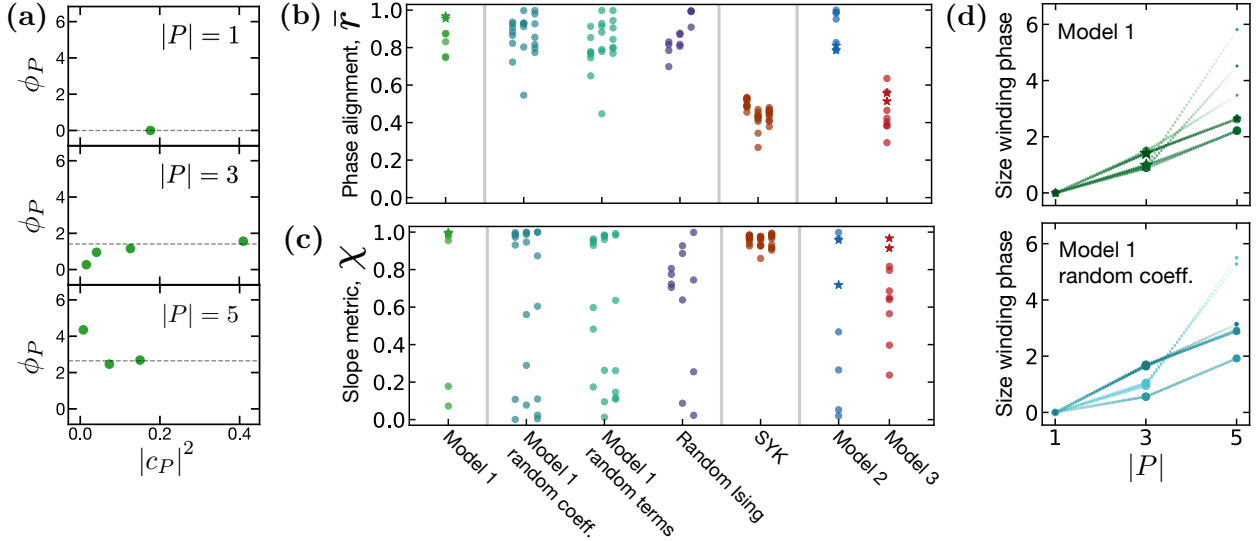


Figure 4.3: **Comparison of size winding behavior in Model 1 and other random small-size fully-commuting Hamiltonians.** (a) Scatter plots depicting the eight non-zero coefficients, c_P^2 , for ψ^1 of Model 1 at $t = 2.8$. The x-values are the coefficient magnitudes, $|c_P|^2$, and the y-values are the coefficient phases, $\phi_P \equiv \arg c_P^2 - \arg q(1)$. Perfect phase alignment occurs when the phase of all coefficients at a given size $|P|$ matches the phase of their sum (dashed line). This occurs trivially for the single coefficient with $|P| = 1$, and via the alignment of ~ 2 -3 coefficients for $|P| = 3, 5$. (b) A comparison of the phase alignment, \bar{r} , for each operator in: Model 1, Model 1 with random coefficients, Model 1 with random terms and coefficients, a random all-to-all Ising model, the $N = 10$ SYK model, Model 2, and Model 3. For Models 1,2,3, the phase alignment for the trained operators, ψ^1 and ψ^2 , is indicated with a star. As in [121], we take $\beta = 4$, and time $t = 2.8$ for Models 1,2 and $t = 2$ for Model 3. For the random models, three different disorder realizations are shown, with small horizontal offsets for clarity. (c) An analogous comparison for the linear slope metric, χ . (d) The size winding phase, $\arg q(|P|) - \arg q(1)$, as a function of the operator size, $|P|$, for Model 1 (top) and Model 1 with random coefficients (bottom). The size of each marker is scaled proportional to $|q(|P|)|$. The stars in Model 1 correspond to operators ψ^1 (replicating Fig. 3d in [121]) and ψ^2 .

4.3 Size winding

Beyond a comparison to the $N = 10$ SYK model, the authors claim that Model 1 satisfies general behavior predicted by gravity. They focus on the property of size winding (Fig. 3d and S14 in [121]), which is defined by decomposing a time-evolved operator as follows:

$$\rho_\beta^{1/2} \psi^i(t) = \sum_P c_P \psi^P \quad (4.2)$$

where c_P is a complex coefficient, and ψ^P is a Majorana string with support $P \in \{0, 1\}^N$. Here, $P_i = 1$ indicates that ψ^P has support on site i . Size winding is the condition that the phases of the squared coefficients, c_P^2 , depend linearly on the size $|P|$ of the Majorana string, i.e. $c_P = e^{i(\alpha|P|/N+\phi)}r_P$ for some real values, α, ϕ, r_P . As in [121], it is convenient to separate size winding into two distinct properties:

1. *Phase alignment*—The phase of c_P^2 is equal for all P of the same size.
2. *Linear slope*—The phase of the sum of coefficients of size l , $q(l) = \sum_{|P|=l} c_P^2$, follows a linear slope with respect to l .

Analytic calculations show that the SYK model exhibits both properties in the limit of large system sizes [188]. The authors emphasize that perfect size winding is a necessary criteria of general holographic systems ¹.

We begin by noting a difference in the structure of time-evolved operators between fully-commuting models such as Model 1, and non-commuting models, such as the SYK model. In fully-commuting Majorana Hamiltonians, a time-evolved operator has non-zero coefficients for up to $2^{\lfloor N/2 \rfloor}$ different strings. In a non-commuting Majorana Hamiltonian, a time-evolved operator has non-zero coefficients for up to 2^{N-1} strings. This difference is particularly pronounced at small system sizes: In Model 1 there are 8 non-zero coefficients (Fig. 4.3a), while in the $N = 7$ SYK model there are 64 non-zero coefficients and in the $N = 10$ SYK model studied in [121] there are 512 non-zero coefficients.

Phase alignment—Ref. [121] quantifies the degree of phase alignment by considering the ratio:

$$r_l = \frac{\left| \sum_{|P|=l} c_P^2 \right|}{\sum_{|P|=l} |c_P|^2}, \quad (4.3)$$

which is unity when phase alignment is perfect. Using ψ^1 (which is one of the operators that was trained upon), the authors show that Model 1 exhibits $r_l \gtrsim 0.95$ for all l (Fig. S14 in [121]). The authors refer to this as perfect size winding. In comparison, Ref. [121] finds that the $N = 10$ SYK model exhibits $r_l \sim 0.75$ (Fig. S19 in [121]), which the authors refer to as “damped” size winding.

To avoid characterizing the phase alignment ratio for each l , we consider the average ratio, $r = \sum_l |q(l)|$. Since r is lower bounded by a two-point correlation function, $W = \text{tr}(\psi^i \rho_\beta^{1/2} \psi^i \rho_\beta^{1/2}) = \sum_P c_P^2$, it is natural to define a rescaled phase alignment ratio as $\bar{r} = \frac{r-W}{1-W}$ (see Appendix C.4 for details).

¹Ref. [121] also contains a stronger statement: “Perfect size winding is equivalent to a maximal Lyapunov exponent at large N , but unlike the Lyapunov exponent, size winding remains a meaningful quantity at small N .” We are not aware of a derivation of this equivalence. In fact, within the approximations of [89], the large- q SYK model provides a counterexample: It displays perfect size winding at all temperatures but a maximal Lyapunov exponent only in the low temperature limit.

In Fig. 4.3b, \bar{r} is plotted for Model 1 and the SYK model, for all operators. Consistent with the authors’ observations (Figs. S14, S19 in [121]), Model 1 exhibits a significantly higher \bar{r} than the SYK model.

We begin by examining to what extent the large phase alignment, \bar{r} , is a result of the authors’ machine learning procedure. In particular, we consider Model 1 with *random* numerical coefficients in front of the five Hamiltonian terms. In all cases, we find that the phase alignment, \bar{r} , is similar to Model 1 and significantly higher than the SYK model. Three specific instances are shown in Fig. 4.3b. Next, we further randomize Model 1, by considering Hamiltonians with five random, commuting, four-body Majorana terms (in addition to random coefficients). Again, we find that the phase alignment, \bar{r} , is similar to Model 1 and significantly higher than the SYK model (Fig. 4.3b).

The above observations suggest that a large phase alignment, \bar{r} , is a generic feature of many fully-commuting models at small system sizes. As a further example, we plot the phase alignment, \bar{r} , for a random all-to-all Ising model with four spins, and find similar behavior to Model 1; as shown in Appendix C.5, we find that the phase alignment, \bar{r} , decreases with increasing system size.

Linear slope—The authors claim that Model 1 exhibits a linear size-winding slope. To demonstrate this, in Fig. 3d of [121], the authors plot the phase of $q(l)$ as a function of l for the Majorana operator ψ^1 (which was trained upon). The phase indeed exhibits a linear slope with respect to l .

We examine how generic this behavior is, and the extent to which it results from the authors’ machine learning procedure. In order to better compare across models, we introduce a metric, χ , for quantifying the linear slope property (see Appendix C.4 for details). As depicted in Fig. 4.3c, ψ^1 is indeed characterized by a large value of χ . For the other operator that was trained upon, ψ^2 , we also find that χ is large. However, for the untrained operators, some Majoranas exhibit large values of χ , while others exhibit small values of χ implying that they do not satisfy the linear slope property. This behavior is illustrated in Fig. 4.3d and contrasts with the SYK model. For the SYK model, all operators exhibit the linear slope property and χ is clustered near unity, as shown in Fig. 4.3c.

As in the preceding discussion about phase alignment, the fact that some operators in Model 1 exhibit a linear slope with large χ , is a generic feature of small-size, fully-commuting Hamiltonians. The distribution of χ across all operators is illustrated in Fig. 4.3c, for the three types of models considered in the preceding subsection: (i) Model 1 with random coefficients, (ii) Model 1 with random terms and coefficients, and (iii) fully-commuting random Ising models. In each case, the behavior is comparable to Model 1—certain operators exhibit the linear slope property with large χ , while others do not.

We note that for all three models studied by the authors (Model 1 in the main text and Models 2,3 in the Supplemental Material), the trained operators exhibit a relatively high degree of linearity compared to other operators. This suggests that the authors’ machine-learning procedure may have introduced a bias among the trained operators. Nevertheless, the distribution of χ over all operators resembles that of generic random small-size fully-commuting models.

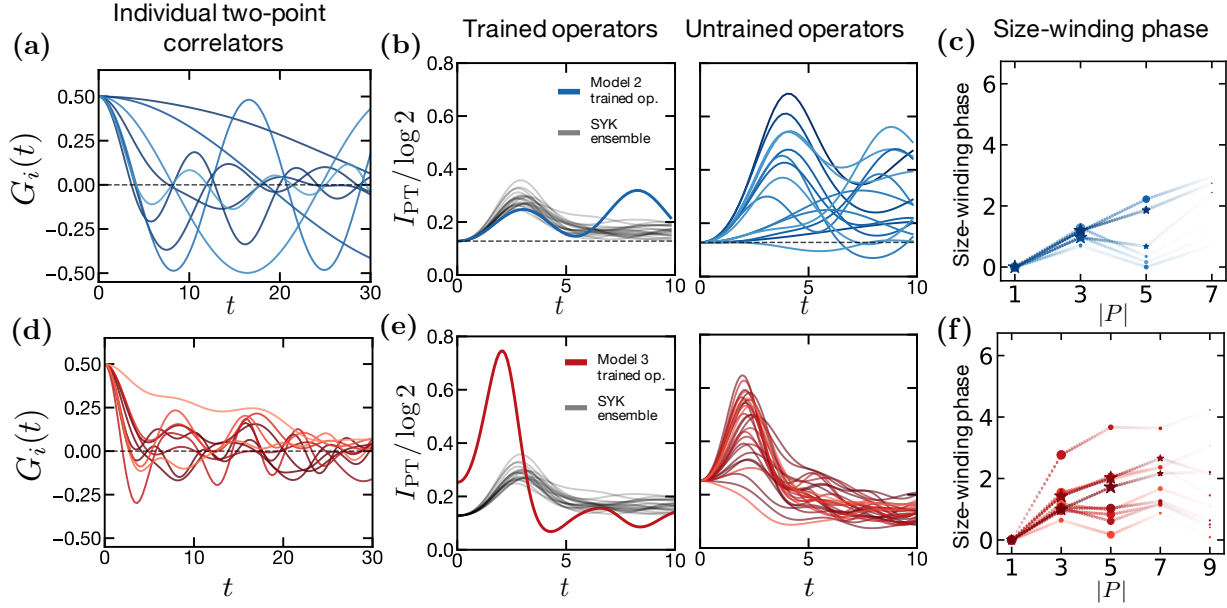


Figure 4.4: **(a)** Two-point correlation functions, $G_i(t)$, for all Majorana operators in Model 2. **(b)** (left) Mutual information for the symmetric teleportation protocol with the trained operators, ψ^1 and ψ^2 , and $\mu = -12$ for: Model 2 (blue), and multiple instances of $N = 10$ SYK model (grey). (right) Mutual information for the symmetric teleportation protocol with all pairs of untrained operators, and $\mu = -12$. **(c)** Size-winding phase for each of the untrained operators at $t = 2.8$. **(d-f)** Depicts the analogous results for Model 3. As in [121], the teleportation protocol is performed with $\mu = -17$ for Model 3 (replicating Fig. S25 of [121]), and the size-winding phase is evaluated at $t = 2$.

Size winding has recently emerged as a prominent feature of the holographic correspondence for systems with a nearly AdS_2 bulk [44], leading to speculation that the presence of perfect size winding could be a strong signature of gravity [188, 224]. The fact that the perfect size winding observed in [121] seems reliant on small-size, fully-commuting models—which defy other features of holography such as thermalization [110, 115], complexity [239], and chaos [171]—raises the question of whether the observed perfect size winding is indeed connected to gravitational physics in a substantive manner.

Chapter 5

Butterfly metrology: a universal protocol for quantum-enhanced sensing

Quantum-enhanced metrology leverages entanglement in a many-particle system to improve the fundamental precision of sensing [71, 98]. The realization of this enhancement with large numbers of interacting particles remains a long-standing objective, with a wide-range of potential applications including atomic time-keeping [36], gravitational wave sensing [221], biological imaging, and the search for new fundamental physics [12].

From a theoretical perspective, the requirements for a many-body state to exhibit “metrologically-useful” entanglement are well understood [71]. However, from an experimental perspective, two overarching challenges remain: signal readout and state preparation. For the first challenge, the key tension is that any *direct* measurement on a metrologically useful state will also be highly susceptible to noise during the read-out process [38]. To address this challenge, seminal recent results have introduced sensing protocols that rely on *time-reversed* dynamics [66, 85, 100, 166]. Crucially, these protocols exhibit significantly improved robustness to read-out noise and have been experimentally realized in the context of spin squeezed [66] and GHZ states [185].

For the second challenge, the most natural strategy to prepare a metrologically useful state is via Hamiltonian evolution from an initial product state; however, the class of Hamiltonians for which this succeeds is extremely limited [71]. Indeed, the only known examples consist of semi-classical, large- S spin models [66, 160], symmetry breaking evolution from a pure state [33], and commuting central spin models [100]. This precisely encodes the challenge that while most quantum states are highly entangled, only a vanishingly small subset can be utilized to perform enhanced sensing [119].

In this Chapter, we address this outstanding challenge by introducing a novel sensing protocol, dubbed “butterfly metrology”. The key insight underlying our approach is to use time-reversed dynamics not only to detect, but also to *prepare* a metrologically-useful state [Fig. 5.1]. To do so, our protocol relies on the quantum butterfly effect: Under chaotic dynamics, a small perturbation causes a significant disruption to the future quantum trajectory. Indeed, our protocol can be understood as performing interferometry between two

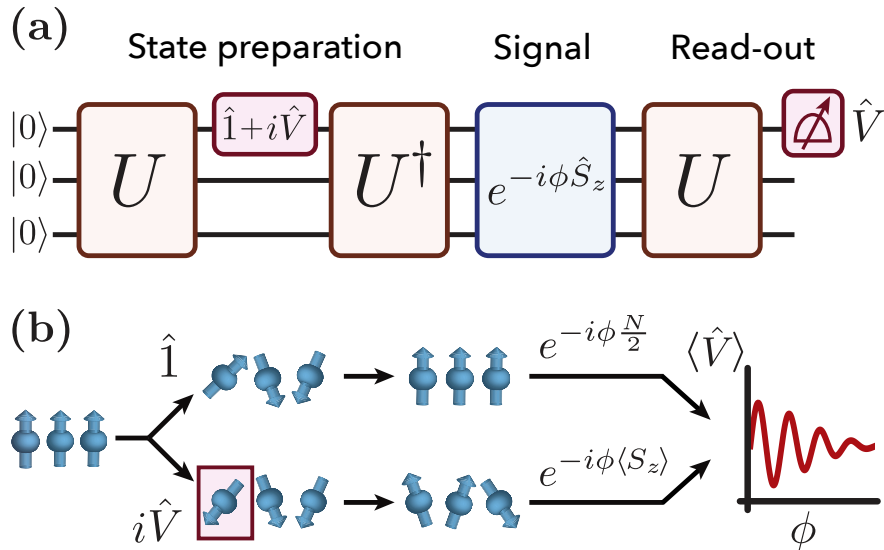


Figure 5.1: **(a)** Butterfly metrology protocol with local control. The “butterfly state” is prepared by evolving forward and backward under a many-body unitary U , interleaved with a local rotation, $(\hat{1} + i\hat{V})/\sqrt{2}$. The signal ϕ is detected via oscillations in the local observable $\langle \hat{V} \rangle$. **(b)** The protocol performs interferometry between two trajectories. In the first (top), the forward and backward evolution cancel, yielding the polarized state $|0\rangle$. In the second (bottom), the local perturbation yields a “scrambled” state, $i\hat{V}(t)|0\rangle$. If U is scrambling, the two trajectories acquire macroscopically different phases under the signal, leading to a Heisenberg-enhanced sensitivity.

alternate trajectories, in which a “butterfly” operator is either applied or not applied during the time evolution.

Our main results are fourfold. First, we establish a precise connection between butterfly metrology and quantum information scrambling; in particular, we derive an equality between the sensitivity of our protocol and a sum of local out-of-time-order correlators (OTOCs) [133, 209, 228]. For fully scrambling dynamics, this implies a measurement sensitivity that exhibits Heisenberg scaling. Second, we introduce a variant of our protocol that utilizes *global* control and readout. This reduces the experimental requirements to implement our protocol and yields a sensitivity that smoothly interpolates between the standard quantum limit and Heisenberg scaling, as a function of evolution time[71]. Third, we analyze the effects of noise and decoherence, demonstrating that our protocol is robust to both measurement and initialization errors, as well as to control errors, provided they are time-reversible. Finally, we highlight the broad applicability of our protocol by providing detailed blueprints and numerical simulations for a variety of experimental platforms. A particularly clear advantage over existing protocols is shown in the case of solid-state spin defects.

5.1 Butterfly metrology protocol

We consider an ensemble of N spin-1/2 particles, coupled to a weak external signal via the collective spin operator $\hat{S}_z = \frac{1}{2} \sum_i \hat{\sigma}_i^z$, where $\hat{\sigma}_i^z$ is a local Pauli operator acting on spin i . Specifically, the system is prepared in a pure state $|\psi\rangle$ and then evolves under the interaction $e^{-i\phi S_z}$ where ϕ is a small parameter. The goal is to maximize the sensitivity η for estimating the parameter ϕ via an observable \hat{M} , where $\eta = \Delta M_\phi / \partial_\phi \langle \hat{M} \rangle_\phi$ and ΔM is the standard deviation of \hat{M} .

The sensitivity η is lower bounded by the quantum Fisher information (QFI) via $\eta \geq 1/\sqrt{\mathcal{F}}$, which for a pure state reduces to the standard deviation of S_z in $|\psi\rangle$, i.e. $\eta \geq 1/\Delta S_z$ [42]. If $|\psi\rangle$ is product state, the standard deviation ΔS_z scales as \sqrt{N} , implying an SQL-limited sensitivity of $\eta \sim 1/\sqrt{N}$. Most quantum states, despite being highly entangled, do not surpass this scaling. Indeed, a Haar random state possesses, on average, the same QFI as an unentangled state, owing to a lack of correlations in the z -basis. On the other hand, the GHZ state, $(|0\rangle^{\otimes N} + |1\rangle^{\otimes N})/\sqrt{2}$, features maximal correlations and thus achieves the Heisenberg-limited sensitivity, $\eta = 1/N$ [40]. Other well-known states that exhibit a QFI beyond the SQL include Dicke states [73], squeezed states [136, 253], critical states [84], and thermalized states in a symmetry-broken phase [33].

Our approach begins by introducing a new class of metrological state, which we call the ‘butterfly state’:

$$|\psi_B\rangle = \frac{|\mathbf{0}\rangle + i\hat{V}(t)|\mathbf{0}\rangle}{\sqrt{2}}. \quad (5.1)$$

Here, $|\mathbf{0}\rangle \equiv |0\rangle^{\otimes N}$ is the fully polarized state, and $\hat{V}(t) = U^\dagger \hat{V} U$ is a local Pauli operator (e.g. $\hat{V} = \hat{\sigma}_0^x$) evolved in the Heisenberg picture under unitary evolution, U . For example, U may correspond to evolution under a time-independent Hamiltonian, $U = e^{-iHt}$, Floquet dynamics, or a digital quantum circuit. As shown in Fig. 5.1, $|\psi_B\rangle$ is prepared by applying a local rotation $(\mathbb{1} + i\hat{V})/\sqrt{2}$ (i.e. a $\pi/2$ -pulse), sandwiched between forward and backward time evolution.

Physically, the butterfly state lies in a superposition between two quantum trajectories: in the first, the forward and backwards evolution perfectly cancel, returning the system to the fully polarized state; in the second, the local operator \hat{V} disrupts this cancellation. If the time evolution is fully ‘scrambling’, this disruption will affect every qubit in the system, and the second trajectory will resemble a random state, with an average polarization of zero. Thus, much like a GHZ state, the butterfly state $|\psi_B\rangle$ features a bimodal polarization distribution with a macroscopic difference between the two peaks [Fig. 5.2(a)]. This suggests that it can serve as a resource state for Heisenberg-scaling sensitivity, $\eta \sim 1/N$.

Following this intuition, we devise the following interferometric protocol for measuring the external signal ϕ , depicted in Fig. 5.1(a). First, we prepare the butterfly state $|\psi_B\rangle$ by evolving forward and backward in time, interleaved with a local rotation. Second, the external signal is applied to the butterfly state, yielding the modified state $(e^{-i\phi \frac{N}{2}} + ie^{-i\phi S_z} V(t)) |\mathbf{0}\rangle / \sqrt{2}$. Last, to detect the signal, we evolve forward in time under U and measure the local operator

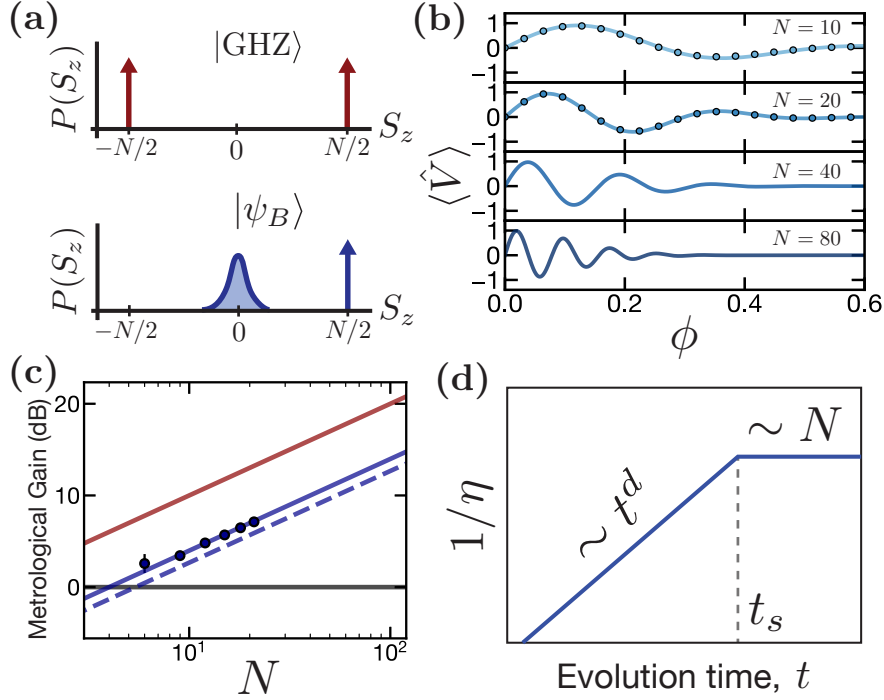


Figure 5.2: **(a)** Schematic of the polarization distribution $P(S_z)$ for (above) a GHZ state and (below) a butterfly state (Eq. 5.1), with evolution U corresponding to a Haar-random unitary. The butterfly state features a delta function at $S_z = N/2$ and bimodal distribution centered $S_z = 0$ with width $\sim \sqrt{N}$; the separation between the peaks is a factor of 2 away from the maximal separation exhibited by the GHZ state. **(b)** The sensing signal under Haar-random evolution features damped oscillations with a frequency $\omega = N$ (see Appendix D). **(c)** Metrological gain, $2N/\eta^2$, vs. N for (red) the Heisenberg limit, (black) the standard quantum limit, our sensing protocol with (blue solid) local and (dashed) global controls. For up to $N = 20$, the Haar-random prediction is in agreement with exact quantum dynamics of a 1D spin chain after the scrambling time (data points). **(d)** Improvement in sensitivity, η , as a function of evolution time, t , for a locally interacting system. The sensitivity initially as $\eta^{-1} \sim t^d$ owing to the ballistic operator growth and saturates at $\eta^{-1} \sim N$ at the scrambling time, t_s .

\hat{V} . The mean outcome is given by

$$\begin{aligned} \langle \hat{V} \rangle_\phi &= \frac{1}{2} \langle \mathbf{0} | \hat{V}(t) | \mathbf{0} \rangle - \frac{1}{2} \langle \mathbf{0} | \hat{V}(t) e^{i\phi S_z} V(t) e^{-i\phi S_z} \hat{V}(t) | \mathbf{0} \rangle \\ &\quad + \text{Im} \left[e^{i\phi N/2} \langle \mathbf{0} | \hat{V}(t) e^{-i\phi S_z} \hat{V}(t) | \mathbf{0} \rangle \right]. \end{aligned} \quad (5.2)$$

For small values of ϕ , the sensitivity is $\eta_{\phi=0}^{-1} \equiv (|\partial_\phi \langle \hat{V} \rangle_\phi| / \Delta V_\phi)_{\phi=0}$. Note that only the last

term in Eq. (D.1) contributes to $\partial_\phi \langle \hat{V} \rangle_{\phi=0}$, and $\Delta V_{\phi=0} = 1$ since $\langle \hat{V} \rangle_\phi = 0$ and \hat{V} is a Pauli operator. Thus, the sensitivity is given by $\eta_{\phi=0}^{-1} = N/2 - \langle \mathbf{0} | \hat{V}(t) S_z \hat{V}(t) | \mathbf{0} \rangle$, which is simply the difference in polarization between the first and second trajectory of $|\psi_B\rangle$.

To understand how our protocol performs when U is generated by many-body time-evolution, let us first analyze the sensitivity at late times. For many classes of dynamics (e.g. ergodic quantum circuits, Floquet dynamics, or Hamiltonian dynamics at infinite temperature), late-time correlation functions can be approximated by modeling the time-evolution U as a Haar random unitary. Applying this approximation to our protocol, the second trajectory of the butterfly state, $\hat{V}(t) |\mathbf{0}\rangle$, becomes a random state, which has a binomial distribution of polarization with mean zero and width $\sim \sqrt{N}$. For angles that are small compared to the inverse width of this distribution, $\phi \ll 1/\sqrt{N}$, we can approximate the action of the signal on the second trajectory by the identity operation, i.e. $e^{i\phi S_z} \hat{V}(t) |\mathbf{0}\rangle \approx \hat{V}(t) |\mathbf{0}\rangle$. The signal thus applies a relative phase of $\phi N/2$ to the second trajectory compared to the first. This results in a sinusoidal expectation value $\langle \hat{V} \rangle_\phi \approx \sin(\phi N/2)$ [Fig. 5.2(b)]. Taking the derivative with respect to ϕ , the sensitivity is $\eta \approx 2/N$: a factor of 2 away from the strict Heisenberg limit.

To analyze the performance of our protocol beyond the late-time limit, it is instructive to rewrite the sensitivity as follows:

$$\eta_{\phi=0}^{-1} = \frac{1}{2} \left(N - \sum_i \langle \mathbf{0} | \sigma_i^z \hat{V}(t) \sigma_i^z \hat{V}(t) | \mathbf{0} \rangle \right). \quad (5.3)$$

The two terms are, again, the mean polarizations of the first and second trajectories of the butterfly state. From the above expression, we see that the latter is given by a sum over local out-of-time-order correlators (OTOCs), a well-known diagnostic for quantum information scrambling. Intuitively, each OTOC quantifies the support of the time-evolved operator $V(t)$ on a qubit i : the OTOC is one when $V(t)$ does not have support on i (since $\hat{V}(t)$ and σ_i^z commute), and decays to zero once $V(t)$ gains support. The sensitivity is given by the number of OTOCs that have decayed. This is proportional to the number of spins in the support of $\hat{V}(t)$, which is known as the *operator size* \mathcal{S} of $\hat{V}(t)$. Specifically, we have $\eta^{-1} \sim \mathcal{S}/2$.

We can leverage this connection to understand the sensitivity of our protocol at earlier times. Under local-interacting ergodic dynamics, the size typically grows ballistically in time, $\mathcal{S} \sim (v_B t)^d$, where v_B is the butterfly velocity and d is the spatial dimension. Hence, the sensitivity improves in time as $\eta^{-1} \sim (v_B t)^d$. This growth continues up to the *scrambling time*, $t_s \sim N^{1/d}/v_B$. After this time, the operator has support on the entire system and we recover the Heisenberg-limited sensitivity obtained from Haar-random dynamics, $\eta^{-1} \approx N/2$.

A few remarks are in order. First, operators can grow faster than ballistic under dynamics with long-range interactions. For instance, under all-to-all-interactions, operators typically grow exponentially in time, $\mathcal{S} \sim e^{\lambda t}$, where λ is the Lyapunov exponent. From Eq. (5.3), this leads to a faster improvement in the sensitivity over time and an earlier saturation to the Heisenberg-limit.

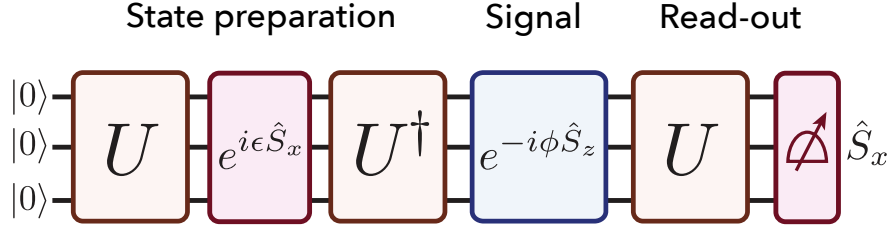


Figure 5.3: Butterfly metrology with only global control. State preparation involves a global rotation $e^{i\epsilon \hat{S}_x}$. The signal is detected by measuring the total spin polarization $\langle \hat{S}_x \rangle$.

Second, the late-time polarization of the second butterfly trajectory may be non-zero for dynamics with a non-zero conserved quantity (e.g. Hamiltonian dynamics at finite temperature). To see this, note that evolution under U cannot change the density of any conserved quantities in the initial state $|\mathbf{0}\rangle$. Therefore, instead of a Haar-random state, we expect the second trajectory of the butterfly state to resemble a random state drawn from the *Gibbs ensemble*, at a temperature/chemical potential set by the energy/charge density of the initial state. This leads to a Heisenberg-enhanced sensitivity with a pre-factor reduced by the polarization density m of the Gibbs state, $\eta^{-1} \approx N(1 - m)/2$.

5.2 Global control

While the above protocol uses a local rotation to generate the butterfly state, this requirement is not strictly necessary. In particular, we can replace both the local rotation and local read-out with entirely global operations (Fig. 5.3). Namely, to prepare the butterfly state, we utilize the global rotation $e^{i\epsilon \hat{S}_x}$, under the spin operator $\hat{S}_x = \frac{1}{2} \sum_i \sigma_i^x$. To read-out, we measure the total polarization along the x -direction, $\langle \hat{S}_x \rangle$.

To understand the sensitivity of the global protocol, we begin by considering two limits. First, in the absence of *any* time-evolution (i.e. $U = \mathbb{1}$), the protocol reduces to N independent copies of Ramsey spectroscopy if we set $\epsilon = \pi/4$. Thus, at time zero, the global protocol is standard quantum limited, $\eta^{-1} \sim \sqrt{N}$. (This contrasts with the local protocol, which had no sensitivity at time zero [3].) Second, in the limit of late times, let us decompose the global rotation into an identity and non-identity component, $e^{i\epsilon \hat{S}_x} \equiv a \hat{1} + i\tilde{V}$, where $a = \cos^N(\epsilon)$ and \tilde{V} is traceless. Thus, the global protocol produces the butterfly state,

$$|\tilde{\psi}_B\rangle = a |\mathbf{0}\rangle + i\tilde{V}(t) |\mathbf{0}\rangle. \quad (5.4)$$

To maximize the QFI, the butterfly state should be an approximately equal superposition of its two trajectories, which entails setting $\epsilon \sim 1/\sqrt{N}$. Deferring the details to Appendix D, we find that for a Haar random unitary, the optimal sensitivity is achieved at $\epsilon = 1/\sqrt{2N}$, and has a Heisenberg-scaling sensitivity, $\eta^{-1} = 1/\sqrt{2eN} \approx 0.43N$.

We find that the sensitivity smoothly interpolates between these two limits as we tune the evolution time from 0 to t_s . To see this, we again leverage the connection to operator spreading. Note that, for a rotation angle ϵ , the operator \tilde{V} initially consists of $\sim \epsilon N$ local operators, separated in space by a typical distance $\sim 1/\epsilon$ (working in 1D for simplicity). This can be seen by expanding the global rotation as a Taylor series in ϵ , and noting that the order- ϵN terms dominate. Now, suppose that we set the evolution time (or conversely, set ϵ) so that each local operator time-evolves to have support on a region of size $\mathcal{S} \sim 1/\epsilon$. In this case, the typical behavior of the global protocol resembles that of $\sim N/\mathcal{S}$ copies of the *local* rotation protocol performed in parallel. Each copy has inverse sensitivity $\sim \mathcal{S}$, which add in quadrature to give a total sensitivity $\eta^{-1} \sim \sqrt{N\mathcal{S}}$. As we increase time, and thus increase \mathcal{S} , the sensitivity smoothly improves from the SQL to the Heisenberg limit.

To quantify the relative improvement in sensitivity compared to the SQL, we can consider the notion of the *metrological gain*, $G \equiv N/\eta^2$. From the discussion above, we expect the metrological gain to increase smoothly in time as $G \sim \mathcal{S}$, from $G \approx 1$ at early times to $G \approx (0.43)^2 N \approx 0.18N$ after the scrambling time.

5.3 Experimental proposals

The universality of our approach opens the door to realizations in a wide variety of quantum sensing platforms. In Appendix D, we describe four implementations of our protocols, in: (i) an array of dipolar Rydberg atoms [49], (ii) atoms coupled in an optical cavity [195], (iii) superconducting qubits with analog interactions [11, 41], and (iv) a trapped ion quantum computer [76, 197]. All of these systems feature readily time-reversible interactions and thus, we show, can attain a Heisenberg-scaling sensitivity using our protocol.

Here, we focus on two additional, particularly promising implementations of our protocol, in ensembles of nitrogen-vacancy (NV) center defects in diamond. Despite immense interest in using NV centers for quantum metrology, achieving a quantum-enhanced sensitivity with NV centers has remained an elusive goal. We provide two experimental blueprints to achieve this goal, making use of our protocol with local and global controls, respectively.

For the first, we consider a diamond sample with a relatively high concentration of spin-1/2 nitrogen (P1) defects, such that each NV center is surrounded by a large cluster of P1 spins [278]. Conventionally, the P1 spins do not provide a sensing resource, since they cannot be read out optically. Nevertheless, in our local control protocol, we can utilize information scrambling among the P1 spins to achieve a large metrological enhancement. Specifically, each NV center interacts with its surrounding P1 centers, and the P1 centers interact with each other, via intrinsic magnetic dipolar interactions. This allows an implementation of our protocol, in which the NV center provides local control and the P1 centers comprise the remaining spins. Crucially, the dipolar interactions can be time-reversed using microwave pulses and standard Hamiltonian engineering techniques (Appendix D). Additionally, the NV center can be polarized and read-out via optical excitation, and the P1 centers can be polarized by working at cryogenic temperatures or using a hyperpolarization scheme.

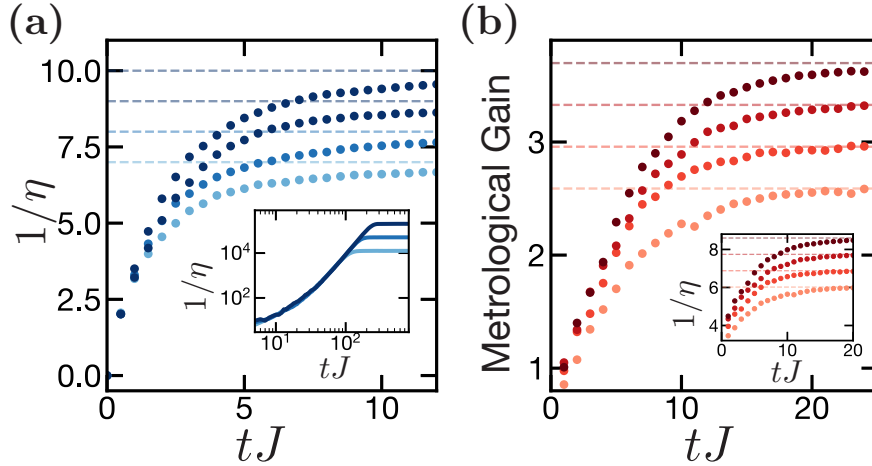


Figure 5.4: Numerical simulations for the sensing protocol under the dynamics of two experimental platforms. (a) The sensitivity of our protocol with *local* controls for a hybrid spin system, consisting of a single NV center surrounded by a cluster of P1 centers. The simulations are performed via exact diagonalization with $N \in [14, 20]$ total spins. After an initial growth period, the sensitivity saturates at $\eta = 2/N$ (dashed line), consistent with our expectation for fully scrambled dynamics. The inset displays the sensitivity for large-scale systems, $N \sim 10^4 - 10^5$, simulated via a stochastic growth model (Appendix D). (b) The metrological gain, $1/(N\eta^2)$, and sensitivity (inset) of our protocol with *global* controls implemented for a dense ensemble of NV centers. The total number of spins is $N \in [14, 20]$ spins. For both systems, the density of spin defects is 100 ppm, corresponding to an average nearest-neighbor interaction of ~ 1 MHz.

We explore the results of our proposal by performing numerical simulations. In Fig. 5.4(c), we simulate the sensitivity as a function of evolution time for a three-dimensional cluster with up to $N = 20$ P1 defects. The density of P1 defects is 100 ppm, corresponding to a typical spacing of ~ 4 nm and a nearest-neighbor interaction strength of ~ 1 MHz. At early times, the sensitivity improves rapidly in time, indicating the initial growth of the time-evolved operator $\hat{V}(t)$. At later times, the sensitivity saturates at $\eta \approx 2/N$, consistent with the Haar-random expectation.

To understand the behavior of larger system sizes, we consider a stochastic model for operator growth dynamics based on the coupling strengths of the magnetic dipolar interaction (see Appendix D) [52, 269, 270]. For a cluster of 10^6 spins, we find that the sensitivity exhibits a sustained period of super-polynomial growth, which is consistent with expectations for long-range $1/r^3$ interactions in three dimensions [270]. In principle, for a bulk diamond sample, the sensitivity would continue increasing for as long as the coherence of the spins is maintained. This timescale is ultimately limited by decay processes, which lead to $T_1 \sim 10$

Table 5.1: Summary of proposed implementations.

Experimental platform	Protocol	Time-reversal method
Hybrid spin system	Local	Hamiltonian engineering
Ensemble of NV centers	Global	Hamiltonian engineering
Dipolar Rydberg atoms	Both	Rydberg-state encoding
Atoms in optical cavity	Global	Sign of laser detuning
Superconducting qubits	Both	Conjugation by π -pulses
Trapped ions	Both	Phase of laser excitation

ms at room temperature and $T_1 \sim 1$ s at low temperatures; in practice, imperfections in the pulse sequence would likely contribute to a faster decoherence.

For our second implementation, we consider a dense ensemble of NV centers and utilize the interactions *between* NV centers to achieve a metrological enhancement. This features a key advantage compared to our previous implementation, by removing the need to polarize the P1 centers. This scenario is naturally suited to our protocol with global controls, since microwave pulses drive the entire ensemble of NV centers simultaneously. As before, time-reversed dynamics can be achieved via Hamiltonian engineering techniques (see Appendix D).

In Fig. 5.4(d), we simulate our global protocol as a function of time for a small cluster of NV centers. We plot both the sensitivity and the metrological gain, $G = \eta^{-2}/N$. After a brief evolution time, the metrological gain surpasses 1, indicating an improved sensitivity compared to the standard quantum limit. The sensitivity continues to improve over time until it reaches the a saturation value of $\eta \approx 0.43/N$, consistent with our Haar-random predictions. As before, we also simulate a stochastic model for the operator growth dynamics and demonstrate that, for a large-scale system, the sensitivity would improve at a super-polynomial rate in time (Appendix D).

5.4 Robustness to errors

An important feature of our protocol is its robustness to experimental errors (see Appendix D for a detailed analysis). Similar to other time-reversal-based sensing protocols [66, 100], our protocols maintain a Heisenberg-limited sensitivity in the presence of both read-out and initialization errors. Our protocol is also particularly robust against coherent errors that can be time-reversed; for example, low-frequency fluctuations in quantum gates [197]. Such errors simply modify the unitary evolution from $U \rightarrow U'$, which has no effect on the sensitivity as long as the modified unitary U' scrambles similarly to the original unitary U .

Incoherent errors that accumulate during time evolution, or near the sensing time, lead to a larger suppression in the sensitivity. The suppression factor is closely related to the fidelity of the so-called Loschmidt echo, and generally decays in time as $e^{-2\gamma \int_0^t dt' \mathcal{S}(t')}$, where γ is the local error rate and $\mathcal{S}(t)$ is the operator size [223]. We emphasize that all quantum-enhanced

sensing schemes are limited by decoherence in a qualitatively similar fashion. Nevertheless, our protocol may offer an advantage with respect to decoherence by allowing for a wider range of interactions, which could lead to a reduction in either the total evolution time, t , or the effective decay rate, γ .

5.5 Conclusion

We have presented a general sensing protocol that employs scrambling dynamics to achieve Heisenberg-limited sensitivities. By eliminating the need for finely tuned interactions, our approach opens the door to realizing quantum enhanced-sensing on a wide range of physical systems and can guide the development of future quantum sensing technologies.

Beyond applications in quantum metrology, experimentally demonstrating a sensitivity beyond the standard quantum limit provides a lower bound on the multi-particle entanglement present in a quantum system [120]. In particular, achieving a sensitivity of $\eta \approx 2/N$ via fully scrambling dynamics guarantees an entanglement depth of $k \geq N/4$, i.e. that there exists a cluster of at least $N/4$ entangled spins. Thus, our protocol can serve as a useful benchmarking tool for verifying the preparation of large-scale entanglement on near-term quantum devices.

Chapter 6

Adiabatic preparation of thermofield double states

Coherent quantum simulators offer the potential to explore correlated quantum phenomena beyond those found in the natural world. A principal challenge to achieve this potential is *cooling*, i.e. preparing low-temperature states of strongly-interacting quantum systems [245]. Cooling is essential to realizing large-scale natural quantum phenomena such as quantum phase transitions [217] and non-Fermi liquids [56], as well more exotic phenomena of interest for quantum computing and even, quantum gravity.

Within the context of quantum gravity, in particular, a central goal is to prepare the so-called thermofield double (TFD) state at low temperatures [168]. The TFD state is the canonical purification of the system's thermal density matrix, which consists of pure quantum state on two copies of the original system. In quantum systems with a gravitational dual, such as the Sachdev-Ye-Kitaev model [173], the TFD state gives rise to a space-time geometry consisting of two entangled black holes [168]. This forms the backbone of leading proposals for experimentally exploring models of quantum gravity, including traversable wormhole dynamics [44, 90, 176], reconstructions of the space-time geometry [162], and the complexity-action conjecture [43]. More generally, for any quantum system, the TFD state can be used to obtain a low-temperature thermal state by tracing out one of its copies.

Despite extensive interest, the experimental requirements for preparing a TFD state remain largely unknown. Existing proposals rely on variational optimization and have been tested only empirically on very small systems [179, 237, 255, 272]. Given a lack of both physical understanding and rigorous performance guarantees, it remains uncertain whether such methods will scale to larger systems. At the same time, rigorous algorithms to prepare TFD states exist, but it is not clear whether they can be implemented in quantum experiments before fault tolerance [50].

In this Chapter, we provide a simple and efficient *adiabatic* protocol for preparing a thermofield double state of the SYK model. Our approach centers upon the Maldacena-Qi

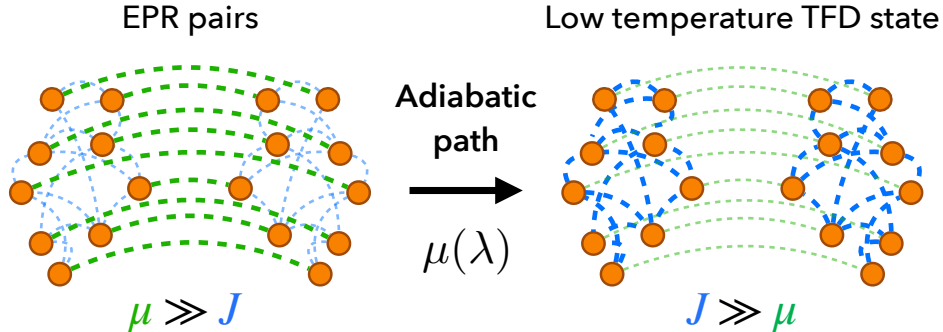


Figure 6.1: Adiabatic protocol to prepare the thermofield double (TFD) state. For couplings much greater than the interaction strength, $\mu \gg J$, the ground state of the coupled Hamiltonian, Eq. (6.1), resembles EPR pairs between the left and right system (left). For small couplings, $\mu \ll J$, the ground state is near the TFD state at a temperature set by μ (right). Our protocol prepares the TFD state by initializing EPR pairs and slowly decreasing the coupling along an adiabatic path $\mu(\lambda)$.

Hamiltonian [170]

$$H_{\text{MQ}} = H_L + H_R + i\mu \sum_{j=1}^N \chi_L^j \chi_R^j, \quad (6.1)$$

which couples two identical copies of the SYK model, H_L and H_R , with a bilinear coupling μ between them. At large μ , the ground state of the coupled Hamiltonian consists of EPR pairs between the two systems, which can be efficiently prepared on a quantum device. At small μ , Maldacena and Qi showed that the ground state is a low temperature TFD state [170]. Our protocol interpolates between these two limits: One starts in the large- μ limit and slowly decreases μ to prepare a low-temperature TFD state (Fig. 6.1).

To establish the effectiveness of this protocol, we perform a detailed analysis of the low-energy properties of the coupled Hamiltonian. Through large- N numerics, we show that the Hamiltonian is gapped with a ground state closely resembling the TFD state at all values of μ . We further show that the low-energy dynamics are controlled by an emergent semi-classical mode, which generalizes the “boundary graviton” mode found at low temperatures [170]. To understand such behavior theoretically, we provide a microscopic framework based on the eigenstate thermalization hypothesis (ETH) [72], which reproduces the relevant low-energy features without any explicit reference to gravitational properties of the Hamiltonian [61].

With this physics in hand, we propose three protocols for preparing the TFD state: (i) a quantum adiabatic protocol, which prepares the ground state of Eq. (6.1) to a high many-body fidelity in time $O(N)$, (ii) a semi-classical adiabatic protocol, which prepares the TFD state to within a high *local* fidelity in time $O(1)$, and (iii) a diabatic protocol, which provides a further speed-up on (ii) by exploiting the specific behavior of the semi-classical

mode. We demonstrate that effectiveness of each approach through a combination of large- N numerics and theoretical analysis. We conclude by discussing corrections for finite-size systems, and extensions to systems beyond the SYK model. Our work opens the door to efficiently realizing low-temperature dynamics and gravitational phenomena on near-term quantum devices.

6.1 Ground state of the coupled system

Consider the SYK Hamiltonian with N Majorana fermions [133, 173, 218]:

$$H_{\text{SYK}} = \sum_{i < j < k < l}^N J_{ijkl} \chi_i \chi_j \chi_k \chi_l \quad (6.2)$$

where J_{ijkl} are random variables drawn from a Gaussian distribution with energy variance $J^2/(6N)$, and hereafter we set $J = 1$. A TFD state is a special purification of the thermal state, defined as:

$$|\text{TFD}_\beta\rangle = \frac{1}{\mathcal{Z}_\beta} e^{-\frac{\beta}{2} E_n} |n\rangle_L |n\rangle_R. \quad (6.3)$$

where L and R are two subsystems of N Majorana fermions, $|n\rangle$ and E_n are the eigenstates / eigenvalues of H_{SYK} , β is the effective temperature, and $\mathcal{Z}_\beta = \sum_n e^{-\beta E_n}$ is the partition function.

The original evidence for a relation between the ground state and a TFD state is based on analytic calculations motivated by the study of eternal traversable wormholes. In Ref. [168], Madacena and Qi analyzed the coupled system in the limit $\mu \gg J$ and showed that the ground state has a relatively is relatively close to TFD state at an effective temperature $\beta \sim \mu^{-2/3}$; namely, the overlap is $e^{-\eta N}$ with $\eta \sim \mu/J$. Similar analysis shows that local observables in the two states differ by a small relative factor of $\sim \mu/J$.

To understand whether such agreement holds outside of the regime of analytic control, we turn to large- N numerics, which provide an exact solution in the thermodynamic limit. We first examine static, local observables. Specifically, we compare the two-sided correlation function $i \langle \chi_L \chi_R \rangle$ between (i) the ground state of Eq. 6.1, and (ii) a thermal Gibbs ensemble for a single copy of the SYK model. If the ground state matches a finite-temperature TFD state, then one expects the correlation function for both states to agree as a function of energy density of a single side (i.e. $\langle H_L \rangle$). In Fig. 6.2, we plot the correlator for the two states and indeed observe nearly perfect agreement at all energy densities. By matching the single-sided energy densities, we also determine the effective temperature of the TFD state as a function of μ (Fig. 6.2(a)). We observe two clear regimes: $\beta_{\text{eff}} \sim \mu$ for large μ , and $\beta_{\text{eff}} \sim \mu^{2/3}$ for small μ , consistent with prior expectations.

We next utilize time-dependent simulations to compare the thermalization dynamics for the two states. In particular, we calculate the dynamical correlation function $\langle \chi_L(t) \chi_R(0) \rangle$, where we begin in the ground state of Eq. 6.1 and evolve under the *uncoupled* Hamiltonian

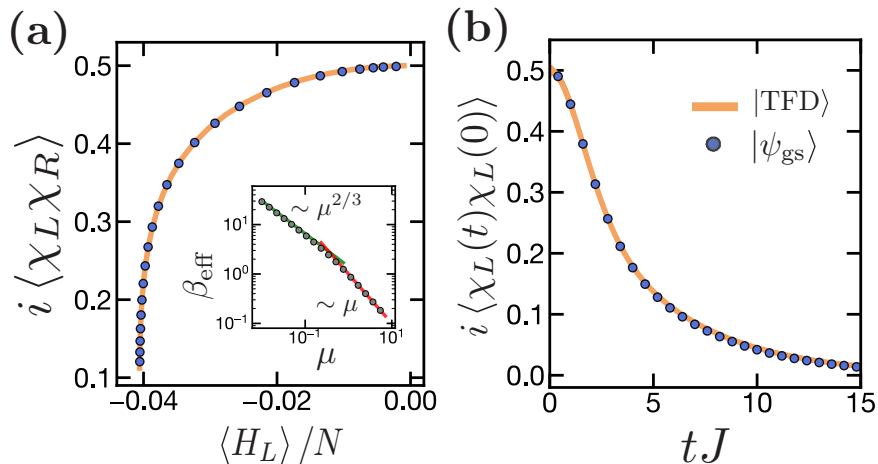


Figure 6.2: Comparison between the ground state of Eq. 6.1 (blue) and a TFD state with respect to Eq. 6.2 (orange). (a) Large- N numerical results for the left-right correlator, $i\langle\chi_L\chi_R\rangle$, in the two states as a function of single-side energy density, $\langle H_L\rangle$. The results are obtained by sweeping μ and β , respectively. (inset) By matching the left-right correlator in the two states, we obtain the effective temperature of the TFD state, β_{eff} as a function of μ . (b) Dynamical correlation function, $i\langle\chi_L(t)\chi_L(0)\rangle$ beginning in the ground-state at $m\mu = 0.2J$ (blue) and the TFD state (yellow) at the corresponding temperature, $\beta = \beta_{\text{eff}}(\mu) = 3.72J$. In both cases, the system is evolved under the uncoupled Hamiltonian, Eq. 6.2. Similar agreement holds for other values of μ within the range of numerical stability, i.e. $\mu \gtrsim 0.1J$.

(i.e. setting $\mu = 0$). This simulates a quenched experiment where one suddenly turns off the coupling. In Fig. 6.2(b), we compare these dynamics to the correlation function for a single-sided SYK model in a thermal state, where the temperature is chosen so that the energy density matches the ground state. We observe close quantitative agreement between the two scenarios across a range of coupling strengths μ .

6.2 Theoretical framework and emergent dynamics

The strong agreement observed above suggests a more general relation between the ground state and the a thermofield double state than established by the original analytic calculations. Following Ref. [61], we consider the coupled system from an analytical framework based on the eigenstate thermalization hypothesis, which relates observable dynamics to microscopic properties. Crucially, this framework predicts the emergence of semi-classical, low-energy dynamics, which we verify with large- N simulations.

We begin by considering the energy eigenstates of the system without the two-sided interaction: $|m, n\rangle$, where $|m\rangle$ and $|n\rangle$ are eigenstates of H_L and H_R , respectively. A key observa-

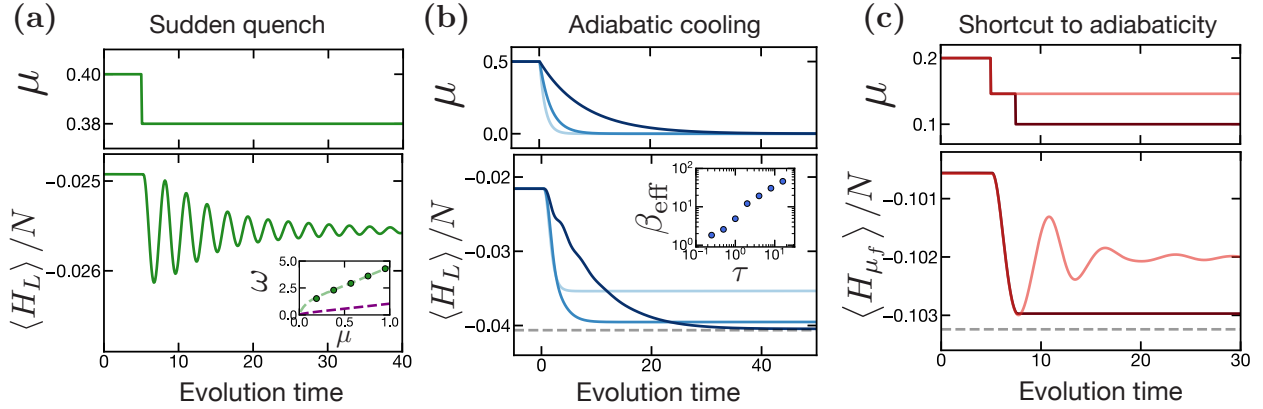


Figure 6.3: Quenched dynamics of Eq. 6.1 simulated with large- N numerics for three types of protocols: (a) a sudden quench, (b) adiabatic cooling, and (c) a two-step non-adiabatic protocol. In all cases, the initial state is a low-temperature state of Eq. 6.1. (a) The coupling is suddenly reduced from $\mu = 0.4$ to $\mu = 0.38$ (above). This gives rise to oscillations in the single-side energy density, $\langle H_L \rangle / N$ (below). (Inset) The oscillation frequency as function of μ based on: (points) the quenched simulations, and (green) the predictions of the semi-classical framework using the mass and potential described in Appendix E. For comparison, the (off-diagonal) gap of Eq. 6.1 is also shown (purple), which was obtained by simulating Eq. 6.1 in imaginary time [94]. (b) The coupling is reduced in an adiabatic fashion; in particular, it follows an exponential decay profile, $\mu(t) = 0.5e^{-t/\tau}$ (above). As τ increases, the energy density of the final state decreases (below). The energy density of the ground state of Eq. 6.2 is shown as a dashed grey line. (Inset) The effective temperature of the final state, determined from the energy density, increases as a function of the decay time, τ . (c) The coupling is reduced suddenly under a single step (light red) and under two steps (dark red). The former shows analogous oscillations to the sudden quenches of (a). By timing the second step to minimum of the first oscillation, one can “catch” the system at this energy density. The resulting state has nearly the same energy density as the final state obtained via adiabatic cooling (dashed grey). The energy density, $\langle H_{\mu_f} \rangle / N$ is shown in terms of the final coupling, i.e. Eq. 6.1 with $\mu = 0.1$.

tion from Ref. [61] is that the two-sided coupling leads to a stronger interaction between pairs of identical eigenstates, $|m, m\rangle$, than among pairs of dissimilar eigenstates. In particular, the matrix element induced by the interaction is $\sum_j \langle m, n | \chi_L^j \chi_R^j | s, r \rangle = \sum_j \langle m | \chi^j | s \rangle \langle n | \chi^j | r \rangle$. For general pairs of eigenvalues, the sum consists of random matrix elements which destructively interfere, yielding a scaling of $\sim \sqrt{N}$; however, if $m = n$ and $s = r$, the matrix elements are squared and constructively interfere, yielding a scaling of $\sim N$.

This motivates a simplifying approximation: The relatively strong interactions decouple the sector of equal eigenstates, which we henceforth refer to as the “diagonal” sector, from

the sector of non-equal eigenstates. Under this assumption, one can solve for the effective dynamics and predict the ground state and low energy properties. Specifically, using the framework of ETH, the interaction between states is described by $\sum_j |\langle m | \chi^j | s \rangle|^2 = f(E_m, E_s)$, where the function $f(E_m, E_s)$ is a smooth function of the energies and short-ranged, i.e. $f(E_m, E_s) \approx 0$ for $|E_m - E_n| \gg 1$.

In the thermodynamic limit, the resulting dynamics are governed by a one-dimensional Schrodinger equation:

$$i\partial_t\psi(E) = \left[-\frac{1}{2m(E)}\partial_E^2 + V(E) \right] \psi(E) \quad (6.4)$$

where the potential energy $V(E)$ and effective mass $m(E)$ are directly related to the Green's function, $G_\beta(t) = i \langle \chi(t)\chi(0) \rangle_\beta$ of the *uncoupled* system (Appendix E). It is instructive to rewrite this equation in terms of energy density, $\epsilon \equiv E/N$:

$$\frac{i}{N}\partial_t\psi(\epsilon) = \left[-\frac{1}{2N^2m(\epsilon)}\partial_\epsilon^2 + V(\epsilon) \right] \psi(\epsilon). \quad (6.5)$$

We observe that the effective Planck constant is $\hbar_{\text{eff}} \equiv 1/N$. Hence, in the semiclassical limit $N \gg 1$, the low-energy dynamics are described by a simple harmonic oscillator centered about the minimum of $V(\epsilon)$. It follows that ground state is a Gaussian wavefunction with energy width $\Delta E \sim \sqrt{N}$. This state possesses an $\mathcal{O}(1)$ overlap with TFD state with matching energy density.

We emphasize that these predictions are only a leading-order approximation, based on the assumption that the diagonal sector is approximately decoupled from the off-diagonal states. Remarkably, we show this approximation closely resembles the leading-order approximation taken in Maldacena and Qi (Appendix E). Indeed, Maldacena and Qi predicted the emergence of a one-dimensional harmonic oscillator, which in the context of gravity, is interpreted as the ‘‘boundary graviton’’ mode. We compare the mass and potential for this mode to the predictions of Eq. 6.5 and find precise agreement (Appendix E). Thus, the diagonal sector provides a microscopic interpretation of the previously observed gravitational mode.

It is not clear, however, whether the semi-classical dynamics will persist in the presence of higher-order corrections outside of the $\mu \ll J$ limit. To test this behavior, we utilize large- N simulations to simulate a quenched experiment. Specifically, we begin close the ground state of the coupled Hamiltonian and suddenly reduce the value the coupling. In the harmonic oscillator picture, this corresponds to a slight shift in the location of the minimum of the potential $V(E)$. Under the predicted semi-classical dynamics, we expect the system to oscillate around the new minimum. In Fig. 6.3(a), we indeed observe such oscillations in the single-side energy density. Moreover, we calculate the oscillation frequency and find close agreement with the prediction from Eq. 6.5 [Fig. 6.3(a)].

6.3 Adiabatic condition and shortcuts to adiabaticity

Having established that the low-energy dynamics of Eq. 6.1 are well-approximated by a simple harmonic oscillator mode, we are now equipped to analyze the resource requirements for preparing a low temperature TFD state. We begin by considering a naive application of the quantum adiabatic theorem. To prevent transitions to the excited states, the following condition must hold:

$$\frac{|\langle \psi_{\text{gs}} | \partial_t | \psi_{\text{exc}} \rangle|}{\Delta E} \ll 1 \quad (6.6)$$

where $|\psi_{\text{gs}}\rangle, |\psi_{\text{exc}}\rangle$ are the wavefunctions for the ground state and first excited state, respectively, and ΔE is their energy gap. The energy gap for the harmonic oscillator is an $\mathcal{O}(1)$ value, while the numerator is $\mathcal{O}(N)$. This implies that the total time required for preparing a state with high many-body overlap with the ground state is $t \sim N$.

However, this analysis is too stringent. As we have seen, the low-energy dynamics are governed by a semiclassical harmonic oscillator. This raises the possibility of more efficiently preparing a semiclassical approximation of the ground state. Consider the analogy of a classical ball in a potential well. By moving the well slowly compared to the oscillation frequency, the ball will remain close the bottom of the well. More specifically, once the well has stopped moving, the ball will retain a small velocity and oscillate at the bottom of the well. But the amplitude of oscillations can be suppressed parametrically by increasing the total timescale of the preparation.

In the coupled system, the position of the ball corresponds to the single-sided energy density of the quantum state. The classical analogy thus implies that the single-side energy density can be lowered in $\mathcal{O}(1)$ time. However, unlike the quantum ground state, the final state prepared in this way would retain small, extensive fluctuations in the single-side energy. In other words, it would resemble a TFD state with small fluctuations in temperature.

To confirm the effectiveness of this approach, we perform quenched simulations using large- N numerics. We begin close to the ground state for $\mu/J = 0.2$ and reduce μ to zero via an exponential ramp, $\mu(t) = \mu_0 e^{-t/\tau}$, with decay time τ . For $\tau = 20J$, the single-sided energy reduces slightly under the ramp, yet remains well above the single-sided ground state. By contrast, extending the decay time to $\tau = 200J$, we observe that the single-side energy continuously decreases and reaches a final value close to the ground state energy of the single side; indeed, we estimate that the final state corresponds to a single-side temperature of $\beta \approx 40J$. By studying the final energy as a function of the ramp time, we observe a direct correspondence between the energy / temperature of the final state and the protocol duration. This is consistent with expectations from the semiclassical dynamics and verifies that low temperature TFD-like states can be prepared adiabatically in $\mathcal{O}(1)$ time.

Interestingly, we can also implement a *non-adiabatic* protocol that takes advantage of the semi-classical dynamics. The idea is to perform a two-step quench: First, we suddenly decrease the value of μ to induce oscillations, but as soon as the system reaches the minimum of the first oscillation we lower the coupling again to “trap” it at the lower energy. To confirm this approach, we begin with $\mu/J = 0.2$ and quench to a lower value $\mu/J = 0.12$.

As expected, we observe large oscillations in the single-side energy about the new minimum. However, we now add a second step: At the time that the energy reaches the bottom of the first oscillation, we shift the coupling again to $\mu/J = 0.1$. We observe that this strongly suppresses the previous oscillations, and the energy remains close to the minimum value. Indeed, the final energy density is close to that reached by adiabatically lowering the coupling adiabatically from $\mu/J = 0.2$ to $\mu/J = 0.1$.

A few comments are in order regarding the numerical simulations. First, we note that initial state in our simulations, unlike in our proposed experimental implementation, is a finite temperature state with respect to Eq. 6.1, rather than the ground state. This is a technical detail related to the large- N calculations and is discussed in more detail in Appendix E. We have verified that our results are qualitatively consistent across a range of initial temperatures, suggesting that they capture the expected behavior of initializing in the ground state. Second, the accuracy of our simulations is limited by discretization errors, which imply that our simulations are stable only for a finite duration of time. As the dynamics are slower with decreasing μ , this restricts us to studying the range $\mu \gtrsim 0.1$ before the errors in our simulations become significant.

Finite-size results—While the discussion so far has focused on the the large- N limit, we now consider the behavior of the coupled model in finite-sized systems. Indeed, prior numerical studies have shown that the ground state closely resembles a TFD state, with a fidelity that decreases slightly for system sizes between $N = 10$ and 14 Majoranas per side [94, 170].

To better understand this behavior, we utilize Krylov subspace methods to compute the ground state $|\psi_{\text{gs}}\rangle$ of Eq. 6.1 for up to system sizes of $N = 24$. We decompose the ground-state wavefunction as:

$$|\psi_{\text{gs}}\rangle = \sum_{m,n} c_{mn} |m\rangle_L |n\rangle_R, \quad (6.7)$$

where $|m\rangle$ and $|n\rangle$ are eigenstates of H_L and H_R , respectively. Based on this decomposition, we compute two quantities: (i) the total support of the wavefunction within the diagonal sector, $\mathcal{N}_d = \sum_n |c_{nn}|^2$; and (ii) the maximum fidelity of the *normalized* diagonal wavefunction with respect to a TFD state, i.e. $\mathcal{F}_d = \max_{\beta} \sum_n |c_{nn} e^{-\beta/2 E_n}|^2 / (\mathcal{N}_d Z_{\beta})$. The maximum fidelity of the ground state with respect to a TFD state is the product of these two quantities: $\mathcal{F} \equiv \max_{\beta} |\langle \psi_{\text{gs}} | \text{TFD}_{\beta} \rangle|^2 = \mathcal{F}_d \mathcal{N}_d$.

In Fig. 6.4(a-b), we plot the two quantities across a range of μ and system sizes. Interestingly, we observe opposite trends for the finite-size scaling: the diagonal support decreases with respect to system size, while the normalized fidelity slightly increases. The latter observation is consistent with our prior analysis based on the ETH framework, where we found that the diagonal wavefunction has $\mathcal{O}(1)$ overlap with a TFD in the thermodynamic limit. Meanwhile, the former observation indicates that the decrease in *overall* fidelity observed in prior numerics is the result of the loss of support in the diagonal sector. It also suggests that decreasing diagonal support is responsible for the eventual exponential decrease in fidelity

computed in analytic calculations (we recall that the predicted fidelity in the small μ limit is $e^{-\eta N}$, with $\eta \sim \mu/J$ [170]).

We next turn to examining the nature of the diagonal coefficients, c_{nn} . Consistent with prior results, we observe that the coefficients at small system sizes follow a power-law decay, $c_{nn} \sim 1/(E_n - k)^p$, rather than the exponential decay expected for a TFD state [94]. However, by examining several system sizes, we find that the best-fit exponent p is non-universal, ranging from $p \approx 1$ at $N = 8$ to $p \approx 4$ at $N = 24$.

The origin of such polynomial decay can, in fact, be understood within the context of the ETH framework under a suitable modification. Recall that our previous analysis assumed the thermodynamic limit, such that the diagonal hoppings due to the two-sided coupling are *local* in energy, i.e. $f(E_m, E_n) \ll 1$ for $|E_m - E_n| \gg 1$. However, in a small-sized system, there is little separation between the energy scale for which $f(E_m, E_n)$ decays and the energy bandwidth of the system. To model such non-local behavior, one can instead consider $f(E_m, E_n)$ to be a flat function, $f(E_m, E_n) = f_0$. A simple derivation based on this ansatz yields a predicted ground state whose coefficients decay linearly with energy, i.e. $c_{nn} \sim 1/(E_n - k)$, closely matching the observed wavefunction at $N = 8$. Moreover, modeling the couplings as non-local in energy also leads to an explanation for the large support of the ground-state wavefunction within the diagonal sector at small system sizes. On the other hand, at larger sizes, we expect the local nature of the interactions to become increasingly relevant, which is consistent with the deviations from linear behavior.

We hasten to emphasize that the ETH framework does *not* predict that the diagonal coefficients will converge to an exponential form in the large- N limit. Rather, the framework indicates only that the course-grained diagonal wavefunction, $\Psi(E)$, will approach a Gaussian peak with variance $\sim N$. At finite sizes, we can approximate the course-grained wavefunction as $\Psi(E_n) \approx \sqrt{\Omega(E_n)}c_n$, where $\Omega(E_n)$ is the analytical density of states [93]. In Fig. , we plot $\Psi(E_n)$ for $N = 24$ and compare it to the corresponding wavefunction of the TFD state with maximum overlap. The close resemblance between the wavefunctions explains the large overlap of the ground state with a TFD state, despite the fact that the individual coefficients do not follow an exponential trend.

6.4 Discussion and outlook

We have demonstrated an efficient adiabatic approach for preparing TFD-like states in the coupled SYK model. Our protocol requires essentially no additional requirements compared to the quantum simulation of the original SYK model; the only experimental overhead is the doubling of the system and the ability to prepare a set of EPR pairs. This establishes that preparing low-temperature TFD states is no longer barrier for “gravity in the lab” simulations.

Prior to this work, it has been conjectured that low energy states for non-local fermionic models cannot be efficiently prepared from a simple state, i.e. via a constant-depth circuit

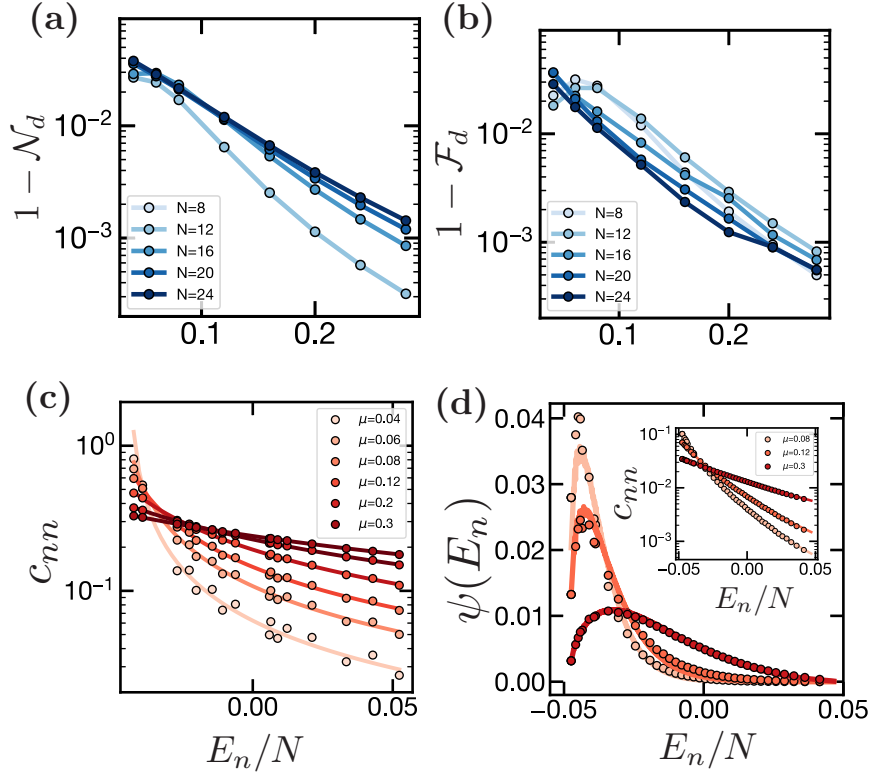


Figure 6.4: Finite-sized analysis of the ground state of Eq. 6.1 for systems with $N \in [8, 24]$ Majoranas per side. The overlap between the ground state and a TFD state is decomposed into two quantities: (a) the support within the diagonal sector, $\mathcal{N}_d = \sum_n |c_{nn}|^2$, and (b) the maximum overlap of the *normalized* diagonal wavefunction, $\mathcal{F}_d = \max_\beta \sum_n |c_{nn} e^{-\beta/2 E_n}|^2 / (\mathcal{N}_d Z_\beta)$. (c) For $N = 8$, the individual diagonal coefficients c_{nn} (points) are well-fit by a linear decay function, $A/(E_n - k)$, where k is a fitting parameter and A is constrained by normalization (solid lines). (d) For $N = 24$, the coefficients are fit by a different polynomial function, $A/(E_n - k)^p$, with $p \approx 4.5$ (inset). Despite the non-exponential behavior, the course-grained wavefunction, $\psi(E_n) \equiv \sqrt{\Omega(E_n)} c_{nn}$, where $\Omega(E_n)$ is the density of states is in reasonable agreement with the wavefunction for the best-fit TFD state (solid lines). Note that the number of coefficients has been subsampled for visual convenience.

[83, 109]. Our results provide explicit counter-evidence for this conjecture for the class of SYK models.

Our work also suggests several future directions. First, while we have focused on preparing entangled TFD states, it is natural to ask if the two copies of the system are necessary for reaching low temperature, or if (single-sided) low energy states can be prepared with a low-

depth circuit acting on a single copy of the system. Previous work has suggests similarities between the low-energy dynamics of the coupled SYK model and a single copy of the SYK model under an applied field [139]. It would be interesting to analyze whether an adiabatic approach would succeed in preparing low energy states in this context.

Second, our analysis relied an assumption regarding the approximate decoupling of the diagonal sector under the ETH framework [61]. We have shown that this assumption is well-motivated for the SYK model using analytic and empirical evidence, e.g. static observables, dynamical correlation functions, and quenched dynamics. (We also find that it holds in small-sized systems, albeit for different reasons.) A key open question is whether this approximation holds in other systems. Previous work relating on boundary state CFTs may provide a framework for addressing this question [51, 201], and large-scale numerical studies, e.g. via DMRG, could provide useful empirical evidence.

Third, we note that there exist certain situations where even small deviations from the diagonal approximation may become relevant. For example, they could lead to large corrections when performing the two-sided teleportation protocol near the scrambling time [177]. In such cases, it would be important to project out the off-diagonal components of the ground state. In principle, this could be achieved by performing phase estimation with respect to the observable, $B = H_L - H_R$, and post-selecting on states for which $B \approx 0$. Understanding the cost of this additional purification would be important for applications in the longer term.

Lastly, we recall that the fact that TFD state is close to the ground state of a *local* system has important consequences for understanding the emergence of a bulk geometry [162]. Indeed, the two-sided Hamiltonian for the coupled SYK model corresponds to the generator of the boost symmetry in the bulk. Identifying other instances in which a TFD state arises as the ground state of a local Hamiltonian system would provide tantalizing evidence for a holographic interpretation.

Appendix A

Details on many-body chaos in the Sachdev-Ye-Kitaev model

A.1 Numerical methods

Jordan-Wigner transformation

To represent the SYK Hamiltonian numerically, we map N Majorana operators into $N/2$ Pauli spin-1/2 operators using the canonical Jordan-Wigner transformation:

$$\chi^i \rightarrow \begin{cases} \left(\prod_{j < k} \sigma_j^z \right) \sigma_k^x, & i \text{ even} \\ \left(\prod_{j < k} \sigma_j^z \right) \sigma_k^y, & i \text{ odd} \end{cases} \quad (\text{A.1})$$

where $0 \leq i < N$ is the Majorana index and $k = \text{floor}(i/2)$. We note that the SYK Hamiltonian (Eq. 1 of Chapter 2) contains a single Z_2 symmetry, corresponding to the conservation of fermionic charge parity, i.e. $P = (\sum_i \sigma_i^z) \pmod 2$ [60]. To take advantage of this symmetry, we prepare initial states in one of the symmetry sectors and evolve under the relevant sector of the Hamiltonian. We verify that this simplification has a negligible effect on correlation functions compared to initial states that span both symmetry sectors.

Krylov subspace methods

The computational workhorse in our study is a class of iterative methods known as Krylov subspace methods [211, 216]. These methods approximate the action of the unitary operator $U(t) = e^{-iHt}$ by projecting H onto a smaller subspace. This subspace – the so-called Krylov subspace – is formed by successively multiplying an initial state $|\psi\rangle$ by the Hamiltonian: $\{|\psi\rangle, H|\psi\rangle, H^2|\psi\rangle, \dots, H^m|\psi\rangle\}$, where $m \sim \mathcal{O}(1)$ is the dimension of the subspace. Time evolution of the initial state is then approximated by $e^{-iHt}|\psi\rangle \approx p_m(H)|\psi\rangle$, where $p_m(H)$ is a polynomial of degree m and is determined by exponentiating the projection of H within the subspace (whose dimensions are $m \times m$).

System size (N)	Hardware	Memory, matrix-free	Memory, full-matrix	Time per curve (10 points)
20	GPU (Nvidia V100)	100 KB	60 MB	<1 sec
30		2 MB	10 GB	20 sec
40		40 MB	1 TB	30 min
50		1 GB	100 TB	20 hrs
60	CPU (Intel KNL) 512 nodes	40 GB	6 PB	70 hrs

Table A.1: Summary of computational requirements for computing OTOCs using Krylov subspace methods [2]. All computations in this work were performed using matrix-free methods; for comparison, we also list the memory requirement for standard, full-matrix computations.

The key advantage of this approach is that its core computational component is matrix-vector multiplication, a significantly more efficient task than exact diagonalization (ED). For example, for the SYK Hamiltonian with N Majoranas, the time complexity of matrix-vector multiplication (using sparse matrix techniques) scales as $\mathcal{O}(N^4 2^{N/2})$, whereas that of exact diagonalization is $\mathcal{O}(2^{3N/2})$. Moreover, matrix-vector operations can take advantage of two important high-performance computing techniques. First, they can be distributed across many parallel processes, thereby reducing the workload of each individual processor. Second, the memory cost can be substantially reduced using matrix-free methods: Instead of storing the Hamiltonian in matrix form, one computes the action of $H|\psi\rangle$ “on the fly” using a symbolic representation of H , which contains only $\mathcal{O}(N^4)$ terms. In particular, we estimate the memory requirement with and without matrix-free methods as:

$$\begin{aligned}
 \text{matrix-free} &= (\text{dimension of Hilbert space}) \times (\text{number of Krylov vectors}) \times (\text{bytes per element}) \\
 &\quad + (\text{number of terms in } H) \times (\text{bytes per coefficient}) \\
 &= 2^{N/2-1} \times 5 \times (16 \text{ bytes}) + \binom{N}{4} \times (20 \text{ bytes})
 \end{aligned}
 \tag{A.2}$$

$$\begin{aligned}
 \text{full-matrix} &= (\text{dimension of Hilbert space}) \times (\text{number of Krylov vectors}) \times (\text{bytes per element}) \\
 &\quad + (\text{dimension of Hilbert space}) \times (\text{number of terms in } H) \times (\text{bytes per coefficient}) \\
 &= 2^{N/2-1} \left[5 \times (16 \text{ bytes}) + \binom{N}{4} \times (24 \text{ bytes}) \right]
 \end{aligned}
 \tag{A.3}$$

In Table A.1, we summarize the computational requirements of our simulations and provide details on the specific hardware used in our study. Crucially, the substantial memory

savings offered by matrix-free methods allowed us to run the majority of our computations (up to $N = 50$) on GPUs, with a run time of at most one day per disorder average. By contrast, prior to implementing matrix-free methods, the largest systems we were able to simulate were $N \approx 40$ due to the intensive memory requirements. All of our numerics were performed with a custom open-source Python package called `dynamite` [2], which provides a frontend interface for PETSc and SLEPc, two standard libraries for parallelized linear algebra computations [15, 113, 211].

We note that there are two potential drawbacks with Krylov subspace techniques. First, as an approximate technique, they introduce small numerical errors compared to exact evolution; nevertheless, these errors are well-controlled by working with a sufficiently large subspace and dividing the time evolution into a series of small time steps. To estimate the magnitude of errors present in our study, we compute the absolute difference of out-of-time-order correlators (OTOCs) using Krylov subspace methods and exact diagonalization,

$$\mathcal{E} = \max_t |F_{\text{ED}}(t) - F_{\text{Krylov}}(t)|. \quad (\text{A.4})$$

The results are shown in Fig. A.1 for system sizes $N \in [12, 24]$ and times $tJ \in [0, 20]$. In all cases, the absolute error is less than 10^{-12} and is thus neglected for the rest of this study. Second, and more substantially, the computational time scales (approximately linearly) with the evolution time. Thus, Krylov subspace methods are best suited for evolving to intermediate timescales (e.g. $tJ \lesssim 100$ where J is the typical coupling strength), which is the case for all correlators considered in this study.

Disorder averaging

As discussed in Chapter 2, we approximate thermal quantities by taking expectation values with respect to Haar-random initial states [101, 165, 235]:

$$\langle \hat{O} \rangle_\beta = \frac{\text{Tr} [\hat{O} e^{-\beta H}]}{\text{Tr} [e^{-\beta H}]} \approx \frac{\langle \tilde{\psi} | e^{-\frac{\beta}{2} H} \hat{O} e^{-\frac{\beta}{2} H} | \tilde{\psi} \rangle}{\langle \tilde{\psi} | e^{-\beta H} | \tilde{\psi} \rangle}. \quad (\text{A.5})$$

The error in this approximation is expected to decrease exponentially with N ; in particular, at infinite temperature the error scales inversely with the dimension of the Hilbert space, while at finite temperature it scales with the number of states in the thermal ensemble, i.e. $\text{Tr}[e^{-\beta(H-E_0)}]$ where E_0 is the ground-state energy [235]. This scaling follows from the concept of quantum typicality and is applicable to generic interacting systems (e.g. as previously demonstrated for a Heisenberg spin chain [235]).

We generate Haar-random states by drawing each (complex) element in $|\tilde{\psi}\rangle$ from a random Gaussian distribution. In practice, we average simultaneously over the initial states and disorder realizations of the coefficients in the Hamiltonian, J_{ijkl} . Both forms of sampling – the Hamiltonian coefficients J_{ijkl} and the random initial state $|\tilde{\psi}\rangle$ – give rise to numerical

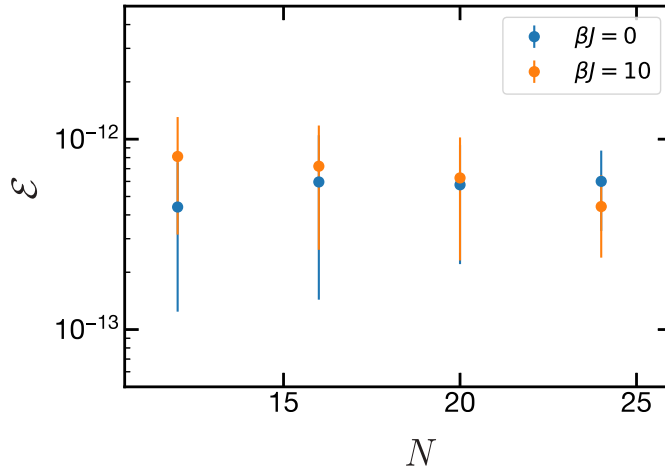


Figure A.1: The numerical error of OTOCs computed with Krylov subspace methods compared to exact diagonalization. The error is quantified as the maximum difference in the OTOCs for timescales $tJ \leq 20$ (Eq. A.4). Error bars represent the standard deviation over 100 disorder realizations.

fluctuations which decrease significantly with system size. For the former, the SYK model is self-averaging, implying that as $N \rightarrow \infty$ the correlation functions for a *single* disorder realization approach the disorder average; specifically, one expects these fluctuations to decrease as a function of the number of random J_{ijkl} coefficients, i.e. polynomially with system size. For the latter, our method for approximating thermal averages with random pure states (Eq. A.5) is expected to be accurate up to exponential corrections in the system size.

To test these expectations, we compute the magnitude of numerical fluctuations with respect to each type of disorder. In particular, we calculate the fluctuations in the timescale t^* given by $\tilde{F}(t^*) = 0.25$ in two different ways: (a) by fixing J_{ijkl} and calculating the standard deviation with respect to different initial states; and (b) by averaging first over initial states and then determining the standard deviation with respect to different realizations of J_{ijkl} . These results are shown in Fig. A.2. In general, both types of fluctuations are on the same order of magnitude, and their magnitude increases dramatically at small system sizes and low temperatures. The size dependence is consistent with the aforementioned self-averaging behavior, while the temperature dependence is attributed to the reduced number of states that contribute to the behavior of the low-temperature correlators.

Although both sources of error decrease with system size, we emphasize that at the system sizes relevant for our study, both types of fluctuations are significant and extensive disorder averaging is required to obtain precise results (e.g. we perform hundreds of disorder realizations even for $N \approx 40$ Majoranas). As a result, while single curves have been obtained for 60 Majoranas, the primary results for this study were based on $N \leq 46$ Majoranas, for

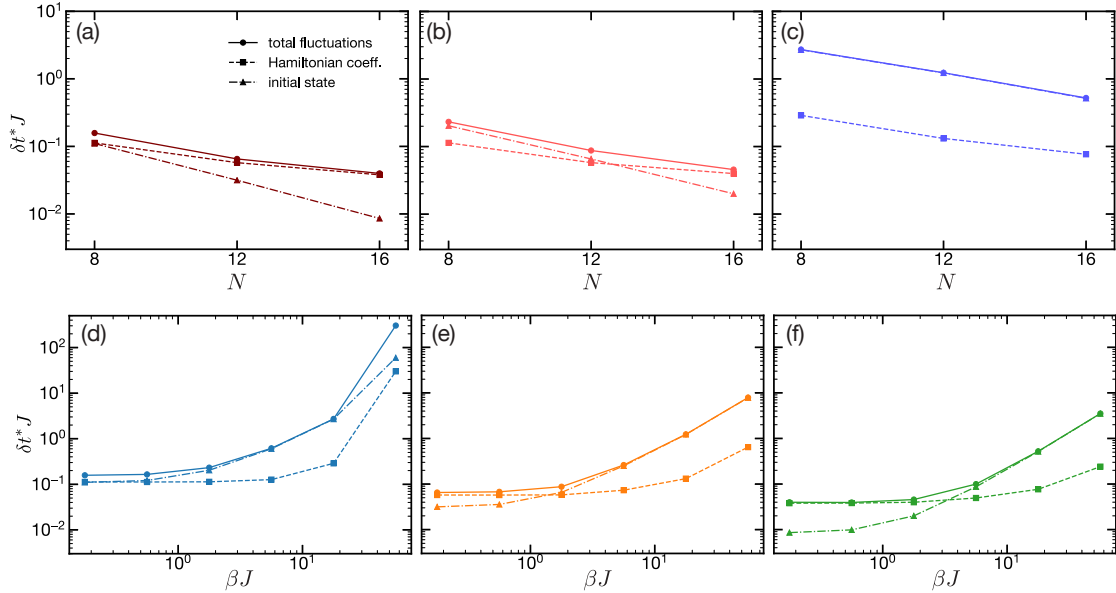


Figure A.2: Disorder fluctuations of the OTOCs, as measured by the standard deviation of t^* given by $1 - \tilde{F}(t^*) = 0.25$. Two sources of disorder contribute to the total fluctuations (solid): the Hamiltonian coefficients J_{ijkl} (dashed) and the initial random state (dot-dashed). (a-c) Fluctuations vs. system size for (a) $\beta J = 0.18$, (b) $\beta J = 1.8$, and (c) $\beta J = 18$. (d-f) Fluctuations vs. temperature for (d) $N = 16$, (e) $N = 24$, and (f) $N = 32$.

which sufficient disorder averaging could be performed.

A.2 Characterizing the Lyapunov exponent

Fitting to a simple exponential

Several prior studies of many-body chaos have characterized Lyapunov exponents by fitting OTOCs to a simple exponential form, $\sim e^{\lambda t}$ [129, 148, 227, 259]. In this section, we apply this fitting procedure to our numerical data and compare our results to the known theoretical values for λ .

More specifically, we perform least squares regression on each regularized OTOC curve, $\tilde{F}(t) \equiv F(t)/F(0)$, using the fitting function, $a + be^{\lambda_{\text{fit}} t}$, within a range defined by $F_0 \leq 1 - \tilde{F}(t) \leq F_1$. We then extrapolate the fits at different system sizes using a quadratic extrapolation, $\lambda_{\text{fit}}(N) = \lambda_0 + \lambda_1/N + \lambda_2/N^2$. In Fig. A.3, we illustrate this procedure and show the extrapolated values for λ using various values for F_0 and F_1 . It is clear that this approach does not converge to the exact values of λ for any temperature; indeed, the estimated values are approximately a factor of 2 smaller than the theoretical expectations.

A few remarks are in order. First, our fitting procedure differs slightly from other studies in the sense that we perform the fits for a fixed range in the (normalized) magnitude of the OTOCs rather than a fixed range in time, i.e. $t_0 \leq t \leq t_1$. We chose this approach because the growth of OTOCs occurs at different timescales, depending on the temperature and system size. To compare directly to previous work, we also tried fitting our data across a fixed range in time and found no improvements in the estimates for λ . Second, we observe that our fitting results depend sensitively on the choice of F_0 and F_1 , though for all choices of these parameters our results for λ were inconsistent with theoretical expectations.

In principle, one expects the best results using $F_1 \ll 1$, as the simple exponential form is only defined for the initial growth. For a more precise estimate of the range of validity, we turn to the semiclassical solution for $F(t)$ at low temperatures, given by (A.6), which takes into account higher order terms. By plotting this full solution against the leading order exponential, we find that the exponential is a good approximation only for $F_1 \lesssim 0.05$. In finite-size numerics, probing such small magnitudes presents several challenges. First, the absolute size of numerical fluctuations is approximately constant at all times, and thus the relative size of fluctuations compared to the signal is enhanced for small F_1 . Second, one requires the timescale for which the exponential reaches F_1 to be much longer than the dissipation time. As the former timescale scales as $\log F_1 N$ and the latter timescale is constant, achieving this separation becomes more difficult as F_1 decreases. These challenges, as well as the poor results of our exponential fits, underscore our motivation for developing a fitting procedure that takes into account higher-order terms.

Fitting to the low-temperature, semiclassical solution

We next consider fitting our numerical data to semiclassical form of the OTOC at low temperatures (see Section below) [175]:

$$\frac{F(t)}{F(0)} = \frac{U(2\Delta, 1, \frac{1}{z})}{z^{2\Delta}}, \quad z = \frac{e^{\lambda_{\text{fit}} t}}{N_{\text{fit}}} \quad (\text{A.6})$$

where U is the confluent hypergeometric function, $\Delta = 1/4$ (i.e. the conformal dimension), and we include two fitting parameters – λ_{fit} and N_{fit} – associated with the Lyapunov exponent and the system size, respectively. This function provides a phenomenological model for capturing higher-order effects that occur after the initial exponential growth (i.e. saturation behavior). Nevertheless, we emphasize that the exact form of the function is only rigorously justified at low temperatures where the SYK model is described by the Schwarzian action.

As before, we perform least squares regression within a window defined by $F_0 \leq F(t) \leq F_1$. We then extrapolate the fitting parameter λ_{fit} using a quadratic function in $1/N$ (the actual system size, not the fitting parameter N_{fit}). In Fig. A.4, we summarize the results of this approach. In general, we find better agreement with theoretical predictions than with the previous exponential fits, especially at high temperatures. Upon closer inspection, however, it is evident that the fitted values for λ do not extrapolate to the theoretical predictions, regardless of the choice for F_0 and F_1 . We conclude that this fitting procedure is not

robust against finite-size and high-temperature corrections away from the low-temperature, semiclassical limit where it was derived.

Finite-size rescaling method

Having ruled out the possibility of fitting our data to a simple functional form, we now introduce a model-free method for extracting the Lyapunov exponent based on finite-size scaling. The only assumption we make is that the OTOCs approximately obey a rescaling

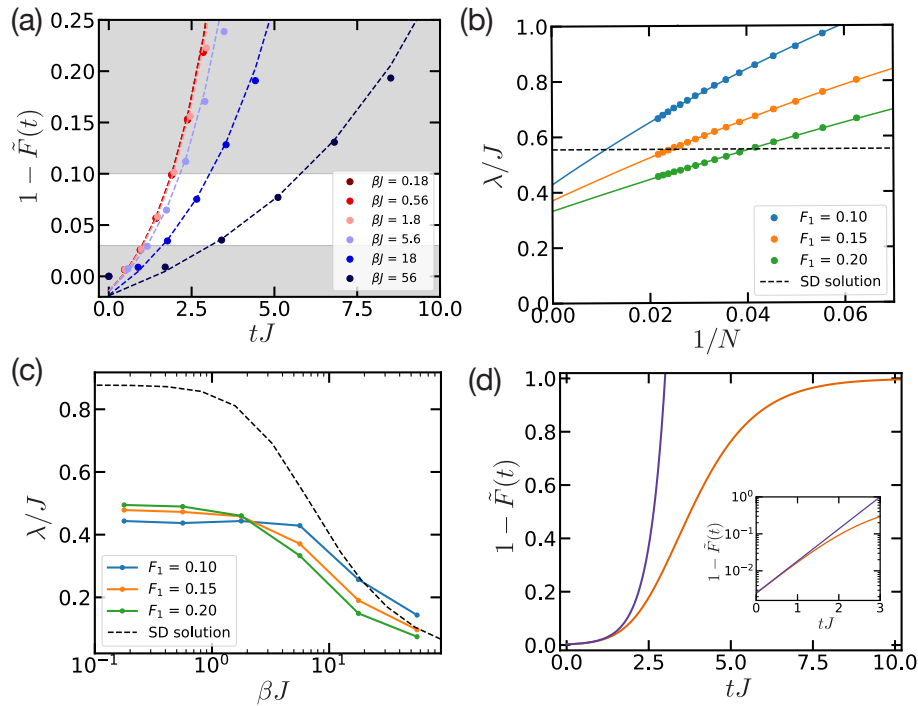


Figure A.3: Extracting λ by fitting to a simple exponential. (a) For each set of data, we apply least squares regression based on the fitting function, $a + be^{\lambda_{\text{fit}}t}$, (dashed line) within a window $F_0 \leq F(t) \leq F_1$ (white area). (b) We then extrapolate λ_{fit} as a function of system size through quadratic function in $1/N$ (solid lines). The results are shown for $\beta J = 5.6$, $F_0 = 0.03$, and various values for F_1 . The dashed line represents the theoretical prediction for λ . (c) Extrapolated results for λ as a function of temperature for several values of F_1 ; these exhibit significant disagreement with the theoretical results (dashed line). (d) The theoretical curve for $\tilde{F}(t)$ at low temperatures, given by (A.6), (orange) compared to the leading-order simple exponential (purple).

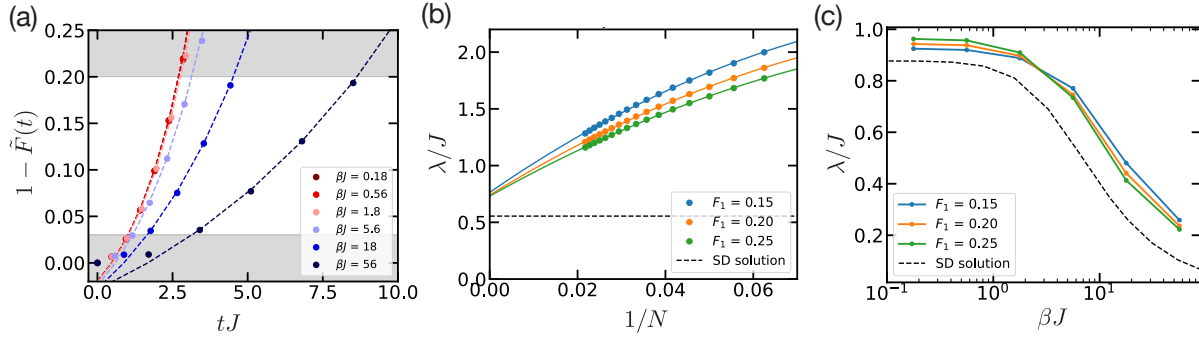


Figure A.4: Extracting λ by fitting to the low-temperature, semiclassical solution, i.e. (A.6) with $\Delta = 1/4$. Analogous to Fig. A.3, we fit each set of data using least squares regression (a) and perform a $1/N$ extrapolation on the best-fit values for λ (b), as shown for $\beta J = 5.6$. (c) The extrapolated results for $\lambda(\beta)$ are compared with the theoretical prediction (dashed line); there is noticeable disagreement regardless of the fitting window specified by F_1 (in all cases $F_0 = 0.03$).

symmetry of the form,

$$\begin{aligned}
 N &\rightarrow rN \\
 t &\rightarrow t + \frac{1}{\lambda} \log r
 \end{aligned}
 \tag{A.7}$$

This symmetry is expected to hold for any many-body chaotic model governed by ladder diagrams close to the semiclassical limit.

Based on this symmetry, we devise the following numerical procedure to extract λ . First, we compute the timescale at which the OTOCs reach a fixed value $\tilde{F}(t_N) = F_0$, for system size N ; this requires interpolating our numerical data and solving for the intercept at F_0 . Second, we estimate $\lambda_{\text{fit}}(N)$ via a numerical derivative, i.e. $1/\lambda_{\text{fit}}(N) = (t_N - t_{N-1})/(\log N - \log(N-1))$. Finally, we extrapolate $\lambda_{\text{fit}}(N)$ to $N \rightarrow \infty$ using a polynomial extrapolation function, e.g. $\lambda_{\text{fit}}(N) = \lambda_0 + \lambda_1/N + \lambda_2/N^2$. The extrapolations for various temperatures are shown in Fig. A.5.

A few comments are in order. First, the extrapolation is performed on a subset of system sizes whose lowest 20 eigenstates lie within $\Delta E = 1/\beta$ of the ground state. This criterion is meant to rule out systems that are dominated by the discreteness of the energy spectrum, for which no effective (replica-diagonal) action exists. Furthermore, to avoid overfitting, we use a quadratic extrapolation function for temperatures corresponding to $\beta \geq 5.6$ and a linear extrapolation for lower temperatures. The reported error bars on our final results correspond to the standard error of the fitting parameter, λ_0 .

Second, we note that the rescaling procedure depends on the value of F_0 . In the large N limit, the choice of this parameter is arbitrary, as the rescaling symmetry (A.7) is expected to hold for all values of F_0 . At finite sizes, however, there are higher-order corrections that

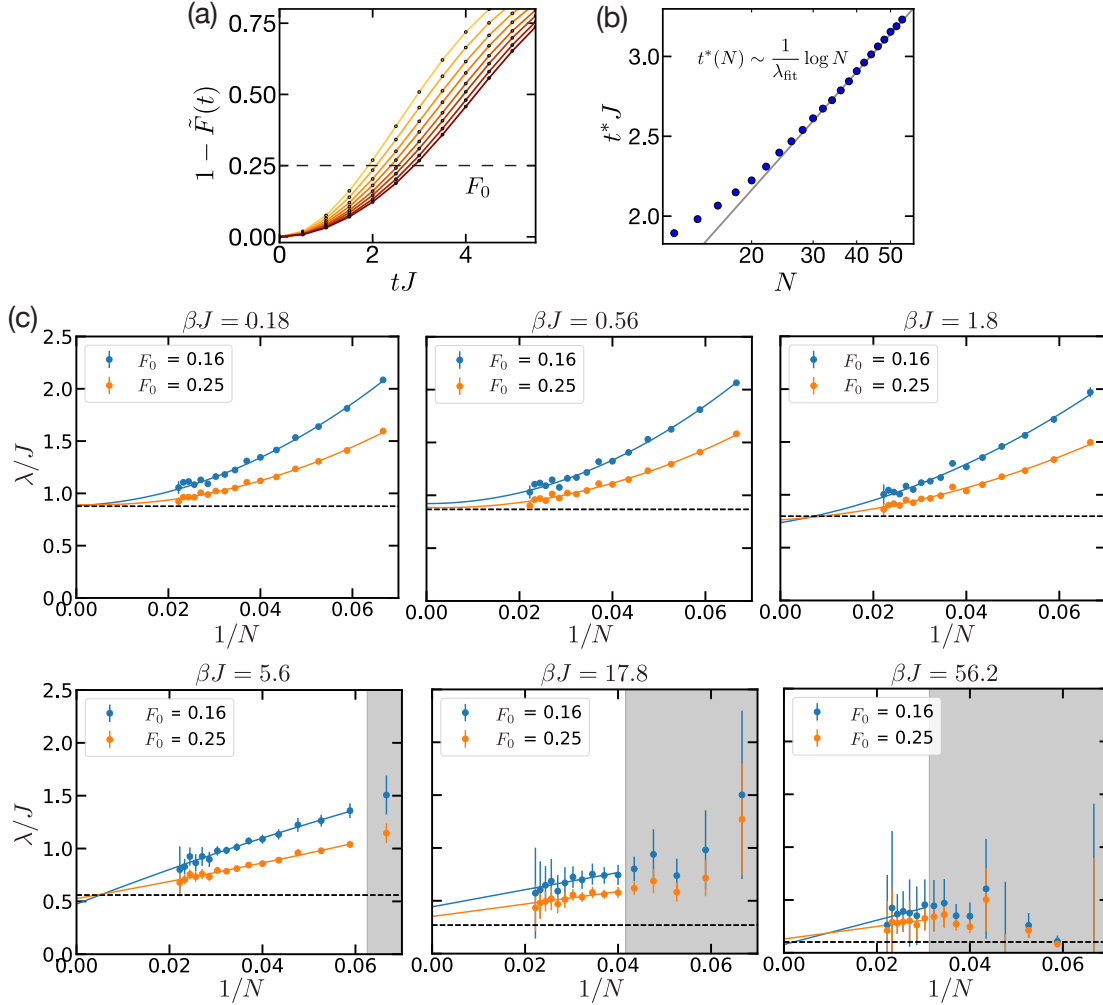


Figure A.5: Finite-size rescaling procedure for extracting λ . (a) For a fixed temperature, we numerically simulate OTOCs across a range of system sizes. At each system size, the time $t^*(N)$ is determined for which the (normalized) OTOC, $\tilde{F}(t) \equiv F(t)/F(0)$, reaches a fixed value, i.e. $\tilde{F}(t^*) = 1 - F_0$. Data shown correspond to $\beta J = 1.8$ and $F_0 = 0.25$. (b) The Lyapunov exponent λ is computed from the slope of $t^*(N)$ with respect to $\log N$ via an extrapolation procedure. (c) The extrapolation procedure is shown for each temperature and $F_0 = 0.16$ and 0.25 . We approximate $\lambda_{\text{fit}}(N)$ (data) by computing the finite difference $\Delta t^*(N)/\Delta(\log N)$ between successive system sizes. We then perform a $1/N$ extrapolation (solid lines) on the subset of system sizes (white area) whose first 20 eigenvalues are within $\Delta E = \beta J$ of the ground state. To avoid over-fitting, the extrapolation relies on a quadratic function for $\beta J \geq 5.6$ and a linear function for lower temperatures.

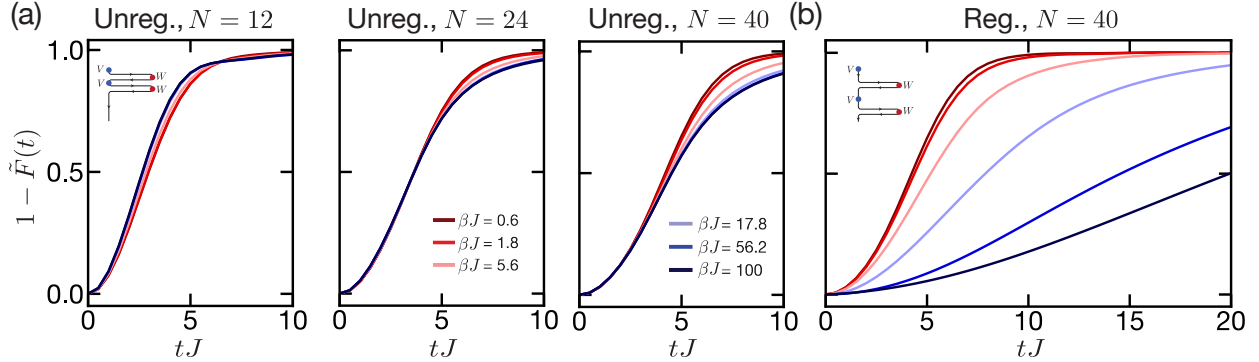


Figure A.6: Numerical data for unregularized (a) and regularized (b) OTOCs at various temperatures. (a) The unregularized data correspond to the real part of the OTOC normalized by the initial value and is shown for three different system sizes: $N = 12, 24$ and 40 . For $N = 12$ the lower temperature correlators grow faster than the high temperature correlators; this trend is reversed for $N \gtrsim 24$. (b) Compared to the unregularized data, the growth timescale for the regularized data increases significantly at low temperatures. This discrepancy is attributed to the difference in the scrambling time for the two types of correlators. In particular, the scrambling time for the unregularized OTOC is highly suppressed at low temperatures, implying that the observed growth in the numerics arises from dissipative dynamics rather than to chaos. (Inset) Schematic of the two configurations (unregularized and regularized), represented as a path in real (horizontal) and imaginary (vertical) time.

break the rescaling symmetry, particularly (i) at early times due to the microscopic cutoff, and (ii) at late times due to the crossover to power-law decay [13]. We thus expect an intermediate choice of F_0 to provide the best approximation. Our results in Chapter 2 are based on $F_0 = 0.25$. In Fig. A.3, we show that a different choice, $F_0 = 0.16$, provides consistent results. This demonstrates that our rescaling procedure is not overly sensitive to the precise value F_0 .

Unregularized OTOCs

In Chapter 2 and in the results presented so far, we have considered a thermally regularized OTOC, given by

$$F^{(r)}(t) \equiv \overline{\left\langle \chi_i(t) \rho^{\frac{1}{4}} \chi_j(0) \rho^{\frac{1}{4}} \chi_i(t) \rho^{\frac{1}{4}} \chi_j(0) \rho^{\frac{1}{4}} \right\rangle}. \quad (\text{A.8})$$

This form of the correlator has the advantage that it is Hermitian and can be analyzed at low temperatures with the effective low-energy action (without needing additional regularization). However, for many experiments, it is more convenient to measure the unregularized

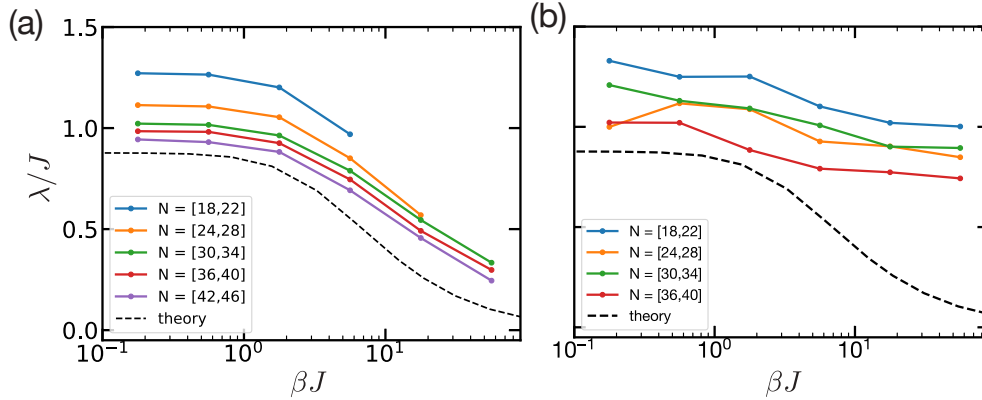


Figure A.7: The finite-size rescaling procedure applied to regularized (a) and unregularized (b) OTOCs. The data points corresponds to $\lambda_{\text{fit}}(N)$ for various size intervals and the dashed line is the theoretical prediction. The unregularized results exhibit a weaker temperature dependence, and there is a larger discrepancy from theoretical predictions at low temperatures.

OTOC, given by

$$F^{(u)}(t) \equiv \overline{\langle \chi_i(t) \chi_j(0) \chi_i(t) \chi_j(0) \rho \rangle}. \quad (\text{A.9})$$

Here, we provide numerical evidence that the unregularized correlator is subject to stronger finite-size corrections at low temperatures, a claim that is supported theoretically in later sections ¹.

In Fig. A.6(a), we present numerical data for the unregularized correlator at three system sizes: $N = 12, 24$ and 40 . As mentioned in Chapter 2, the correlator at the smallest size exhibits the *opposite* temperature dependence as expected, i.e. OTOCs at low temperatures appear to grow *faster* than at high temperatures. This trend is consistent with previous studies based on exact diagonalization [86]. At $N = 24$ we observe an inversion in this trend, and thereafter the correlator exhibits the expected qualitative temperature dependence.

However, even at the largest system size, the temperature dependence of the unregularized correlator is significantly weaker than the regularized correlator [Fig. A.6(b)]. This difference can be quantified by repeating our finite-size scaling analysis with the unregularized correlator (Fig. A.7). For temperatures above $\beta J \approx 10$, regularization has little effect on $\lambda_{\text{fit}}(N)$, i.e. the estimate for λ at size N . However, for lower temperatures, the values for $\lambda_{\text{fit}}(N)$ using the unregularized correlator show a weaker temperature dependence than in the regularized case and are substantially farther from the theoretical predictions ². This

¹Similar numerical data showing larger finite-size corrections for the unregularized correlators was also presented in [148].

²We emphasize that $\lambda_{\text{fit}}(N)$ should not be interpreted as a size-dependent Lyapunov exponent, but rather as a fitting parameter that can be extrapolated to $N \rightarrow \infty$ to determine the Lyapunov exponent.

implies that the unregularized correlator is subject to more pronounced finite-size effects, and larger system sizes are required to accurately determine the Lyapunov exponent.

We attribute these results to the fact that the scrambling time is shorter for the unregularized correlator and, hence, there is less separation between the early-time dissipative dynamics and the chaotic growth (see Sec. A.2 and A.4). Such considerations are important for numerical and experimental studies of OTOCs; however, we emphasize that they do not imply that the two forms of the correlator are characterized by distinct Lyapunov exponents. Indeed, we justify mathematically in Sec. A.3 that the Lyapunov exponent (for the SYK model) is independent of regularization.

A.3 Large N solutions

In this section, we describe the large N , semiclassical solutions for the dynamics of the SYK model. These results were derived previously via either a diagrammatic approach or from the saddle-point of a disorder averaged effective action [14, 133, 174, 219]. Finite-size corrections beyond the semiclassical solution can be computed at low temperatures via the Schwarzian action and are discussed in Sec. A.4. In Fig. A.8, we illustrate schematically the relationship between these various theories.

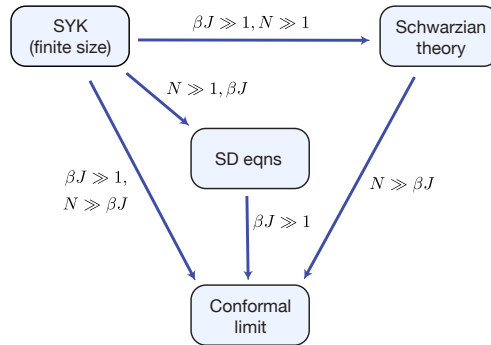


Figure A.8: Schematic relationship between various theories describing the dynamics of the SYK model. The Schwinger-Dyson (SD) equations represent the large N solution at all temperatures (A.10), while the Schwarzian action (A.24) captures finite N behavior at low temperatures. In the limit $N \gg \beta \gg 1$, both theories approach the conformal limit (A.11).

Schwinger-Dyson equations

The large N solution for the average Green's functions is given in imaginary time by the self-consistent Schwinger-Dyson equations:

$$\frac{1}{G(\omega)} = i\omega + \Sigma(\omega), \quad \Sigma(\tau) = J^2 [G(\tau)^3], \quad (\text{A.10})$$

where ω are the Fourier components with respect to τ . The real-time version of these equations is obtained by setting $\tau = it$. At low temperatures ($\beta J \gg 1$) and long timescales ($\tau J, tJ \gg 1$), the derivative term $i\omega$ can be neglected, leading to an emergent conformal symmetry. The solution in this limit is [174, 191]

$$G_c(\tau) = b \left[\frac{\pi}{\beta \sin \frac{\pi\tau}{\beta}} \right]^{1/2}, \quad G_c(it) = b \left[\frac{\pi}{i\beta \sinh \frac{\pi t}{\beta}} \right]^{1/2}, \quad (\text{A.11})$$

where $b = 1/(\sqrt{2}\pi^{1/4}) \approx 0.531$. More generally, the Green's functions can be computed at all temperatures by solving (A.10) through an iterative numerical approach [174]. This procedure converges quickly in imaginary time and yields the results shown in Fig. 3(a) of Chapter 2. In real time, the numerical analysis is more subtle, and we found that the most stable approach is the implementation proposed in [75]. We present these results in Fig. 3(b) of Chapter 2 and in Fig. A.11 below. We also rely on the real-time correlators to compute the Lyapunov exponent and magnitude of OTOCs, as described in the following section. For both real and imaginary time, we benchmarked the numerical solutions by comparing to (A.11) at low temperatures.

Kernel equation

The leading order behavior for OTOCs is computed via a set of diagrams known as ladder diagrams. In particular, one defines

$$F(t_1, t_2) \equiv \langle \chi_i(t_1) \chi_j(0) \chi_i(t_2) \chi_j(0) \rangle = \mathcal{F}_0 + \frac{1}{N} \mathcal{F}(t_1, t_2) \quad (\text{A.12})$$

and makes a growth ansatz of the form

$$\mathcal{F}(t_1, t_2) = e^{\lambda(t_1+t_2)/2} \gamma(t_{12}) \quad (\text{A.13})$$

where $t_{12} = t_2 - t_1$. The exponent is determined by solving the eigenvalue equation

$$\mathcal{F}(t_1, t_2) = \int dt_3 dt_4 K_R(t_1, t_2, t_3, t_4) \mathcal{F}_1(t_3, t_4) \quad (\text{A.14})$$

with eigenvalue one. Here K_R is the retarded kernel given by

$$K_R(t_1, t_2, t_3, t_4) = J^2 (q-1) G_R(t_{13}) G_R(t_{24}) G_W(t_{34})^{q-2} \quad (\text{A.15})$$

where $G_R(t)$ is the retarded Green's function, $G_W(t)$ is known as the Wightman function, and $q = 4$ is the number of fermions involved in each interaction in the SYK Hamiltonian (from here on, we generalize to q -body interactions). Crucially, the Wightman function depends on the regularization. In the case of the regularized OTOC, the Wightman function is given by $G_W(t) = G(t + i\beta/2)$ and can be computed numerically from the Schwinger-Dyson equations.

To determine the Lyapunov exponent (for the regularized OTOC), we perform the following numerical procedure. First, we solve for the eigenvalues of K_R for a given value of λ . This relies on the numerical results for $G_R(t)$ and $G_W(t)$ and the discretization of time into M steps. Second, we perform a binomial search to find λ corresponding to a maximum eigenvalue of one. Finally, we repeat the procedure with different values for M and extrapolate to estimate λ in the continuous limit. The numerical results for λ are shown in Fig. 1(b) of Chapter 2; we verify that the results agree with the low-temperature limit, $\lambda \approx 2\pi/\beta$.

Regularized vs. unregularized exponent

In principle, one can obtain the Lyapunov exponent for the unregularized OTOC in an analogous way: by calculating the Wightman function with no imaginary-time separation, i.e. $G_W(t) = G(t)$, and repeating the numerical procedure outlined above. However, the numerical analysis is more challenging, as the kernel is no longer Hermitian; in particular, we found that the eigenvalues are highly sensitive to numerical errors that arise from discretization and the imprecision of the Green's functions.

Nevertheless, one can show theoretically that the Lyapunov exponent is independent of regularization (for the SYK model or similar ladder-diagram theories). To do so, we begin by defining the kernel ansatz in the regularized case as

$$e^{\lambda(t_1+t_2)/2}\gamma^{(r)}(t_{12}) = J^2(q-1) \int dt_3 dt_4 G_R(t_{13}) G_R(t_{24}) G_W^{(r)}(t_{34})^{q-2} e^{\lambda(t_3+t_4)/2}\gamma^{(r)}(t_{34}) \quad (\text{A.16})$$

and in the unregularized case as

$$e^{\lambda(t_1+t_2)/2}\gamma^{(u)}(t_{12}) = J^2(q-1) \int dt_3 dt_4 G_R(t_{13}) G_R(t_{24}) G_W^{(u)}(t_{34})^{q-2} e^{\lambda(t_3+t_4)/2}\gamma^{(u)}(t_{34}) \quad (\text{A.17})$$

where $G_W^{(r)}(t) = G(t + i\beta/2)$ and $G_W^{(u)}(t) = G(t)$ and $\gamma^{u,r}(t_{12})$ is the normalizable eigenvector with respect to inner product:

$$(\gamma, \gamma)_{r,u} = (q-1) J^2 \int_{-\infty}^{\infty} dt \gamma(t) G_W^{(r,u)}(t)^{q-1} \gamma(t). \quad (\text{A.18})$$

The proof is then as follows³. By definition, (A.17) can be written in terms of the $G_W^{(r)}(t)$ as

$$e^{\lambda(t_1+t_2)/2}\gamma^{(u)}(t_{12}) = J^2(q-1) \int dt_3 dt_4 G_R(t_{13}) G_R(t_{24}) G_W^{(r)}(t_{34} - i\beta/2)^{q-2} e^{\lambda(t_3+t_4)/2}\gamma^{(u)}(t_{34}). \quad (\text{A.19})$$

³We note that during the preparation of this manuscript a similar proof was presented in [212].

We next reparameterize the time variables as $t'_1 = t_1 + i\beta/4$, $t'_2 = t_2 - i\beta/4$, $t'_3 = t_3 + i\beta/4$, and $t'_4 = t_4 - i\beta/4$. Using the fact that the integrand goes to zero at $t_{3,4} \rightarrow \pm\infty$, we can deform the integration contour and get:

$$\begin{aligned} & e^{\lambda(t'_1+t'_2)/2}\gamma^{(u)}(t'_{12} + i\beta/2) \\ &= J^2(q-1) \int dt'_3 dt'_4 G_R(t'_{13}) G_R(t'_{24}) G_W^{(r)}(t'_{34})^{q-2} e^{\lambda(t'_3+t'_4)/2} \gamma^{(u)}(t'_{34} + i\beta/2). \end{aligned} \tag{A.20}$$

In addition, using the fact that $\gamma^r(t)$ is normalizable, one can show that $\gamma^r(t + i\beta/2)$ is also normalizable with respect to the inner product for the unregularized case. We thus recover the regularized equation (A.16) and identify the relation $\gamma^{(r)}(t) = \gamma^{(u)}(t + i\beta/2)$.

In summary, changing the regularization has no effect on the growth exponent but only on the the eigenfunction $f(t)$ (which controls the magnitude of OTOCs, as shown below). More generally, this argument applies to any degree of regularization, i.e. $G_W(t) = G(t + i\eta)$, and to any other many-body chaotic model whose OTOCs are described by ladder diagrams.

Magnitude of OTOCs

The magnitude of the growing term of the OTOC is important because it determines the scrambling time and, thus, the separation between early-time dissipative dynamics and chaotic growth. In particular, we define the magnitude of exponential growth C_1 as

$$\tilde{F}(t) \equiv \frac{F(t)}{F(0)} \approx 1 - \frac{C_1}{N} e^{\lambda t} + \mathcal{O}(1/N^2) \tag{A.21}$$

Having a well-separated scrambling time, $t^* \approx 1/\lambda \log(N/C_1)$, then corresponds to $N \gg C_1$.

Recently, Gu and Kitaev derived an identity that relates the magnitude of the leading order growth term in OTOCs with other quantities computable from the Schwinger-Dyson equations and the kernel equation. The identity is given by

$$\frac{1}{C_1} = 2 \cos\left(\frac{\lambda\beta}{4}\right) t_B(\gamma, \gamma) \tag{A.22}$$

where $t_B = k'(\lambda)$ is the ‘‘branching time’’, k is the eigenvalue of the retarded kernel, (A.15), and (γ, γ) is given by

$$(\gamma, \gamma) \equiv (q-1) J^2 \int_{-\infty}^{\infty} dt \gamma(t) (G_W(t))^{q-2} \gamma(t) \tag{A.23}$$

We note that $\gamma(t)$ and $G_W(t)$ are defined in the previous section, and both depend on the choice of regularization.

For the regularized OTOC, we solve for C_1 as a function of temperature using (A.22) and the numerical solution of the kernel equation. These results are shown in Fig. A.9. At

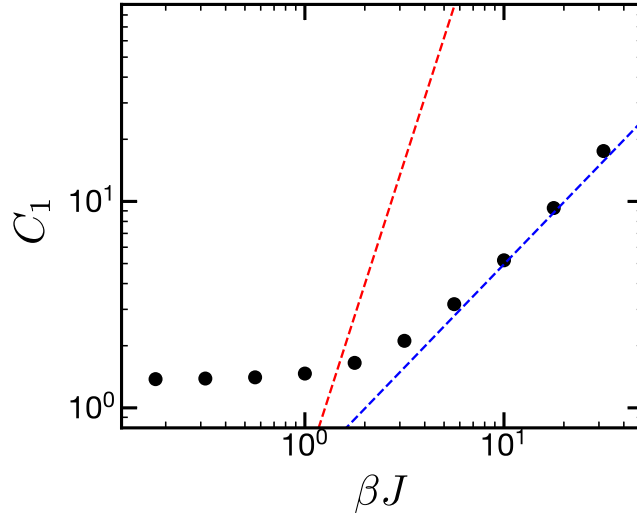


Figure A.9: The normalized magnitude, C_1 , of the leading-order term in the OTOC, $C_1/Ne^{\lambda t}$, as a function of temperature. The magnitude is calculated numerically (black) for the regularized OTOC using (A.22); at high temperatures $C_1 \approx 1.4$ and at low temperatures $C_1 \approx 0.5\beta J$, in agreement with the semiclassical solution, (A.29) (blue). For the unregularized OTOC, the semiclassical solution predicts the low-temperature scaling $C_1 \sim (\beta J)^3$ (red).

high temperatures C_1 approaches 1.4, while at low temperatures $C_1 \approx 0.5\beta J$. This latter result is consistent with previous work [104, 174] and provides validation of our numerical methods.

For the unregularized OTOC, the magnitude can in principle be calculated following the same approach; however, we confront the same numerical difficulties regarding the kernel equation as discussed in Sec. A.3 and thus leave this computation for a future work. Of course, at high temperatures ($\beta J \ll 1$), the magnitude must be the same regardless of regularization. At low temperatures ($\beta J \gg 1$), we can use the Schwarzian action to determine the scaling $C_1 \sim (\beta J)^3$, as discussed in Sec. A.4.

In combination, these results imply that having a separation of timescales is achieved in the regularized case when $N \gg \beta J$ and in the unregularized case when $N \gg (\beta J)^3$. As the latter condition is more stringent, it provides an explanation for the more severe finite-size effects observed with the unregularized correlator (see Sec. A.2).

A.4 Schwarzian action

In the previous section, we focused on the semiclassical solution of the SYK dynamics. We now discuss corrections about this limit obtained via the Schwarzian action. This 0+1 dimensional action is valid for describing the SYK model at low energies (i.e. $\beta J, \tau J \gg 1$), and is given by

$$S_{\text{Sch}} = -C_{\text{Sch}} \int_0^\beta d\tau \{f, \tau\}, \quad \{f, \tau\} \equiv \frac{f'''}{f'} - \frac{3}{2} \left(\frac{f''}{f'} \right)^2 \quad (\text{A.24})$$

where $f(\tau)$ is a function describing reparameterizations of time, i.e. $\tau \rightarrow f(\tau)$. Prior work has established the relation between the coupling coefficient C_{Sch} and parameters of the SYK model: $C_{\text{Sch}} \approx 0.01N/J$ [174]⁴. This prefactor controls the size of fluctuations about the $C_{\text{Sch}} \rightarrow \infty$ saddle-point solution.

Recently, analytical methods have been developed to solve the full dynamics of the Schwarzian action, enabling the calculation of correlation functions at all orders in $1/C_{\text{Sch}}$ [14, 144, 258]. Furthermore, these developments have established a direct correspondence between the Schwarzian action and near AdS in 1+1 dimensions [135]. In particular, the saddle-point solution is dual to classical gravity, while higher order $1/C_{\text{Sch}}$ corrections correspond to gravitational fluctuations.

Two-point correlators

We consider the two-point function, $G(z) = \langle \chi_i(z) \chi_i(0) \rangle_\beta$, where $z = it + \tau$ is complexified time and the thermal average is computed at inverse temperature β . Using the Schwarzian action, the exact result for $G(z)$ can be computed and is given by [14, 144, 258]

$$G_{\text{Sch}}(z) = \frac{1}{\mathcal{N} (2C_{\text{Sch}})^{2\Delta} \Gamma(2\Delta)} \int ds_1 ds_2 \rho(s_1) \rho(s_2) e^{-\frac{s_1^2}{2C} z - \frac{s_2^2}{2C} (\beta - z)} |\Gamma(\Delta - i(s_1 + s_2)) \Gamma(\Delta + i(s_1 - s_2))|^2 \quad (\text{A.25})$$

where $\rho(s) = \frac{s}{2\pi^2} \sinh(2\pi s)$ is the density of states, $\Gamma(\cdot)$ is the Gamma function, and the normalization factor is equal to

$$\mathcal{N} = \frac{C_{\text{Sch}}^{\frac{3}{2}}}{\sqrt{2\pi} \beta^{\frac{3}{2}}} e^{\frac{2C_{\text{Sch}} \pi^2}{\beta}}. \quad (\text{A.26})$$

The behavior of $G(z)$ can be understood qualitatively in several regimes. At short times $t \ll C_{\text{Sch}}$, the integrals are well-approximated by the classical saddle point, leading to the

⁴We note that there is some disagreement about this relation; in particular, some studies suggest $C_{\text{Sch}} = 1/(64\pi^{1/2}J) \log J/\Delta$ [14]. Our numerics for two-point functions support the original relation derived in [174]

aforementioned conformal solution (A.11). In contrast, at late times $t \gg C_{\text{Sch}}$, the behavior is dominated by the low-energy edge of the spectrum, which respects the Wigner semicircle law: $\rho(E) \sim \sqrt{E}$ or $\rho(s) \sim s^2$. This gives rise to a power-law decay with an exponent independent of the operator dimension. In particular, we can identify two cases, depending on the temperature relative to C_{Sch} :

(a) High temperature, $\beta \ll C_{\text{Sch}}$:

$$G_{\text{Sch}}(t) \sim \begin{cases} G_c(t), & t \ll C_{\text{Sch}} \\ t^{-3}, & t \gg C_{\text{Sch}} \end{cases} \quad (\text{A.27})$$

(b) Low temperature, $\beta \gg C_{\text{Sch}}$:

$$G_{\text{Sch}}(t) \sim \begin{cases} G_c(t), & t \ll C_{\text{Sch}} \\ \frac{\beta^{3/2}}{(it(\beta-it))^{3/2}}, & t \gg C_{\text{Sch}} \end{cases} \quad (\text{A.28})$$

While observing a clear separation between these regimes is challenging at finite-sizes, we expect our numerical results to be described quantitatively by the full functional form of $G_{\text{Sch}}(z)$. To this end, we compute the integrals in (A.25) numerically in Mathematica. The integrals converge quickly for the imaginary-time correlator, $G_{\text{Sch}}(\tau)$; for the real-time correlator, obtaining convergence requires us to introduce a small imaginary-time separation, i.e. $G_{\text{Sch}}(it) \rightarrow G_{\text{Sch}}(it + \epsilon)$. The numerical results in imaginary and real time are shown in Fig. A.10 and A.11, respectively, for the temperatures and timescales relevant to our study.

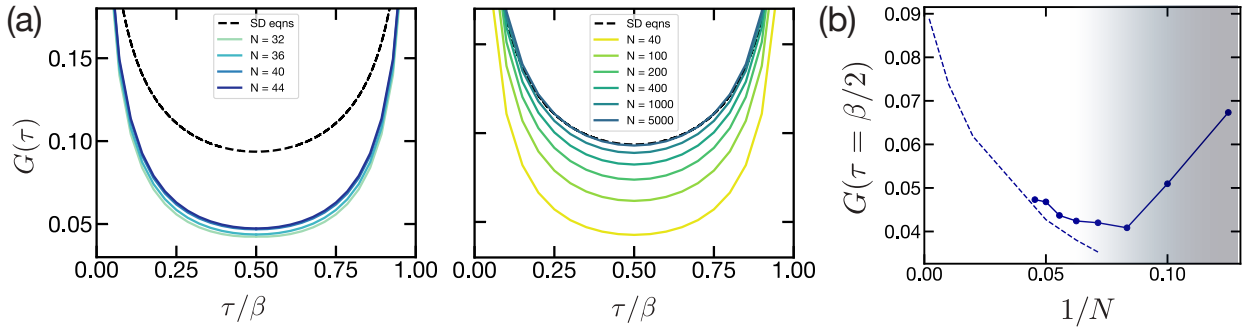


Figure A.10: (a) Results for the imaginary-time Green's function, $G(\tau)$, at $\beta J = 100$ from our numerics (left) and the solution of the Schwarzian action (right). (b) Finite-size scaling of $G(\tau = \beta/2)$. Our numerics (data) begin to agree with the Schwarzian solution (dashed line) at $N \approx 30$. For smaller sizes (gray area), we observe finite-size effects that cannot be accounted for by the Schwarzian action, which we attribute to the discreteness of the energy spectrum.

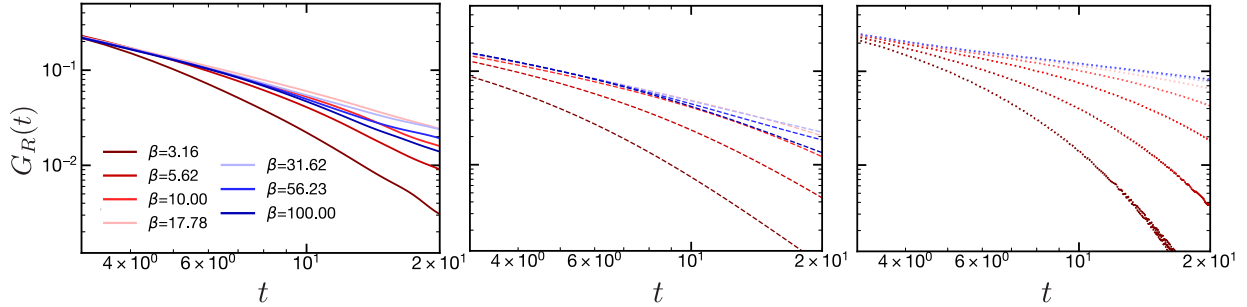


Figure A.11: The retarded Green’s function for the SYK model with 40 Majoranas (left), the Schwarzian action with $C_{\text{Sch}} = 0.4$ (middle), and the large N Schwinger-Dyson equations (right). The late-time behavior of the SYK results and the Schwarzian action is governed by the random-matrix-like form of the energy spectrum, which manifests as a non-monotonicity with respect to temperature.

We note that the retarded Green’s function corresponds to the real part of G_{Sch} . A key feature of this correlator is a non-monotonic decay with respect to temperature; this results from the non-trivial dependence of the *phase* on t and β in (A.28) and is in stark contrast with the prediction of the conformal solution or of the semiclassical solution of the SYK model (i.e. the Schwinger-Dyson equations).

Out-of-time-order correlators

While previous studies have derived an exact integral expression for the OTOC analogous to (A.25), the integrals are significantly more complex and solving them numerically is beyond the scope of this study [144]. Instead, we rely on the semiclassical limit of the OTOC, which is valid for $C_{\text{Sch}} \rightarrow \infty, t \lesssim 1/\lambda \log C_{\text{Sch}}$. This expression was derived using the correspondence to quantum gravity (i.e. by summing over tree-level graviton diagrams) and is given by [175]

$$\frac{F(z_1, z_2, z_3, z_4)}{F(\tau_1, \tau_2, \tau_3, \tau_4)} = \frac{U(2\Delta, 1, \frac{1}{z})}{z^{2\Delta}}, \quad z = \frac{i\beta}{16\pi C_{\text{Sch}}} \frac{e^{\frac{2\pi}{\beta}(z_3+z_4-z_1-z_2)/2}}{\sinh \frac{\pi z_{12}}{\beta} \sinh \frac{\pi z_{34}}{\beta}} \quad (\text{A.29})$$

where $z_i = t_i + i\tau_i$ are the complexified times at which the four operators are inserted, i.e. $\langle V(z_1)W(z_3)V(z_2)W(z_4) \rangle$, and $U(\cdot)$ is the confluent hypergeometric function.

From (A.29), we can determine the behavior of different regularizations. The regularized OTOC corresponds to

$$z_1 = i\frac{\beta}{2}, \quad z_2 = i\frac{\beta}{2}, \quad z_3 = t - i\frac{\beta}{4}, \quad z_4 = t + i\frac{\beta}{4} \quad (\text{A.30})$$

which leads to

$$\frac{F(t)}{F(0)} = \frac{U(2\Delta, 1, \frac{1}{z})}{z^{2\Delta}}, \quad z = \frac{\beta}{16\pi C_{\text{Sch}}} e^{\frac{2\pi}{\beta} t} \quad (\text{A.31})$$

Crucially, this expression can be expanded in powers of $e^{\lambda t}/C_{\text{Sch}}$. For example, setting $\Delta = 1/4$, leads to

$$\frac{F(t)}{F(0)} = 1 - \frac{\beta}{64\pi} \left(\frac{e^{\lambda t}}{C_{\text{Sch}}} \right) + \frac{9\beta^2}{8192\pi} \left(\frac{e^{\lambda t}}{C_{\text{Sch}}} \right)^2 + \dots \quad (\text{A.32})$$

As $C_{\text{Sch}} \sim N$, this manifestly satisfies the rescaling ansatz discussed in Sec. A.2 and Chapter 2. Moreover, the magnitude of the leading order term

$$\frac{F(t)}{F(0)} \approx 1 - \frac{0.5\beta J}{N} e^{\lambda t} \quad (\text{A.33})$$

agrees with the numerical results determined numerically in Sec. A.3.

To obtain different regularizations, we can reduce the imaginary-time separation between the operators. For example, setting

$$z_1 = i2\eta, \quad z_2 = i2\eta, \quad z_3 = t - i\eta, \quad z_4 = t + i\eta \quad (\text{A.34})$$

corresponds to a symmetric separation with energy scale η . It is evident that any finite value for η leads to a well-defined OTOC with the same Lyapunov exponent as the fully regularized case. To represent the fully unregularized correlator, the naive expectation is to take the limit $\eta \rightarrow 0$, which causes the denominator in (A.29) to vanish. For the SYK model, this UV divergence is clearly unphysical, and one should instead impose a microscopic cutoff of order J . The net effect is to enhance to growth term by a factor of $(\beta J)^2$ and thus decrease the scrambling time by a factor of $\log(\beta J)^2$. More precisely, the leading order term for the unregularized correlator is given by

$$\frac{F(t)}{F(0)} \approx 1 - c_1 \frac{(\beta J)^3}{N} e^{\lambda t} \quad (\text{A.35})$$

where c_1 is an order one prefactor. The exact numerical value of c_1 cannot be determined by these methods, as the microscopic cutoff corresponds to “smearing” the operators over an energy scale J rather than setting an exact value for η .

To summarize, regularization changes the magnitude of the exponential growth but has no effect on the Lyapunov exponent. The intuition behind this conclusion can be understood from the dual gravitational theory, where the Lyapunov exponent corresponds to the coupling strength of the graviton interaction and the regularization corresponds to the initial energy of an incoming shock wave. While the energy of the initial state has no effect on the coupling strength, it determines the timescale at which nonlinear graviton effects become relevant, leading to the saturation of the correlator. In particular, the unregularized correlator corresponds to a higher energy initial state, which reaches saturation at an earlier time.

While this intuition applies directly to the SYK model at low temperatures, we expect the same qualitative effects to hold at all temperatures due to the form of the ladder diagrams; in the general case, the graviton interaction would be replaced by a ‘scramblon’ interaction whose strength is governed by $\lambda(\beta)$.

Appendix B

Details on many-body quantum teleportation via operator spreading in the traversable wormhole protocol

B.1 Precise bound for the peaked size regime

In this Section, we provide a precise mathematical bound guaranteeing that the teleportation correlator obeys the peaked-size prediction [Eq. (3.32), Section 3.4] when the size distribution is sufficiently tightly peaked. We apply this bound to two examples where the size distribution is known exactly: late times in all scrambling systems (Section 3.6), and the large- q SYK model (Sections 3.7 and 3.8). Notably, in the latter we find that our bound applies *only* at infinite temperature, despite the profile of the size distribution (e.g. its ratio of size width to average size) behaving similarly at all temperatures. The discrepancy arises instead because the correlator magnitude, $(G_\beta)^p$, decreases exponentially in the encoding size p at all finite temperatures.

Precise bound

As in Chapter 3, we decompose a time-evolved finite temperature operator into a sum of Pauli strings:

$$Q_A(t)\rho^{1/2} = \sum_R c_R(t)S \tag{B.1}$$

In this basis, for qubit systems the correlator takes the form

$$C_Q = \langle \text{TFD} | \tilde{Q}_{A,r}^\dagger(-t)e^{igV}Q_{A,l}(t) | \text{TFD} \rangle = e^{ig+i\pi\mathcal{S}[Q_A(t=0)]} \sum_R e^{-i\eta_{ag}\mathcal{S}[R]/N} c_R^2(t) \tag{B.2}$$

$$= e^{ig+i\pi\mathcal{S}[Q_A(t=0)]} \sum_n e^{i\eta_{ag}n/N} f(n) \tag{B.3}$$

where again $\tilde{Q}_{A,r}^\dagger = DQ_{A,r}^\dagger D^\dagger$ for the decoding operation $D = Y \otimes \dots \otimes Y$, and we use $\langle \text{TFD} | \tilde{Q}_{A,r}^\dagger(-t) = e^{i\pi S[Q_A]} \langle \text{EPR} | Q_{A,l}(t) \rho^{1/2}$ for qubit Pauli operators Q_A . Here we define the winding size distribution [44, 188]

$$f(n) \equiv \sum_{S: S[R]=n} c_R^2(t). \quad (\text{B.4})$$

At finite temperature, this size wavefunction is distinct from the size distribution:

$$P(n) \equiv \sum_{S: S[R]=n} |c_R(t)|^2, \quad (\text{B.5})$$

which is a real, normalized probability distribution probed by the *one*-sided correlator [202]

$$\langle \text{TFD} | Q_{A,l}^\dagger(t) e^{igV} Q_{A,l}(t) | \text{TFD} \rangle = e^{ig} \sum_R e^{-inagS[R]/N} |c_R|^2(t) = \sum_n e^{inagn/N} P(n). \quad (\text{B.6})$$

Nevertheless, the size distribution bounds the size wavefunction magnitude via the triangle inequality:

$$|f(n)| \leq P(n), \quad (\text{B.7})$$

with equality achieved when all Pauli operators of size n contribute the same phase to $f(n)$.

The average size and size variance are easily found from the size distribution as

$$\mathcal{S} = \int_0^\infty dn n P(n), \quad \delta\mathcal{S}^2 + \mathcal{S}^2 = \int_0^\infty dn n^2 P(n) \quad (\text{B.8})$$

where we work in the continuum limit replacing sums over the size by integrals for simplicity. We now define the *asymptotic size width with error* ε as the minimal width W_ε about the average size such that

$$1 - \int_{\mathcal{S}-W_\varepsilon}^{\mathcal{S}+W_\varepsilon} dn P(n) \leq \varepsilon, \quad (\text{B.9})$$

i.e. a fraction $1 - \varepsilon$ of the size distribution's support is contained in the interval $I = [\mathcal{S} - W_\varepsilon, \mathcal{S} + W_\varepsilon]$ (the lower limit of the integral should be bounded by zero; for simpler notation we'll deal with this by instead defining $P(n) = f(n) = 0$ for $n < 0$). We can now separate the correlator into two pieces, one arising from sizes in the interval I and the other from the interval's complement $\bar{I} = [-\infty, \mathcal{S} - W_\varepsilon] \cup [\mathcal{S} + W_\varepsilon, \infty]$:

$$C_Q = \int_I dn f(n) e^{inagn/N} + R \quad (\text{B.10})$$

where the remainder $R = \int_{\bar{I}} dn f(n) e^{i\eta_{dg} n/N}$ is strictly smaller than ε :

$$\begin{aligned}
 |R| &= \left| \int_{\bar{I}} dn f(n) e^{i\eta_{dg} n/N} \right| \\
 &\leq \int_{\bar{I}} dn |f(n) e^{i\eta_{dg} n/N}| \\
 &\leq \int_{\bar{I}} dn |P(n)| \\
 &\leq \varepsilon
 \end{aligned} \tag{B.11}$$

Peaked size teleportation occurs in the regime where $gW_\varepsilon/N \ll 1$. In this limit, we can expand

$$e^{i\eta_{dg} n/N} = e^{i\eta_{dg} S/N} [1 + E(n)] \tag{B.12}$$

where the deviation for $n \in I$ is bounded by

$$|E(n)| \leq \max_{n \in I} \left| 1 - e^{i\eta_{dg}(n-S)/N} \right| = \left| \sin(\eta_{dg} W_\varepsilon/N) \right|, \tag{B.13}$$

which holds as long as $gW_\varepsilon/N \leq \pi/2$. We then have

$$\begin{aligned}
 C_Q &= \int_I dn f(n) e^{i\eta_{dg} S/N} [1 + E(n)] + R \\
 &= e^{i\eta_{dg} S/N} G_\beta(Q_A) + R + R' + R''
 \end{aligned} \tag{B.14}$$

where $G_\beta(Q_A) = \int_0^\infty dn f(n) = \text{tr}(Q_A^\dagger \rho^{1/2} Q_A \rho^{1/2})$ is the imaginary time two-point function, and the error $R' = e^{igS/N} \int_I dn f(n) E(n)$ is bounded by

$$\begin{aligned}
 |R'| &= \left| \int_I dn f(n) E(n) \right| \\
 &\leq \int_I dn |f(n)| |E(n)| \\
 &\leq \left| \sin(\eta_{dg} W_\varepsilon/N) \right| \int_I dn |f(n)| \\
 &\leq \left| \sin(\eta_{dg} W_\varepsilon/N) \right|
 \end{aligned} \tag{B.15}$$

and the second error $R'' = G_\beta(Q_A) - \int_I dn f(n)$ is bounded by

$$|R''| = \left| G_\beta(Q_A) - \int_I dn f(n) \right| = \left| \int_{\bar{I}} dn f(n) \right| \leq \varepsilon. \tag{B.16}$$

We therefore conclude that whenever $\eta_{dg}W_\varepsilon/N \leq \pi/2$, the deviation of C_Q from the peaked size value is controlled by the upper bound

$$|C_Q - e^{i\eta_{dg}\mathcal{S}/N} G_\beta(Q_A)| \leq 2\varepsilon + \left| \sin(\eta_{dg}W_\varepsilon/N) \right| \equiv \mathcal{B}. \quad (\text{B.17})$$

Practically speaking, the lowest value of g for successful peaked-size teleportation is $\eta_{dg}\mathcal{S}/N = \pi$. Therefore, for a given size distribution, we can guarantee that peaked-size teleportation is possible if we find ε such that $\mathcal{B} \ll G_\beta(Q_A)$, i.e. the error in the correlator is small compared to the correlator magnitude.

Application to late times

We illustrate this with some examples, in the few cases where we can exactly solve for operators' full size distribution. First, consider a thermalized system at late times, which we will approximate by setting the size distribution of $Q_A(t)$ to be that of a random Pauli string. For large n, N is a Gaussian distribution with mean $\mathcal{S} = 3N/4$ and variance $\delta\mathcal{S}^2 = 3N/16$:

$$P(n) = (3/4)^n (1/4)^{N-n} \approx \frac{1}{\sqrt{2\pi\delta\mathcal{S}}} \exp\left(-\frac{(n - \mathcal{S})^2}{2\delta\mathcal{S}^2}\right). \quad (\text{B.18})$$

We therefore have

$$1 - \int_{\mathcal{S}-W_\varepsilon}^{\mathcal{S}+W_\varepsilon} dn P(n) = 2 \operatorname{erfc}\left(\frac{W_\varepsilon}{\sqrt{2\delta\mathcal{S}}}\right) = \varepsilon. \quad (\text{B.19})$$

The error function decays exponentially in its argument, so even for exponentially small ε we require only $W_\varepsilon = A\delta\mathcal{S}$ for some constant $A \sim \mathcal{O}(1)$. Setting g equal to its minimal value, $\eta_{dg}\mathcal{S}/N = \pi$, we have both $\varepsilon \ll 1$ and $|\sin(\eta_{dg}W_\varepsilon/N)| \approx A\delta\mathcal{S}/\mathcal{S} \sim 1/\sqrt{N} \ll 1$, and so peaked size teleportation is guaranteed.

Application to the large- q SYK model

We can also use this method to guarantee peaked-size teleportation in the large- q SYK model at infinite temperature.

We begin by writing down the size distribution for the large- q SYK model in detail, quoting the results of Ref. [202]. The generating function for the size distribution is:

$$\sum_n P(n) e^{-\mu n} = \frac{e^{-\mu p}}{(1 + (1 - e^{-\mu q}) \sinh^2 Jt)^{2p/q}} = \sum_n \frac{\Delta_n}{n!} x^n (1-x)^\Delta e^{-\mu(qn+p)} \quad (\text{B.20})$$

where we define

$$\Delta_n \equiv \frac{\Gamma(\Delta + n)}{\Gamma(\Delta)}, \quad x \equiv \frac{\sinh^2 Jt}{1 + \sinh^2 Jt}, \quad \Delta \equiv 2p/q. \quad (\text{B.21})$$

From this, we can identify the size distribution:

$$P(qn + p) = \frac{\Delta_n}{n!} x^n (1-x)^\Delta. \quad (\text{B.22})$$

The size and size width are

$$\mathcal{S} = \bar{n} = \sum_n n \frac{\Delta_n}{n!} x^n (1-x)^\Delta = \frac{\Delta x}{1-x}, \quad \delta\mathcal{S} = \sqrt{n^2 - \bar{n}^2} = \frac{\sqrt{\Delta x}}{1-x}. \quad (\text{B.23})$$

Therefore, the ratio of size width to average size is

$$\delta\mathcal{S}/\mathcal{S} = \sqrt{\frac{x}{\Delta}} \frac{1}{1+x}, \quad (\text{B.24})$$

which approaches zero when $p \rightarrow \infty$ ($\Delta \rightarrow \infty$).

To apply the upper bound Eq. (B.17), we need to integrate (i.e. sum) the tail of the size distribution in order to compute its asymptotic width [Eq. (B.9)]. In this example, the discrete tail can be summed explicitly and we define

$$I(k) \equiv \sum_{n=k}^{\infty} P(qk + p) = \sum_{n=k}^{\infty} \frac{\Delta_n}{n!} x^n (1-x)^\Delta = \frac{B_x(k, \Delta)}{B(k, \Delta)} \quad (\text{B.25})$$

where $B_x(a, b)$ and $B(a, b)$ are incomplete and ordinary beta function respectively. Let us take $k = \bar{n}(1 \pm \zeta)$ for some small ζ representing the asymptotic width

$$W_\varepsilon = \bar{n}\zeta q. \quad (\text{B.26})$$

This width corresponds to an error

$$\varepsilon = 1 - I(\bar{n}(1 - \zeta)) + I(\bar{n}(1 + \zeta)). \quad (\text{B.27})$$

Taking $g\mathcal{S}/N = \pi$, the upper bound is

$$\begin{aligned} \mathcal{B} &= 2[1 - I(\bar{n}(1 - \zeta)) + I(\bar{n}(1 + \zeta))] + \sin \frac{2\pi\zeta x}{1+x} \\ &= 2 \left(1 - \frac{B_x(\frac{\Delta x(1-\zeta)}{1-x}, \Delta)}{B(\frac{\Delta x(1-\zeta)}{1-x}, \Delta)} + \frac{B_x(\frac{\Delta x(1+\zeta)}{1-x}, \Delta)}{B(\frac{\Delta x(1+\zeta)}{1-x}, \Delta)} \right) + \sin \frac{2\pi\zeta x}{1+x}. \end{aligned} \quad (\text{B.28})$$

At infinite temperature $G_\beta(Q_A) = 1$, we need to show that the minimum of \mathcal{B} tends to zero when $\Delta \rightarrow \infty$.

For early time $\sinh Jt \sim \mathcal{O}(1)$, $1-x$ is an order 1 number, and we take $\Delta \rightarrow \infty$ limit to get

$$\frac{B_x(\frac{\Delta x(1-\zeta)}{1-x}, \Delta)}{B(\frac{\Delta x(1-\zeta)}{1-x}, \Delta)} \rightarrow 1, \quad \frac{B_x(\frac{\Delta x(1+\zeta)}{1-x}, \Delta)}{B(\frac{\Delta x(1+\zeta)}{1-x}, \Delta)} \rightarrow 0 \quad (\text{B.29})$$

The bound becomes

$$\mathcal{B} \rightarrow \sin \frac{2\pi\zeta x}{1+x} \quad (\text{B.30})$$

This basically means that the integrated probability between $\bar{n}(1-\zeta)$ and $\bar{n}(1+\zeta)$ for any finite ζ is 1. One can thus take $\zeta \rightarrow 0$ with speed slower than $1/\Delta \rightarrow 0$ in order to have the bound vanish. This computation applies for $x \in (0, 1)$, which means that the peaked size always holds for early time. This is physically reasonable as the operator has not yet been scrambled extensively. However, since the size is small at such early times, in order for teleportation to work we must choose $g \sim N$.

For intermediate times, such that $\sinh^2 Jt \sim N$ and $\Delta \ll N \sim 1/(1-x)$, we must take the $x \rightarrow 1$ limit first. Using the fact that

$$\frac{B_x\left(\frac{\Delta x(1-\zeta)}{1-x}, \Delta\right)}{B\left(\frac{\Delta x(1-\zeta)}{1-x}, \Delta\right)} = 1 - \frac{(1-x)^\Delta x^{\frac{\Delta x(1-\zeta)}{1-x}} \Gamma\left(\frac{\Delta(1-x\zeta)}{1-x}\right)}{\Gamma\left(\frac{\Delta x(1-\zeta)}{1-x}\right) \Gamma(1+\Delta)} F\left(1, \frac{\Delta(1-x\zeta)}{1-x}; \Delta+1; 1-x\right) \quad (\text{B.31})$$

where F is Gauss hypergeometric function, in $x \rightarrow 1$ limit the right portion of Eq. (B.31) tends to

$$\begin{aligned} F\left(1, \frac{\Delta(1-x\zeta)}{1-x}; \Delta+1; 1-x\right) &\rightarrow {}_1F_1(1; \Delta+1; \Delta(1-\zeta)) \\ &= \Delta^{1-\Delta} e^{\Delta(1-\zeta)} (1-\zeta)^{-\Delta} (\Gamma(\Delta) - \Gamma(\Delta, \Delta(1-\zeta))) \end{aligned} \quad (\text{B.32})$$

where $\Gamma(x, a)$ is incomplete gamma function. Meanwhile, the left portion of the second term of Eq. (B.31) gives

$$\frac{(1-x)^\Delta x^{\frac{\Delta x(1-\zeta)}{1-x}} \Gamma\left(\frac{\Delta(1-x\zeta)}{1-x}\right)}{\Gamma\left(\frac{\Delta x(1-\zeta)}{1-x}\right) \Gamma(1+\Delta)} \rightarrow \frac{\Delta^\Delta (1-\zeta)^\Delta e^{-\Delta(1-\zeta)}}{\Gamma(1+\Delta)} \quad (\text{B.33})$$

under $x \rightarrow 1$. Combining the two, we have

$$\lim_{x \rightarrow 1} \frac{B_x\left(\frac{\Delta x(1-\zeta)}{1-x}, \Delta\right)}{B\left(\frac{\Delta x(1-\zeta)}{1-x}, \Delta\right)} = \frac{\Gamma(\Delta, \Delta(1-\zeta))}{\Gamma(\Delta)}. \quad (\text{B.34})$$

It follows that the upper bound is

$$\mathcal{B} = 2 \left(1 - \frac{\Gamma(\Delta, \Delta(1-\zeta))}{\Gamma(\Delta)} + \frac{\Gamma(\Delta, \Delta(1+\zeta))}{\Gamma(\Delta)} \right) + \sin \pi\zeta \quad (\text{B.35})$$

This function has a unique minimum for $\zeta \in [0, 1/2]$ and this minimum decreases as Δ increases. Taking derivative with respect to ζ , we get

$$\begin{aligned} \partial_\zeta \mathcal{B} &= \pi \cos \pi\zeta - \frac{2\Delta^\Delta}{\Gamma(\Delta)} [(1+\zeta)^{\Delta-1} e^{-\Delta(1+\zeta)} + (1-\zeta)^{\Delta-1} e^{-\Delta(1-\zeta)}] \\ &\rightarrow \pi \cos \pi\zeta - \sqrt{\frac{2\Delta}{\pi}} [(1+\zeta)^{\Delta-1} e^{-\Delta\zeta} + (1-\zeta)^{\Delta-1} e^{\Delta\zeta}] \end{aligned} \quad (\text{B.36})$$

where in the second step we have taken large Δ limit. Solving $\partial_\zeta \mathcal{B} = 0$ in this limit, we find the minimum at

$$\zeta \approx \sqrt{\frac{1}{\Delta} \log \frac{8\Delta}{\pi^3}} \rightarrow 0 \quad (\text{B.37})$$

which in turn gives the limit value of \mathcal{B} to be zero. This proves that at infinite temperature, teleportation exactly matches the peaked-size prediction for both early and intermediate times. For late times $t \gg \frac{1}{2J} \log N$ the size distribution above breaks down, as can be seen since $P(n)$ is dominated by some $n > N$, which is unphysical since N is the total number of fermions.

In contrast, we can also show that the above bound does *not* apply at low temperatures for large- q SYK, as expected from Chapter 3. At low temperature, the upper bound \mathcal{B} needs to be much smaller than the two-sided correlation function $G_\beta(Q_A) \sim (\beta J)^{-2\Delta}$ in order to guarantee peaked-size teleportation. The low temperature size distribution is essentially the same as at infinite temperature, requiring only the replacement [202]:

$$x \rightarrow \frac{\sinh^2 \pi t / \beta}{(\pi / \beta J)^2 + \sinh^2 \pi t / \beta} \in [0, 1] \quad (\text{B.38})$$

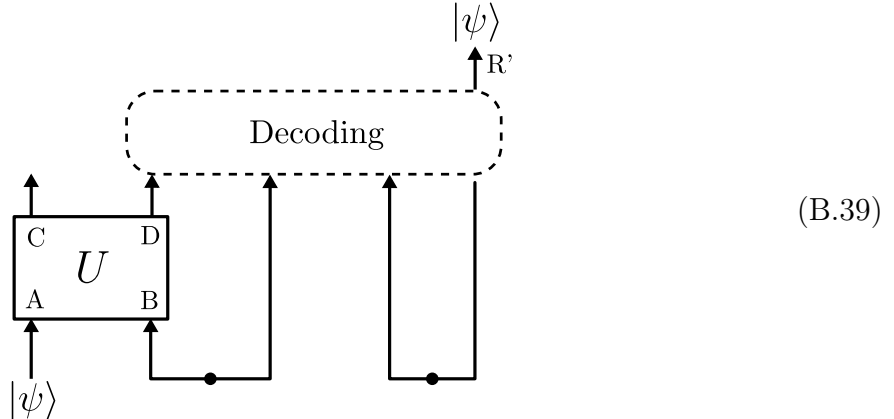
and adding $e^{-\mu N \delta_\beta}$ to the distribution, which shifts the initial size by a constant amount $N \delta_\beta$ (accounting for the size of the thermal density matrix [202]). Following a similar computation to above, one can show that \mathcal{B} still asymptotes to zero, but now with a *slower* speed than $G_\beta(Q_A)$. For example, in the early time and large Δ limits, $\mathcal{B} \sim \exp(-\Delta C(x, \zeta)) / \sqrt{\Delta}$ where $C(x, \zeta)$ is order 1, while $G_\beta(Q_A) \sim \exp(-2\Delta \log(\beta J))$ is exponentially smaller for large βJ . Therefore, the upper bound \mathcal{B} fails to guarantee peaked-size teleportation. This is consistent with the fact that the correlation function $C_Q(t)$ in Eq. (3.86) in low temperature is far from being a pure phase.

B.2 The Hayden-Preskill recovery protocol

In this appendix we review the HPR protocol following Refs. [263, 265] and derive its equivalence to the TW protocol in the case of infinite temperature teleportation of a single qubit (introduced in Section 3.6). This single-qubit variant of the HPR protocol was experimentally implemented in Ref. [147], although an explicit derivation of its quantum circuit was not provided.

There are two variants of the HPR protocol: a probabilistic variant, which teleports successfully only with some finite probability, and a deterministic variant, which uses an analog of Grover's search algorithm and succeeds with unit probability, but involves a more

complex decoding operation. Both protocols take the general form,

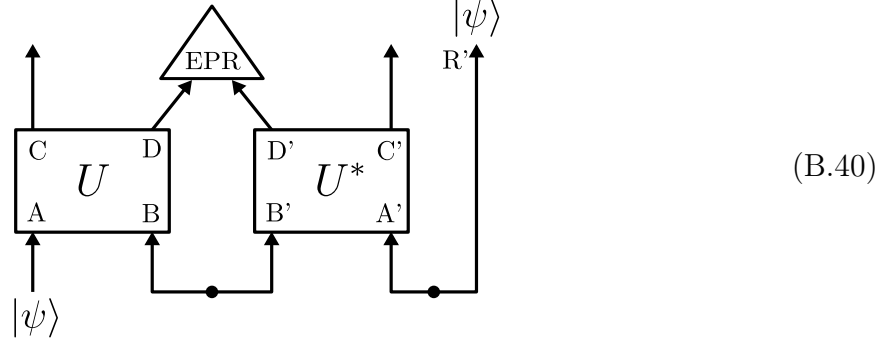


shown for teleportation of a quantum state $|\psi\rangle$ (the generalization to EPR teleportation is straightforward). We now outline the interpretation of each aspect of the above protocol in the context of the Hayden-Preskill thought experiment. For consistency with past literature, we have used *different* subsystem labels than introduced in Chapter 3—most notably, subsystem D now denotes the coupled qubits, and subsystem C denotes its complement. Subsystem B represents an eternal black hole that is maximally entangled with its past Hawking radiation subsystem B', as represented by a dimension $d_B = d'_B$ EPR pair between the two subsystems. Subsystem A contains the initial state $|\psi\rangle$ of an observer Alice's diary. Upon falling into the black hole, the diary's information is scrambled by the unitary time-evolution U acting on the left subsystem $l \equiv AB = CD$. Far from destroying the information of Alice's diary, scrambling by U in fact allows an outside observer Bob to decode the diary if he has access to *any* few qubits of new Hawking radiation D, along with the past Hawking radiation B' and an ancillary EPR pair between A' and R', where $d'_A = d_A$. This decoding relies on OTOCs between subsystem A and D being minimal, a general feature of thermalizing time-evolution after the scrambling time. We describe each of the decoding protocols of Ref. [263] in detail below.

Probabilistic decoding: intuition

Although our main focus will be on the deterministic teleportation protocol, we review the probabilistic protocol here for completeness, and as a convenient platform to introduce the intuition connecting operator spreading to the success of teleportation. The decoding operation of the probabilistic HPR protocol consists of projection onto EPR pairs on a

subsystems D, D':



Perfect teleportation requires $d_D \geq d_A$, and succeeds with probability $1/d_A^2$ when U is maximal scrambling. The non-unity success probability signifies that the decoding protocol becomes exponentially more complex with the number of qubits to be teleported.

To provide intuition for the protocol's success, we analyze the action of EPR projection on the initial states $Q_{A,l}(t) |\text{EPR}\rangle$. We restrict to infinite temperature, i.e. EPR pairs in place of the TFD state, in keeping with the original introduction of the HPR protocol in Ref. [263]. We write $Q_A(t)$ as a sum of Pauli strings S on the entire system:

$$Q_A(t) = \sum_R c_R(t) S. \quad (\text{B.41})$$

Denoting the EPR projector on subsystems D, D' as $P_{\text{EPR},D}$ and writing each Pauli string as a tensor product $R = R_C \otimes R_D$ of Paulis on subsystems D and C, we have

$$P_{\text{EPR},D} R_l |\text{EPR}\rangle = \delta_{R_D, \mathbb{1}} R_l |\text{EPR}\rangle, \quad (\text{B.42})$$

since $\langle \text{EPR}_{D,D'} | S_{D,l} | \text{EPR}_{D,D'} \rangle = \text{tr}_D(R_D)/d_D = \delta_{R_D, \mathbb{1}}$. Perfect teleportation is achieved when all input Pauli operators on subsystem A have spread to subsystem D, such that every Pauli string S composing $Q_A(t)$ has non-identity support on subsystem D, for all non-identity Q_A . In this situation, the EPR projector has eigenvalue 1 on the thermofield double state and eigenvalue 0 in *all* perturbed states:

$$P_{\text{EPR},D} |\text{EPR}\rangle = |\text{EPR}\rangle, \quad P_{\text{EPR},D} Q_{A,l}(t) |\text{EPR}\rangle = 0. \quad (\text{B.43})$$

However, this is no different than projecting onto EPR pairs between subsystems A and A' before time-evolution by $U_l U_r^*$! This projection would, of course, have an action

$$P_{\text{EPR}} |\text{EPR}\rangle = |\text{EPR}\rangle, \quad P_{\text{EPR}} Q_{A,l} |\text{EPR}\rangle = \text{tr}(Q_A) = 0. \quad (\text{B.44})$$

Expressed diagrammatically, this equivalence is:

for all initial states ψ . However, performing EPR projection between subsystems A, A' before time-evolution is precisely the standard quantum teleportation protocol, applied to subsystems A, A', and R'. The scrambling dynamics of U allow one to perform this teleportation via coupling *any* subsystem D of the system's qubits.

Deterministic decoding

After scrambling, the probability of successful EPR projection on subsystem D, $\mathcal{O}(1/d_A^2)$, is exponentially small in the size of subsystem A, the state to be teleported. In contrast to standard teleportation, non-successful EPR projection (i.e. projection onto a different maximally entangled state, not $|\text{EPR}_{D,D'}\rangle$) *cannot* be corrected via an additional decoding operation. This exponential decrease in success probability is overcome in the deterministic HPR protocol, which uses an analog of Grover's search algorithm to search for an EPR pair between subsystems D, D'. The protocol requires $\mathcal{O}(d_A)$ steps for completion, again exponential in the number of qubits to be teleported (albeit with half the exponent of the probabilistic decoding).

Grover's search algorithm involves two operations: the first applies a minus sign to the state one is searching for, and the second applies a minus sign to the system's initial state. We will search for an EPR pair on subsystem D, so for the first step we apply $W_D \equiv 1 - 2P_{\text{EPR},D} = e^{i\pi P_{\text{EPR},D}}$:

In the second step, we flip the sign of the initial state (the time-evolved EPR pair between

A' and the reference qubit R') by applying $\widetilde{W}_A \equiv U^*W_AU^T$:

(B.47)

where $W_A = 1 - 2P_{\text{EPR},A}$ acts on A', R' to apply a minus sign if the two are in an EPR pair.

The entire Grover protocol is identical to the probabilistic protocol, but with EPR measurement replaced by repeated applications of the two above steps until the EPR pair is found. Displaying, for instance, only the first two iterations:

(B.48)

After $\mathcal{O}(d_A)$ iterations, the state $|\psi\rangle$ is found on subsystem R'.

Single qubit deterministic decoding

Two important simplifications occur to the deterministic HPR protocol in the case of single qubit teleportation, $d_A = 2$. The first is that the Grover operator W_A is equal to a SWAP operator composed with single-qubit Y operations. To see this, we expand W_A in terms of Pauli operators:

$$\begin{aligned}
 W_A &= 1 - 2P_{\text{EPR},A} \\
 &= 1 - \frac{2}{d_A^2} \sum_{P_A} P_{A,l} P_{A,r}^* \\
 &= \frac{1}{2} - \frac{1}{2} X_l X_r + \frac{1}{2} Y_l Y_r - \frac{1}{2} Z_l Z_r \\
 &= \frac{1}{2} Y_l [1 + X_l X_r + Y_l Y_r + Z_l Z_r] Y_l \\
 &= Y_l (\text{SWAP}) Y_l, \\
 &= Y_l Y_r (\text{SWAP})
 \end{aligned} \tag{B.49}$$

where in the final equality we used $Y_r \text{SWAP} = \text{SWAP} Y_l$, and in the second equality we used the Pauli decomposition for the swap operator between two d_A -dimensional boson systems:

$$\text{SWAP} = \frac{1}{d_A} \sum_{P_A} P_{A,l} P_{A,r}^\dagger. \tag{B.50}$$

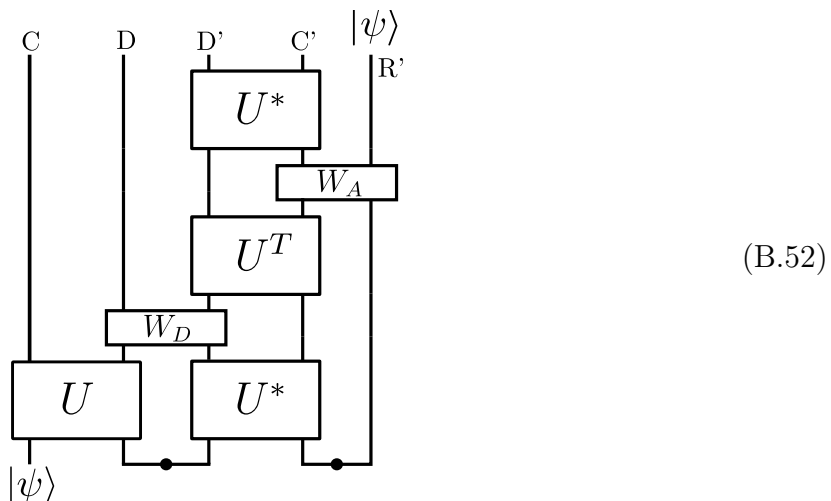
Expressed graphically, we have



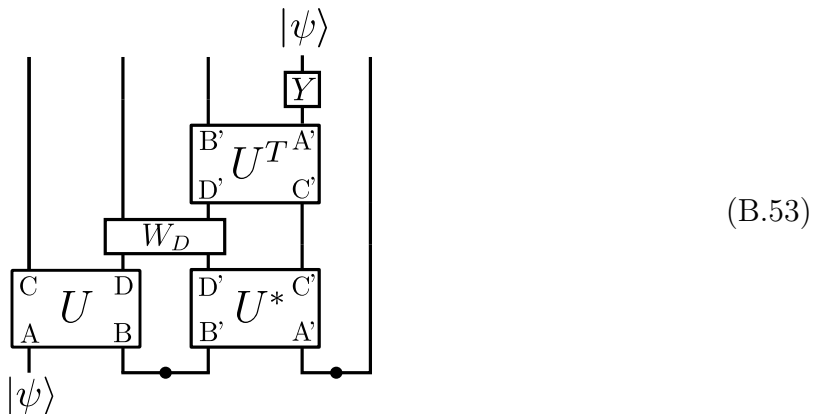
(B.51)

The second simplification is that Grover's search for an EPR pair D, D' succeeds after only one step; this is a general result for Grover's search in a $d_D^2 = 4$ -dimensional database [189].

It implies that the Grover protocol can teleport one qubit through the circuit:

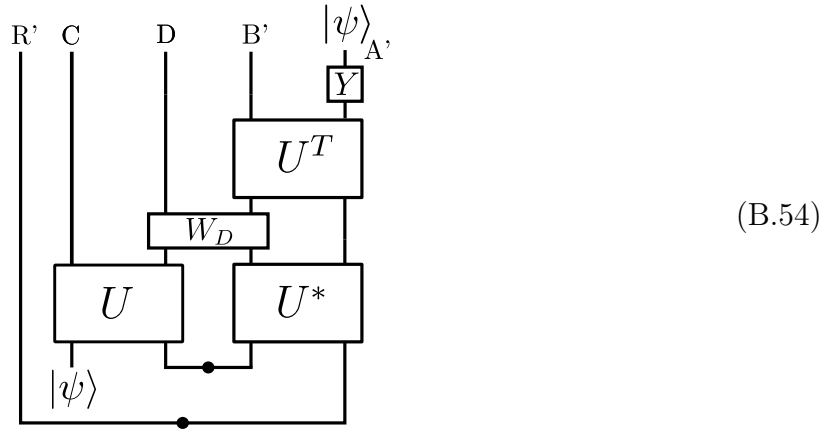


If we only care about the fidelity of the teleported state, we can neglect the final application of U^* . Performing the SWAP gate explicitly, and neglecting the action of the final Y operator on R' , we have:

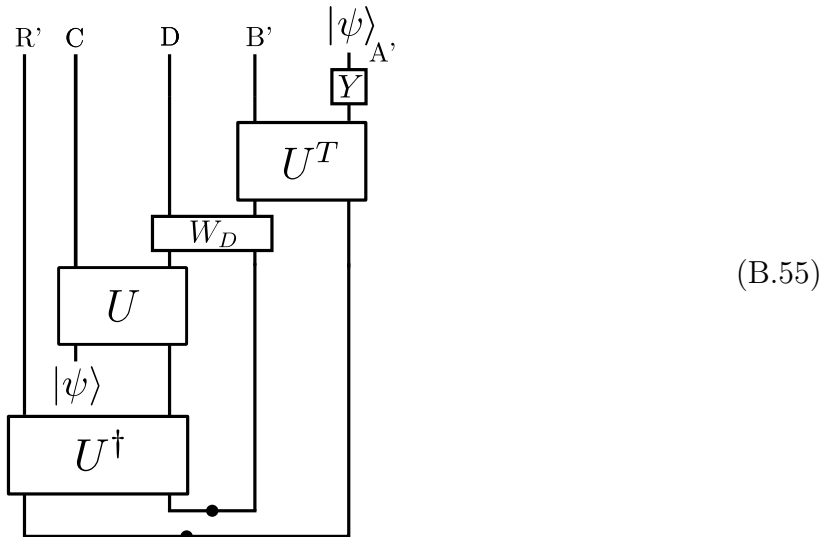


This exact circuit has been performed in trapped ion experiment [147]. We now make a

small cosmetic adjustment, and move the reference qubit R' from the far right to the far left,

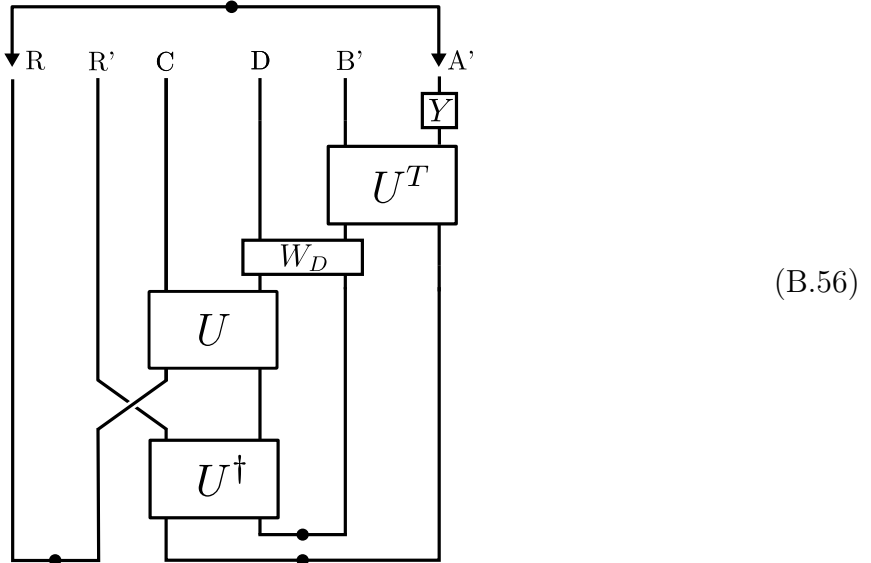


Sliding U^* to the left side using Eq. (3.9), we have:



This is the same circuit appearing the teleportation protocol of Ref. [44, 188], modulo the

precise form of the coupling. In the case of EPR teleportation, we would instead have



where subsystems R' and A' are in an EPR pair when teleportation is successful. This is the circuit appearing in Ref. [88], modulo the form of the coupling as well as the Y decoding operation. The lack of a Y decoding operation for fermionic teleportation is discussed in Appendix B.7.

B.3 State teleportation fidelity

In Section 3.5, we provided a detailed derivation of the teleportation fidelity's relation to the teleportation correlators in the case where one teleports one half of an EPR pair. This allowed us to lower bound the fidelity in Eq. (3.42) and calculate the peaked-size fidelity in Eq. (3.44). In this appendix we do the same for teleportation of a quantum state, as shown in Fig. 6.1(a) and outlined in Section 3.2. Our results provide a rigorous foundation for the arguments of Section 3.3, in particular the insertion of the state $\langle\phi|$ and the subsequent replacement of $|\psi\rangle\langle\phi|$ with a Pauli operator Q_A .

We begin with the insertion of $\langle\phi|$ into the protocol Eq. (3.16). We do so by inserting the resolution of the identity $\frac{1}{d_A} \sum_{|\phi\rangle} |\phi\rangle\langle\phi| = \mathbb{1}$ into the ancillary qubit leg of the diagram

for the state teleportation fidelity. We find:

$$F_\psi = \text{Diagram 1} = \frac{1}{d_A} \sum_{|\phi\rangle} \text{Diagram 2} \quad (\text{B.57})$$

Plugging Eq. (3.18) into this diagram provides unit teleportation fidelity, as described in Chapter 3. When teleportation is successful each of the d_A terms of the sum must succeed individually, so the right input state $|\phi\rangle$ will not affect the success of the teleportation.

As with EPR distillation [Eq. (3.40)], we can relate the state teleportation fidelity to

correlators of Pauli operators by decomposing the SWAP operator. Diagrammatically,

$$F_\psi = \text{[Diagrammatic Expression]} = \frac{1}{d_A^2} \sum_{P_1, P_2} \text{[Diagrammatic Expression]}, \quad (\text{B.58})$$

and in equation form,

$$F_\psi = \frac{1}{d_A^2} \sum_{P_1, P_2} \langle \psi | P_2 P_1^\dagger | \psi \rangle \cdot \langle \text{TFD} | P_{2,l}^\dagger(t) e^{-igV} | \psi \rangle \langle \psi | P_{1,r}(-t) e^{igV} P_{1,l}(t) | \text{TFD} \rangle. \quad (\text{B.59})$$

When the correlators are maximal with phases $e^{i\theta_P}$, i.e. when $e^{igV} P_{1,l}(t) | \text{TFD} \rangle = e^{i\theta_P} P_{1,r}(-t) | \text{TFD} \rangle$, we can simplify this expression as

$$\begin{aligned} F_\psi &\approx \frac{1}{d_A^2} \sum_{P_1, P_2} \langle \psi | P_2 P_1^\dagger | \psi \rangle \cdot \langle \text{TFD} | P_{2,r}^\dagger(-t) | \psi \rangle \langle \psi | P_{1,r}(-t) P_{1,r}(-t) | \text{TFD} \rangle \\ &= \frac{1}{d_A^2} \sum_{P_1, P_2} e^{i(\theta_{P_1} - \theta_{P_2})} \cdot \langle \psi | P_2 P_1^\dagger | \psi \rangle \cdot \text{tr} \left(\rho P_2^\dagger | \psi \rangle \langle \psi | P_1 \right) \\ &= \frac{1}{d_A^2} \sum_{P_1, P_2} e^{i(\theta_{P_1} - \theta_{P_2})} \cdot \text{tr} \left(P_1^\dagger | \psi \rangle \langle \psi | P_2 \right) \cdot \text{tr} \left(\rho P_2^\dagger | \psi \rangle \langle \psi | P_1 \right). \end{aligned} \quad (\text{B.60})$$

As expected, when the phases $e^{i\theta_P}$ are the same for all operators, this gives unit fidelity:

$$\begin{aligned}
 F_\psi &= \frac{1}{d_A^2} \sum_{P_1, P_2} \text{tr}\left(P_1^\dagger |\psi\rangle\langle\psi| P_2\right) \cdot \text{tr}\left(\rho P_2^\dagger |\psi\rangle\langle\psi| P_1\right) \\
 &= \frac{1}{d_A} \sum_{P_1} \text{tr}\left(P_1^\dagger |\psi\rangle\langle\psi| |\psi\rangle\langle\psi| P_1 \rho\right) \\
 &= \text{tr}(|\psi\rangle\langle\psi|) \text{tr}(\rho) \\
 &= 1,
 \end{aligned} \tag{B.61}$$

using properties of Pauli operators as a 1-design [277]. Differing phases $e^{i\theta_P}$ cause the terms in the sum to interfere with each other, giving lower fidelity. At finite temperature, the fidelity of peaked-size teleportation is again limited. For instance, if $|\psi\rangle$ is a single-qubit eigenstate of the Pauli Z operator, we have:

$$\begin{aligned}
 F_{\text{EPR}} &= \frac{1}{2^2} \sum_{P_1, P_2} \langle\psi| P_2 P_1^\dagger |\psi\rangle \cdot \langle\text{TFD}| P_{2,t}^\dagger e^{-igV} [Y |\psi\rangle\langle\psi| Y]_r(-t) e^{igV} P_{1,t} |\text{TFD}\rangle \\
 &= \frac{1}{2^2} \sum_{P_1, P_2} \langle\psi| P_2 P_1^\dagger |\psi\rangle \cdot \text{tr}\left(|\psi\rangle\langle\psi| \rho^{1/2} P_2^\dagger P_1 \rho^{1/2}\right) \\
 &= \sum_P \langle\psi| P^\dagger |\psi\rangle \cdot \text{tr}\left(|\psi\rangle\langle\psi| \rho^{1/2} P \rho^{1/2}\right) \\
 &= 2 \text{tr}\left(|\psi\rangle\langle\psi| \rho^{1/2} |\psi\rangle\langle\psi| \rho^{1/2}\right) \\
 &\approx \frac{1}{2} \text{tr}\left((\mathbb{1} + Z) \rho^{1/2} (\mathbb{1} + Z) \rho^{1/2}\right) \\
 &\approx \frac{1}{2} + \frac{1}{2} G(t' - t + i\beta/2) + \langle Z \rangle_\beta,
 \end{aligned} \tag{B.62}$$

where $\langle Z \rangle_\beta = \text{tr}(Z\rho)$, which averages to zero for different initial states $|\psi\rangle$.

B.4 Rydberg numerical simulations

For the numerical results shown in Fig. 3.7 and 3.8, we simulate the full TW protocol with time evolution generated by the analog Rydberg Hamiltonian [Eq. (3.104)]. In particular, we implement the *one-sided* version of state teleportation, which is obtained by replacing the EPR measurement in Fig. 3.6(b) with a measurement of a two-qubit state $|\psi\rangle \otimes |\psi^*\rangle$. The many-body unitary corresponds to $U = e^{-iHt}$, where H is given in Eq. (3.104) with $\Omega_i = .9$, $\Delta_i = -1.5$, $J_0 = 1$ and open boundary conditions. The teleported state $|\psi\rangle$ is inserted in the middle qubit, and the remaining $K = N - 1$ qubits serve as ‘measured’ qubits, with $\hat{O}_i = \hat{Z}_i$ (see Section 3.9).

More explicitly, the numerical procedure is given as follows: (i) begin in a random initial state, $|\sigma_1 \cdots \sigma_N\rangle$; (ii) evolve forward for time t under the Rydberg Hamiltonian; (iii) apply

the operator $|\phi\rangle\langle\psi|$ onto the middle qubit; (iv) evolve backward in time, apply $\hat{V}_i = e^{igo_i\hat{Z}_i/K}$ to each of the $K = N - 1$ ‘measured’ qubits (where o_i is determined by the initial state), and evolve forward again; (v) measure the projector $|\psi\rangle\langle\psi|$ on the middle qubit. We repeat this procedure for $|\phi\rangle \in \{|0\rangle, |1\rangle\}$ [see Eq. (B.58)] and starting from ~ 100 random initial states. Moreover, to compute the *average* state fidelity, we average $|\psi\rangle$ over all single-qubit states in a 2-design [147], i.e. $|\psi\rangle \in \{|0\rangle, |1\rangle, \frac{1}{\sqrt{2}}(|0\rangle \pm |1\rangle), \frac{1}{\sqrt{2}}(|0\rangle \pm i|1\rangle)\}$. Lastly, we note that the time evolution is implemented with Krylov subspace methods, an iterative technique that is amenable to parallelization and is more computationally efficient than exact diagonalization [2, 137].

B.5 Random unitary circuit numerics

In this section, we provide additional details and numerical data from our random unitary circuit simulations (Section 3.7 B, C).

Algorithm

Our goal for the RUC simulations is to compute the Haar-averaged EPR fidelity and operator size distribution for the circuit layouts shown in Fig. 3.2. Crucially, the relevant diagrams for computing these quantities—Eq. (3.40) for the EPR fidelity, and Eq. (3.31) for the operator size distribution—contain at most three copies of U and U^\dagger . Together with the fact that Clifford unitaries form a 3-designs for qubits, this implies that can compute the averaged quantities by replacing each Haar-random gate with a random *Clifford* gate [142, 250, 274]. This dramatic simplification has been exploited in prior studies of operator growth in random unitary circuits [187, 249]; here, we adapt these same techniques for computing the full size distribution and the teleportation fidelity.

In more detail, our algorithm consists of the following three ingredients. First, following a standard approach [4, 187], we represent an initial n -qubit Pauli operator, Q , as a binary string $v = x_1x_2 \cdots x_nz_1z_2 \cdots z_n$ of length $2n$:

$$Q = \prod_{i=1}^n Q_i(x_i, z_i) \tag{B.63}$$

where $Q_i(0, 0) = I_i$, $Q_i(1, 0) = X_i$, $Q_i(0, 1) = Z_i$, and $Q_i(1, 1) = Y_i$ denote individual Pauli operators within the Pauli string. For example, the operator $\mathbb{1} \otimes \mathbb{1} \otimes Z \otimes \mathbb{1} \otimes \mathbb{1}$ is represented as $x = 00000$ and $z = 00100$. Normally, one would also keep track of the overall phase of Q , but for our purposes the phase will be irrelevant and is dropped in the above notation.

Second, we evolve Q under a random Clifford unitary U to obtain $Q(t) = UQU^\dagger$. We consider the circuits shown in Fig. 3.2, which are composed of random 2-qubit Clifford unitaries laid out in a ‘brick-layer’ fashion. Each of the 2-qubit unitaries is sampled uniformly from the set of 2-qubit Clifford unitaries. While an algorithm exists to perform this sampling

directly [158], in practice we find it more convenient to pre-compute and enumerate the entire 2-qubit Clifford set (which consists of 11520 distinct unitaries)¹. In the binary notation, each 2-qubit Clifford unitary corresponds to a map which acts on the relevant components v , i.e. a unitary with support on the j th and k th qubits updates the values of (x_j, z_j, x_k, z_k) . The time complexity of applying the full circuit thus scales linearly with the number of 2-qubit gates and does not otherwise depend on the number of qubits n . As a reference point, simulating a 0D circuit until the scrambling time with 10^8 qubits for a single realization takes approximately one day on a standard single-core processor.

Third, we compute the average operator size distribution and EPR fidelity of the time-evolved operators. For the former, we simply count the size, i.e. number of non-identity terms, of a time-evolved operator $Q(t)$ for a single circuit realization and determine the distribution of sizes with respect to $\sim 10^3$ circuit realizations. Depending on the simulation, we either initialize Q with support on a single site (i.e. $p=1$) or as a p -body operator. In either case, the specific terms in Q (e.g. whether each site is initialized as X , Y , or Z) is arbitrary since the averaged quantities are basis independent.

Computing the averaged EPR fidelity requires an additional average over the initial operators. In particular, for a single circuit realization U , we compute the EPR fidelity using [Eq. (3.44)]:

$$F_{\text{EPR}} = \left| \frac{1}{d_A^2} \sum_{Q_A} e^{i\theta_{Q_A}} \right|^2 \quad (\text{B.64})$$

where

$$\theta_{Q_A} = \eta_d g \mathcal{S}_K[UQ_A U^\dagger]/K + \pi \mathcal{S}[Q_A]. \quad (\text{B.65})$$

and $\eta_d \equiv 1/(1-1/d^2)$, as defined in Section 3.4. Note that the first term in θ_{Q_A} corresponds to the phase applied by the coupling, while the second term accounts for minus signs associated with transposition and decoding (see Section 3.7). The sum in Eq. (B.64) is over the complete basis of Pauli operators in subsystem A. For single-qubit teleportation, this consists of three non-trivial Pauli operators and the identity (for which $\theta = 0$), and the sum can be performed explicitly. However, for teleporting many qubits, the number of terms quickly becomes intractable, and we instead approximate the sum by sampling Q_A (e.g. ~ 100 randomly selected operators). To compute the average EPR fidelity, we repeat this procedure for ~ 100 realizations of U . Finally, we note that the coupling strength g enters the fidelity calculation in a computationally efficient manner; in particular, upon determining the distribution of sizes for a particular circuit realization, we can compute the teleportation fidelity for arbitrary values of g “offline” with no additional simulation cost.

Extended data for 1D and 2D RUCs

Size distribution— The average size and size width for time-evolved operators in 1D and 2D for various system sizes are shown in Fig. B.1. In each case, we apply periodic boundary

¹We are grateful to Maxwell Block for sharing code to generate the full set of 2-qubit Clifford unitaries.

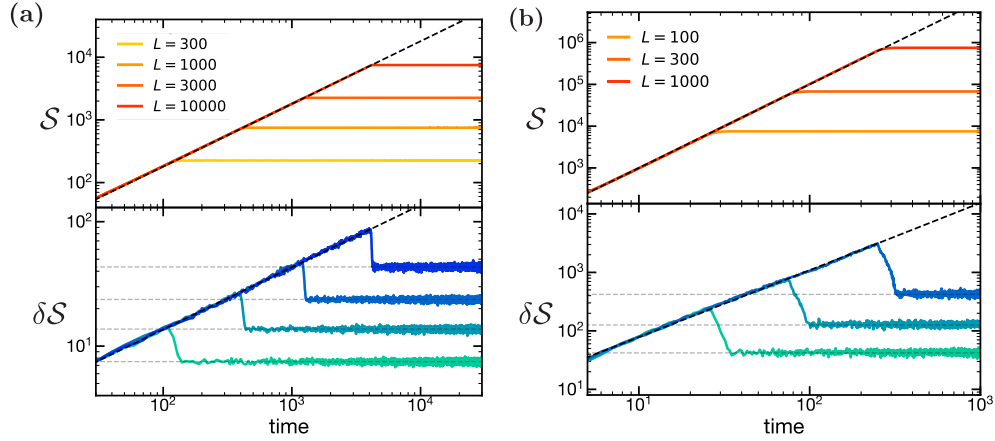


Figure B.1: Extended data for average operator size and size width in 1D **(a)** and 2D **(b)** RUCs. The average size grows ballistically $\sim t^d$ (dashed line) and saturates at $t_{\text{scr}} \sim L \sim N^{1/d}$. The size width matches the predictions from the KPZ universality class (dashed lines) and allows us to extract the prefactors in Eq. (3.56) and (3.57). In particular, we determine α_{bulk} and β_{bulk} from the saturation values (light gray), and α_{boundary} and β_{boundary} from the initial growth rate (dark gray).

conditions and begin with a single-qubit operator. These results match the functional forms predicted by the KPZ universality class [Eq. (3.56) and (3.57)] and allow us to extract the growth parameters $\{\alpha_{\text{bulk}}, \alpha_{\text{boundary}}, \beta_{\text{bulk}}, \beta_{\text{boundary}}\} = \{0.66, 0.70, 1.2, 4.5\}$.

Multiple qubits—In Fig. B.2, we present numerical evidence to support our claim that multiple qubits can be teleported in ≥ 1 D short-range models if their operator light cones are non-overlapping (Section 3.7). In particular, we simulate the teleportation of $n = 5$ qubits that are initially evenly spaced in a 1D RUC with periodic boundary conditions. At early times ($t < 1300$, Region I), we confirm that high-fidelity teleportation is possible for a wide range of coupling strengths, and by measuring the average operator size we infer that during this time the operator light cones have not overlapped. In contrast, after the light cones have overlapped, we generally observe a large suppression in the teleportation fidelity.

Interestingly, there is one noticeable exception to this reasoning: When only adjacent light cones have overlapped (i.e. $1300 < t < 2600$, Region II), high-fidelity teleportation can still occur for specific values of g . This situation corresponds to when the multi-qubit size is a multiple of $2\pi K/\eta_{dg}$ off from the size addition value, e.g. $\mathcal{S}[Q_1(t)Q_2(t)] = \mathcal{S}[Q_1(t)] + \mathcal{S}[Q_2(t)] - 2\pi m(K/\eta_{dg})$, where m is an integer value. Therefore, strictly speaking, it is possible to satisfy the conditions for many-body teleportation *without* size addition; nevertheless, it is a non-generic effect that requires finely tuned values of g and evenly spaced input qubits.

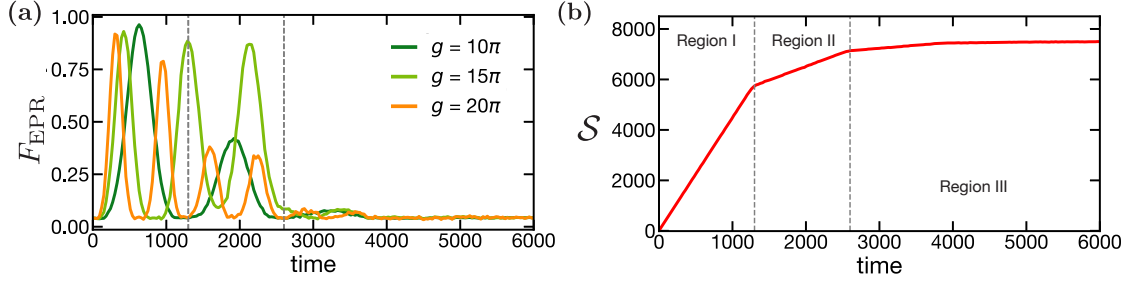


Figure B.2: Teleporting multiple qubits ($n = 5$) in 1D, where the input qubits are evenly spaced in the system ($N = 10000$). **(a)** Teleportation is achieved with high fidelity for $t \leq 1300$ (Region I). This corresponds to the regime in which the light cones of the operators are non-overlapping. Interestingly, order-one fidelity can also occur for $1300 < t < 2600$ (Region II), when adjacent light cones have overlapped, but only for certain values of g . No multi qubit teleportation is possible for $t \geq 2600$ (Region III), as expected from the lack of size addition. **(b)** The three Regions can be detected by changes in the slope of the operator size as a function of time. In particular, the growth rate decreases when nearest neighbor light cones, then next nearest neighbor light cones, etc. begin to overlap.

Channel capacity for 0D RUCs

An important result of our numerical simulations is substantiating the claim that 0D RUCs exhibit a channel capacity that scales linearly with the number of coupled qubits K . To this end, we first recall that our working definition for the channel capacity is based on setting a threshold for the *per qubit fidelity*. The most direct way to compute this fidelity would be to take the n -th root of the many-body EPR fidelity; in practice, however, this approach is numerically unstable for large n . Thus, we instead consider a modified protocol for estimating the per qubit fidelity where one attempts to send n qubits but only measures the fidelity of one of the n qubits. At infinite temperature and generalizing from one to m qubits, this fidelity is given by:

$$\begin{aligned}
 F_{\text{EPR}}^{(m)} &= \frac{1}{d_A^4} \sum_{Q_1, Q_2} \langle \text{TFD} | Q_{2,l}^\dagger(t) e^{-igV} \tilde{Q}_{2,r}^m(-t) \tilde{Q}_{1,r}^{m\dagger}(-t) e^{igV} Q_{1,l}(t) | \text{TFD} \rangle \cdot \text{tr} \left(Q_1^{u\dagger} Q_2^u \right) \\
 &= \frac{1}{d_m^4 d_u^2} \sum_{Q_1, Q_2} e^{i(\theta_{Q_1} - \theta_{Q_2})} \delta_{Q_1^u, Q_2^u}
 \end{aligned} \tag{B.66}$$

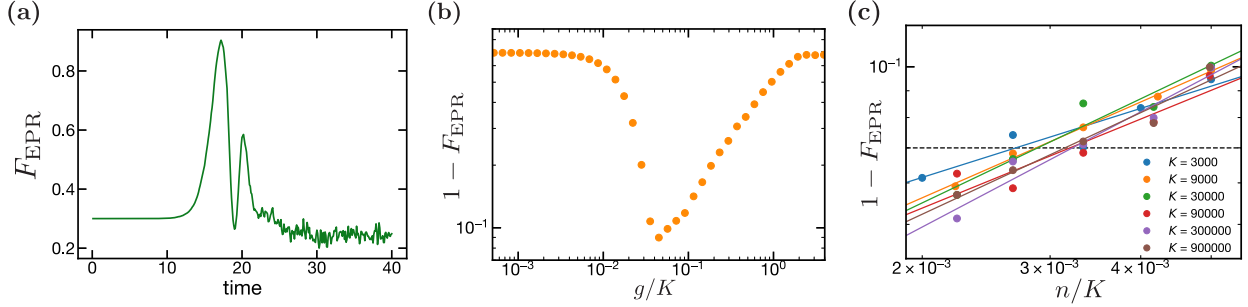


Figure B.3: Procedure for determining the channel capacity in 0D RUCs. **(a-b)** For fixed n and K , we compute the per qubit fidelity while sweeping both the evolution time and coupling strength g . (a) The fidelity as a function of evolution time with coupling strength fixed is optimized at the first local maximum, which corresponds to $\eta_{ag}\mathcal{S}/N = \pi$. (b) After optimizing the evolution time, the fidelity as a function of the coupling strength g is maximal when g (and correspondingly the average operator size \mathcal{S}) is tuned to balance errors due to size addition and the finite number of couplings (see Section 3.7 for details). The data shown correspond to $n = 38$ and $K = 9000$. **(c)** The channel capacity is defined as the maximum number of qubits that can be teleported while maintaining the fidelity per qubit above a fixed threshold, i.e. $1 - F_{\text{EPR}}^{(1)} \leq 0.07$ (dashed line). To determine this number, we fit the optimal fidelity as a function of n (for each K) with a linear fit in log space and compute the intercept of the fit with the threshold fidelity. The fits approximately collapse with respect to n/K , indicating that the channel capacity is linear in K .

where $Q = Q^m \otimes Q^u$ and $d_A = d_m d_u$, such that Q^m acts on the measured qubit(s), and Q^u acts on the unmeasured qubits. This can be derived diagrammatically via

$$\begin{aligned}
 F_{\text{EPR}} &= \text{Diagram 1} \\
 &= \frac{1}{d_A^2} \sum_{Q_1^m, Q_1^u, Q_2^m, Q_2^u} \text{Diagram 2} \\
 &= \frac{d_u}{d_A^4} \sum_{Q_1^m, Q_1^u, Q_2^m, Q_2^u} \text{Diagram 3} \\
 &= \frac{d_u^2}{d_A^4} \sum_{Q_1^m, Q_1^u, Q_2^m, Q_2^u} \text{Diagram 4}
 \end{aligned}
 \tag{B.67}$$

Hence, computing the per qubit fidelity, $F_{\text{EPR}}^{(1)}$, is nearly identical to computing the full many-body fidelity, except we sample only over pairs of Pauli operators (Q_1, Q_2) which are identical on every qubit except for one.

We next discuss how to determine the channel capacity from the teleportation fidelity. Specifically, we compute the maximum number of qubits n_{max} that can be teleported above a certain teleportation fidelity, where we fix the number of coupled qubits K and optimize over the evolution time t and the coupling strength g . We consider each of these parameters in turn. First, when sweeping the evolution time and holding all other parameters fixed, the maximum fidelity occurs during the first peak in the time profile; this corresponds to a size $\eta_d g \mathcal{S} = \pi/N$. After optimizing the evolution time (but holding n and K fixed), the fidelity is non-monotonic with respect to g , owing to the competition among errors due the size addition and finite K . Finally, after optimizing evolution time and g , we determine the maximum number of qubits that can be teleported while maintaining a per qubit fidelity above a fixed threshold value, i.e. $1 - F_{\text{EPR}}^1 \geq 0.07$. Our results from this procedure are shown in Fig. B.3 and demonstrate that the channel capacity follows a linear trend in K across two orders of magnitude, in agreement with our analytical predictions.

B.6 Random circuit calculations

Here we provide more detailed technical calculations of the size overlap and K -size distribution of random Pauli operators of a fixed size. The former is relevant to 0D RUCs (Section 3.7), as the vanishingly small overlap of random Pauli strings with size much less than the system size underlies the circuit's ability to teleport multiple qubits at intermediate times. The latter is applicable to all systems when the K coupled qubits are chosen randomly, and quantifies the width introduced to the K -size by this random sampling (Section 3.4). In the appropriate limits, these calculations reproduce the intuitive binomial scalings we argued for in Chapter 3.

Distribution of the overlap of two random Pauli strings

We are interested in the probability distribution of the size of the overlap, p (not to be confused with the large- p encoding, which we do not reference in this Appendix) of two randomly samples Pauli strings of fixed size R_1, R_2 , in a system of N qubits. We expect this to quantify errors to the size addition formula, Eq. (3.54) in Section 3.7, for 0D RUCs with large- p encoding (Section 3.7), where the assumption of random Pauli strings of a fixed size is appropriate. Our precise derivation is necessarily quite technical, however our final result matches that obtained by intuitive arguments in Section 3.7 [see beneath Eq. (3.62)].

This probability distribution is computed exactly as a product of various factorials:

$$P[p] = \frac{C_p^N C_{R_1-p}^{N-p} C_{R_2-p}^{N-R_1}}{C_{R_1}^N C_{R_2}^N} = \frac{1}{p!} \frac{R_1!}{(R_1-p)!} \frac{R_2!}{(R_2-p)!} \frac{(N-R_1)!(N-R_2)!}{N!(N-R_1-R_2+p)!} \quad (\text{B.68})$$

The numerator computes the number of distinct configurations with Pauli strings of size R_1, R_2 and overlap p , while the denominator computes the number of distinct Pauli strings of size R_1, R_2 regardless of the overlap. We are interested in the case where all variables are extensive (scale with N), but $N \gg R_1, R_2 \gg p$. We will proceed by applying Stirling's approximation to each term above, which holds as long as all quantities are large compared to 1. For instance, for dummy variables n, k , we have:

$$\frac{n!}{(n-k)!} \approx \sqrt{\frac{n}{n-k}} \frac{n^n}{(n-k)^{n-k}} e^{-k} = n^k \left(1 - \frac{k}{n}\right)^{-n+k-1/2} e^{-k} \quad (\text{B.69})$$

or, taking the logarithm,

$$\log \frac{n!}{(n-k)!} \approx k \log(n) - \left(n - k + \frac{1}{2}\right) \log\left(1 - \frac{k}{n}\right) - k. \quad (\text{B.70})$$

We will apply this to a few pairs of factorials in our original expression for $P[p]$. For convenience, we only keep track of the p -dependence of the probability, and neglect overall constants which serve to normalize the distribution. Anticipating that the average p will be $R_1 R_2 / N$, we expand $p = R_1 R_2 / N + \delta$ and work to second order in δ . At the end we will show that this is justified. We have:

$$\log \frac{R_1!}{(R_1 - p)!} \approx p \log(R_1) - \left(R_1 - \frac{R_1 R_2}{N} + \frac{1}{2}\right) \log\left(1 - \frac{R_2}{N} - \frac{\delta}{R_1}\right) - \frac{R_1 R_2}{N} - \delta \quad (\text{B.71})$$

Expanding the logarithm using

$$\log(1 - y - x) \approx \log(1 - y) - \frac{x}{1 - y} - \frac{1}{2} \frac{x^2}{(1 - y)^2} + \mathcal{O}(x^3) \quad (\text{B.72})$$

we have

$$\begin{aligned} & \log \frac{R_1!}{(R_1 - p)!} \\ & \approx p \log(R_1) - \left(R_1 - \frac{R_1 R_2}{N} - \delta + \frac{1}{2}\right) \left[\log\left(1 - \frac{R_2}{N}\right) - \frac{\delta/R_1}{1 - R_2/N} - \frac{(\delta/R_1)^2}{(1 - R_2/N)^2} \right] - \delta + \dots \\ & \approx p \log(R_1) + \delta \log\left(1 - \frac{R_2}{N}\right) - \frac{1}{2} \delta^2 \left[\frac{1}{R_1} \frac{1}{1 - R_2/N} \right] + \mathcal{O}(\delta/R) + \mathcal{O}(\delta^3/R^2) + \dots \end{aligned} \quad (\text{B.73})$$

This gives

$$\begin{aligned} & \log \frac{R_1!}{(R_1 - p)!} \frac{R_2!}{(R_2 - p)!} \\ & \approx p \log(R_1 R_2) + \delta \log\left(\left(1 - \frac{R_2}{N}\right)\left(1 - \frac{R_1}{N}\right)\right) - \frac{1}{2} \delta^2 \left[\frac{1}{R_1} \frac{1}{1 - R_2/N} + \frac{1}{R_2} \frac{1}{1 - R_1/N} \right] \\ & \quad + \mathcal{O}(\delta/R) + \mathcal{O}(\delta^3/R^2) + \dots \end{aligned} \quad (\text{B.74})$$

The last piece is

$$\begin{aligned}
 & \log \frac{N!}{(N - R_1 - R_2 + p)!} \\
 & \approx -p \log(N) - \left(N - R_1 - R_2 + \frac{R_1 R_2}{N} + \delta + \frac{1}{2} \right) \log \left(1 - \frac{R_1}{N} - \frac{R_2}{N} + \frac{R_1 R_2}{N^2} + \frac{\delta}{N} \right) + \delta + \dots \\
 & \approx -p \log(N) - \left(N - R_1 - R_2 + \frac{R_1 R_2}{N} + \delta + \frac{1}{2} \right) \times \\
 & \quad \left[\log \left(\left(1 - \frac{R_1}{N} \right) \left(1 - \frac{R_2}{N} \right) \right) + \frac{\delta/N}{\left(1 - \frac{R_1}{N} \right) \left(1 - \frac{R_2}{N} \right)} - \frac{\delta^2/N^2}{\left(1 - \frac{R_1}{N} \right)^2 \left(1 - \frac{R_2}{N} \right)^2} \right] + \delta + \dots \\
 & \approx -p \log(N) - \delta \left[\log \left(\left(1 - \frac{R_1}{N} \right) \left(1 - \frac{R_2}{N} \right) \right) \right] - \frac{1}{2} \delta^2 \left[\frac{1}{N \left(1 - R_1/N \right) \left(1 - R_2/N \right)} \right] + \\
 & \quad \mathcal{O}(\delta/N) + \mathcal{O}(\delta^3/N^2)
 \end{aligned} \tag{B.75}$$

Combining these together, we have

$$\begin{aligned}
 \log P[p] & \approx -\log(p!) + p \log \left(\frac{R_1 R_2}{N} \right) - \\
 & \quad \frac{1}{2} \delta^2 \left[\frac{1}{R_1} \frac{1}{1 - R_2/N} + \frac{1}{R_2} \frac{1}{1 - R_1/N} + \frac{1}{N} \frac{1}{\left(1 - R_1/N \right) \left(1 - R_2/N \right)} \right] + \mathcal{O}(\delta/R) + \mathcal{O}(\delta^3/R^2).
 \end{aligned} \tag{B.76}$$

Exponentiating,

$$P[p] \approx \frac{1}{p!} \left(\frac{R_1 R_2}{N} \right)^p \exp \left(-\frac{1}{2} \left(p - \frac{R_1 R_2}{N} \right)^2 \left[\frac{R_1 R_2}{R_1 + R_2} + \mathcal{O}(1/N) \right]^{-1} + \mathcal{O}(\delta/R) + \mathcal{O}(\delta^3/R^2) \right). \tag{B.77}$$

The first two terms are precisely a Poisson distribution, which has mean $R_1 R_2/N$ and width $\sqrt{R_1 R_2/N}$. The exponential is a Gaussian with the same mean $R_1 R_2/N$, and a larger width $\sqrt{R_1 R_2/(R_1 + R_2)}$. The smaller width determines the width of the product of the two functions, so we conclude:

$$\langle p \rangle = \frac{R_1 R_2}{N}, \quad \langle p^2 \rangle - \langle p \rangle^2 \approx \frac{R_1 R_2}{N}. \tag{B.78}$$

This is what we would expect for drawing p random sites out of N , where each site has independent probability R_i/N of being in either Pauli string (Section 3.7). The width is subextensive, $\delta \sim \varepsilon \sqrt{N}$, justifying the higher order terms we neglected along the way.

Distribution of the K -size

Here we are interested in the probability distribution of the K -size of a Pauli string of fixed total size \mathcal{S} , with K randomly chosen couplings. Our results substantiate those obtained by intuitive arguments beneath Eq. (3.34) in Section 3.4 in Chapter 3.

This objective is in fact an identical problem to calculating the overlap: the K -size is the overlap of the K coupled qubits with the \mathcal{S} qubits acted on by the operator of interest. We should just replace $R_1 \rightarrow K$, $R_2 \rightarrow \mathcal{S}$, $p \rightarrow n$ above, where n is the K -size. This is confirmed by comparing the factorial expressions:

$$P[n] = \frac{C_n^{\mathcal{S}} C_{K-n}^{N-\mathcal{S}}}{C_K^N} = \frac{1}{n!} \frac{\mathcal{S}!}{(\mathcal{S}-n)!} \frac{K!}{(K-n)!} \frac{(N-\mathcal{S})!(N-K)!}{N!(N-\mathcal{S}-K+n)!} \quad (\text{B.79})$$

where the numerator computes the number of distinct configurations with n qubits overlapping the Pauli operator support of size \mathcal{S} and $K-n$ qubits not overlapping, and the denominator computes the number of distinct configurations of the K coupled qubits. There are two regimes of interest: when K and \mathcal{S} are both extensive, and when \mathcal{S} is extensive but K is not. The former provides a more accurate measure of the full operator size ($K \rightarrow N$), while the latter is relevant for probing the channel capacity. Both regimes share the same mean K -size \mathcal{S}_K and K -size width $\delta\mathcal{S}_K$:

$$\mathcal{S}_K \equiv \langle n \rangle = \frac{\mathcal{S}K}{N}, \quad \delta\mathcal{S}_K^2 \equiv \langle n^2 \rangle - \langle n \rangle^2 \approx \frac{\mathcal{S}K}{N} = \mathcal{S}_K. \quad (\text{B.80})$$

This matches our prediction in Section 3.4, which was based on a simple scenario of picking K sites, each with a \mathcal{S}/N chance of being in the support of the Pauli operator.

B.7 Teleportation of fermions

Here we generalize the teleportation protocol to Majorana fermion systems, as discussed in Chapter 3 for the SYK model. This involves a few small modifications, stemming from (i) a different definition of fermionic EPR (FEPR) pairs, and (ii) a different relation between FEPR pair projector and the SWAP gate. These modifications explain the results of Ref. [88], which find that late time teleportation in the SYK model occurs with less than unit fidelity even at infinite temperature (where we would generally expect perfect fidelity, from late time peaked-size teleportation [Section 3.5, VI]). In particular, we find that the encoding procedure for the late time fermionic protocol must be modified for teleportation to succeed with perfect fidelity, due to modification (ii) above.

Consider two complex fermions χ_l and χ_r , decomposed into pairs of Majorana fermions via $\chi_l = \psi_l^1 + i\psi_l^2$, $\chi_r = \psi_r^1 + i\psi_r^2$. The number operators of the original fermions are Majorana bilinears, e.g. $i\psi_l^1\psi_l^2 = 2\hat{N}_l - 1 = (-1)^{\hat{N}_l}$. We define a single FEPR pair as the positive eigenstate of $i\psi_l^1\psi_r^1$ and $i\psi_l^2\psi_r^2$. In the number operator basis of the original complex fermions, this is the maximally entangled state $(|10\rangle - i|01\rangle)/\sqrt{2}$. Multiple fermion EPR pairs are formed as a tensor product of single FEPR pairs.

This definition leads to some simple relations when ‘sliding’ fermion operators around FEPR bras and kets in diagrammatic calculations. We have:

$$\begin{aligned} \psi_l^j |\text{FEPR}\rangle &= i\psi_r^j |\text{FEPR}\rangle \\ \langle \text{FEPR} | \psi_l^j &= -i \langle \text{FEPR} | \psi_r^j, \end{aligned} \quad (\text{B.81})$$

diagrammatically,

$$\begin{array}{c} \boxed{\psi^j} \\ \text{---} \\ \bullet \\ \text{---} \end{array} = i \begin{array}{c} \text{---} \\ \boxed{\psi^j} \\ \text{---} \\ \bullet \\ \text{---} \end{array}, \quad \begin{array}{c} \bullet \\ \text{---} \\ \boxed{\psi^j} \\ \text{---} \\ \bullet \\ \text{---} \end{array} = -i \begin{array}{c} \text{---} \\ \bullet \\ \text{---} \\ \boxed{\psi^j} \\ \text{---} \\ \bullet \\ \text{---} \end{array} \quad (\text{B.82})$$

As in bosonic systems, the thermofield double state is obtained by applying $\rho^{1/2}$ to one side, $|\text{TFD}\rangle = \rho_l^{1/2} |\text{FEPR}\rangle$. Since the SYK Hamiltonian is composed of 4-fermion terms, we have

$$H_l |\text{TFD}\rangle = (i)^4 H_r |\text{TFD}\rangle = H_r |\text{TFD}\rangle. \quad (\text{B.83})$$

As in bosonic systems, the coupling for Majorana systems [Eq. (3.69)] measures the size of Majorana strings.

There are two options teleportation in fermionic system. First, we could teleport an ordinary bosonic qubit by encoding it into Majorana fermion operators, for instance:

$$\begin{aligned} X &\equiv i\psi_1\psi_2 \\ Y &\equiv i\psi_2\psi_3 \\ Z &\equiv i\psi_1\psi_3. \end{aligned} \quad (\text{B.84})$$

At infinite temperature before coupling, each of the above operators has a correlator equal to -1 , which is exactly the result for bosonic systems, but without a need for the decoding operation Y . At late times, the coupling e^{igV} applies a relative phase between the identity and non-identity Paulis, giving correlator phases:

$\mathbb{1}$	$e^{ig\langle V \rangle}$
$i\psi_1\psi_2$	-1
$i\psi_2\psi_3$	-1
$i\psi_1\psi_3$	-1

When $g\langle V \rangle = \pi$ all correlators have the same phase, and peaked-size teleportation succeeds with perfect fidelity at infinite temperature. At intermediate times, peaked-size teleportation of multiple bosonic qubits will succeed just as in bosonic systems.

The second option is to send a fermionic qubit, for instance by inserting half of an ancillary FEPR pair. Here we begin with intermediate times, and discuss a modification necessary for late time teleportation afterwards. We represent a single complex fermion with two Majorana operators ψ_1, ψ_2 , and suppose that the operators' size distributions are tightly peaked, and the size of $i\psi_1\psi_2$ is twice that of the individual Majorana sizes, denoted \mathcal{S} (this assumption of size addition is appropriate in all-to-all coupled systems, e.g. SYK, but would not necessarily hold for e.g. a 1D Majorana chain). The relevant operator correlators after coupling with a bilinear fermionic interaction, as in Eq. (3.69), are:

$\mathbb{1}$	1
ψ_1	$-i \cdot e^{ig\mathcal{S}/qN}$
ψ_2	$-i \cdot e^{ig\mathcal{S}/qN}$
$i\psi_1\psi_2$	$-1 \cdot e^{ig2\mathcal{S}/qN}$

At $g\mathcal{S}/qN = \pi/2$ we have perfect teleportation. This generalizes straightforwardly to multiple fermionic qubits: a p -fermion operator will gain a phase i^p from sliding across the FEPR pair, and a phase $e^{igp\mathcal{S}/qN}$ from coupling.

At late times, the sizes of initial single-body and two-body Majorana operators are equal, since they have saturated the size of the system, and the above operator correlators do not have the same phase. We now show that an alteration of the encoding procedure can rectify this and lead to perfect late time teleportation. This alteration is explained by the HPR protocol, and we derive it by reexamining the equivalence between the HPR and TW protocols in the case of fermionic qubits. Here, the relevant difference between bosons and fermions is that the fermionic SWAP gate is *not* related to the Grover search operation $1 - 2P_{\text{FEPR}}$ by single-qubit rotations. Since fermions gain a minus sign upon exchange, the fermionic SWAP gate takes the form

$$\text{SWAP}_F = \begin{pmatrix} 1 & 0 & 0 & 0 \\ 0 & 0 & 1 & 0 \\ 0 & 1 & 0 & 0 \\ 0 & 0 & 0 & -1 \end{pmatrix} = \frac{i\psi_{1,l}\psi_{2,l} + i\psi_{1,r}\psi_{2,r} + i\psi_{1,l}\psi_{2,r} - i\psi_{2,l}\psi_{1,r}}{2}. \quad (\text{B.85})$$

This is a *two-qubit* controlled-phase (CZ) gate away from $1 - 2P_{\text{FEPR}}$:

$$\begin{aligned} 1 - 2P_{\text{FEPR}} &= \begin{pmatrix} 1 & 0 & 0 & 0 \\ 0 & 0 & i & 0 \\ 0 & -i & 0 & 0 \\ 0 & 0 & 0 & 1 \end{pmatrix} \\ &= \frac{1 - i\psi_{1,l}\psi_{1,r} - i\psi_{2,l}\psi_{2,r} - (i\psi_{1,l}\psi_{1,r})(i\psi_{2,l}\psi_{2,r})}{2} \\ &= \text{SWAP}_F \cdot \text{CZ}, \end{aligned} \quad (\text{B.86})$$

where the CZ gate is defined as

$$\begin{aligned} \text{CZ} &= \begin{pmatrix} 1 & 0 & 0 & 0 \\ 0 & i & 0 & 0 \\ 0 & 0 & -i & 0 \\ 0 & 0 & 0 & -1 \end{pmatrix} = (1 + i) \frac{\psi_{1,l}\psi_{2,l} + i\psi_{1,r}\psi_{2,r}}{2} \\ &= \exp\left(i\frac{\pi}{4}\right) \cdot \exp\left(-i\frac{\pi}{2}[i\psi_{1,l}\psi_{2,l}]\right) \cdot \exp\left(i\frac{\pi}{4}[i\psi_{1,l}\psi_{2,l}][i\psi_{1,r}\psi_{2,r}]\right). \end{aligned} \quad (\text{B.87})$$

The single-fermion $\exp\left(-i\frac{\pi}{2}[i\psi_{1,l}\psi_{2,l}]\right)$ gate occurs on the swapped-out fermion and may be neglected. Inserting this in place of the second Grover search operation gives the appropriate

teleportation protocol:

$$F_{\text{EPR}} = \text{[Circuit 1]} = \text{[Circuit 2]} \quad (\text{B.88})$$

In the second diagram we have slid the action of each side of the CZ gate such that the gate acts at the same time and on the same qubits as the initial SWAP gate.

We can relate the fidelity of teleportation to operator correlators by decomposing the encoding gate as

$$\text{CZ} \cdot \text{SWAP}_F = \frac{1}{2} \sum_{j=1}^4 S_{j,l}^L S_{j,r}^R \quad (\text{B.89})$$

where we define the operators:

j	S_j^L	S_j^R	$S_j^R S_j^L$
1	$\mathbb{1}$	$\mathbb{1}$	$\mathbb{1}$
2	$i\psi_1\psi_2$	$i\psi_1\psi_2$	$\mathbb{1}$
3	$i\psi_1$	ψ_1	$i\mathbb{1}$
4	$i\psi_2$	ψ_2	$i\mathbb{1}$

according to Eq. (B.86). The final column displays the product $S_j^L S_j^R$, where both act on

the same qubit, which will be useful shortly. We find a fidelity:

$$F_{\text{EPR}} = \text{Diagram 1} = \frac{1}{2^2} \sum_{j,k} \text{Diagram 2} = \frac{1}{2^4} \sum_{j,k} \text{Diagram 3} \tag{B.90}$$

In the peaked-size regime with correlator phases $\theta_{R,j}$, we have

$$\begin{aligned}
 F_{\text{EPR}} &= \frac{1}{2^4} \sum_{j,k} \langle \text{TFD} | S_{R,j,l}(t) e^{-igV} [S_{L,j,r} S_{L,k,r}^\dagger](-t') e^{igV} S_{R,k,l}^\dagger(t) | \text{TFD} \rangle \\
 &= \frac{1}{2^4} \sum_{j,k} \exp(-i[\theta_{R,j} - \theta_{R,k}]) \text{tr} \left(S_{R,j}(t-t') \rho^{1/2} S_{L,j}(0) S_{L,k}^\dagger(0) \rho^{1/2} S_{R,k}^\dagger(t-t') \right)
 \end{aligned} \tag{B.91}$$

At infinite temperature, late times, and $g \langle V \rangle = \pi$, we have correlator phases $\theta_{R,j} = 0$ for the identity and two-bosonic operator and $\theta_{R,j} = \pi/2$ for single-body fermionic operators,

and find perfect teleportation fidelity:

$$\begin{aligned}
 F_{\text{EPR}} &= \frac{1}{2^4} \sum_{j,k} \exp(-i[\theta_{R,j} - \theta_{R,k}]) \text{tr} \left(S_{R,j} S_{L,j} S_{L,k}^\dagger S_{R,k}^\dagger \right) \\
 &= \frac{1}{2^4} \sum_{j,k} \exp(-i[\theta_{R,j} - \theta_{R,k}]) \cdot i^{F_j} \cdot (-i)^{F_k} \cdot \text{tr}(i\psi_1\psi_2 i\psi_1\psi_2) \\
 &= \frac{1}{2^4} \sum_{j,k} \exp(-i[\theta_{R,j} - \theta_{R,k}]) \cdot i^{F_j} \cdot (-i)^{F_k} \\
 &= \frac{1}{2^4} \sum_{j,k} (-i)^{F_j} \cdot i^{F_k} \cdot i^{F_j} \cdot (-i)^{F_k} \\
 &= 1,
 \end{aligned} \tag{B.92}$$

where we define $F_j = 1$ if $S_{L/R,j}$ is fermionic, and 0 if bosonic.

We note that for state, as opposed to EPR, teleportation, the above CZ gate turns out not to be necessary. Since coherent superpositions of different fermion parity cannot be created by physical Hamiltonians, which contain only even combinations of fermionic operators, we should only consider teleporting states of definite fermion parity. The CZ gate applies only an overall phase on these states, and so does not affect the success of teleportation.

We can also briefly analyze the low temperature results of Ref. [88] through the lens of operator correlator phases. Here, state teleportation is found to succeed perfectly at low temperatures only when the initial operators are encoded in p -body Majoranas, with $p = q/2 + 1$, despite the operator correlators having maximal magnitude for any value of p . At the semiclassical gravity teleportation time, the correlators have phases:

$\mathbb{1}$	1
ψ_1	$i^p (i)^{2p/q}$
ψ_2	$i^p (i)^{2p/q}$
$i\psi_1\psi_2$	$(-1)^p (i)^{4p/q}$

For single-body Majoranas, $p = 1$, the correlators clearly do not have the same phase—in fact, their phases are nearly identical to their phases at infinite temperature with no coupling—so state teleportation is not possible. When $p = q/2 + 1$, in the large- q limit, these phases are $1, \pm 1, \pm 1, 1$, respectively, where the sign is determined by whether $p = 1, 3 \pmod{4}$. When the sign is odd, it can be corrected via the decoding operation $i\psi_1\psi_2 = (-1)^N$, which applies a minus sign when conjugating fermionic operators. Either case can therefore achieve perfect teleportation.

B.8 Teleportation and inelastic scattering at infinite temperature

In Section 3.8, we found that strong stringy corrections to a bulk theory of gravity led to peaked-size teleportation as well as a deeply inelastic scattering amplitude. We will now demonstrate that these two phenomena—peaked-size teleportation and inelastic scattering—also coincide at infinite temperature, for arbitrary functional forms of the wavefunctions and scattering amplitudes. As we argued before, for a UV complete theory of quantum gravity, strong stringy (and in general deep inelastic) effects are expected to dominate only at high temperatures, $\beta \rightarrow 0$.

At infinite temperature, the form of the correlator is constrained by the equality

$$C_\psi(t; g)^* = -C_\psi(t; -g). \quad (\text{B.93})$$

This implies that $C_\psi(t)$ can be written as a real function of ig multiplied by the two-point function:

$$C_\psi(t) = \langle \psi_l \psi_r \rangle e^{-F(ig, t)}. \quad (\text{B.94})$$

When $g = 0$, $C_\psi(t)$ is equal to $\langle \psi_l \psi_r \rangle$, implying

$$F(ig) = igf_1(t) + \mathcal{O}(g^2), \quad (\text{B.95})$$

where $f_1(t)$ is a real function. Therefore, at this order in g , the infinite temperature correlator is simply the two-point function multiplied by a pure phase, matching peaked-size teleportation [Eq. (3.37)].

To justify that higher order terms in g are subleading, we need an additional assumption: that the wavefunction of $\psi(t)$ has a saddle point at some momentum k . This is analogous to the boundary assumption that operator sizes are tightly peaked. At early times, this saddle will not be significantly changed by the coupling, since the derivative of the scattering matrix with respect to k will be suppressed by G_N , and at early times the time-dependence of the wavefunction will not be strong enough to compensate for this suppression (for example, in semiclassical AdS₂, we observed competition between $e^{2\pi t/\beta}$ and $1/G_N$). In such cases, it is easy to see that Eq. (3.95) becomes $\langle \psi_l \psi_r \rangle$ times a pure phase linear in g , with higher powers of g suppressed by G_N .

Infinite temperature also implies purely inelastic scattering, i.e. the scattering amplitude, $e^{i\delta} = 1 - S(k, s)$, is automatically real. To see this, we first rewrite the correlator in terms of the in-falling momentum operators, \hat{P} and \hat{K} , for ψ_1 and $\psi(t)$ respectively. For instance, for the former we have:

$$\begin{aligned} \Psi_{1,r}(s, 0) \Psi_{1,l}^*(s, 0) &= \langle \psi_{1,l}(0) | s \rangle \langle s | \psi_{1,r}(0) \rangle \\ &= \int \frac{da}{2\pi} \langle \psi_{1,l}(0) e^{-ia\hat{P}} \psi_{1,r}(0) \rangle e^{ias}. \end{aligned} \quad (\text{B.96})$$

As $\psi(t)$ and ψ_1 are in principle independent operators, we have $[\hat{K}, \hat{P}] = 0$. Using this, we can rewrite Eq. (3.95) as

$$C_\psi(t) = \langle \psi_r(-t) \exp\left(-igS(\hat{K}, \hat{P})i\psi_{1,l}\psi_{1,r}\right) \psi_l(t) \rangle. \quad (\text{B.97})$$

Taking the complex conjugate gives

$$\begin{aligned} C_\psi(t)^* &= \langle \psi_l(t) \exp\left(igS(\hat{K}, \hat{P})^*(-i)\psi_{1,r}\psi_{1,l}\right) \psi_r(-t) \rangle \\ &= -\langle \psi_r(-t) \exp\left(igS(\hat{K}, \hat{P})^*i\psi_{1,l}\psi_{1,r}\right) \psi_l(t) \rangle \end{aligned} \quad (\text{B.98})$$

where we used the fact that \hat{K}, \hat{P} are Hermitian and that at infinite temperature $\psi_l(t)|\text{TFD}\rangle = \psi_r(-t)|\text{TFD}\rangle$. Combining this with Eq. (B.93) then enforces $S(\hat{K}, \hat{P})^* = S(\hat{K}, \hat{P})$, i.e. purely inelastic scattering.

Appendix C

Details on comment on “Traversable wormhole dynamics on a quantum processor”

C.1 Other learned models

In the Supplemental Material of [121], two additional learned Hamiltonians are studied numerically.

Model 2—The first of these, which we refer to as Model 2, is given in Eq. (S16) of [121]:

$$\begin{aligned}
 H = & -0.35\psi^1\psi^2\psi^3\psi^6 + 0.11\psi^1\psi^2\psi^3\psi^8 - 0.17\psi^1\psi^2\psi^4\psi^7 \\
 & - 0.67\psi^1\psi^3\psi^5\psi^7 + 0.38\psi^2\psi^3\psi^6\psi^7 - 0.05\psi^2\psi^5\psi^6\psi^7.
 \end{aligned}
 \tag{C.1}$$

Model 2 is produced from the same machine-learning procedure as Model 1, i.e. designed to match the teleportation signal of the $N = 10$ SYK model. The authors claim that Model 2 demonstrates perfect size winding and “is consistent with other gravitational signatures”.

As noted in [121], Model 2 is not fully commuting. Nevertheless, we observe that Model 2 becomes fully-commuting if: (i) the two *smallest* terms in Eq. (C.1) are removed, and (ii) one performs a basis rotation:

$$\begin{aligned}
 \psi^1 & \rightarrow \cos(\theta)\psi^1 + \sin(\theta)\psi^7, \\
 \psi^7 & \rightarrow \cos(\theta)\psi^7 - \sin(\theta)\psi^1,
 \end{aligned}
 \tag{C.2}$$

with $\theta = \tan^{-1}(-0.35/0.38)$. At the timescale of teleportation ($t = 2.8$), the two smallest terms provide relatively small corrections to physical observables. Thus, Model 2 can be considered weakly perturbed from a fully-commuting limit.

Consistent with this observation, we find that our main observations regarding Model 1 also apply to Model 2 (Fig. 4.4a-d). In particular, the individual two-point correlation functions exhibit strong revivals, the teleportation signal does not resemble the SYK model

for untrained operators, and the size winding behavior resembles that of a random fully-commuting Hamiltonian (Fig. 4.3c). In addition, we note that the teleportation signal for the *trained* operators in Model 2 displays a significant revival within the timescale on which it was trained (Fig. 4.4b). This contrasts with the $N = 10$ SYK model and indicates that the training procedure was not fully successful; such disagreement is not shown or commented on in [121].

Model 3—The second additional model, which we refer to as Model 3, is given in Eq. (S17) of [121]:

$$\begin{aligned}
 H = & 0.60\psi^1\psi^3\psi^4\psi^5 + 0.72\psi^1\psi^3\psi^5\psi^6 + 0.49\psi^1\psi^5\psi^6\psi^9 \\
 & + 0.49\psi^1\psi^5\psi^7\psi^8 + 0.64\psi^2\psi^4\psi^8\psi^{10} - 0.75\psi^2\psi^5\psi^7\psi^8 \\
 & + 0.58\psi^2\psi^5\psi^7\psi^{10} - 0.53\psi^2\psi^7\psi^8\psi^{10}.
 \end{aligned}
 \tag{C.3}$$

Model 3 is produced via a different machine-learning procedure, which is designed to optimize the asymmetry in the teleportation signal between positive and negative couplings. Unlike Models 1 and 2, Model 3 is not fully-commuting or near fully-commuting.

Referring to the average two-point correlator, the authors demonstrate that “no periodicities are present despite the small number of terms in the Hamiltonian” (Fig. S26 of [121]). In Fig. 4.4d, we observe that the individual two-point correlators also exhibit thermalizing behavior at long time scales ($t \sim 30$). This is consistent with Model 3 being non-commuting. At earlier times, the correlators exhibit oscillations that are smaller than those of Model 1 and 2, but larger than fluctuations in the $N = 10$ SYK model.

The teleportation signal for Model 3 exhibits a single-peak structure for nearly all operators, albeit with large variations in peak height (Fig. 4.4e).

The authors note that Model 3 does not exhibit perfect size winding, but rather features a “consistently large ratio [of phase alignment], suggesting slightly damped size winding”. Indeed, we find that the phase alignment, \bar{r} , for Model 3 is comparable to that of the $N = 10$ SYK model and lower than that of small-size fully-commuting models (Fig. 4.3b). This is consistent with our observation that perfect phase alignment at small system sizes is a generic feature of fully-commuting Hamiltonians and not of non-commuting Hamiltonians. We note that only some operators in Model 3 (including the trained operators) exhibit a high degree of linearity χ (Fig. 4.3c). In this respect, Model 3 resembles the behavior of fully-commuting or nearly fully-commuting models (including Model 1 and 2) and not the SYK model.

C.2 Four-point correlators with $i \neq j$

Scrambling is quantified in [121] via the behavior of the four-point correlation functions, $F_{\text{avg}}(t) = \sum_{i=1}^8 F_i(t)$, with $F_i(t) = -\text{Re} \left[\langle [\psi^i(t), \psi^i(0)]^2 \rangle_\beta \right]$. We note that such correlation functions, consisting of the same Majorana ψ^i for the time-evolved and static operators, are not the most direct probe of scrambling dynamics, since their initial growth occurs on

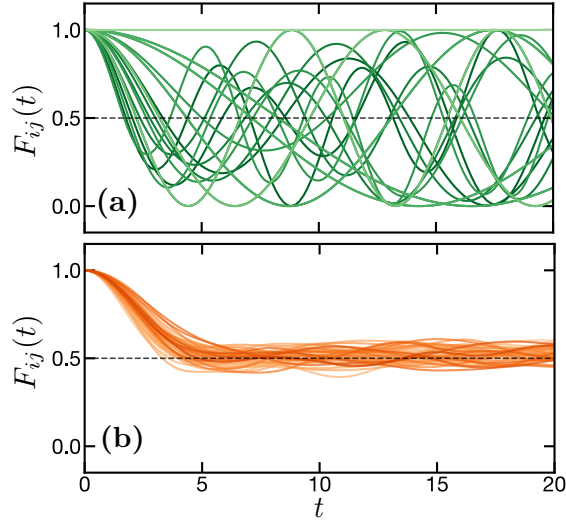


Figure C.1: **(a)** Four-point correlation functions, $F_{ij}(t)$, for Model 1, shown for all pairs of Majorana operators, $i < j \in [1, 7]$. **(b)** The same correlation functions for a specific instance of the $N = 10$ SYK model with $J = 1.125$ and $i < j \in [1, 10]$.

the same timescale as the decay of two-point correlation functions (i.e. the thermalization time). In the SYK model at large system sizes, the initial growth reaches a value of unity and is followed by a slower decay to value $1/2$ on the timescale of the scrambling time; such non-monotonic behavior is evident in the time traces of the $N = 10$ SYK model shown in Fig. 4.1d. A more typical probe of scrambling is the four-point correlator, $F_{ij}(t) = -\text{Re}[\langle [\psi^i(t), \psi^j(0)]^2 \rangle_\beta]$, for different operators, $i \neq j$. In the SYK model at large system sizes, this correlator decays monotonically from unity to value $1/2$ on the timescale of the scrambling time.

In Fig. C.1, we plot the four-point correlation functions, $F_{ij}(t)$ with $i \neq j$, for both Model 1 and the $N = 10$ SYK model. Much like the four-point correlation functions with $i = j$ (i.e. $F_i(t)$, see Fig. 4.1), we find that the four-point correlation functions in Model 1 exhibit strong oscillations in time for all $i \neq j$. In fact, the oscillations for many pairs of operators have unit amplitude. In contrast, in the $N = 10$ SYK model, all correlation functions exhibit a smooth decay to value $1/2$.

C.3 Teleportation at fixed injection time

As previously discussed, two versions of the teleportation protocol are analyzed in [121]: using symmetric injection / readout times and fixed injection time. In Fig. C.2, we present results for latter protocol for Model 1 and the $N = 10$ SYK model. For Model 1, when the protocol is performed with the pair of operators that were trained on, the mutual informa-

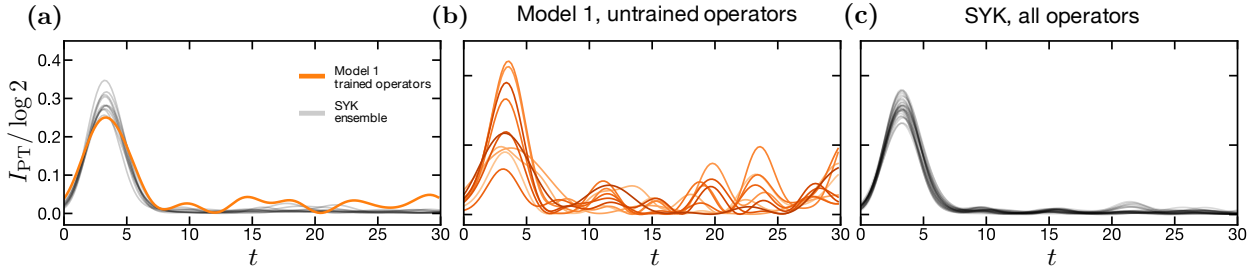


Figure C.2: **(a)** Mutual information of the teleportation protocol with fixed injection time as a function of the readout time (i.e. $t_0 = 2.8$ and $t = t_1$). The mutual information for Model 1 and the trained operators, ψ^1 and ψ^2 , is in reasonable agreement with that of multiple instances of the $N = 10$ SYK model (grey). **(b)** The mutual information for Model 1 and all pairs of untrained operators, ψ^i and ψ^j with $i < j \in [2, 7]$, exhibits variations and revivals as a function of time. **(c)** The mutual information for all pairs of operators in the $N = 10$ SYK model exhibits a single consistent peak.

tion displays a single peak as a function of time. For other pairs of operators, the mutual information displays an initial peak, whose height varies significantly for different pairs of operators, followed by revivals at later times. This contrasts with the SYK model, in which the mutual information displays a single consistent peak for all pairs of operators, with small and infrequent fluctuations at late times.

C.4 Size-winding metrics

Here, we elaborate on the phase alignment, \bar{r} , and the linear slope metric, χ , which are plotted in Fig. 4.3b and Fig. 4.3c.

Phase alignment—We recall that in [121], the phase alignment is quantified by plotting the ratio, $r_l = \left| \sum_{|P|=l} c_P^2 \right| / \sum_{|P|=l} |c_P|^2$, for different sizes l (Figs. S14 and S19 of [121]). The denominator of this quantity is the operator size distribution, $p(l) = \sum_{|P|=l} |c_P|^2$, which is normalized to one, $\sum_l p(l) = 1$. To facilitate comparison between different operators and models, we consider the weighted average of r_l , $r = \sum_l p(l) r_l = \sum_l \left| \sum_{|P|=l} c_P^2 \right| = \sum_l |q(l)|$. For a given Hamiltonian, r is lower bounded by the two-point function, $W = \text{tr}(\psi^i(t) \rho^{1/2} \psi^i(t) \rho^{1/2}) = \sum_P c_P^2$. We note that this two-point function is constant in time, and therefore the sum of the squared coefficients is also constant in time. Taking into account this lower bound motivates us to rescale r as $\bar{r} = \frac{r-W}{1-W}$, which ranges from zero to one.

Linear slope—We seek to quantify the degree to which the phases of $q(l)$ follow a linear slope with respect to the size l . The fit of a line of slope μ can be quantified via $C(\mu) = \left| \sum_l q(l) e^{-i\mu l} \right|$. When deviations from a linear slope are small, this reduces to unity

minus a weighted sum of squared errors; when deviations are large, it takes into account the periodicity of the phases. The best fit, C^* , is found by maximizing over μ , $C^* = \max_{\mu} C(\mu)$.

We define the metric, χ , to interpolate between zero and one as C^* interpolates between its minimum and maximum values. The maximum value of $C(\mu)$ is given by the weighted average, r , of the phase alignment ratio. The minimum value is lower bounded by the two-point function, $W = C(\mu = 0)$. In addition, at small system sizes it is relevant to consider a second lower bound, corresponding to fitting a line between the two coefficients, $q(l_1)$ and $q(l_2)$, with the largest magnitude. This consideration is necessary to avoid concluding that functions $q(l)$ with support on only two values of l have non-trivial size winding. This fit produces a C of value at least $M = |q(l_1)| + |q(l_2)| - (r - |q(l_1)| + |q(l_2)|) = 2|q(l_1)| + 2|q(l_2)| - r$. We thus define the metric,

$$\chi = \frac{C^* - L}{r - L}, \quad (\text{C.4})$$

where L is the larger of the two lower bounds, $L = \max(W, M)$.

C.5 Other fully-commuting models

Here we include details on the random fully-commuting models presented in Fig. 4.3. For all random models in Fig. 4.3, we take $\beta = 4$ and $t = 2.8$, identical to Model 1.

Majorana models—In Model 1 with randomized coefficients, we draw each coefficient from a normal distribution with mean zero and standard deviation equal to the root-mean-square of the coefficients of Model 1. In Model 1 with randomized terms and coefficients, we generate five random fully-commuting terms by successively drawing random four-Majorana terms (from $N = 7$ total Majorana operators) and keeping each term only if it commutes with all terms already kept.

Ising models—We consider random all-to-all Ising models with Hamiltonian, $H = \frac{1}{\sqrt{N}} \sum_{i < j} J_{ij} Z^i Z^j$. The coefficients J_{ij} are drawn from a normal distribution with mean zero and standard deviation $J = 0.17$.

Finite-size scaling—To explore whether the size winding behavior of fully-commuting models persists at larger system sizes, in Fig. C.3 we plot the phase alignment, \bar{r} , for random all-to-all Ising models as a function of the system size N . We focus on Ising models to avoid subtleties with scaling random fully-commuting Majorana models to larger system sizes (namely, there is no canonical choice of which fully-commuting terms to include). We scale the evolution time t with the square root of the system size, $t = 2.8\sqrt{N}/4$, to ensure that operators grow to the same fraction of the system size for each N . We find that the phase alignment, \bar{r} , exhibits a decreasing trend with the system size.

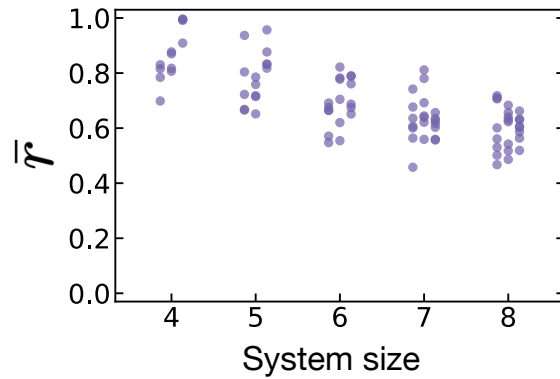


Figure C.3: Phase alignment, \bar{r} , of the random all-to-all Ising model as a function of the system size $N \in [4, 8]$, with $J = 0.17$ and $\beta = 4$. Three disorder realizations are shown at each system size, with small horizontal offsets for clarity.

Appendix D

Details on butterfly metrology

D.1 Comparison to previous time-reversed sensing protocols

Previous metrology proposals have considered the use of time-reversed dynamics through variants of a so-called echo protocol, depicted in Fig. D.1. Compared to our protocol, the key distinction is that the echo protocol consists of a *single* step of forward and backward time evolution, i.e. the metrological state is prepared via the forward evolution, i.e. $U|\mathbf{0}\rangle$, and time-reversed evolution is applied prior to the detection. As a result, it only achieves a metrological enhancement for specific classes of unitary dynamics—namely, U must generate a state with a large quantum Fisher information (QFI). In contrast, our protocol relies on forward and backward time evolution *during* the state preparation stage; this provides a quantum enhancement in sensitivity under a vastly larger class of unitaries.

To illustrate this distinction, let us recall a few classes of unitaries U for which the standard echo protocol has previously been applied. First, consider U to be a Clifford circuit that prepares a GHZ state, i.e. $U|\mathbf{0}\rangle = |\text{GHZ}\rangle \sim |00\dots\rangle + |11\dots\rangle$. The full sensing scheme consists of applying U to generate a GHZ state, accumulating a phase under the external signal, and then applying the inverse preparation circuit. The last step focuses the acquired phase to a single-body observable. Although this last step is not strictly necessary—one could instead detect the phase via global parity measurements of the GHZ state—it is important in practice as it leads to much greater robustness to readout noise [185]¹. A second class of unitaries under which an enhancement can be achieved consists of evolution under a large-spin Hamiltonian, e.g. the one-axis twisting model, $H = S_z^2$ with $S_z = \frac{1}{2} \sum_i \sigma_i^z$.

¹Interestingly, sensing with a GHZ state can be understood as special cases of our protocol. In particular, consider a protocol which prepares a GHZ state by applying a $\pi/2$ pulse to the first qubit, $(\hat{1} + i\sigma_0^x)/\sqrt{2}$, followed by a CNOT “ladder” denoted U . To detect the accumulated phase from an external signal, the inverse ladder U^\dagger is applied and the first qubit is measured. The final state is $U^\dagger e^{i\phi S_z} U (\hat{1} + i\sigma_0^x) |\mathbf{0}\rangle$. Because $|\mathbf{0}\rangle$ is an eigenstate of CNOT gates, we can insert an additional copy of U^\dagger at the beginning of the circuit without changing the final outcome: $U^\dagger e^{i\phi S_z} U (\hat{1} + i\sigma_0^x) U^\dagger |\mathbf{0}\rangle$. This is precisely of the form of our protocol (upon substituting $U \rightarrow U^\dagger$).

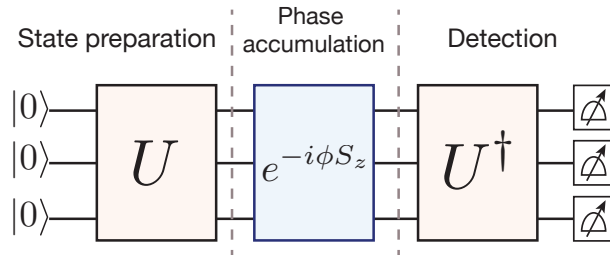


Figure D.1: The general form of an echo protocol, which underlies previous time-reversal-based sensing proposals. In contrast to our protocol, time-reversed evolution is employed only in the detection stage, rather than during the state preparation.

Such Hamiltonians give rise to semi-classical dynamics, which can be used to generate a squeezed state [66, 160]. Much like for the GHZ state, the effect of the perturbation may be detected directly via measurements on the squeezed state; however, applying the inverse preparation circuit to “un-squeeze” the state improves the robustness to readout noise [58, 66]. Other examples of unitaries that have been proposed to generate metrologically useful states include evolution under certain integrable Hamiltonians [100] or Hamiltonians with a continuous-symmetry breaking phase [33].

However, the standard echo protocol shown in Fig. D.1 *does not* provide a metrological enhancement for generic unitary dynamics outside of these few isolated classes. In particular, consider U to be a Haar-random unitary, which correspond to the late-time dynamics of generic scrambling systems. The state prepared under forward evolution, $U|\mathbf{0}\rangle$ has, on average, no correlation in the Z-basis, implying a QFI that scales as $\mathcal{F} \sim N$ and a sensitivity that is bounded by the standard quantum limit.

As discussed in Chapter 5 and shown in detail below, this restriction does not apply to our protocol and, indeed, a Heisenberg-like enhancement can be achieved under generic thermalizing dynamics. This greater versatility opens the door to achieving a metrological enhancement in a wider variety of experimental platforms (e.g. the spin systems discussed in Sections D.5 and D.5). Furthermore, even in systems that could achieve a metrological enhancement using the previous echo approach, our protocol may offer certain advantages with respect to decoherence and robustness to control errors, as discussed in Sections D.5 and D.5.

D.2 Haar-random evolution

In this section, we calculate the sensitivity of our sensing protocol for a Haar-random unitary U . These results provide a general expectation for the *late-time* behavior of generic scrambling dynamics.

Local control—As discussed in Chapter 5, the mean outcome of the local protocol is

$$\begin{aligned} \langle \hat{V} \rangle_\phi &= \frac{1}{2} \langle \mathbf{0} | \hat{V}(t) | \mathbf{0} \rangle - \frac{1}{2} \langle \mathbf{0} | \hat{V}(t) e^{i\phi S_z} V(t) e^{-i\phi S_z} \hat{V}(t) | \mathbf{0} \rangle \\ &+ \text{Im} \left[e^{i\phi N/2} \langle \mathbf{0} | \hat{V}(t) e^{-i\phi S_z} \hat{V}(t) | \mathbf{0} \rangle \right], \end{aligned} \quad (\text{D.1})$$

where \hat{V} is a Pauli operator and $\hat{V}(t) = U^\dagger \hat{V} U$. For a Haar-random unitary U , the first two terms have vanishing expectation value, leaving only the final term. To analyze this quantity, we express the perturbed state $\hat{V}(t) | \mathbf{0} \rangle$ in the computational basis as $\sum_{s \in \{0,1\}^N} c_s |s\rangle$ and consider its *polarization distribution* $P(S_z) = \sum_{|s|=2S_z} |c_s|^2$, where $|s| = \sum_i (-1)^{s_i}$. We observe that $\langle \hat{V} \rangle_\phi$ is related to the characteristic function of $P(S_z)$:

$$\langle \hat{V} \rangle_\phi = \text{Im} \left[e^{i\phi N/2} \sum_{S_z=-N/2}^{N/2} e^{-i\phi S_z} P(S_z) \right] \quad (\text{D.2})$$

$$= \text{Im} \left[e^{i\phi N/2} \Phi(\phi) \right] \quad (\text{D.3})$$

where $\Phi(\phi) = \sum_{S_z=-N/2}^{N/2} e^{-i\phi S_z} P(S_z)$. Since the perturbed state is a Haar-random state, its polarization obeys a binomial distribution, $P(S_z) = \frac{1}{2^N} \binom{N}{N/2-S_z}$ with $S_z = -N/2, -N/2 + 1, \dots, N/2 - 1, N/2$. Plugging this distribution into the formula above allows us to directly calculate the mean outcome as a function of ϕ , as shown in Fig. 2(b) of Chapter 5.

To analyze the sensitivity for small values of ϕ , we Taylor expand Eq. D.2 to leading order. We find that the sensitivity is given by the first moment of $P(S_z)$,

$$\eta_{\phi=0}^{-1} = N/2 - \sum_{S_z} S_z P(S_z). \quad (\text{D.4})$$

The polarization distribution for a Haar-random unitary has mean zero and thus leads to $\eta_{\phi=0} = 2/N$, a factor of 2 above the strict Heisenberg limit.

To determine the sensitivity for finite ϕ , we assume that the real part of the characteristic function is also measured (via the protocol in Section D.3). The optimal sensitivity is obtained by taking a linear combination of the real and imaginary parts, $C(\phi, \theta) = \cos(\theta) \text{Re} [e^{i\phi N/2} \Phi(\phi)] + \sin(\theta) \text{Im} [e^{i\phi N/2} \Phi(\phi)]$, and maximizing $|\partial_\phi C(\phi, \theta)|$ with respect to θ . This yields an optimal sensitivity $\eta_\phi^{-1} = |-iN/2\Phi(\phi) + \Phi'(\phi)|$. Note that range of ϕ for which this sensitivity is achieved is $\phi \lesssim 1/\sqrt{N}$. This follows from a simple intuition: In the limit $N \gg 1$, the binomial distribution can be approximated as a Gaussian, i.e. $P(S_z) \sim e^{-2S_z^2/N}$, which yields $\eta_\phi^{-1} \approx (N/2)e^{-\phi^2 N/8}$.

Global control—The measurement outcome of the protocol with global controls (Fig. 3 of the Chapter 5) is qualitatively similar to the case of local control, but differs by an overall constant. To see this, we begin by expanding the global rotation as $e^{i\epsilon S} = a\hat{1} + i\tilde{V}(t)$, where $S = \frac{1}{2} \sum_i \sigma_i^\mu$ is a sum of local Pauli operators, $a = \cos^N(\epsilon/2)$, and \tilde{V} is a traceless operator

satisfying $\text{tr}(\tilde{V}^\dagger \tilde{V}) = (1 - a^2) \text{tr}(\mathbb{1})$. Analogous to Eq. D.1, the expected outcome is given by

$$\begin{aligned} \langle S \rangle_\phi &= a^2 \langle \mathbf{0} | S(t) | \mathbf{0} \rangle - \langle \mathbf{0} | \tilde{V}(t) e^{i\phi S_z} S(t) e^{-i\phi S_z} \tilde{V}(t) | \mathbf{0} \rangle \\ &+ 2a \text{Im} \left[e^{i\phi \frac{N}{2}} \langle \mathbf{0} | S(t) e^{-i\phi S_z} \tilde{V}(t) | \mathbf{0} \rangle \right], \end{aligned} \quad (\text{D.5})$$

and, for Haar-random evolution, only the third term is non-vanishing. However, there are a few key differences from the case of local control. First, the prefactor a is a free parameter determined by the rotation angle ϵ . Second, the third term involves a matrix element between two distinct states $\tilde{V}(t) | \mathbf{0} \rangle$ and $S(t) | \mathbf{0} \rangle$. For a Haar-random unitary, only the projection of $\tilde{V}(t) | \mathbf{0} \rangle$ onto $S(t) | \mathbf{0} \rangle$ contributes to the matrix element. To determine this projection, we re-express the global rotation as $e^{i\epsilon S} = a\hat{1} + i2a \tan(\epsilon/2)S + S_\perp$, where $\text{tr}(SS_\perp) = 0$. The Haar average keeps only the term proportional to S , so the measurement outcome simplifies to

$$\langle S \rangle_\phi = 4a^2 \tan(\epsilon/2) \cdot \text{Im} \left[e^{-i\phi \frac{N}{2}} \langle \mathbf{0} | S(t) e^{i\phi S_z} S(t) | \mathbf{0} \rangle \right]. \quad (\text{D.6})$$

We note that the state $S(t) | \mathbf{0} \rangle$ is non-normalized, i.e. $\langle \mathbf{0} | S(t) S(t) | \mathbf{0} \rangle = N/4$. Thus, in combination, the measurement outcome for the global protocol differs from local control by a factor of $a^2 N \tan(\epsilon/2)$.

We proceed to calculate the sensitivity, $\eta_{\phi=0}^{-1} \equiv (\partial_\phi \langle S \rangle_\phi / \Delta S_\phi)_{\phi=0}$, for small values of ϕ . We also take the limit $N \gg 1$, for which $a = \cos^N(\epsilon/2) \approx \exp(-\bar{\epsilon}^2/2)$, where $\epsilon \equiv 2\bar{\epsilon}/\sqrt{N}$ and $\bar{\epsilon}$ is an order-one constant. From Eq. D.6, we have $\partial_\phi \langle S \rangle_{\phi=0} \approx a^2 \bar{\epsilon} N^{3/2}/2$, and the standard deviation for the measurement is $\Delta S_{\phi=0} = \sqrt{N}/2$. This yields $\eta_{\phi=0}^{-1} \approx \bar{\epsilon} e^{-\bar{\epsilon}^2} N$, whose optimum is $\eta^{-1} = (1/\sqrt{2e})N \approx 0.43N$ at $\bar{\epsilon} = 1/\sqrt{2}$. In Fig. D.2, we compare this prediction to exact simulations of a spin model with $N = 18$ spins and observe excellent agreement.

Interestingly, we note that measuring S is not, in fact, the optimal approach for Haar-random evolution, and a small improvement in sensitivity may be achieved by measuring a different global quantity, namely $M = \tilde{V} + \tilde{V}^\dagger = 2 \sin(\epsilon S)$. Deriving the sensitivity is straightforward but tedious, so we simply quote the result: $\eta_{\phi=0}^{-1} = (a/\sqrt{2})(1-a^4)^{1/2}N$, which yields a maximum sensitivity of $\eta^{-1} = (1/3^{3/4})N \approx 0.44N$. Although this offers a minute advantage over the original protocol, it may be more challenging to realize experimentally since it involves measuring higher powers of S . Furthermore, while measuring M provides better sensitivity for Haar-random evolution, we find in numerical simulations that this is not the case for early-time evolution, which is not Haar-random.

D.3 Measuring the opposite quadrature

As discussed in the previous section, the protocols shown in the Chapter 5 (i.e. Fig. 1 and 3) are directly related to the imaginary part of the characteristic function $\Phi(\phi)$ of the polarization distribution $P(S_z)$. This implies that they achieve a high sensitivity only at certain values of ϕ , which notably includes $\phi = 0$. In order to maintain a high sensitivity

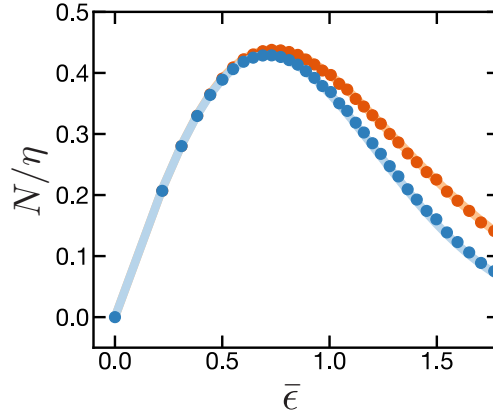


Figure D.2: Global sensitivity as a function of $\bar{\epsilon}$ for the measurement operator (blue) S and (orange) $M = 2 \sin(\epsilon S)$. We observe excellent agreement between the analytic prediction for Haar-random evolution (solid line) and the late-time dynamics of a $N = 18$ spin system (points). The spin system consists of all-to-all, random two-body terms: $H = \sum_{i < j} \sum_{\mu, \nu} J_{ij}^{\mu\nu} \sigma_{\mu}^i \sigma_{\nu}^j$, where $\mu, \nu \in \{X, Y, Z\}$ and $J_{ij}^{\mu\nu}$ is drawn from a Gaussian distribution with standard deviation J/\sqrt{N} . The evolution time is $tJ = 10$. Similar results are obtained for generic Hamiltonians evolved past the scrambling time, though the agreement is not as precise as the disordered, all-to-all spin system at the accessible system sizes.

over a continuous range of ϕ , it is necessary to measure the opposite quadrature—i.e. the real part of the characteristic function.

There are two straightforward modifications of our protocol that achieve this goal, as depicted in Fig. D.3. The first approach, which applies only to the protocol with local controls, is to replace the local rotation by a *projection*, e.g. $(\hat{1} + \hat{V})/2$ for a Pauli operator \hat{V} . The measurement outcome then becomes

$$\begin{aligned} \langle \hat{V} \rangle_{\phi} &= \frac{1}{2} \langle \mathbf{0} | \hat{V}(t) | \mathbf{0} \rangle - \frac{1}{2} \langle \mathbf{0} | \hat{V}(t) e^{i\phi S_z} V(t) e^{-i\phi S_z} \hat{V}(t) | \mathbf{0} \rangle \\ &\quad + \text{Re} \left[e^{i\phi \frac{N}{2}} \langle \mathbf{0} | \hat{V}(t) e^{-i\phi S_z} \hat{V}(t) | \mathbf{0} \rangle \right] \\ &= \text{Re} \left[e^{i\phi \frac{N}{2}} \Phi(\phi) \right], \end{aligned} \quad (\text{D.7})$$

where $\Phi(\phi)$ is defined below Eq. D.2, and, in the second line, we assume that the first two terms have vanishing expectation values². While conceptually simple, measuring the real part of $\Phi(\phi)$ in this way requires the ability to reset an individual qubit during the execution of the protocol. Alternatively, one can delay the projection to the end of the protocol by

²The first two terms may also be directly cancelled by projecting onto the opposite state, i.e. using $(1 - \hat{V})/2$, and measuring $-\hat{V}$. Averaging this outcome with Eq. D.8 leaves only the final term, $\text{Re} [e^{i\phi N} \Phi(\phi)]$.

swapping in an ancilla qubit in the state $|0\rangle$ (taking $\hat{V} = \hat{\sigma}^z$), and post-selecting on the final state of the ancilla qubit.

Our second approach, which is analogous to a standard Loschmidt echo, is to perform the full inverse of the state preparation procedure, as shown in Fig. D.3. This approach can be applied with either local or global controls, but, for specificity, let us focus on the variant with local controls. The conceptually simplest quantity to analyze is the return probability, P_0 , given by

$$\begin{aligned} P_0 &= \frac{1}{4} \left| \langle \mathbf{0} | (1 - i\hat{V}(t)) e^{-i\phi S_z} (1 + i\hat{V}(t)) | \mathbf{0} \rangle \right|^2 \\ &= \frac{1}{4} \left| e^{-i\phi \frac{N}{2}} + \langle \mathbf{0} | V(t) e^{i\phi S_z} \hat{V}(t) | \mathbf{0} \rangle \right|^2 \\ &= \frac{1}{4} \left(1 + |\Phi(\phi)|^2 + 2\text{Re} \left[e^{-i\phi \frac{N}{2}} \Phi(\phi) \right] \right) \end{aligned} \quad (\text{D.8})$$

The real part of $\Phi(\phi)$ can easily be inferred by combining this quantity with the outcome from Eq. D.2. This approach directly generalizes to the case of global controls by replacing the local rotation with a global one, i.e. $e^{i\epsilon S}$. In either case, an additional many-body unitary (i.e. 2 copies of U and U^\dagger) is required compared to the previous protocols.

We note that, although measuring the return probability is straightforward to analyze, it is highly sensitive to readout errors. In practice, therefore, it is better to measure either the average polarization or polarization distribution of the final state, both of which display qualitatively similar behavior to the return probability. In particular, if the external signal applies a relative phase between the two components of the butterfly state, $|\mathbf{0}\rangle$ and $\hat{V}(t)|\mathbf{0}\rangle$, then the polarization distribution of the final state features two peaks—a fully polarized state and a random state centered about zero polarization—with a relative height that oscillates as function of ϕ . Readout noise broadens the two peaks, but they remain extensively separated.

D.4 Stochastic growth model

In this section, we introduce a stochastic model for operator growth dynamics which allows us to predict the large-scale behavior of our protocol for the two proposed systems of spin defects. The model is inspired by previous work on quantum information scrambling, where it has been argued that growth of operators under *long-range* Hamiltonian dynamics can be qualitatively captured at long timescales by stochastic transitions [52, 269, 270]. For our purposes, we model these transitions using Haar-random gates and determine the probability of each gate based on the strength of the spin interactions.

In more detail, consider a Hamiltonian composed of two-body interactions, $H = \sum_{ij\mu} h_{ij}^\mu$, where h_{ij}^μ indicates a particular two-body operator acting on qubits i and j . Our model consists of mapping the analog evolution $U = e^{-iHt}$ to a circuit composed of D time steps, $\tilde{U} = U_D \cdots U_2 U_1$. In each time step, we apply a set of two-qubit, Haar-random gates, where the probability of a gate occurring between qubits i and j is $P_{ij} = \delta t \sum_\mu |h_{ij}^\mu|^2$. We set

$\delta t \ll 1/J_{\text{typ}}$, where J_{typ} is the typical interaction strength, such that there is a low density of gates per time step.

A key feature of Haar-random gates is that, for measuring certain quantities, the average over Haar-random gates is equivalent to the average over random Clifford gates [187]. The average sensitivity of our protocol (with either global or local control) represents such a quantity; this results from the fact that the sensitivity contains three copies of U and U^\dagger , and Clifford unitaries form a 3-design for qubits [142, 250, 275]. Thus, the average sensitivity of the stochastic model can be computed efficiently using Clifford numerics.

We can apply this model to predict the sensitivity of our protocol for either local or global control. For the local protocol, we compute the sensitivity $\eta_{\phi=0}$ by measuring the average polarization density $P(S_z)$ of $\tilde{U}^\dagger \hat{V} \tilde{U} |\mathbf{0}\rangle$ (see Eq. D.4). This is easily accomplished by evolving \hat{V} in the Heisenberg picture with Clifford gates, and then counting the number of σ_x and σ_y operators within the Pauli string $\hat{V}(t)$.

Computing the sensitivity for the global protocol is somewhat more involved. We begin by expressing the mean outcome as

$$\langle S_x \rangle_\phi = \langle \mathbf{0} | U^\dagger e^{i\epsilon S_x} U e^{i\phi S_z} U^\dagger S_x U e^{-i\phi S_z} U^\dagger e^{-i\epsilon S_x} U | \mathbf{0} \rangle, \quad (\text{D.9})$$

where without loss of generality we have chosen the global operator $S = S_x = \frac{1}{2} \sum_i \sigma_x^i$. To

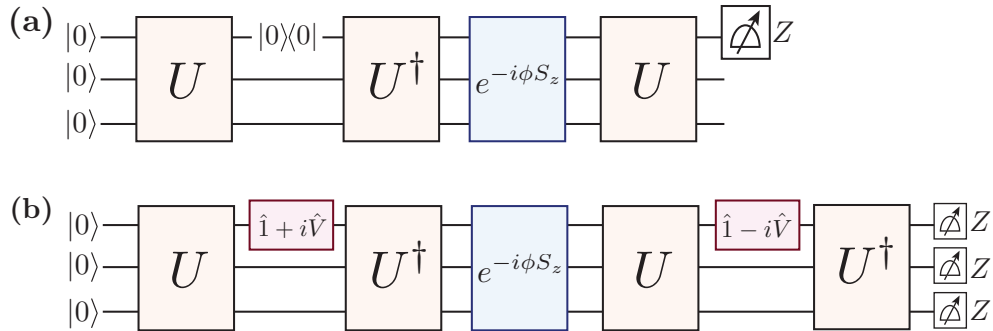


Figure D.3: Two protocols for measuring the real part of $\Phi(\phi)$. (a) The first protocol is identical to the original protocol with local controls [Fig. 1(a) of Chapter 5], except we replace the local rotation $e^{i\frac{\epsilon}{4}\hat{V}} \sim \hat{1} + i\hat{V}$ with a local projection, e.g. $|0\rangle\langle 0| \sim \hat{1} + \hat{Z}$. (b) The second protocol, which we dub a “double echo”, involves applying the butterfly state preparation circuit and its inverse. The final state is measured in the computational basis, and either the return probability to the initial state or the average polarization is computed. This approach may be applied with either local or global controls to prepare the butterfly state.

proceed, we expand the operator S_x in a Pauli basis:

$$= \frac{1}{2} \sum_{a,b \in \{0,1\}^N} \sum_{i=1}^N c_a c_b^* \langle \mathbf{0} | U^\dagger P_a U e^{i\phi S_z} U^\dagger \sigma_x^i U e^{-i\phi S_z} U^\dagger P_b U | \mathbf{0} \rangle, \quad (\text{D.10})$$

where $P_a = \prod_{i \in a} \sigma_x^i$ contains σ_x^i on all sites for which a is non-zero, $c_a = (i \sin(\epsilon/2))^{|a|} (\cos(\epsilon/2))^{N-|a|}$, and $|a| = \sum_i a_i$ is the Hamming weight of a . For a Clifford unitary U , the state $U^\dagger P_b U | \mathbf{0} \rangle$ is an eigenstate of S_z . This allows us to pull the factors of $e^{\pm i\phi S_z}$ outside the expectation value, giving

$$= \frac{1}{2} \sum_{a,b \in \{0,1\}^N} \sum_{i=1}^N c_a c_b^* e^{i\phi_{ab}} \langle \mathbf{0} | U^\dagger P_a \sigma_x^i P_b U | \mathbf{0} \rangle, \quad (\text{D.11})$$

where $\phi_{ab} = \phi(\mathcal{S}_z\{U^\dagger P_a U\} - \mathcal{S}_z\{U^\dagger P_b U\})$ and $\mathcal{S}_z\{P\} = \#$ of σ_x, σ_y in P . With high probability, the matrix element $\langle \mathbf{0} | U^\dagger P_a \sigma_x^i P_b U | \mathbf{0} \rangle$ is non-zero if and only if $P_a \sigma_x^i P_b = \mathbb{1}$. With this simplification, we have

$$\approx \frac{1}{2} \sum_{a \in \{0,1\}^N} \sum_{i=1}^N |c_a|^2 (i \tan(\epsilon/2))^{|b_i| - |a|} e^{i\phi_{ab_i}}, \quad (\text{D.12})$$

where b_i differs from a only on the i^{th} bit. We note that $|c_a|^2$ is the probability of sampling $|a|$ from a binomial process with N draws of probability $\sin^2(\epsilon/2)$, and thus we can approximate the above expression using Monte Carlo sampling. The full procedure for calculating $\langle S_x \rangle_\phi$ is as follows:

1. Sample a from a binomial distribution and i from a uniform distribution. The bitstring b_i is immediately given by flipping a on the i^{th} bit.
2. Compute $\phi_{ab} = \phi(\mathcal{S}_z\{U^\dagger P_a U\} - \mathcal{S}_z\{U^\dagger P_b U\})$ by time-evolving X_a and X_b under a Clifford circuit.
3. Average the quantity $(i \tan \epsilon)^{|b_i| - |a|} e^{i\phi_{ab_i}}$ over many samples.

We estimate the sensitivity via $\eta_{\phi=0}^{-1} \equiv (\partial_\phi \langle S_x \rangle_\phi / \Delta S_{x,\phi})_{\phi=0} \approx \langle S_x \rangle_\phi / \sqrt{N}$, where $\phi \ll 1$, and for circuits with Haar-random gates, on average, $\langle S_x \rangle_{\phi=0}$ and $(\Delta S_x)_{\phi=0} = \sqrt{N}/2$.

To benchmark our model, we calculate the sensitivities for up to $N = 20$ spins for (i) the local protocol based the interactions of the hybrid spin system, and (ii) the global protocol based on the interactions of an ensemble of NV centers (Fig. D.4). We compare these results to the exact dynamics shown in Fig. D.4 and find reasonable qualitative agreement. Moreover, by matching the growth rate at early times, we can estimate the conversion factor between discrete time steps in the model and evolution time for the exact dynamics. Utilizing this conversion factor, we simulate the behavior of much larger spin systems, as shown in the insets of Fig. 3 of Chapter 5. We expect the results of the stochastic model to provide a good qualitative approximation for the exact behavior of the experimental system, in a regime that would be intractable to simulate with the exact dynamics.

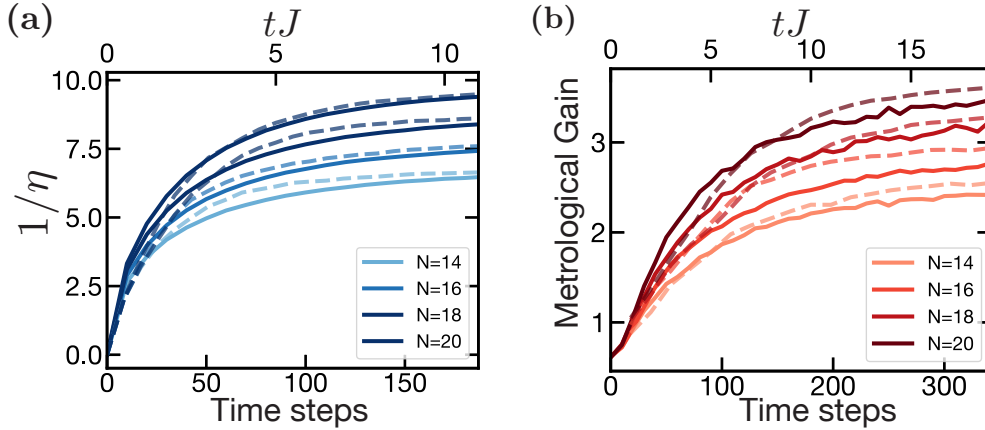


Figure D.4: Comparison between the stochastic model (solid lines) and exact dynamics (dashed) for the two proposed spin models at small sizes. (a) The sensitivity for the local protocol using the hybrid spin system. (b) The metrological gain for the global protocol using an ensemble of NV centers. The stochastic model is plotted with respect to the number of discrete time steps, while the exact dynamics are plotted with respect to continuous time evolution. By comparing the results, we estimate the conversion factor between discrete steps and continuous evolution time. We average the stochastic model over $\sim 10^4$ realizations (i.e. different Clifford circuits) and the exact dynamics over ~ 10 positional configurations.

D.5 Experimental proposals

In this section, we present additional details on the two experimental platforms highlighted in Chapter 5, along with four additional platforms that are amenable to implementing our protocol. A brief overview of these systems and our proposed implementations is provided in Table D.1.

Before discussing the systems individually, we note that a few features are in common in all of the proposals. First, we choose the initial state of the protocol to be quantized along the X direction. This is motivated by the fact that all of the systems (except the trapped ion quantum computer) feature native interactions that conserve total polarization in the Z basis. Specifically, we either consider a fully polarized state, or we average over random initial states in the X basis. The latter approach allows us to circumvent low-energy effects associated with a polarized state; this is most relevant for the two systems with entirely ferromagnetic interactions, i.e. the dipolar Rydberg atoms and the superconducting qubits. Moreover, in all cases, we select a “butterfly” operator that lies the transverse plane (i.e. $\hat{V} = \sigma_x$ or $S = S_x$). This generally leads to faster scrambling compared to an operator that overlaps with the conserved quantity S_z [130].

Dipolar Rydberg atoms

One particularly suitable platform for realizing our protocol—with either local or global controls—is a quantum simulator based on a 1D or 2D array of atoms trapped in optical tweezers [39, 49]. For each atom, an effective spin-1/2 degree of freedom is encoded in a pair of Rydberg states, which is governed by a long-range XY interaction:

$$H = -J \sum_{i < j} \frac{a^3}{r_{ij}^3} (\sigma_x^i \sigma_x^j + \sigma_y^i \sigma_y^j) \quad (\text{D.13})$$

where $J \approx \text{MHZ}$ is the dipolar interaction strength, $a \sim 10 \mu\text{m}$ is the lattice spacing, and r_{ij} is the distance between atoms. Crucially, the sign of J is controlled by the specific Rydberg state encoding; for example, $J > 0$ for the encoding $|0\rangle = |60S_{1/2}, m = 1/2\rangle$ and $|1\rangle = |60P_{3/2}, m = -1/2\rangle$. Switching between the two encodings (via a microwave pulse) allows one to realize time-reversed dynamics. Furthermore, one can implement global rotations via microwave pulses and single-site rotations by applying a focused laser beams, which generates a local Stark shift. Such control is necessary to prepare a random initial state, as well as to apply the local rotation $e^{i\frac{\pi}{4}\hat{V}}$ (for the local control protocol).

In Fig. 5.4(a), we present simulated results for the protocol with local controls with a 2D array of atoms. The initial state is randomized over product states in the X basis, and the butterfly operator is $\hat{V} = \sigma_x^{N/2}$ (located in the center of the array). At early times, we observe a rapid improvement in sensitivity, which for a large system we would expect to follow a quadratic trend, i.e. $1/\eta \sim t^2$. At later times, the sensitivity abruptly saturates at $\eta \approx 2/N$, consistent with our prediction from Haar-random evolution and indicating that the system has fully scrambled.

In practice, the improvement in sensitivity over time would compete with the suppression due to accumulation of errors (see Section D.6 for details). A leading source of decoherence in the system is the lifetime of the Rydberg state, which is typically $T_1 \sim 100 \mu\text{s}$ [68]. Based on an interaction strength of $J \sim 1 \text{ MHz}$ [49], we estimate this would enable a high-fidelity preparation of a fully scrambled state for $N \sim 25$ in 1D and $N \sim 100$ in 2D, corresponding to a metrological gain of 8 and 14 dB, respectively.

Interestingly, a recent work proposed also proposed the use of 2D Rydberg arrays for generating spin squeezed states [33]. This approach enables an enhanced sensitivity $N^{-7/10}$ after an evolution time $t \sim N^{2/5}$. With the same 2D array of atoms, we observe that our protocol could obtain a comparable sensitivity at a time $t \sim N^{1/5}$, i.e. representing a quadratic speedup. Moreover, the scaling difference between the two protocols is dependent on the dimensionality. Whereas the scaling in our protocol improves for higher dimensions, spin-squeezing occurs with the same functional form for all dimensions [33]. For example, in 1D, the sensitivity for the two protocols would exhibit the same scaling in time, and, in 3D, our protocol would feature a cubic speedup. This highlights the fact that scrambling occurs at a near-maximal rate under many-body dynamics.

Experimental platform	Form of interaction	Local / global	Initial state	Mechanism for time-reversal
Dipolar Rydberg atoms	Dipolar XY	Either	Random	Rydberg-state encoding
Hybrid spin system	Dipolar Ising + XXZ	Local	Polarized	Hamiltonian engineering
Ensemble of NV centers	Dipolar XXZ	Global	Polarized	Hamiltonian engineering
Atoms in optical cavity	Long-range XY	Global	Polarized	Sign of laser detuning
Superconducting qubits	Local XY	Either	Random	Conjugation by pi-pulses
Trapped ions	Digital gates	Either	Either	Phase of laser excitation

Table D.1: Summary of proposed experimental platforms.

Hybrid spin system in diamond

As discussed in Chapter 5, our protocol with local controls can naturally be realized in a bulk diamond sample containing two species of electronic spin defects: a relatively high concentration of spin-1/2 nitrogen substitutional defects (P1 centers), and a low density of spin-1 nitrogen-vacancy (NV) centers [278].

When the two species are off-resonant, the intrinsic magnetic dipole interaction between a single NV center and the surrounding P1 centers gives rise to an effective Hamiltonian [278]

$$H = H_{NV-P1} + H_{P1-P1} \quad (\text{D.14})$$

$$H_{NV-P1} = J_0 \sum_i \frac{1}{r_{ij}} (1 - 3n_{ij}^z) S_z P_z^i \quad (\text{D.15})$$

$$H_{P1-P1} = -\frac{J_0}{2} \sum_{i<j} \frac{1}{r_{ij}} (1 - 3n_{ij}^z) (P_x^i P_x^j + P_y^i P_y^j - 2P_z^i P_z^j). \quad (\text{D.16})$$

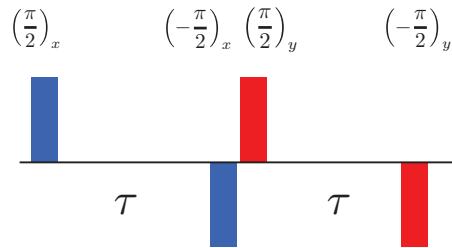


Figure D.5: A pulse sequence for engineering the hybrid spin Hamiltonian H (Eq. D.14) into \tilde{H}^+ (Eq. D.18). The sequence consists of two frame rotations with equal duration, τ . In the first, a $\pi/2$ pulse applied along the X direction brings P_z into P_y and P_y into $-P_z$. In the second, a $\pi/2$ pulse applied along the Y direction brings P_z into P_x and P_x into $-P_z$. By rotating in the opposite direction (i.e. switching $\pi/2$ into $-\pi/2$ and vice versa), the pulse sequence instead generates \tilde{H}^- .

Here, $J_0 \approx 52 \text{ MHz-nm}^3$ is the magnetic dipole interaction; \vec{S} , \vec{P}^i are spin-1/2 operators acting on the NV center (within the $|m=0\rangle$ and $|m=-1\rangle$ subspace) and individual P1 centers, respectively; r_{ij} is the distance between two defects; and $n_{ij}^z = \hat{z} \cdot \hat{r}_{ij}$.

The sign of H_{NV-P1} can easily be reversed by conjugating the evolution via a π -pulse on the NV center, leading to the effective Hamiltonian

$$H^- = -H_{NV-P1} + H_{P1-P1}. \quad (\text{D.17})$$

To reverse the sign of H_{P1-P1} , we can apply global pulses to the P1 centers following the pulse sequence shown in Fig. D.5. From average Hamiltonian theory, the engineered Hamiltonian in the toggling frame is

$$\tilde{H}^\pm = \pm \tilde{H}_{NV-P1} - \frac{1}{2} H_{P1-P1} \quad (\text{D.18})$$

$$\tilde{H}_{NV-P1} = \frac{J_0}{2} \sum_i \frac{1}{r_{ij}} (1 - 3n_{ij}^z) S_z (P_x^i + P_y^i), \quad (\text{D.19})$$

where the sign of \tilde{H}_{NV-P1} is determined by direction of the pulses (Fig. D.5). Combining these ingredients, we can realize the following forward and reverse evolution:

$$U = e^{-it\tilde{H}^+} \quad (\text{D.20})$$

$$U^\dagger = e^{-i2t[\frac{1}{2}\tilde{H}^- + \frac{1}{4}(H+H^-)]} = e^{itH^+}. \quad (\text{D.21})$$

Implementing the full protocol would require the following steps:

1. Initialize in a fully polarized state in the Z direction. For the NV centers, this is accomplished via optical polarization, and for the P1 centers, it requires operating under cryogenic conditions.
2. Rotate the state to the X direction by applying a microwave pulse resonant with (a) the two levels of the P1 center, and (b) the $|m_s=0\rangle \leftrightarrow |m_s=-1\rangle$ transition of the NV center.
3. Evolve under the engineered Hamiltonian \tilde{H}_+ by applying the appropriate pulse sequence.
4. Apply a local rotation to the NV and evolve backwards under $-\tilde{H}_+$. Then apply the global sensing signal $e^{-i\phi S_z}$, and evolve forward again under \tilde{H}_+ .
5. Measure the polarization of the NV center using optical excitation.

We emphasize that the protocol would despite the presence of strong positional disorder in the spin system. Indeed, any position configurations would lead to many-body interactions

which produce scrambling behavior and thus an enhancement in sensitivity³. Moreover, as discussed in Chapter 5, the scrambling occurs very fast—i.e. at super-polynomial rate—due to the long-range interactions in three dimensions. For comparison, a previous scheme has been proposed for entanglement-enhanced sensing with the NV-P1 hybrid system, in which the sensitivity improves linearly in time, i.e. $1/\eta \sim t$ [100].

A particularly attractive feature of electronic spins in diamond is their extremely long intrinsic lifetimes, i.e. $T_1 \sim$ seconds at low temperatures. In most samples, the coherence times are instead determined by interactions with other spin defects (both electronic or nuclear spins). Fortunately, these interactions can be echoed out through the same pulse engineering sequences described above. We therefore expect that the limiting factor for implementing our protocol will be the ability to implement the pulse sequence with high fidelity and at a pulse rate that is faster than the interaction strength. Recent work has led to significant improvements in the robustness of such pulse sequences [54]. We anticipate that our protocol will be a useful setting to test and refine these techniques.

Ensemble of NV centers in diamond

A second system of spin defects which can realize our protocol with global control is an ensemble of strongly interacting NV centers [141]. Compared with a hybrid NV-P1 system, the main benefit of this implementation is that the NV centers can be optically polarized at room temperature, thereby circumventing the need for cryogenic temperatures.

To reverse the Hamiltonian, we will again utilize pulse engineering techniques. We first consider effective interaction between NV centers within the $m_s = 0, -1$ subspace [141]:

$$H_0 = J_0 \sum_{i < j} \frac{1}{r_{ij}} (1 - 3n_{ij}^z) (S_x^i S_x^j + S_y^i S_y^j - S_z^i S_z^j), \quad (\text{D.22})$$

where \vec{S} are spin-1/2 operators with respect to the two-level system. Notably, this Hamiltonian *cannot* be reversed using a sequence of frame rotations. This results from the fact the matrix representation of the individual Hamiltonian terms—i.e. $h_{\mu\nu}$ where $H_{ij} = \sum_{\mu\nu} h_{\mu\nu} S_\mu^i S_\nu^j$ and $\mu, \nu \in \{X, Y, Z\}$ —has non-zero trace $\sum_\mu h_{\mu\mu}$ [54]. Nevertheless, we can exploit the fact that the NV center contains another potential two-level subspace composed of the $m_s = +1, -1$ sublevels. In this subspace, the effective interaction becomes

$$H_{\pm 1} = -4J_0 \sum_{i < j} \frac{1}{r_{ij}} (1 - 3n_{ij}^z) S_z^i S_z^j. \quad (\text{D.23})$$

Because the trace of $H_{\pm 1}$ has the opposite sign of H_0 , one can engineer a pulse sequence that utilizes H_{\pm} to generate an effective interaction proportional to $-H_0$. In particular, through

³We note that, for an ensemble of NV centers, the total sensitivity $\eta_{\phi=0}$ is given by the average sensitivity over the position configurations contained in the ensemble. The positional disorder does, however, affect the sensitivity for finite ϕ . This is because it contributes additional dephasing to $\langle \hat{V} \rangle$ with respect to ϕ .

the pulse sequence shown in Fig. D.5, one can generate

$$\tilde{H}_{\pm 1} = -2J_0 \sum_{i < j} \frac{1}{r_{ij}} (1 - 3n_{ij}^z) (S_x^i S_x^j + S_y^i S_y^j). \quad (\text{D.24})$$

This allows us to define the following forward and backward evolution:

$$U = e^{-itH_0} \quad (\text{D.25})$$

$$U^\dagger = e^{-i2t(\frac{1}{2}H_0 + \frac{1}{2}H_{\pm 1})} = e^{itH_0}. \quad (\text{D.26})$$

The rest of the protocol follows directly from the steps outlined in the previous section. Since we are working with the global protocol, the angle of the global rotation that generates the butterfly state $e^{i\epsilon S}$ should be optimized as function of time.

To our knowledge, the above technique for implementing backward time evolution, which we refer to as “subspace engineering”, has not been proposed before. Successfully demonstrating this technique, and comparing it to more standard pulse sequences involving a single subspace, represents an exciting experimental prospect.

Atoms in an optical cavity

One of the most successful platforms for demonstrating entanglement-enhanced sensing consists of atoms coupled in an optical cavity [58, 160, 192]. Conventionally, this enhancement is achieved by evolving under collective large-spin interactions (e.g. the one-axis twisting Hamiltonian) to generate a squeezed state. However, this approach does not succeed for more general types of dynamics, arising in e.g. a multi-mode cavity [247] or via programmable interactions [195].

We consider the latter setting with a system of spin-1/2 atoms. The programmable spin-exchange interactions are described by an effective Hamiltonian [195]:

$$H = \sum_{i,j} J(r_{ij}) (\sigma_x^i \sigma_x^j + \sigma_y^i \sigma_y^j), \quad (\text{D.27})$$

where the sign and magnitude $J(r_{ij})$ are controllable by laser drives. Motivated by Ref. [26], we select the interaction strength to be of the form

$$J(r_{ij}) = \begin{cases} (-1)^n |i - j|^s & \text{if } |i - j| = 2^n, n \in \mathbb{Z} \\ 0 & \text{otherwise} \end{cases} \quad (\text{D.28})$$

where the parameter s interpolates between a quasi-one-dimensional geometry ($s < 0$) and a tree-like geometry ($s > 0$). Note that we include a mix of ferromagnetic and anti-ferromagnetic couplings. This is anticipation of initializing to protocol with a fully polarized initial state, $|\mathbf{0}\rangle = |+\rangle^{\otimes N}$; the anti-ferromagnetic interactions serve to raise the temperature this state.

Although local control is theoretically possible in this setup [243], it is most natural to realize our protocol with global controls. Numerical simulations for the sensitivity as a function of evolution time are depicted in Fig. D.6. For $s < 0$, we observe that the sensitivity quickly reaches a saturation value that improves with system size $\sim N$, indicating a Heisenberg-like enhancement. Intriguingly, in the case of $s > 0$, we find a qualitatively different behavior: the sensitivity exhibits large fluctuations and does not improve systematically with system size. This suggests that the tree-like geometry does not lead to fully scrambling behavior. Understanding the subtle interplay between many-body dynamics and improved sensitivity for such non-trivial geometries would be an interesting future direction.

Superconducting qubits with analog interactions

Tremendous progress has been made in developing quantum processors based on 2D arrays of superconducting transmon qubits [11, 41, 131]. While such processors are often controlled with digital gates, we consider an implementation of our protocol which utilizes the intrinsic (analog) interactions between tunable-frequency qubits. In particular, when the qubits are brought on resonance, their interaction is described by a local XY model [41],

$$H = J \sum_{\langle i,j \rangle} (\sigma_x^i \sigma_x^j + \sigma_y^i \sigma_y^j), \quad (\text{D.29})$$

where the coupling strength J is typically 10 – 100 MHz [82]. As demonstrated in Ref. [41], when the lattice of qubits is bipartite, the sign of interaction can be quite easily reversed by conjugating the evolution with π -pulses, i.e. $-H = (\prod_{i \in \mathcal{S}} \sigma_x^i) H (\prod_{i \in \mathcal{S}} \sigma_x^i)$, where \mathcal{S} is one part of the bipartite lattice. This reversibility, in addition to local rotations generated by microwave pulses, enables the realization of our protocol with local control.

In Fig. D.6, we show numerical results for our protocol in a 2D array of up to 20 qubits. While the functional form of the early-time growth cannot be discerned, at larger sizes one expects the nearest-neighbor interactions to lead to ballistic growth of the form $\sim (Jt)^2$. Based on an estimate of this growth rate, a qubit lifetime of $T_1 \sim 20\mu\text{s}$ [213], and a coupling strength $J \sim 50$ MHz [82], we predict that a fully scrambled state can be prepared with ~ 400 qubits, leading to a metrological gain of 20 dB. This would significantly surpass the current record for metrological gain of 11.8 dB, recently demonstrated via atoms in an optical cavity [58].

For comparison, a more conventional approach for obtaining a metrological gain in a digital quantum processor would be to prepare a GHZ state (the current record is a GHZ state with 27 qubits and a fidelity of 0.5) [185]. It is natural to consider which of these strategies would lead to a larger metrological gain on realistic devices. On the one hand, the theoretical sensitivity for a GHZ state at equivalent sizes is a factor of two better than our protocol. Additionally, sensing based on a GHZ state requires two layers of entangling gates (i.e. the state preparation circuit and its inverse, assuming that robustness to noise is desired), whereas our protocol requires three steps of many-body evolution. On the other

hand, our protocol is much more robust against control errors, since it does not require precisely calibrated two-qubit gates; indeed, such errors often represent a significant fraction of the total error [181]. Moreover, the total evolution time for implementing our protocol may be shorter, since the analog interactions are “always on”, thereby reducing the effect of decoherence. Testing these advantages in practice would be of tremendous interest and may provide a useful benchmarking tool for large-scale quantum processors.

Trapped-ion quantum computer

Lastly, we consider an implementation of protocol on a trapped-ion quantum computer [76, 197]. Unlike the previous proposals which rely on analog evolution, we utilize discrete quantum gates to generate the many-body unitary U . Specifically, we construct circuits with interspersed layers of two-qubit and single-qubit gates. For the two-qubit gates, we choose $N/2$ pairs of qubits at random and apply the native Molmer-Sorensen interaction, $e^{i\frac{\pi}{4}\sigma_i^x\sigma_j^x}$, to each pair. This arrangement takes advantage of the all-to-all connectivity of trapped ions. For the single-qubit gates, we apply $e^{i\alpha_i\sigma_z^i}e^{i\frac{\pi}{4}\sigma_y^i}e^{i\beta_i\sigma_z^i}$, where $\alpha_i, \beta_i \in [0, 2\pi]$ are chosen from a uniform distribution. In Fig. D.6(d), we plot numerical results for the sensitivity as function of circuit depth using the sensing protocol with local controls. Much like our previous results with analog evolution, we observe an initial rise in sensitivity, followed by saturation at $\eta \approx 2/N$. Owing to the all-to-all connectivity, the circuit depth to reach saturation scales favorably with system size; indeed, one expects it to occur in $\sim \log N$ layers at large system sizes.

As discussed in Chapter 5, an important feature of our protocol is its robustness against coherent errors, which are considered to be a dominant error source in trapped-ion systems. Physically, such errors arise from low-frequency fluctuations in the laser drive amplitudes, causing imperfections in the rotation angles, i.e. $\theta_{ij} \rightarrow \theta'_{ij}$. These errors will limit the ability to prepare finely-tuned metrological states, including a GHZ state. However, in our protocol, if these errors can be time-reversed they have essentially no impact on the achievable sensitivity—they would simply adjust the many-body unitary, $U \rightarrow U'$, and, at late times, this would still result in a fully scrambled state. Thus, at large system sizes and / or high coherent error rates, we expect our protocol to provide a larger metrological gain compared to sensing based on a GHZ state.

D.6 Error analysis

We now provide a detailed accounting of the effect of experimental errors on our sensing protocols. We begin with a brief discussion of readout and initialization errors, which as mentioned in Chapter 5, decrease the sensitivity by only a constant factor. We then turn to incoherent errors during time-evolution, and, borrowing from the results of Ref. [223], derive the suppression factor indicated in Chapter 5.

Readout errors have a particularly small effect on our protocol. For the local control protocol, a local readout error rate γ_r suppresses the expectation value of \hat{V} by a constant factor, $\langle \hat{V} \rangle_\phi \rightarrow (1 - \gamma_r) \langle \hat{V} \rangle_\phi$. A similar suppression occurs for the global protocol, $\langle \hat{S} \rangle_\phi \rightarrow (1 - \gamma_r) \langle \hat{S} \rangle_\phi$, since \hat{S} is a sum of single-body operators. In both cases, the sensitivity is suppressed by the same factor, $\eta_\phi^{-1} \rightarrow (1 - \gamma_r) \eta_\phi^{-1}$.

To address initialization errors, consider performing the protocol with an initial density matrix ρ instead of $|\mathbf{0}\rangle\langle\mathbf{0}|$. We denote the mean polarization of ρ as $\text{tr}(\rho S_z) = (1 - \gamma_i)N/2$, where γ_i quantifies the local initialization error rate. We also suppose that the polarization distribution of ρ has width $\lesssim \sqrt{N}$, which is appropriate for local initialization errors. After butterfly state preparation, the density matrix becomes

$$\left(\frac{1 + i\hat{V}(t)}{\sqrt{2}} \right) \rho \left(\frac{1 - i\hat{V}(t)}{\sqrt{2}} \right) = \frac{1}{2} \left(\rho + \hat{V}(t)\rho\hat{V}(t) + i \left[\hat{V}(t)\rho - \rho\hat{V}(t) \right] \right), \quad (\text{D.30})$$

where $\hat{V}(t) = U^\dagger \hat{V} U$. The first and second terms correspond to the two trajectories of the butterfly state, and the third term to the coherence between them. As in the error-free case, for small angles $\phi \lesssim 1/\sqrt{N}$ the rotation $e^{-\phi S_z}$ simply applies an overall phase to each trajectory of the butterfly state. Working in the late time regime where $e^{i\phi S_z} \hat{V}(t)\rho \approx \hat{V}(t)\rho$, this leads to the density matrix

$$\begin{aligned} e^{i\phi S_z} \left(\frac{1 + i\hat{V}(t)}{\sqrt{2}} \right) \rho \left(\frac{1 - i\hat{V}(t)}{\sqrt{2}} \right) e^{-i\phi S_z} \\ \approx \frac{1}{2} \left(\rho + \hat{V}(t)\rho\hat{V}(t) + i \left[e^{-i\phi(1-\gamma_i)N/2} \hat{V}(t)\rho - e^{i\phi(1-\gamma_i)N/2} \rho\hat{V}(t) \right] \right). \end{aligned} \quad (\text{D.31})$$

As in the error-free case, only the third term (in square brackets) will contribute to the final expectation value of \hat{V} . Applying the final unitary and taking the expectation value gives

$$\langle \hat{V} \rangle_\phi \approx \sin \left(\phi \frac{(1 - \gamma_i)N}{2} \right). \quad (\text{D.32})$$

Taking the derivative with respect to ϕ , we see that the sensitivity is decreased by only a constant factor relative to the error-free case, $\eta_\phi^{-1} \rightarrow (1 - \gamma_i) \eta_\phi^{-1}$.

We now turn to incoherent errors during time-evolution. As mentioned in Chapter 5, incoherent errors have two effects on the protocol: they suppress the mean polarization in the first trajectory of the butterfly state, and they suppress the coherence between the two butterfly trajectories. Both effects suppress the sensitivity, the first by suppressing the first derivative of $\langle \hat{V} \rangle_\phi$ with respect to ϕ (similar to initialization errors), and the second by suppressing the overall magnitude of $\langle \hat{V} \rangle_\phi$ (similar to readout errors). However, unlike initialization and readout errors, errors during time-evolution occur when the state is highly-entangled and thus have a stronger effect (Fig. D.7).

To explore this in more detail, let us replace the unitary evolution $\rho \rightarrow U\rho U^\dagger$ by evolution under a noisy quantum channel, $\rho \rightarrow \mathcal{E}_\gamma\{\rho\}$. For analog evolution, the quantum channel might be generated by a Lindbladian, $\mathcal{E}_\gamma = e^{\mathcal{L}_\gamma t}$, where \mathcal{L}_γ includes both Hamiltonian evolution and local noise operators with strength γ . For digital evolution, the quantum channel might correspond to a sequence of unitary gates interspersed with local noise channels of strength γ . In any case, we will assume that the quantum channel corresponding to U^\dagger is the *conjugate* of the channel corresponding to U , defined via $\text{tr}(\hat{M} \cdot \mathcal{E}_\gamma\{\rho\}) = \text{tr}(\mathcal{E}_\gamma^\dagger\{\hat{M}\} \cdot \rho)$ ⁴. This reduces to standard time-reversal when the evolution is unitary.

Let us now analyze the sensitivity of the protocol at $\phi = 0$. We have

$$\partial_\phi \langle V \rangle_\phi = \text{Im} \left[\text{tr} \left(S_z \cdot \mathcal{E}_\gamma^\dagger\{\hat{V}\} \cdot \mathcal{E}_\gamma^\dagger \left\{ \frac{1+i\hat{V}}{\sqrt{2}} \mathcal{E}_\gamma\{|\mathbf{0}\rangle\langle\mathbf{0}|\} \frac{1-i\hat{V}}{\sqrt{2}} \right\} \right) \right], \quad (\text{D.33})$$

where we apply (the conjugate of) the final time-evolution to the measurement operator \hat{V} instead of the quantum state. As in the error-free case, we can drop terms that contain an odd number of \hat{V} . Moreover, terms where a single \hat{V} operator appears in between S_z and the initial state $|\mathbf{0}\rangle\langle\mathbf{0}|$ can also be dropped if the system is fully scrambled after application of \mathcal{E}_γ . These correspond to the polarization of the second trajectory of the butterfly state or, in other language, to OTOCs that have decayed to zero. Dropping these terms gives

$$\partial_\phi \langle V \rangle_\phi \approx \text{tr} \left(S_z \cdot \mathcal{E}_\gamma^\dagger\{\hat{V}\} \cdot \mathcal{E}_\gamma^\dagger \left\{ \hat{V} \cdot \mathcal{E}_\gamma\{|\mathbf{0}\rangle\langle\mathbf{0}|\} \right\} \right). \quad (\text{D.34})$$

Now, note that the initial state $|\mathbf{0}\rangle\langle\mathbf{0}|$ can be decomposed as a sum of stabilizers as

$$|\mathbf{0}\rangle\langle\mathbf{0}| = \frac{1}{2^N} \sum_{s \in \{0,1\}^N} \bigotimes_{i=1}^N (\sigma_i^z)^{s_i}. \quad (\text{D.35})$$

To good approximation, only the single-body stabilizers σ_i^z contribute to the expectation value, since they can “contract” with the same stabilizer in S_z . Keeping only these stabilizers, we have

$$\partial_\phi \langle V \rangle_\phi \approx \frac{1}{2} \sum_{i=1}^N \frac{1}{2^N} \text{tr} \left(\sigma_i^z \cdot \mathcal{E}_\gamma^\dagger\{\hat{V}\} \cdot \mathcal{E}_\gamma^\dagger \left\{ \hat{V} \cdot \mathcal{E}_\gamma\{\sigma_i^z\} \right\} \right), \quad (\text{D.36})$$

which is our final approximation. The approximation resembles a “doubled” version of the Loschmidt echo, which depends on both the fidelities of a local operator σ_i^z at time zero and a local operator \hat{V} at time t .

To understand how this approximation depends on the local noise rate γ , we invoke the results of Ref. [223]. There, it was argued that for ergodic many-body quantum dynamics, the decay of the Loschmidt echo,

$$\mathcal{N}_\gamma(\hat{M}) = \frac{1}{2^N} \text{tr} \left(\hat{M} \cdot \mathcal{E}_\gamma^\dagger \left\{ \mathcal{E}_\gamma\{\hat{M}\} \right\} \right), \quad (\text{D.37})$$

⁴On a technical level, this requires assuming that the noise is unital. We expect non-unitality of the noise channel to contribute at sub-leading order in γ ; see the supplemental material of Ref. [223] for a full discussion.

is controlled by the effective space-time volume of the time-evolved operator \hat{M} ,

$$\mathcal{N}_\gamma(\hat{M}) \approx \exp\left(-2\gamma \text{Vol}\left[\hat{M}(0 \rightarrow t)\right]\right). \quad (\text{D.38})$$

Here, the space-time volume is defined as the integral over time of the *size* of the operator \hat{M} ,

$$\text{Vol}\left[\hat{M}(0 \rightarrow t)\right] = \int_0^t dt' \mathcal{S}(t'), \quad (\text{D.39})$$

where the size is given by the (average) number of qubits that \hat{M} acts upon,

$$\mathcal{S}(t') = \sum_P |c_P(t')|^2 \mathcal{S}_P, \quad (\text{D.40})$$

where $\hat{M}(t') = \sum_P c_P(t')$ is the Pauli decomposition of \hat{M} at time t' and $\mathcal{S}_P = (\# \text{ of } \sigma_x, \sigma_y, \sigma_z \text{ in } P)$ is the weight of the Pauli operator P . In principle, one should compute this volume for time-evolution under the noisy quantum channel [223]. However, to estimate the leading order dependence in γ we can substitute the volume under unitary evolution. In short-range interacting systems, the space-time volume is proportional to the volume of the operators' light-cone, and Eq. (D.38) simply states that only errors within the light-cone contribute to the decay of the Loschmidt echo.

We can straightforwardly apply this approximation to the sensitivity in Eq. (D.41). The first quantum channel (applied to σ_i^z) contributes a factor $\gamma \text{Vol}[\sigma_i^z(0 \rightarrow t)]$ to the exponent. The final quantum channel (applied to \hat{V}) contributes a factor $\gamma \text{Vol}[\hat{V}(0 \rightarrow t)]$. The only subtlety is the middle quantum channel (applied to $\hat{V} \cdot \mathcal{E}_\gamma\{\sigma_i^z\}$). This contributes a factor proportional to the space-time volume of the *product* of σ_i^z and \hat{V} , where the former is local at the end of the evolution and the latter at the beginning. In a slight abuse of notation, we denote this quantity as $\text{Vol}[\sigma_i^z(t \rightarrow 0) \cup \hat{V}(0 \rightarrow t)]$. Putting it all together, we estimate

$$\partial_\phi \langle V \rangle_\phi \approx \frac{1}{2} \sum_{i=1}^N \exp\left(-\gamma \left(\text{Vol}[\sigma_i^z(0 \rightarrow t)] + \text{Vol}[\hat{V}(0 \rightarrow t)] + \text{Vol}[\sigma_i^z(t \rightarrow 0) \cup \hat{V}(0 \rightarrow t)] \right)\right). \quad (\text{D.41})$$

The relevant light-cones are depicted visually in Fig. D.7. Note that the volume of the product will (typically) be upper bounded by the sum of the individual volumes. This gives a lower bound on the sensitivity,

$$\begin{aligned} \partial_\phi \langle V \rangle_\phi &\gtrsim \left(\frac{1}{2} \sum_{i=1}^N \exp\left(-2\gamma \text{Vol}[\sigma_i^z(0 \rightarrow t)]\right) \right) \cdot \exp\left(-2\gamma \text{Vol}[\hat{V}(0 \rightarrow t)]\right) \\ &= \frac{N}{2} \cdot \overline{\mathcal{N}_\gamma(\sigma_i^z)} \cdot \mathcal{N}_\gamma(\hat{V}) \end{aligned} \quad (\text{D.42})$$

The first term is given by $N/2$ multiplied by the average Loschmidt echo of σ_i^z . This corresponds to the loss in polarization of the first butterfly trajectory. The second term is given

by the Loschmidt echo of \hat{V} , and corresponds to the loss of coherence between the first and second trajectories of the butterfly state.

Let us consider this final expression for a system with local interactions in d dimensions. We assume local operators spread ballistically with a butterfly velocity v_B , resulting in an operator size $S(t) \approx (v_B t)^d$ and a volume $\text{Vol}[\hat{V}(0 \rightarrow t)] \approx \text{Vol}[\sigma_i^z(0 \rightarrow t)] \approx \frac{1}{(d+1)v_B} (v_B t)^{d+1}$. To reach a fully scrambled state, we take $t \approx N^{1/d}/v_B$, which leads to a sensitivity

$$\partial_\phi \langle V \rangle_\phi \gtrsim \frac{N}{2} \exp\left(-\frac{4}{d+1} \frac{\gamma}{v_B} N^{\frac{d+1}{d}}\right). \quad (\text{D.43})$$

We utilize this expression to estimate the sensitivity under decoherence for the dipolar Rydberg atoms and superconducting qubits.

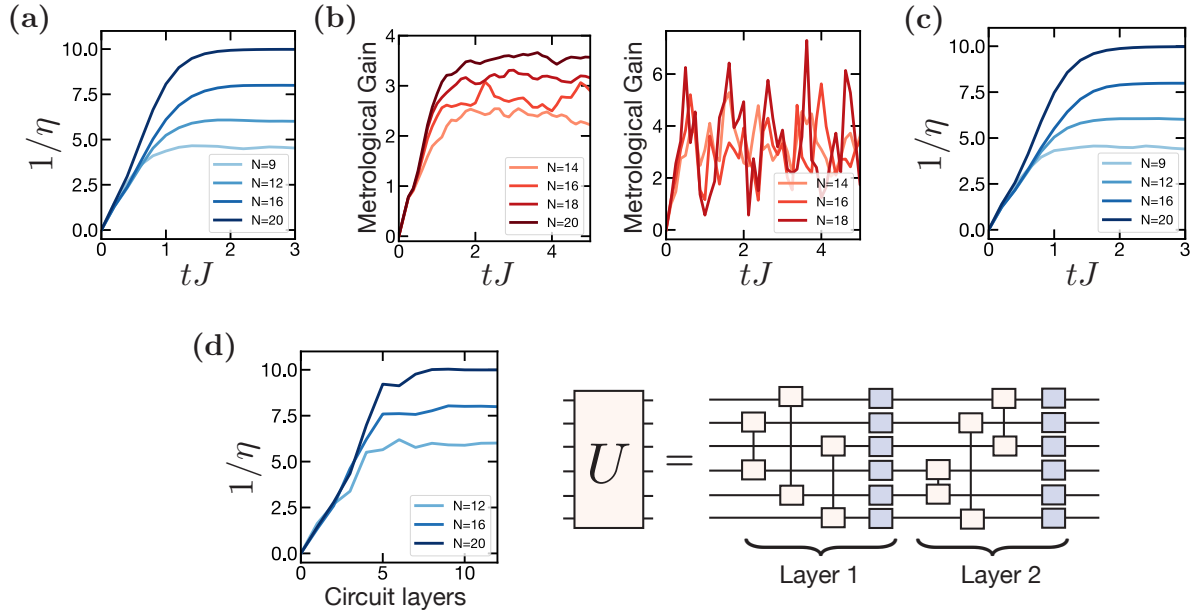


Figure D.6: Numerical simulations of our protocol with four proposed experimental platforms: (a) Rydberg dipolar atoms in two-dimensions, i.e. Eq. D.13 with $a/r_{ij} = 1$ for nearest neighbors; (b) atoms in an optical cavity, i.e. Eq. (D.27-D.28), with (left) $s = -\frac{1}{2}$ and (right) $s = \frac{1}{2}$; (c) superconducting qubits with analog interactions, Eq. D.29; (d) trapped ions under a non-local, random unitary circuit. In (a),(c), and (d), the protocol with local controls is performed and the initial state is a random product state in the X basis (averaged over ~ 10 realizations). In (b), we implement the protocol with global controls and a fully polarized state initial state, $|\mathbf{0}\rangle = |+\rangle^{\otimes N}$. The circuit geometry for the trapped ion simulations is shown in (d). Each layer consists of $N/2$ two-qubit gates (yellow), acting on random pairs of qubits, and a random-qubit rotation on each of the qubits (blue).

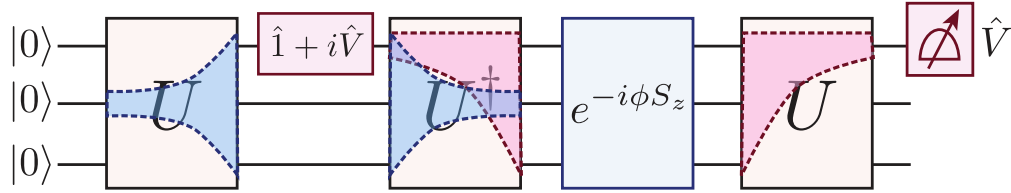


Figure D.7: Illustration of the effect of errors on our sensing protocol. Errors within the light-cone of \hat{V} (red dashed areas) suppress the coherence between the two trajectories of the butterfly state. Errors within the light-cone of a local polarization operator σ_i^z (blue dashed areas, shown for a representative polarization operator) suppress the polarization of the first trajectory of the butterfly state. The sensitivity of the protocol is affected by both types of errors, and is thus suppressed proportional to the local error rate γ multiplied by the space-time volume of the four light-cones. Note that initialization and readout errors can be included in this diagram as well; since they only act at times when the light-cones have size one, they have only an $\mathcal{O}(1)$ effect on the sensitivity.

Appendix E

Details on adiabatic preparation of thermofield double states

E.1 Thermofield double dynamics from the eigenstate thermalization hypothesis

In the beginning of this section, we provide a condensed derivation of the results from Ref. [61], which computes the matrix elements of the coupled Hamiltonian using the eigenstate thermalization hypothesis (ETH). We begin with a short summary of the ETH, and then turn to the coupled Hamiltonian. In the latter half of this section, we build upon this framework to analyze the low-energy dynamics of the Maldacena-Qi Hamiltonian. We show that the low-energy Hamiltonian derived from ETH agrees exactly with the dynamics of the “graviton” mode in Ref. [170]. In the final subsection, we discuss and quantify corrections to the ETH framework.

Review of the eigenstate thermalization hypothesis

Consider a many-body Hamiltonian H with eigenstates $|i\rangle$ and energies E_i . The ETH posits that the matrix elements of few-body operators in the energy eigenbasis, are described as follows. First, the diagonal matrix elements are given by the expectation value of the operator in the corresponding thermal state,

$$A_{ii} \equiv \langle i| A |i\rangle \approx \text{tr}(\rho_{\beta_i} A). \quad (\text{E.1})$$

Here, $\rho_{\beta} = e^{-\beta H} / \text{tr}(e^{-\beta H})$ is the thermal density matrix, and β_i is the inverse temperature such that $\text{tr}(\rho_{\beta_i} H) = E_i$. Second, the off-diagonal matrix elements are given by

$$A_{ij} \equiv \langle i| A |j\rangle = e^{-S_{ij}/2} f_{ij} r_{ij}^A. \quad (\text{E.2})$$

Here, $S_{ij} = S(E_{ij})$ is the entropy of a thermal state, at temperature β_{ij} corresponding to the average energy $E_{ij} = (E_i + E_j)/2$. The function $f_{ij} = f(E_{ij}, \omega_{ij})$ is a smooth function of the

average energy E_{ij} and the energy difference $\omega_{ij} = E_i - E_j$. Finally, the r_{ij}^A are independent Gaussian random variables with zero mean and unit variance.

One can better understand the second formula by examining the auto-correlation function of the operator A . Decomposing A in the energy eigenbasis, we have

$$G_\beta(t) = \text{tr}(A(t)\rho^{1/2}A(0)\rho^{1/2}) = \frac{1}{\mathcal{Z}} \sum_{ij} e^{-\beta E_{ij}} e^{i\omega_{ij}t} |A_{ij}|^2 \approx \frac{1}{\mathcal{Z}} \sum_{ij} e^{-\beta E_{ij}} e^{i\omega_{ij}t} e^{-S(E_{ij})} |f_{ij}|^2 \quad (\text{E.3})$$

Here, we work with a particular thermal regularization of the auto-correlation function for later convenience (The analogous expression for the usual auto-correlation function can be obtained by shifting $t \rightarrow t + i\beta/2$). In the final step, we assume that the squared random variables can be approximated by their average (that is, one), since the sum is over exponentially many matrix elements.

Changing coordinates from E_i, E_j to E_{ij}, ω_{ij} , and converting the sums to integrals, we have:

$$\begin{aligned} G_\beta(t) &= \frac{1}{\mathcal{Z}} \int dE e^{-\beta E + S(E)} \int d\omega [e^{S(E+\omega/2) + S(E-\omega/2) - 2S(E)}] e^{i\omega t} |f(E, \omega)|^2 \\ &\approx \int d\omega [e^{S(E_\beta + \omega/2) + S(E_\beta - \omega/2) - 2S(E_\beta)}] e^{i\omega t} |f(E_\beta, \omega)|^2 \\ &\approx \int d\omega e^{i\omega t} |f(E_\beta, \omega)|^2. \end{aligned} \quad (\text{E.4})$$

In the second line, we use the standard saddle point approximation for the thermodynamic limit. In the third line, we note that the difference of entropies vanishes to leading order in ω^2/N . Taking the Fourier transform, we have:

$$\tilde{G}_\beta(\omega) \equiv \int dt e^{-i\omega t} G_\beta(t) \approx |f(E_\beta, \omega)|^2. \quad (\text{E.5})$$

We see that the function $f(E_{ij}, \omega_{ij})$ is simply the Fourier transform of the auto-correlation function. For local Hamiltonians, the support of the Fourier transform is tightly constrained within the band $|\omega| \lesssim \beta^{-1}$, and for large ω decays as $f(E_\beta, \omega) \sim e^{-\beta\omega}$.

Matrix elements of the coupled Hamiltonian

We will work in a slightly more general context than the specific SYK Hamiltonian presented in Chapter 6. For any Hamiltonian H , we consider the coupled Hamiltonian

$$H = H_L + H_R^* - \mu \sum_{i=\alpha}^N O_L^\alpha O_R^{\alpha,*}, \quad (\text{E.6})$$

which acts on two copies of the original system. For generality, we allow the Hamiltonian to be complex, in which case the left system should be acted upon by H and the right

system by its complex conjugate H^* . We work with bosonic coupling operators O^α for simplicity, to avoid subtleties associated with defining matrix elements of fermionic operators. Nonetheless, we will show that our final expressions are consistent with those obtained for fermionic couplings in the low-temperature and large- q limits of the SYK model.

We will now compute the matrix elements of the coupled Hamiltonian in the energy eigenbasis formed by the two single-sided Hamiltonians. That is, for the two-sided system, we construct a complete basis of states $|ij^*\rangle = |i\rangle \otimes |j^*\rangle$, where $|i\rangle$ is an eigenstate of H_L with energy E_i and $|j^*\rangle$ is an eigenstate of H_R^* with energy E_j . The matrix elements of H_L and H_R^* in this eigenbasis are clearly diagonal,

$$\langle lk^* | H_L + H_R^* | ij^* \rangle = (E_i + E_j) \cdot \delta_{il} \delta_{jk}. \quad (\text{E.7})$$

Meanwhile, the matrix elements of the coupling can be expressed using the ETH:

$$\langle lk^* | \sum_{\alpha=1}^N O_L^\alpha O_R^{\alpha,*} | ij^* \rangle = \sum_{\alpha=1}^N O_{li}^\alpha (O_{kj}^\alpha)^* = \sum_{\alpha=1}^N e^{-\frac{S_{li} + S_{jk}}{2}} f_{li}^\alpha f_{jk}^\alpha r_{li}^\alpha r_{jk}^\alpha. \quad (\text{E.8})$$

Here, we assume that the operators have no thermal expectation values (if they do, it is a constant term that can simply be subtracted from each operator in the coupling). This is guaranteed in the SYK model since the operators are fermionic.

In general, the hopping matrix elements above have wildly varying phases for different initial and final states. This simplifies in one particular instance: when both the initial and final state are ‘‘diagonal’’ in the energy eigenbasis, $i = j$ and $k = l$. Within this subspace of states, the matrix elements of the coupling drastically simplify,

$$\langle kk^* | \sum_{\alpha=1}^N O_L^\alpha O_R^{\alpha,*} | ij^* \rangle = e^{-S_{ik}} \sum_{\alpha=1}^N |f_{ik}^\alpha|^2 |r_{ik}^\alpha|^2 \approx e^{-S_{ik}} \sum_{\alpha=1}^N |f_{ik}^\alpha|^2. \quad (\text{E.9})$$

Notably, the matrix elements are *positive* for all values of i, k . Thus, despite each matrix element having exponentially small magnitude, they can constructively interfere when summed over many eigenstates.

The thermofield states that we are interested in lie entirely in the diagonal sector above. Namely, for inverse temperature β , the thermofield double state takes the form

$$|\text{TFD}\rangle = \sum_i \frac{e^{-\beta E_i/2}}{\text{tr}(e^{-\beta H})} |ii^*\rangle. \quad (\text{E.10})$$

This motivates us to restrict our analysis to states within the diagonal sector. In principle, one might worry that this restriction is not valid, if diagonal states ‘‘leak’’ significantly to off-diagonal states, i.e. $|ij^*\rangle$ with $i \neq j$, under the dynamics of the coupled Hamiltonian. With this in mind, we will benchmark our approximation by comparing our results that follow to existing calculations for the SYK model in certain limits, and our own numerics. We find that this approximation is, to a large extent, justified for the SYK Hamiltonian.

In summary, restricting to the diagonal sector of states, the coupled Hamiltonian has matrix elements,

$$H_{kk^*,ii^*} = 2E_i \delta_{ik} + \mu N e^{-S_{ik}} |f_{ik}|^2, \quad (\text{E.11})$$

where we denote the average auto-correlation function as $|f_{ik}|^2 \equiv \frac{1}{N} \sum_{\alpha=1}^N |f_{ik}^\alpha|^2$. The first term resembles an on-site potential energy, while the second term induces hoppings between nearby states. In the following section, we will derive a continuum approximation for this Hamiltonian and show that it corresponds to a simple semi-classical harmonic oscillator.

Continuum approximation for the coupled Hamiltonian

To derive a continuum approximation for the coupled Hamiltonian, let us assume that the wavefunction of our state takes the form:

$$|\psi\rangle = \sum_i e^{-S(E_i)/2} \cdot \psi(E_i) |ii^*\rangle, \quad (\text{E.12})$$

where the amplitudes $\psi(E_i)$ vary smoothly with the energy E_i . The prefactor $e^{-S(E_i)/2}$ corresponds to the inverse square root density of states, which guarantees that the function $\psi(E_i)$ is normalized,

$$\int dE |\psi(E)|^2 \approx \sum_i e^{-S(E_i)} \cdot |\psi(E_i)|^2 = \langle \psi_d | \psi_d \rangle = 1. \quad (\text{E.13})$$

We will derive an effective Schrodinger's equation for the continuum wavefunction $\psi(E)$. Taking a time-derivative using $i\partial_t |\psi\rangle = H |\psi\rangle$, and restricting to the diagonal basis, we have

$$i \sum_i e^{-S(E_i)/2} \cdot \partial_t \psi(E_i) |ii^*\rangle = \sum_i e^{-S(E_i)/2} \cdot \psi(E_i) \cdot \sum_k H_{kk^*,ii^*} |kk^*\rangle. \quad (\text{E.14})$$

or, taking the inner product with a given basis state $\langle ii^* |$ and using the matrix elements Eq. (E.11),

$$i\partial_t \psi(E_i) = 2E_i \cdot \psi(E_i) - \mu N \sum_k e^{\frac{1}{2}(S_i - S_k - 2S_{ik})} |f_{ik}|^2 \cdot \psi(E_k). \quad (\text{E.15})$$

As we noted previously, the first term corresponds to an on-site potential in the and the second term to hoppings between different energies. Using the fact that the summand is a smooth function of the energy, we can make a continuum approximation,

$$\begin{aligned} i\partial_t \psi(E_i) &\approx 2E_i \cdot \psi(E_i) - \mu N \int dE_k e^{\frac{1}{2}(S_i + S_k - 2S_{ik})} |f_{ik}|^2 \cdot \psi(E_k) \\ &\approx 2E_i \cdot \psi(E_i) - \mu N \int d\omega_{ik} |f(E_i + \omega_{ik}/2, \omega_{ik})|^2 \cdot \psi(E_i + \omega_{ik}) \end{aligned} \quad (\text{E.16})$$

In the second line we switch integration coordinates to $\omega_{ik} = E_i - E_k$, and use that $e^{\frac{1}{2}(S_i+S_k-2S_{ik})} \approx e^{-\omega_{ik}^2\beta^2/8cN} \approx 1$. Here, $c \sim O(1)$ is the specific heat, and the exponential is near one because $\omega_{ik}\beta \sim O(1)$ due to the factor of f . Finally, let us Taylor expand $\psi(E_i + \omega_{ik}) \approx \psi(E_i) + \omega_{ik}\partial_{E_i}\psi(E_i) + (\omega_{ik}^2/2)\partial_{E_i}^2\psi(E_i)$ to obtain an effective Schrodinger equation

$$i\partial_t\psi(E) \approx 2E \cdot \psi(E) - \mu N [a(E)\psi(E) + b(E)\partial_E\psi(E) + c(E)\partial_E^2\psi(E)], \quad (\text{E.17})$$

with coefficients

$$\begin{aligned} a(E) &= \int d\omega |f(E + \omega/2, \omega)|^2 \approx \int d\omega |f(E, \omega)|^2 = G_{\beta(E)}(0), \\ b(E) &= \int d\omega \omega \cdot |f(E + \omega/2, \omega)|^2 \approx \int d\omega \omega^2 \cdot f(E, \omega)\partial_E f(E, \omega) \sim O\left(\frac{1}{\beta N}\right), \\ c(E) &= \frac{1}{2} \int d\omega \omega^2 \cdot |f(E + \omega/2, \omega)|^2 \approx \frac{1}{2}G''_{\beta(E)}(0). \end{aligned} \quad (\text{E.18})$$

The linear term is suppressed by $1/N$ because $f(E, \omega)$ is even in ω if the dynamics are time-reversal invariant, and each derivative applied to the first argument of f gives a factor of $1/N$. In the final line, we use double primes to denote the second time-derivative of $G''_{\beta(E)}$, evaluated at $t = 0$.

To write this equation in a nicer form, let us switch coordinates to the energy *density*, $e \equiv E/N$, and drop the linear term in the thermodynamic limit. This gives

$$iN^{-1}\partial_t\psi(e) \approx [2e - \mu G_{\beta(e)}] \cdot \psi(e) - \mu G''_{\beta(e)} \frac{N^{-2}\partial_e^2}{2}\psi(e). \quad (\text{E.19})$$

This is the usual single-particle Schrodinger equation for a particle in a potential $V(e) = 2e - \mu G_{\beta(e)}$ with (position-dependent) mass, $m = (\mu G''_{\beta(e)})^{-1}$. The effective Planck's constant is N^{-1} , which is small in the thermodynamic limit. We expect this Schrodinger equation to describe the low-energy physics in the diagonal sector of states.

Low-energy dynamics of the coupled Hamiltonian

We can simplify the Schrodinger equation even further by Taylor expanding about its potential minimum. The minimum occurs at the energy density that solves the equation,

$$2 = \mu\partial_e G_{\beta(e_{\min})}. \quad (\text{E.20})$$

Thus, the minimum is set by the value of μ . Nearby this minimum, we can expand the potential to quadratic order,

$$2e - \mu G_{\beta(e)} \approx \text{constant} + \frac{\mu\partial_e^2 G_{\beta(e_{\min})}}{2} e^2. \quad (\text{E.21})$$

We can also approximate the mass by its value at the potential minimum e_{\min} . Thus, nearby the potential minimum, the behavior of the diagonal sector is described by a simple harmonic oscillator,

$$iN^{-1}\partial_t\psi(e) \approx \left(\text{constant} + \frac{\mu\partial_e^2 G_{\beta(e_{\min})}}{2} e^2 \right) \cdot \psi(e) - \mu G''_{\beta(e_{\min})} \frac{N^{-2}\partial_d e^2}{2} \psi(e), \quad (\text{E.22})$$

with spring constant $k(\mu) = \mu\partial_e^2 G_{\beta(e_{\min})}$ and mass $m(\mu) = (\mu G''_{\beta(e_{\min})})^{-1}$.

Applying standard formulas for the quantum harmonic oscillator, the ground state of the coupled Hamiltonian with coupling strength μ is

$$\psi_{\text{gs}}(e; \mu) = \left(\frac{Nm\omega}{\pi} \right)^{1/4} \exp\left(-\frac{Nm\omega}{2}(e - e_{\min})^2 \right), \quad (\text{E.23})$$

where again m, ω, e_{\min} depend on μ , and we define the frequency

$$\omega(\mu) = \sqrt{\frac{k(\mu)}{m(\mu)}} = \mu \sqrt{\partial_e^2 G_{\beta(e_{\min})} \cdot G''_{\beta(e_{\min})}}. \quad (\text{E.24})$$

The ground state has average energy density $e_{\min}(\mu)$ and standard deviation $\sqrt{Nm\omega}$. The Hamiltonian is gapped, with

$$\Delta_{\text{diag}}(\mu) = N (N^{-1}\omega(\mu)) = \omega(\mu). \quad (\text{E.25})$$

The factor of N arises when we convert to energies instead of energy densities, and the factor of N^{-1} is the effective Planck's constant. Within the low-energy approximation, the excited states are simply the higher eigenstates of the quantum harmonic oscillator. We note this discussion only concerns excited states within the diagonal sector, and neglects potential off-diagonal excited states (which lie outside our approximation, and may have a smaller gap than Δ_{diag} [170]).

Finally, we can ask how close the ground state is to our desired state, the thermofield double. The thermofield double state has a wavefunction

$$\psi_{\text{tfd}}(e; \beta) = \frac{e^{(S(e) - \beta Ne)/2}}{\text{tr}(e^{-\beta H})} \approx \left(\frac{N\beta^2}{c} \right)^{1/4} \exp\left(-\frac{N\beta^2}{2c}(e - e_\beta)^2 \right), \quad (\text{E.26})$$

where we obtain the latter expression by Taylor expanding the entropy, where c is the specific heat at inverse temperature β . Like the ground state [Eq. (E.23)], the thermofield double state has a Gaussian wavefunction, with average energy density e_β and standard deviation $\sqrt{N\beta^2/c}$. For a desired inverse temperature β , we can maximize the overlap of the actual ground state with the desired thermofield double state by setting μ such that $e_{\min}(\mu) = e_\beta$. With this choice, the states have a many-body overlap which is $O(1)$. We note that in general, the many-body overlap is not unity because the widths of the two wavefunctions

may differ by an $O(1)$ factor. More importantly, we expect corrections to the ground state due to off-diagonal matrix elements to cause the many-body overlap with the thermofield state to decay exponentially in system size [170]. Nonetheless, we expect local observables and correlation functions in the ground state to remain close to those in the thermofield double state, as has been verified at low temperatures in the SYK model [170].

Parameters for the SYK model and comparison to known results

We can benchmark our approximation by calculating the parameters of our Hamiltonian in the analytically solvable limits of the SYK model. We begin with the large- q limit, which has been analyzed in Refs. [151, 170]. The auto-correlation function is

$$G_\beta(t) = \left(\frac{\alpha_\beta}{J \cosh(\alpha_\beta t)} \right)^{2/q}, \quad (\text{E.27})$$

where the energy scale α_β is set by the temperature via $\alpha_\beta = J \cos(\alpha_\beta \beta/2)$. Our effective Schrodinger equation becomes

$$iN^{-1} \partial_t \psi(e) \approx \left[2e - \mu \left(\frac{\alpha_{\beta(e)}}{J} \right)^{2/q} \right] \cdot \psi(e) - \mu \frac{2\alpha_{\beta(e)}^2}{q} \left(\frac{\alpha_{\beta(e)}}{J} \right)^{2/q} \frac{N^{-2} \partial_e^2}{2} \psi(e). \quad (\text{E.28})$$

To compute further, we can convert between energy density and temperature using the following expression for the large- q SYK model [93],

$$e_\beta = (J/q^2) \sin(\alpha_\beta \beta/2) = \frac{J}{q^2} \sqrt{1 - (\alpha_\beta/J)^2}, \quad (\text{E.29})$$

which in turn gives the specific heat, $\partial\beta/\partial e \equiv -\beta^2 c^{-1}$. In principle, this allows one to compute

$$\partial_e G_\beta(e) = \frac{\partial\beta}{\partial e} \cdot \frac{2}{q} \frac{\partial \log(\alpha_\beta)}{\partial\beta} G_\beta(e) \quad (\text{E.30})$$

and

$$\partial_e^2 G_\beta(e) = \frac{2}{q} G_\beta(e) \left[\frac{\partial^2 \beta}{\partial e^2} \cdot \frac{\partial \log(\alpha_\beta)}{\partial\beta} + \left(\frac{\partial\beta}{\partial e} \right)^2 \left(\frac{\partial^2 \log(\alpha_\beta)}{\partial\beta^2} + \frac{2}{q} \left(\frac{\partial \log(\alpha_\beta)}{\partial\beta} \right)^2 \right) \right]. \quad (\text{E.31})$$

However, the algebra become unwieldy.

We will content ourselves to analyze the behavior in the low-temperature limit, and show that our effective Schrodinger equation recovers that computed from the large- N analysis in Ref. [170]. At low temperatures, $\beta J \gg 1$, we have $\alpha_\beta \approx \pi/\beta - 2\pi/(\beta^2 J)$, $\partial\beta/\partial e \approx -(q^2/2\pi^2)\beta^3 J$, and $\partial \log(\alpha_\beta)/\partial\beta \approx -1/\beta$. In this limit, our Schrodinger equation becomes

$$iN^{-1} \partial_t \psi(e) \approx \left[2e - \mu \left(\frac{\pi}{\beta_e J} \right)^{2/q} \right] \cdot \psi(e) - \mu \frac{2\pi^2}{q\beta_e^2} \left(\frac{\pi}{\beta_e J} \right)^{2/q} \frac{N^{-2} \partial_e^2}{2} \psi(e). \quad (\text{E.32})$$

The potential minimum lies at inverse temperature $\beta_{e_{\min}} = \pi J^{-1} \left(\frac{q\mu}{2J}\right)^{-\frac{1}{2-2/q}}$. Expanding about the potential minimum, we find the harmonic oscillator

$$iN^{-1}\partial_t\psi(e) \approx \left[\text{constant} + \frac{2q^2\beta^2 J (e - e_{\min})^2}{\pi^2 \cdot 2} \right] \cdot \psi(e) - \frac{4\pi^4}{q^2\beta^4 J} \frac{N^{-2}\partial_e^2}{2} \psi(e), \quad (\text{E.33})$$

where we abbreviate $\beta_{e_{\min}}$ as β . The oscillator has spring constant, mass, and frequency

$$k = \frac{2q^2\beta^2 J}{\pi^2}, \quad m = \left(\frac{4\pi^4}{q^2\beta^4 J}\right)^{-1}, \quad \omega = \sqrt{\frac{k}{m}} = \frac{2\pi\sqrt{2}}{\beta}. \quad (\text{E.34})$$

The oscillator frequency precisely matches that of the ‘‘graviton mode’’, given in Eq. (4.37) of Ref. [170]. (Note that, in their work, $t' = 2\pi/\beta$ and the large- q limit corresponds to $\Delta \rightarrow 0$.) We have also checked that oscillator frequency at finite- q derived from the ETH framework is $\omega = 2\pi\sqrt{2(1-\Delta)}/\beta$, again in agreement with Ref. [170].

Self-consistency of the diagonal approximation

In the previous sections, we simplified our analysis of the coupled Hamiltonian by restricting to its action on diagonal states, of the form $\sum_i \psi(E_i) |ii^*\rangle$. This was motivated by the fact that both the initial and desired final state of our preparation protocol (i.e. EPR pairs and the thermfield double state) lie in the diagonal sector, and by the particularly simple form of the hoppings between diagonal states. This approximation also closely resembles the ladder diagram approximation made in Ref. [170]. In this section, we provide a basic self-consistency check to measure the accuracy of this approximation.

Our check is to compute the variance of the coupled Hamiltonian in its putative ground state. (We thank Daniel Jafferis for this idea.). To do so, let us expand the Hamiltonian into its diagonal and off-diagonal components, $H = H_d + H_{\text{od}}$, where H_d contains all matrix elements between states of the form $|ii^*\rangle$, and H_{od} contains all other matrix elements. In the previous section, we obtained the ground state $|\psi_d\rangle$ of the diagonal component H_d . The variance of the Hamiltonian in state $|\psi_d\rangle$ thus arises solely from the off-diagonal component,

$$\langle \psi_d | H^2 | \psi_d \rangle - \langle \psi_d | H | \psi_d \rangle^2 = \langle \psi_d | H_{\text{od}}^2 | \psi_d \rangle = \mu^2 \sum_{j,j'} \langle \psi_d | (i\psi_L^j \psi_R^j)_{\text{od}} (i\psi_L^{j'} \psi_R^{j'})_{\text{od}} | \psi_d \rangle, \quad (\text{E.35})$$

where we use the subscript to denote that we are considering only off-diagonal matrix elements. The leading contribution to this correlation function comes from contracting ψ_L^j with $\psi_L^{j'}$ and ψ_R^j with $\psi_R^{j'}$. This restricts $j = j'$, and gives a variance

$$\langle \psi_d | H^2 | \psi_d \rangle - \langle \psi_d | H | \psi_d \rangle^2 \approx \mu^2 N, \quad (\text{E.36})$$

which indicates energy fluctuations of order μ^2 per fermion. At low temperatures, these fluctuations are much smaller than the energy scale of the local dynamics, β^{-1} , since $\mu\beta \sim (\beta J)^{-1+2/q} \ll 1$. A similar validity condition was derived in Ref. [170] based on arguments regarding the gravitational dynamics of the SYK model. Here, we show that the same approximation and validity conditions can be derived solely from knowledge of the two-point function of the single-sided Hamiltonian, using the ETH framework of Ref. [61].

E.2 Analysis of quantum adiabatic protocol

In Chapter 6, we outlined how the quantum adiabatic theorem enables one to prepare the ground state of the coupled Hamiltonian with high fidelity, by slowly interpolating the coupling strength from a large to small value. Here, we estimate the time required to achieve this to within a small many-body infidelity. We do so by leveraging the harmonic oscillator approximation (see previous section) to calculate the error in the quantum adiabatic protocol.

The dominant errors in the quantum adiabatic protocol arise from leakage to the first excited state of the harmonic oscillator. By Fermi’s golden rule, this leakage occurs at a rate

$$\partial_t (|\langle \psi_{\text{gs}} | \psi_{\text{gs}} \rangle|^2) \approx -\frac{|\langle \psi_{\text{exc}} | \partial_t | \psi_{\text{gs}} \rangle|^2}{\Delta_{\text{diag}}}, \quad (\text{E.37})$$

where $|\psi_{\text{gs}}\rangle, |\psi_{\text{exc}}\rangle$ are the ground state and first excited state, respectively, and Δ_{diag} is the gap in the diagonal sector (see Appendix E.1). This approximation neglects any leakage into “off-diagonal” states. Notably, in the SYK model, the matrix elements and gap of such contributions scale identically to those of diagonal states [170], and thus they will only increase the error by a constant factor.

The time-dependence of the ground state arises from its dependence on the coupling μ , which we vary along an adiabatic path $\mu(t/T)$ where $\mu(0) = \mu_i \gg J$ and $\mu(1) = \mu_f \ll J$. Here, T is the total time of preparation. The total error in the quantum adiabatic protocol is thus

$$\int_0^T dt \frac{|\langle \psi_{\text{exc}} | \partial_\mu | \psi_{\text{gs}} \rangle|^2}{\Delta_{\text{diag}}} \cdot \frac{(\partial_\lambda \mu)^2}{T^2} = \frac{1}{T} \int_0^1 d\lambda \frac{|\langle \psi_{\text{exc}} | \partial_\mu | \psi_{\text{gs}} \rangle|^2}{\Delta_{\text{diag}}} \cdot (\partial_\lambda \mu)^2, \quad (\text{E.38})$$

where each variable depends implicitly on λ .

The leading order contribution to the matrix element above arises from the shift in the center position of the harmonic oscillator. We can compute the derivative with respect to the center position,

$$|\langle \psi_{\text{exc}} | \partial_{e_{\text{min}}} | \psi_{\text{gs}} \rangle|^2 = \frac{\sqrt{2}}{1/(Nm\omega)}. \quad (\text{E.39})$$

The latter expression is proportional to the inverse width squared of the ground state wavefunction.

To proceed further, it is convenient to re-express all variables, integrals, and derivatives in terms of the temperature $\beta_{e_{\text{min}}}^{-1}$ (abbreviated as β from hereon). For convenience, we also specify to the SYK model at low temperatures. Taking $|\partial_\lambda \beta^{-1}| \sim \beta^{-1}$ to ensure a constant

relative rate of change, we find a total error

$$\begin{aligned}
 \frac{1}{T} \int_0^1 d\lambda \frac{|\langle \psi_{\text{exc}} | \partial_\mu | \psi_{\text{gs}} \rangle|^2}{\Delta_{\text{diag}}} \cdot (\partial_\lambda \mu)^2 &= \frac{1}{T} \int_0^1 d\lambda \frac{|\langle \psi_{\text{exc}} | \partial_{\beta^{-1}} | \psi_{\text{gs}} \rangle|^2}{\Delta_{\text{diag}}} \cdot (\partial_\lambda \beta^{-1})^2 \\
 &= \frac{1}{T} \int_{\beta_i^{-1}}^{\beta_f^{-1}} d\beta^{-1} \beta^{-1} \cdot \frac{|\langle \psi_{\text{exc}} | \partial_{\beta^{-1}} | \psi_{\text{gs}} \rangle|^2}{\Delta_{\text{diag}}} \\
 &\sim \frac{1}{T} \int_{\beta_i^{-1}}^{\beta_f^{-1}} d\beta^{-1} \beta^{-1} \cdot \frac{Nm\omega}{\omega} \cdot |\partial_{\beta^{-1}} e_{\text{min}}|^2 \\
 &\sim \frac{1}{T} \int_{\beta_i^{-1}}^{\beta_f^{-1}} d\beta^{-1} \beta^{-1} \cdot N\beta^4 J \cdot (\beta J)^{-2} \\
 &= \frac{N}{JT} \int_{\beta_i^{-1}}^{\beta_f^{-1}} d\beta^{-1} \frac{1}{\beta^{-1}} \\
 &= \frac{N}{JT} \log(\beta_i/\beta_f).
 \end{aligned} \tag{E.40}$$

In the second line, we change integration coordinates and apply $|\partial_\lambda \beta^{-1}| \sim \beta^{-1}$. In the third line, we change coordinates in the derivative and apply Eq. (E.39). In the fourth through sixth lines, we express all variables in terms of β^{-1} and evaluate the integral.

Applying the above expression, to ensure that the many-body infidelity in the adiabatic protocol is less than ε , we must take

$$T \gtrsim \frac{N}{J\varepsilon} \log(\beta_i/\beta_f). \tag{E.41}$$

As discussed in Chapter 6, the time scales linearly in the system size, since the quantum adiabatic theorem guarantees a high *many-body* fidelity in the resulting state. In the following section, we address how to achieve a high *local* fidelity in order one times, leveraging our semi-classical approximation for the wavefunction's dynamics.

E.3 Analysis of semi-classical adiabatic protocol

As outlined in Chapter 6 and Appendix E.1, the low-energy dynamics of the coupled Hamiltonian are described by a semi-classical harmonic oscillator in the large- N limit. In Chapter 6, leveraging this mapping, we argued that the notion of *classical* adiabaticity allows us to efficiently prepare a semi-classical approximation of the thermofield double state in $\mathcal{O}(1)$ time. In this section, we provide a more detailed analysis of this scenario.

The Hamiltonian of our semi-classical approximation is equivalent to that of a particle in a harmonic oscillator,

$$H = \frac{1}{2m(t)} p^2 + \frac{1}{2} k(t) [q - q_c(t)]^2, \tag{E.42}$$

where the position q corresponds to the energy density, and the momentum p is its canonical conjugate. Here, the mass m , spring constant k , and center q_c will vary in time through their dependence on μ , the coupling strength in the coupled Hamiltonian [see Appendix E.1 for full details].

The coordinates evolve in time according to Hamilton's equations of motion,

$$\begin{aligned}\dot{q} &= \frac{\partial H}{\partial p} = \frac{1}{m}p, \\ \dot{p} &= -\frac{\partial H}{\partial q} = -k(q - q_c),\end{aligned}\tag{E.43}$$

where we suppress the time-dependencies for convenience. In what follows, it will be convenient to work in a moving (and, potentially, accelerating) frame about the center of the harmonic oscillator. To do so, we define the new variables

$$\delta q = q - q_c, \quad \delta p = p - m\dot{q}_c,\tag{E.44}$$

which, by straightforward algebra, undergo their own equations of motion,

$$\begin{aligned}\delta\dot{q} &= \frac{1}{m}\delta p, \\ \delta\dot{p} &= -k\delta q - (\dot{m}\dot{q}_c + m\ddot{q}_c),\end{aligned}\tag{E.45}$$

The final term, in parentheses, corresponds to the fictitious force induced by a non-inertial frame. When the mass is constant in time, $\dot{m} = 0$, the frame is inertial when the center has zero acceleration, $\ddot{q}_c = 0$, as expected. When the mass varies in time, the condition for the frame to be inertial corresponds to the requirement that the fictitious force vanish, $\ddot{q}_c = -(\dot{m}/m)\dot{q}_c$.

We are interested in how the system evolves as we vary μ slowly from an initial value μ_i to a final value μ_f . To describe this interpolation, let us introduce a function $\mu(\lambda)$ with $\lambda \in [0, 1]$, and the endpoints $\mu(0) = \mu_i$ and $\mu(1) = \mu_f$. We take the value of the coupling at time t to be $\mu(t/T)$, where T is the total time of our interpolation. We would like to know how large T must be, such that the particle remains near to the center of harmonic oscillator throughout the interpolation.

To estimate this, let us first make a simplifying assumption: that the frame is inertial for all times besides the start and end point, $t \in (0, T)$. This can be achieved with a suitable choice of $\mu(\lambda)$. We discuss the effect of a non-inertial frame at the end of our computation.

In the inertial frame, there are three contributions that cause the particle to deviate from the center of the harmonic oscillator. First, at time zero, the jerk from the stationary frame to the moving frame causes the particle to instantaneously acquire a velocity $v_i = \dot{q}_c|_{t=0}$ in the moving frame. This corresponds to an energy $E_i = \frac{1}{2}m_i v_i^2$. Second, as we time-evolve from time zero to T , this initial energy E_i may change as a result of our changing the parameters k, m . We address this using the notion of adiabatic invariants in the following paragraph. Finally, at time T , the jerk from the moving frame back to a stationary frame causes the

particle to instantaneously acquire an additional velocity $\Delta v_f = -\dot{q}_c|_{t=T}$. Assuming the jerk occurs at a random point in the particle's oscillation, this contributes an additional energy $\Delta E_f = \frac{1}{2}m_f v_f^2$.

It remains only to compute the second process: the change in the initial energy E_i as a result of the change in parameters k, m from time zero to T . To do so, we leverage the notion of an adiabatic invariant. For a classical mechanical system with closed orbits in phase space, the classical adiabatic theorem states that the area enclosed by the orbits in phase space remains constant under a slow change in the Hamiltonian parameters [10]. This is easily derived in the case of the harmonic oscillator. The time-derivative of the energy is

$$\dot{E} = \frac{1}{2}\dot{k}\delta q^2 + \frac{1}{2}(\dot{m}^{-1})\delta p^2. \quad (\text{E.46})$$

Assuming δq and δp oscillate much faster than the parameters change (specifically, that $\dot{k}/k, \dot{m}/m \ll 1$), we can approximate the squared coordinates in the above expression by their average values, $\delta q^2 \rightarrow E/k$ and $\delta p^2 \rightarrow E/m^{-1}$. This gives

$$\frac{\dot{E}}{E} = \frac{1}{2}\frac{\dot{k}}{k} + \frac{1}{2}\frac{\dot{m}^{-1}}{m^{-1}}, \quad (\text{E.47})$$

which is easily solved to give

$$\frac{E}{\omega} = \text{constant}, \quad (\text{E.48})$$

where $\omega = \sqrt{k/m}$ is the frequency of the oscillator. This ratio of the energy to the frequency is the adiabatic invariant of the harmonic oscillator.

Applying the classical adiabatic theorem to our problem, we find that the initial energy E_i at time zero is propagated to an energy $E_i(\omega_f/\omega_i)$ at time T . Adding to this the energy of the final jerk, we find that the final energy of the particle after adiabatic evolution is given by

$$E_f = E_i(\omega_f/\omega_i) + \Delta E_f = \frac{1}{2}\frac{m_i\omega_f}{\omega_i}v_i^2 + \frac{1}{2}m_f v_f^2. \quad (\text{E.49})$$

To interpret this in the context of the SYK model, we can use the formulas in Appendix E.1 to derive the uncertainty in temperature of our approximate thermofield double state. Setting $m_i \sim J^{-3}, k_i \sim J^{-1}, v_f \sim 1/T$ for the large- μ initial state, and $m_f \sim \beta^4 J, k_f \sim \beta^2 J, v_f \sim 1/(\beta^2 J T)$ for the small- μ final state, we have a final energy

$$E_f \sim O\left(N\frac{1}{\beta J}J^{-3}(J/T)^2\right) + O\left(N\beta^4 J\frac{1}{(\beta^2 J T)^2}\right) = O\left(\frac{N}{\beta J^2 T^2}\right) + O\left(\frac{N}{J T^2}\right). \quad (\text{E.50})$$

The velocities are set according to $\dot{e}_{\min} = (\partial e/\partial \beta)\dot{\beta} \sim (\dot{\mu}/\mu)/(\beta^2 J)$. Assuming $\dot{\mu}/\mu \sim O(1/T)$, this quantity is $O(J/T)$ at large μ and $O(1/(\beta^2 J T))$ at small μ . The second term above is leading, and translates to a relative uncertainty in temperature,

$$\frac{\delta\beta^{-1}}{\beta^{-1}} = \beta \left| \frac{\partial\beta^{-1}}{\partial E} \right| E_f = \frac{1}{\beta} \left| \frac{\partial\beta}{\partial e} \right| \frac{E_f}{N} = O\left(\frac{\beta^2}{T^2}\right). \quad (\text{E.51})$$

Thus, the relative uncertainty in temperature is small whenever the time of preparation is much larger than the time-scale β of the low temperature dynamics. The relative error in local correlation functions will be determined by propagating the uncertainty in temperature to the correlation function, and will be suppressed by the same factor.

Finally, we address the effect of a non-inertial frame. At leading order, the non-inertial frame can be incorporated by noting that the fictional force simply shifts the *effective* center of the harmonic oscillator from q_c to $q_{c,\text{eff}} \equiv q_c + k^{-1}(\dot{m}\dot{q}_c + m\ddot{q}_c)$. Assuming the particle's oscillations track the effective center, this leads to an additional energy $(1/2)k_f(q_{c,\text{eff}} - q_c)^2$ at time T . This additional energy can be tuned to be small by reducing the acceleration of the non-inertial frame near time T . Otherwise, it generically contributes as $\sim m_f v_f^2 / (\omega_f T)^2$, which is subleading in $1/(\omega_f T)$ compared to the previous contributions.

Bibliography

- [1] See Appendix A for additional numerics, derivations, and analysis.
- [2] Our parallelized dynamics code is available open-source as the package dynamite: <https://dynamite.readthedocs.io/> DOI:10.5281/zenodo.3606826.
- [3] In: *We note that the low sensitivity at early times is not a fundamental restriction of the local protocol. In particular, at time zero, one could achieve the SQL by performing N copies of the local protocol in parallel, with each copy containing a single qubit. More generally, if local operators have size \mathcal{S} , one can perform N/\mathcal{S} copies of the local protocol in parallel, with sensitivity $\eta^{-1} \sim \sqrt{N\mathcal{S}}$. Effectively, this partitioning occurs intrinsically for the global protocol, whereas it would need to be implemented explicitly with the local protocol ()*.
- [4] Scott Aaronson and Daniel Gottesman. “Improved simulation of stabilizer circuits”. In: *Physical Review A* 70.5 (2004), p. 052328.
- [5] Dmitry A Abanin and Eugene Demler. “Measuring entanglement entropy of a generic many-body system with a quantum switch”. In: *Physical review letters* 109.2 (2012), p. 020504.
- [6] Rafael N Alexander, Glen Evenbly, and Israel Klich. “Exact holographic tensor networks for the Motzkin spin chain”. In: *arXiv preprint arXiv:1806.09626* (2018).
- [7] Ahmed Almheiri et al. “Replica wormholes and the entropy of Hawking radiation”. In: *Journal of High Energy Physics* 2020.5 (2020), pp. 1–42.
- [8] Ahmed Almheiri et al. “The entropy of bulk quantum fields and the entanglement wedge of an evaporating black hole”. In: *Journal of High Energy Physics* 2019.12 (2019), pp. 1–47.
- [9] Alexander Altland, Dmitry Bagrets, and Alex Kamenev. “Sachdev-Ye-Kitaev non-Fermi-liquid correlations in nanoscopic quantum transport”. In: *Physical Review Letters* 123.22 (2019), p. 226801.
- [10] Vladimir Igorevich Arnol’d. *Mathematical methods of classical mechanics*. Vol. 60. Springer Science & Business Media, 2013.
- [11] Frank Arute et al. “Quantum supremacy using a programmable superconducting processor”. In: *Nature* 574.7779 (2019), pp. 505–510.

- [12] Deniz Aybas et al. “Search for axionlike dark matter using solid-state nuclear magnetic resonance”. In: *Physical Review Letters* 126.14 (2021), p. 141802.
- [13] Dmitry Bagrets, Alexander Altland, and Alex Kamenev. “Power-law out of time order correlation functions in the SYK model”. In: *Nuclear Physics B* 921 (2017), p. 727. DOI: 10.1016/j.nuclphysb.2017.06.012. arXiv: 1702.08902.
- [14] Dmitry Bagrets, Alexander Altland, and Alex Kamenev. “Sachdev–Ye–Kitaev model as Liouville quantum mechanics”. In: *Nuclear Physics B* 911 (2016), p. 191. DOI: 10.1016/j.nuclphysb.2016.08.002.
- [15] Satish Balay et al. “Efficient Management of Parallelism in Object Oriented Numerical Software Libraries”. In: *Modern Software Tools in Scientific Computing*. Ed. by E. Arge, A. M. Bruaset, and H. P. Langtangen. Birkhäuser Press, 1997, pp. 163–202.
- [16] CL Baldwin and B Swingle. “Quenched vs Annealed: Glassiness from SK to SYK”. In: *Physical Review X* 10.3 (2020), p. 031026.
- [17] C. J. Ballance et al. “High-Fidelity Quantum Logic Gates Using Trapped-Ion Hyperfine Qubits”. In: *Phys. Rev. Lett.* 117 (6 2016), p. 060504. DOI: 10.1103/PhysRevLett.117.060504.
- [18] Ning Bao et al. “Traversable wormholes as quantum channels: exploring CFT entanglement structure and channel capacity in holography”. In: 2018.11 (2018), p. 71.
- [19] Daniel Barredo et al. “Synthetic three-dimensional atomic structures assembled atom by atom”. In: *Nature* 561.7721 (2018), pp. 79–82.
- [20] M. D. Barrett et al. “Sympathetic cooling of $^9\text{Be}^+$ and $^{24}\text{Mg}^+$ for quantum logic”. In: *Phys. Rev. A* 68 (4 2003), p. 042302. DOI: 10.1103/PhysRevA.68.042302. URL: <https://link.aps.org/doi/10.1103/PhysRevA.68.042302>.
- [21] MD Barrett et al. “Deterministic quantum teleportation of atomic qubits”. In: *Nature* 429.6993 (2004), pp. 737–739.
- [22] Ron Belyansky et al. “Minimal model for fast scrambling”. In: *Physical review letters* 125.13 (2020), p. 130601.
- [23] Charles H Bennett et al. “Teleporting an unknown quantum state via dual classical and Einstein-Podolsky-Rosen channels”. In: *Physical review letters* 70.13 (1993), p. 1895.
- [24] Gregory Bentsen, Yingfei Gu, and Andrew Lucas. “Fast scrambling on sparse graphs”. In: *Proceedings of the National Academy of Sciences* 116.14 (2019), pp. 6689–6694.
- [25] Gregory Bentsen et al. “Treelike Interactions and Fast Scrambling with Cold Atoms”. In: *Phys. Rev. Lett.* 123 (2019), p. 130601. DOI: 10.1103/PhysRevLett.123.130601. arXiv: 1905.11430.
- [26] Gregory Bentsen et al. “Treelike interactions and fast scrambling with cold atoms”. In: *Physical review letters* 123.13 (2019), p. 130601.

- [27] Micha Berkooz et al. “Towards a full solution of the large N double-scaled SYK model”. In: *Journal of High Energy Physics* 2019.3 (2019), pp. 1–72.
- [28] Micha Berkooz et al. “Towards a full solution of the large N double-scaled SYK model”. In: *J. High Energ. Phys.* 2019 (2019), p. 79. DOI: 10.1007/JHEP03(2019)079. arXiv: 1811.02584.
- [29] H. Bernien et al. “Probing many-body dynamics on a 51-atom quantum simulator”. In: *Nature* 551.7682 (2017), pp. 579–584.
- [30] Prabudhya Bhattacharyya et al. “Imaging the Meissner effect and flux trapping in a hydride superconductor at megabar pressures using a nanoscale quantum sensor”. In: *arXiv preprint arXiv:2306.03122* (2023).
- [31] RMW van Bijnen and T Pohl. “Quantum magnetism and topological ordering via enhanced Rydberg-dressing near Forster-resonances”. In: *arXiv preprint arXiv:1411.3118* (2014).
- [32] R. Blatt and D. Wineland. “Entangled states of trapped atomic ions”. In: *Nature* 453 (2008), pp. 1008–1014. URL: <https://www.nature.com/articles/nature07125>.
- [33] Maxwell Block et al. “A universal theory of spin squeezing”. In: *arXiv preprint arXiv:2301.09636* (2023).
- [34] Maxwell Block et al. “Optically enhanced electric field sensing using nitrogen-vacancy ensembles”. In: *Physical Review Applied* 16.2 (2021), p. 024024.
- [35] MS Blok et al. “Quantum Information Scrambling in a Superconducting Qutrit Processor”. In: *arXiv preprint arXiv:2003.03307* (2020).
- [36] BJ Bloom et al. “An optical lattice clock with accuracy and stability at the 10⁻¹⁸ level”. In: *Nature* 506.7486 (2014), pp. 71–75.
- [37] Justin G Bohnet et al. “Quantum spin dynamics and entanglement generation with hundreds of trapped ions”. In: *Science* 352.6291 (2016), pp. 1297–1301.
- [38] Justin G Bohnet et al. “Reduced spin measurement back-action for a phase sensitivity ten times beyond the standard quantum limit”. In: *Nature Photonics* 8.9 (2014), pp. 731–736.
- [39] Guillaume Bornet et al. “Scalable spin squeezing in a dipolar Rydberg atom array”. In: *arXiv preprint arXiv:2303.08053* (2023).
- [40] Dik Bouwmeester et al. “Observation of three-photon Greenberger-Horne-Zeilinger entanglement”. In: *Physical Review Letters* 82.7 (1999), p. 1345.
- [41] Jochen Braumüller et al. “Probing quantum information propagation with out-of-time-ordered correlators”. In: *Nature Physics* 18.2 (2022), pp. 172–178.
- [42] Samuel L Braunstein and Carlton M Caves. “Statistical distance and the geometry of quantum states”. In: *Physical Review Letters* 72.22 (1994), p. 3439.

- [43] Adam R Brown et al. “Holographic complexity equals bulk action?” In: *Physical review letters* 116.19 (2016), p. 191301.
- [44] Adam R Brown et al. “Quantum gravity in the lab: teleportation by size and traversable wormholes”. In: *arXiv preprint arXiv:1911.06314* (2019).
- [45] Todd Brun, Igor Devetak, and Min-Hsiu Hsieh. “Correcting quantum errors with entanglement”. In: *science* 314.5798 (2006), pp. 436–439.
- [46] Tiff Brydges et al. “Probing Rényi entanglement entropy via randomized measurements”. In: *Science* 364.6437 (2019), pp. 260–263. ISSN: 0036-8075. DOI: 10.1126/science.aau4963. eprint: <https://science.sciencemag.org/content/364/6437/260.full.pdf>. URL: <https://science.sciencemag.org/content/364/6437/260>.
- [47] M. Cetina et al. “Quantum Gates on Individually-Addressed Atomic Qubits Subject to Noisy Transverse Motion”. In: *arXiv preprint arXiv:2007.06768* (2020).
- [48] Anffany Chen et al. “Quantum holography in a graphene flake with an irregular boundary”. In: *Physical review letters* 121.3 (2018), p. 036403.
- [49] Cheng Chen et al. “Continuous symmetry breaking in a two-dimensional Rydberg array”. In: *Nature* 616.7958 (2023), pp. 691–695.
- [50] Chi-Fang Chen et al. “Quantum Thermal State Preparation”. In: *arXiv preprint arXiv:2303.18224* 10 (2023).
- [51] Xiao Chen and Eduardo Fradkin. “Quantum entanglement and thermal reduced density matrices in fermion and spin systems on ladders”. In: *Journal of Statistical Mechanics: Theory and Experiment* 2013.08 (2013), P08013.
- [52] Xiao Chen and Tianci Zhou. “Quantum chaos dynamics in long-range power law interaction systems”. In: *Physical Review B* 100.6 (2019), p. 064305.
- [53] Aaron Chew, Andrew Essin, and Jason Alicea. “Approximating the Sachdev-Ye-Kitaev model with Majorana wires”. In: *Phys. Rev. B* 96 (2017), p. 121119. DOI: 10.1103/PhysRevB.96.121119. arXiv: 1703.06890.
- [54] Joonhee Choi et al. “Robust dynamic hamiltonian engineering of many-body spin systems”. In: *Physical Review X* 10.3 (2020), p. 031002.
- [55] Debanjan Chowdhury and Brian Swingle. “Onset of many-body chaos in the O(N) model”. In: *Phys. Rev. D* 96 (2017), p. 065005. DOI: 10.1103/PhysRevD.96.065005. arXiv: 1703.02545.
- [56] Debanjan Chowdhury et al. “Sachdev-Ye-Kitaev models and beyond: Window into non-Fermi liquids”. In: *Reviews of Modern Physics* 94.3 (2022), p. 035004.
- [57] J. I. Cirac and P. Zoller. “Quantum Computation with Cold Trapped Ions”. In: *Phys. Rev. Lett.* 74 (1995), pp. 4091–4094.
- [58] Simone Colombo et al. “Time-reversal-based quantum metrology with many-body entangled states”. In: *Nature Physics* 18.8 (2022), pp. 925–930.

- [59] Ivan Corwin. “The Kardar–Parisi–Zhang equation and universality class”. In: *Random matrices: Theory and applications* 1.01 (2012), p. 1130001.
- [60] Jordan S. Cotler et al. “Black holes and random matrices”. In: *J. High Energ. Phys.* 2017 (2017), p. 118. DOI: 10.1007/JHEP05(2017)118. arXiv: 1611.04650.
- [61] William Cottrell et al. “How to build the thermofield double state”. In: *Journal of High Energy Physics* 2019.2 (2019), pp. 1–43.
- [62] Luca D’Alessio et al. “From quantum chaos and eigenstate thermalization to statistical mechanics and thermodynamics”. In: *Advances in Physics* 65.3 (2016), pp. 239–362.
- [63] AJ Daley et al. “Measuring entanglement growth in quench dynamics of bosons in an optical lattice”. In: *Physical review letters* 109.2 (2012), p. 020505.
- [64] Christoph Dankert et al. “Exact and approximate unitary 2-designs and their application to fidelity estimation”. In: *Physical Review A* 80.1 (2009), p. 012304.
- [65] Ippei Danshita, Masanori Hanada, and Masaki Tezuka. “Creating and probing the Sachdev–Ye–Kitaev model with ultracold gases: Towards experimental studies of quantum gravity”. In: *Progress of Theoretical and Experimental Physics* 2017.8 (2017). DOI: 10.1093/ptep/ptx108. arXiv: 1606.02454.
- [66] Emily Davis, Gregory Bentsen, and Monika Schleier-Smith. “Approaching the Heisenberg limit without single-particle detection”. In: *Physical review letters* 116.5 (2016), p. 053601.
- [67] Emily J Davis et al. “Probing many-body dynamics in a two-dimensional dipolar spin ensemble”. In: *Nature Physics* (2023), pp. 1–9.
- [68] Sylvain De Léséleuc et al. “Analysis of imperfections in the coherent optical excitation of single atoms to Rydberg states”. In: *Physical Review A* 97.5 (2018), p. 053803.
- [69] S. Debnath et al. “Demonstration of a Small Programmable Quantum Computer with Atomic Qubits”. In: *Nature* 563 (2016), p. 63. URL: <https://www.nature.com/articles/nature18648>.
- [70] Shantanu Debnath. “A Programmable Five Qubit Quantum Computer Using Trapped Atomic Ions”. PhD thesis. University of Maryland, College Park, 2016.
- [71] Christian L Degen, Friedemann Reinhard, and Paola Cappellaro. “Quantum sensing”. In: *Reviews of modern physics* 89.3 (2017), p. 035002.
- [72] Joshua M Deutsch. “Eigenstate thermalization hypothesis”. In: *Reports on Progress in Physics* 81.8 (2018), p. 082001.
- [73] Robert H Dicke. “Coherence in spontaneous radiation processes”. In: *Physical review* 93.1 (1954), p. 99.
- [74] Justin Dressel et al. “Strengthening weak measurements of qubit out-of-time-order correlators”. In: *Physical Review A* 98.1 (2018), p. 012132.

- [75] Andreas Eberlein et al. “Quantum quench of the Sachdev-Ye-Kitaev model”. In: *Phys. Rev. B* 96 (2017), p. 205123. DOI: 10.1103/PhysRevB.96.205123. arXiv: 1706.07803.
- [76] Laird Egan et al. “Fault-tolerant control of an error-corrected qubit”. In: *Nature* 598.7880 (2021), pp. 281–286.
- [77] A. Elben et al. “Rényi Entropies from Random Quenches in Atomic Hubbard and Spin Models”. In: *Phys. Rev. Lett.* 120 (5 2018), p. 050406. DOI: 10.1103/PhysRevLett.120.050406. URL: <https://link.aps.org/doi/10.1103/PhysRevLett.120.050406>.
- [78] Dominic V Else et al. “An improved Lieb-Robinson bound for many-body Hamiltonians with power-law interactions”. In: *arXiv preprint arXiv:1809.06369* (2018).
- [79] Dominic V. Else et al. “Improved Lieb-Robinson bound for many-body Hamiltonians with power-law interactions”. In: *Phys. Rev. A* 101 (2 2020), p. 022333. DOI: 10.1103/PhysRevA.101.022333. URL: <https://link.aps.org/doi/10.1103/PhysRevA.101.022333>.
- [80] Julius Engelsöy, Thomas G. Mertens, and Herman Verlinde. “An investigation of AdS2 backreaction and holography”. In: *J. High Energ. Phys.* 2016 (2016), p. 139. DOI: 10.1007/JHEP07(2016)139. arXiv: 1606.03438.
- [81] László Erdős and Dominik Schröder. “Phase Transition in the Density of States of Quantum Spin Glasses”. In: *Math Phys Anal Geom* 17 (2014), p. 441. DOI: 10.1007/s11040-014-9164-3. arXiv: 1407.1552.
- [82] Brooks Foxen et al. “Demonstrating a continuous set of two-qubit gates for near-term quantum algorithms”. In: *Physical Review Letters* 125.12 (2020), p. 120504.
- [83] Michael H Freedman and Matthew B Hastings. “Quantum systems on non- k -hyperfinite complexes: A generalization of classical statistical mechanics on expander graphs”. In: *arXiv preprint arXiv:1301.1363* (2013).
- [84] Irénée Frérot and Tommaso Roscilde. “Quantum critical metrology”. In: *Physical review letters* 121.2 (2018), p. 020402.
- [85] Florian Fröwis, Pavel Sekatski, and Wolfgang Dür. “Detecting large quantum Fisher information with finite measurement precision”. In: *Physical review letters* 116.9 (2016), p. 090801.
- [86] Wenbo Fu and Subir Sachdev. “Numerical study of fermion and boson models with infinite-range random interactions”. In: *Phys. Rev. B* 94 (2016), p. 035135. DOI: 10.1103/PhysRevB.94.035135. arXiv: 1603.05246.
- [87] J. P. Gaebler et al. “High-Fidelity Universal Gate Set for ${}^9\text{Be}^+$ Ion Qubits”. In: *Phys. Rev. Lett.* 117 (6 2016), p. 060505. DOI: 10.1103/PhysRevLett.117.060505. URL: <https://link.aps.org/doi/10.1103/PhysRevLett.117.060505>.

- [88] Ping Gao and Daniel Louis Jafferis. “A Traversable Wormhole Teleportation Protocol in the SYK Model”. In: *arXiv preprint arXiv:1911.07416* (2019).
- [89] Ping Gao and Daniel Louis Jafferis. “A traversable wormhole teleportation protocol in the SYK model”. In: *Journal of High Energy Physics* 2021.7 (2021), pp. 1–44.
- [90] Ping Gao, Daniel Louis Jafferis, and Aron C Wall. “Traversable wormholes via a double trace deformation”. In: *Journal of High Energy Physics* 2017.12 (2017), pp. 1–25.
- [91] Ping Gao, Daniel Louis Jafferis, and Aron C. Wall. “Traversable wormholes via a double trace deformation”. In: *J. High Energ. Phys.* 2017 (2017), p. 151. DOI: 10.1007/JHEP12(2017)151. arXiv: 1608.05687.
- [92] Ping Gao and Hong Liu. “Regenesis and quantum traversable wormholes”. In: *arXiv preprint arXiv:1810.01444* (2018).
- [93] Antonio M García-García and Jacobus JM Verbaarschot. “Analytical spectral density of the Sachdev-Ye-Kitaev model at finite N ”. In: *Physical Review D* 96.6 (2017), p. 066012.
- [94] Antonio M García-García et al. “Quantum chaos transition in a two-site Sachdev-Ye-Kitaev model dual to an eternal traversable wormhole”. In: *Physical Review D* 100.2 (2019), p. 026002.
- [95] Antonio M. García-García and Jacobus J.M. Verbaarschot. “Analytical spectral density of the Sachdev-Ye-Kitaev model at finite N ”. In: *Phys. Rev. D* 96 (2017), p. 066012. DOI: 10.1103/PhysRevD.96.066012. arXiv: 1701.06593.
- [96] Martin Gärttner et al. “Measuring out-of-time-order correlations and multiple quantum spectra in a trapped-ion quantum magnet”. In: *Nature Physics* 13.8 (2017), pp. 781–786.
- [97] A. Georges, O. Parcollet, and S. Sachdev. “Quantum fluctuations of a nearly critical Heisenberg spin glass”. In: *Phys. Rev. B* 63 (2001), p. 134406. DOI: 10.1103/PhysRevB.63.134406. arXiv: cond-mat/0009388.
- [98] Vittorio Giovannetti, Seth Lloyd, and Lorenzo Maccone. “Advances in quantum metrology”. In: *Nature photonics* 5.4 (2011), pp. 222–229.
- [99] A. W. Glaetzle et al. “Designing Frustrated Quantum Magnets with Laser-Dressed Rydberg Atoms”. In: *Phys. Rev. Lett.* 114 (2015), p. 173002.
- [100] Garry Goldstein et al. “Environment-assisted precision measurement”. In: *Physical review letters* 106.14 (2011), p. 140502.
- [101] Sheldon Goldstein et al. “Canonical typicality”. In: *Physical review letters* 96.5 (2006), p. 050403.
- [102] T. M. Graham et al. “Rydberg mediated entanglement in a two-dimensional neutral atom qubit array”. In: *Phys. Rev. Lett.* 123 (2019), p. 230501.

- [103] Yingfei Gu and Alexei Kitaev. “On the relation between the magnitude and exponent of OTOCs”. In: 2019.2 (2019), p. 75.
- [104] Yingfei Gu and Alexei Kitaev. “On the relation between the magnitude and exponent of OTOCs”. In: *J. High Energ. Phys.* 2019 (2019), p. 75. DOI: 10.1007/JHEP02(2019)075. arXiv: 1812.00120.
- [105] Yingfei Gu, Xiao-Liang Qi, and Douglas Stanford. “Local criticality, diffusion and chaos in generalized Sachdev-Ye-Kitaev models”. In: 2017.5 (2017), p. 125.
- [106] Guy Gur-Ari, Raghu Mahajan, and Abolhassan Vaezi. “Does the SYK model have a spin glass phase?” In: *J. High Energ. Phys.* 2018 (2018), p. 70. DOI: 10.1007/JHEP11(2018)070. arXiv: 1806.10145.
- [107] Martin Gärttner et al. “Measuring out-of-time-order correlations and multiple quantum spectra in a trapped-ion quantum magnet”. In: *Nature Phys* 13 (2017), p. 781. DOI: 10.1038/nphys4119. arXiv: 1608.08938.
- [108] Felix M Haehl, Alexandre Streicher, and Ying Zhao. “Six-point functions and collisions in the black hole interior”. In: *arXiv preprint arXiv:2105.12755* (2021).
- [109] Arijit Haldar, Omid Tavakol, and Thomas Scaffidi. “Variational wave functions for Sachdev-Ye-Kitaev models”. In: *Physical Review Research* 3.2 (2021), p. 023020.
- [110] Stephen W Hawking. “Particle creation by black holes”. In: *Communications in mathematical physics* 43.3 (1975), pp. 199–220.
- [111] Patrick Hayden and John Preskill. “Black holes as mirrors: quantum information in random subsystems”. In: 2007.09 (2007), p. 120.
- [112] WK Hensinger et al. “T-junction ion trap array for two-dimensional ion shuttling, storage, and manipulation”. In: *Applied Physics Letters* 88.3 (2006), p. 034101.
- [113] Vicente Hernandez, Jose E. Roman, and Vicente Vidal. “SLEPc”. In: *ACM Trans. Math. Softw.* 31 (2005), p. 351. DOI: 10.1145/1089014.1089019.
- [114] Gerard’T Hooft. “Dimensional reduction in quantum gravity”. In: *arXiv preprint gr-qc/9310026* (1993).
- [115] Gary T Horowitz and Veronika E Hubeny. “Quasinormal modes of AdS black holes and the approach to thermal equilibrium”. In: *Physical Review D* 62.2 (2000), p. 024027.
- [116] Pavan Hosur et al. “Chaos in quantum channels”. In: *J. High Energ. Phys.* 2016 (2016), p. 4. DOI: 10.1007/JHEP02(2016)004. arXiv: 1511.04021.
- [117] S Hsieh et al. “Imaging stress and magnetism at high pressures using a nanoscale quantum sensor”. In: *Science* 366.6471 (2019), pp. 1349–1354.
- [118] Quirin Hummel et al. “Reversible quantum information spreading in many-body systems near criticality”. In: *Physical review letters* 123.16 (2019), p. 160401.

- [119] Philipp Hyllus, Otfried Ghne, and Augusto Smerzi. “Not all pure entangled states are useful for sub-shot-noise interferometry”. In: *Physical Review A* 82.1 (2010), p. 012337.
- [120] Philipp Hyllus et al. “Fisher information and multiparticle entanglement”. In: *Physical Review A* 85.2 (2012), p. 022321.
- [121] Daniel Jafferis et al. “Traversable wormhole dynamics on a quantum processor”. In: *Nature* 612.7938 (2022), pp. 51–55.
- [122] D. Jaksch et al. “Fast Quantum Gates for Neutral Atoms”. In: *Phys. Rev. Lett.* 85 (2000), p. 2208.
- [123] Kristan Jensen. “Chaos in AdS2 Holography”. In: *Phys. Rev. Lett.* 117 (2016), p. 111601. DOI: 10.1103/PhysRevLett.117.111601. arXiv: 1605.06098.
- [124] V John et al. “Techniques for the reconstruction of a distribution from a finite number of its moments”. In: *Chemical Engineering Science* 62.11 (2007), pp. 2890–2904.
- [125] Sonika Johri, Damian S. Steiger, and Matthias Troyer. “Entanglement spectroscopy on a quantum computer”. In: *Phys. Rev. B* 96 (19 2017), p. 195136. DOI: 10.1103/PhysRevB.96.195136. URL: <https://link.aps.org/doi/10.1103/PhysRevB.96.195136>.
- [126] Manoj K. Joshi et al. “Quantum information scrambling in a trapped-ion quantum simulator with tunable range interactions”. In: (). arXiv: 2001.02176.
- [127] Mehran Kardar, Giorgio Parisi, and Yi-Cheng Zhang. “Dynamic scaling of growing interfaces”. In: *Physical Review Letters* 56.9 (1986), p. 889.
- [128] H. Kaufmann et al. “Fast ion swapping for quantum-information processing”. In: *Phys. Rev. A* 95 (5 2017), p. 052319. DOI: 10.1103/PhysRevA.95.052319. URL: <https://link.aps.org/doi/10.1103/PhysRevA.95.052319>.
- [129] Ahmet Keleş, Erhai Zhao, and W. Vincent Liu. “Scrambling dynamics and many-body chaos in a random dipolar spin model”. In: *Phys. Rev. A* 99 (2019), p. 053620. DOI: 10.1103/PhysRevA.99.053620. arXiv: 1810.03815.
- [130] Vedika Khemani, Ashvin Vishwanath, and David A Huse. “Operator spreading and the emergence of dissipative hydrodynamics under unitary evolution with conservation laws”. In: *Physical Review X* 8.3 (2018), p. 031057.
- [131] Youngseok Kim et al. “Evidence for the utility of quantum computing before fault tolerance”. In: *Nature* 618.7965 (2023), pp. 500–505.
- [132] Alexei Kitaev. <https://www.youtube.com/watch?v=0Q9qN8j7EZI>. Talk given at the Fundamental Physics Prize Symposium, Nov. 10, 2014.
- [133] Alexei Kitaev. *A simple model of quantum holography*. 2015.
- [134] Alexei Kitaev and S Josephine Suh. “The soft mode in the Sachdev-Ye-Kitaev model and its gravity dual”. In: 2018.5 (2018), p. 183.

- [135] Alexei Kitaev and S. Josephine Suh. “The soft mode in the Sachdev-Ye-Kitaev model and its gravity dual”. In: *J. High Energ. Phys.* 2018 (2018), p. 183. DOI: 10.1007/JHEP05(2018)183. arXiv: 1711.08467.
- [136] Masahiro Kitagawa and Masahito Ueda. “Squeezed spin states”. In: *Physical Review A* 47.6 (1993), p. 5138.
- [137] Bryce Kobrin et al. “Many-body chaos in the Sachdev-Ye-Kitaev model”. In: *Physical review letters* 126.3 (2021), p. 030602.
- [138] Simcha Korenblit et al. “Quantum simulation of spin models on an arbitrary lattice with trapped ions”. In: *New Journal of Physics* 14.9 (2012), p. 095024.
- [139] Ioanna Kourkoulou and Juan Maldacena. “Pure states in the SYK model and nearly- AdS_2 gravity”. In: *arXiv preprint arXiv:1707.02325* (2017).
- [140] Alexander Kruchkov et al. “Thermoelectric power of Sachdev-Ye-Kitaev islands: Probing Bekenstein-Hawking entropy in quantum matter experiments”. In: *arXiv preprint arXiv:1912.02835* (2019).
- [141] Georg Kucsko et al. “Critical thermalization of a disordered dipolar spin system in diamond”. In: *Physical review letters* 121.2 (2018), p. 023601.
- [142] Richard Kueng and David Gross. “Qubit stabilizer states are complex projective 3-designs”. In: *arXiv preprint arXiv:1510.02767* (2015).
- [143] H. Labuhn et al. “Tunable two-dimensional arrays of single Rydberg atoms for realizing quantum Ising models”. In: *Nature* 534.7609 (2016), pp. 667–70.
- [144] Ho Tat Lam et al. “Shockwave S-matrix from Schwarzian quantum mechanics”. In: *J. High Energ. Phys.* 2018 (2018), p. 182. DOI: 10.1007/JHEP11(2018)182. arXiv: 1804.09834.
- [145] K. A. Landsman et al. “Two-qubit entangling gates within arbitrarily long chains of trapped ions”. In: *Phys. Rev. A* 100 (2 2019), p. 022332. DOI: 10.1103/PhysRevA.100.022332. URL: <https://link.aps.org/doi/10.1103/PhysRevA.100.022332>.
- [146] K. A. Landsman et al. “Verified quantum information scrambling”. In: *Nature* 567 (2019), p. 61. DOI: 10.1038/s41586-019-0952-6. arXiv: 1806.02807.
- [147] Kevin A Landsman et al. “Verified quantum information scrambling”. In: *Nature* 567.7746 (2019), p. 61.
- [148] Étienne Lantagne-Hurtubise et al. “Diagnosing quantum chaos in many-body systems using entanglement as a resource”. In: *Physical Review Research* 2.1 (2020), p. 013254.
- [149] A. I. Larkin and Y. N. Ovchinnikov. “Quasiclassical method in the theory of superconductivity”. In: *Sov Phys JETP* 28.6 (1969), pp. 1200–1205.
- [150] AI Larkin and Yu N Ovchinnikov. “Quasiclassical method in the theory of superconductivity”. In: *Sov Phys JETP* 28.6 (1969), pp. 1200–1205.

- [151] Yuri D Lensky and Xiao-Liang Qi. “Rescuing a black hole in the large- q coupled SYK model”. In: *Journal of High Energy Physics* 2021.4 (2021), pp. 1–42.
- [152] Sylvain de Léséleuc et al. “Observation of a symmetry-protected topological phase of interacting bosons with Rydberg atoms”. In: *Science* 365.6455 (2019), pp. 775–780.
- [153] H. Levine et al. “High-fidelity control and entanglement of Rydberg atom qubits”. In: *Phys. Rev. Lett.* 121 (2018), p. 123603.
- [154] H. Levine et al. “Parallel implementation of high-fidelity multi-qubit gates with neutral atoms”. In: *arXiv preprint arXiv:1908.06101* (2019).
- [155] R. J. Lewis-Swan et al. “Unifying scrambling, thermalization and entanglement through measurement of fidelity out-of-time-order correlators in the Dicke model”. In: *Nat Commun* 10 (2019), p. 1581. DOI: 10.1038/s41467-019-09436-y. arXiv: 1808.07134.
- [156] Jun Li et al. “Measuring Out-of-Time-Order Correlators on a Nuclear Magnetic Resonance Quantum Simulator”. In: *Phys. Rev. X* 7 (2017), p. 031011. DOI: 10.1103/PhysRevX.7.031011. arXiv: 1609.01246.
- [157] Jun Li et al. “Measuring out-of-time-order correlators on a nuclear magnetic resonance quantum simulator”. In: *Physical Review X* 7.3 (2017), p. 031011.
- [158] Yaodong Li, Xiao Chen, and Matthew PA Fisher. “Measurement-driven entanglement transition in hybrid quantum circuits”. In: *Physical Review B* 100.13 (2019), p. 134306.
- [159] Yaodong Li, Xiao Chen, and Matthew PA Fisher. “Quantum Zeno effect and the many-body entanglement transition”. In: *Physical Review B* 98.20 (2018), p. 205136.
- [160] Zeyang Li et al. “Improving metrology with quantum scrambling”. In: *Science* 380.6652 (2023), pp. 1381–1384.
- [161] Yunxiang Liao and Victor Galitski. “Nonlinear sigma model approach to many-body quantum chaos: Regularized and unregularized out-of-time-ordered correlators”. In: *Phys. Rev. B* 98 (2018), p. 205124. DOI: 10.1103/PhysRevB.98.205124. arXiv: 1807.09799.
- [162] Henry W Lin, Juan Maldacena, and Ying Zhao. “Symmetries Near the Horizon”. In: *arXiv preprint arXiv:1904.12820* (2019).
- [163] Henry W Lin and Leonard Susskind. “Complexity Geometry and Schwarzian Dynamics”. In: *arXiv preprint arXiv:1911.02603* (2019).
- [164] N. M. Linke et al. “Measuring the Rényi entropy of a two-site Fermi-Hubbard model on a trapped ion quantum computer”. In: *Phys. Rev. A* 98 (5 2018), p. 052334. DOI: 10.1103/PhysRevA.98.052334. URL: <https://link.aps.org/doi/10.1103/PhysRevA.98.052334>.
- [165] David J. Luitz and Yevgeny Bar Lev. “The ergodic side of the many-body localization transition”. In: *ANNALEN DER PHYSIK* 529 (2017), p. 1600350. DOI: 10.1002/andp.201600350. arXiv: 1610.08993.

- [166] Tommaso Macrì, Augusto Smerzi, and Luca Pezzè. “Loschmidt echo for quantum metrology”. In: *Physical Review A* 94.1 (2016), p. 010102.
- [167] I. S. Madjarov et al. “High-fidelity entanglement and detection of alkaline-earth Rydberg atoms”. In: *Nat. Phys.* (2020).
- [168] Juan Maldacena. “Eternal black holes in anti-de Sitter”. In: *Journal of High Energy Physics* 2003.04 (2003), p. 021.
- [169] Juan Maldacena. “The large-N limit of superconformal field theories and supergravity”. In: *International journal of theoretical physics* 38.4 (1999), pp. 1113–1133.
- [170] Juan Maldacena and Xiao-Liang Qi. “Eternal traversable wormhole”. In: *arXiv preprint arXiv:1804.00491* (2018).
- [171] Juan Maldacena, Stephen H Shenker, and Douglas Stanford. “A bound on chaos”. In: *Journal of High Energy Physics* 2016.8 (2016), pp. 1–17.
- [172] Juan Maldacena, Stephen H. Shenker, and Douglas Stanford. “A bound on chaos”. In: *J. High Energ. Phys.* 2016 (2016), p. 106. DOI: 10.1007/JHEP08(2016)106. arXiv: 1503.01409.
- [173] Juan Maldacena and Douglas Stanford. “Remarks on the sachdev-ye-kitaev model”. In: *Physical Review D* 94.10 (2016), p. 106002.
- [174] Juan Maldacena and Douglas Stanford. “Remarks on the Sachdev-Ye-Kitaev model”. In: *Phys. Rev. D* 94 (2016), p. 106002. DOI: 10.1103/PhysRevD.94.106002. arXiv: 1604.07818.
- [175] Juan Maldacena, Douglas Stanford, and Zhenbin Yang. “Conformal symmetry and its breaking in two dimensional Nearly Anti-de-Sitter space”. In: (). arXiv: 1606.01857.
- [176] Juan Maldacena, Douglas Stanford, and Zhenbin Yang. “Diving into traversable wormholes”. In: *Fortschritte der Physik* 65.5 (2017), p. 1700034.
- [177] Juan Maldacena, Douglas Stanford, and Zhenbin Yang. “Diving into traversable wormholes”. In: *Fortschr. Phys.* 65 (2017), p. 1700034. DOI: 10.1002/prop.201700034. arXiv: 1704.05333.
- [178] K. M. Maller et al. “Rydberg-blockade controlled-NOT gate and entanglement in a two-dimensional array of neutral-atom qubits”. In: *Phys. Rev. A* 92 (2015), p. 022336.
- [179] John Martyn and Brian Swingle. “Product spectrum ansatz and the simplicity of thermal states”. In: *Physical Review A* 100.3 (2019), p. 032107.
- [180] Eric J Meier, Fangzhao Alex An, Bryce Gadway, et al. “Exploring quantum signatures of chaos on a Floquet synthetic lattice”. In: *Physical Review A* 100.1 (2019), p. 013623.
- [181] Xiao Mi et al. “Information scrambling in quantum circuits”. In: *Science* 374.6574 (2021), pp. 1479–1483.
- [182] Thomas Mittiga et al. “Imaging the local charge environment of nitrogen-vacancy centers in diamond”. In: *Physical review letters* 121.24 (2018), p. 246402.

- [183] C Monroe et al. “Programmable Quantum Simulations of Spin Systems with Trapped Ions”. In: *arXiv preprint arXiv:1912.07845* (2019).
- [184] Christopher Monroe and Jungsang Kim. “Scaling the ion trap quantum processor”. In: *Science* 339.6124 (2013), pp. 1164–1169.
- [185] Gary J Mooney et al. “Generation and verification of 27-qubit Greenberger-Horne-Zeilinger states in a superconducting quantum computer”. In: *Journal of Physics Communications* 5.9 (2021), p. 095004.
- [186] Klaus Mølmer and Anders Sørensen. “Multiparticle Entanglement of Hot Trapped Ions”. In: *Phys. Rev. Lett.* 82.9 (Mar. 1999), pp. 1835–1838. DOI: 10 . 1103 / PhysRevLett.82.1835. URL: <https://link.aps.org/doi/10.1103/PhysRevLett.82.1835> (visited on 02/13/2020).
- [187] Adam Nahum, Sagar Vijay, and Jeongwan Haah. “Operator spreading in random unitary circuits”. In: *Physical Review X* 8.2 (2018), p. 021014.
- [188] Sepehr Nezami et al. “Quantum gravity in the lab: teleportation by size and traversable wormholes, Part II”. In: *arXiv preprint arXiv:2102.01064* (2021).
- [189] Michael A Nielsen and Isaac Chuang. *Quantum computation and quantum information*. 2002.
- [190] S. Olmschenk et al. “Quantum Teleportation Between Distant Matter Qubits”. In: *Science* 323.5913 (2009), pp. 486–489. ISSN: 0036-8075. DOI: 10 . 1126 / science . 1167209.
- [191] Olivier Parcollet and Antoine Georges. “Non-Fermi-liquid regime of a doped Mott insulator”. In: *Physical Review B* 59.8 (1999), p. 5341.
- [192] Edwin Pedrozo-Peñafiel et al. “Entanglement on an optical atomic-clock transition”. In: *Nature* 588.7838 (2020), pp. 414–418.
- [193] Geoff Penington et al. “Replica wormholes and the black hole interior”. In: *Journal of High Energy Physics* 2022.3 (2022), pp. 1–87.
- [194] Geoffrey Penington. “Entanglement wedge reconstruction and the information paradox”. In: *Journal of High Energy Physics* 2020.9 (2020), pp. 1–84.
- [195] Avikar Periwal et al. “Programmable interactions and emergent geometry in an array of atom clouds”. In: *Nature* 600.7890 (2021), pp. 630–635.
- [196] Stephan Plugge, Étienne Lantagne-Hurtubise, and Marcel Franz. “Revival dynamics in a traversable wormhole”. In: *Physical review letters* 124.22 (2020), p. 221601.
- [197] Ivan Pogorelov et al. “Compact ion-trap quantum computing demonstrator”. In: *PRX Quantum* 2.2 (2021), p. 020343.
- [198] Joseph Polchinski and Vladimir Rosenhaus. “The spectrum in the Sachdev-Ye-Kitaev model”. In: *Journal of High Energy Physics* 2016.4 (2016), pp. 1–25.

- [199] I.-D. Potirniche et al. “Floquet Symmetry-Protected Topological Phases in Cold-Atom Systems”. In: *Phys. Rev. Lett.* 119 (2017), p. 123601.
- [200] John Preskill. “Quantum computing in the NISQ era and beyond”. In: *Quantum* 2 (2018), p. 79.
- [201] Xiao-Liang Qi, Hosho Katsura, and Andreas WW Ludwig. “General relationship between the entanglement spectrum and the edge state spectrum of topological quantum states”. In: *Physical review letters* 108.19 (2012), p. 196402.
- [202] Xiao-Liang Qi and Alexandre Streicher. “Quantum epidemiology: operator growth, thermal effects, and SYK”. In: 2019.8 (2019), p. 12.
- [203] Xiao-Liang Qi et al. “Measuring operator size growth in quantum quench experiments”. In: *arXiv preprint arXiv:1906.00524* (2019).
- [204] Tibor Rakovszky, CW von Keyserlingk, and Frank Pollmann. “Dissipation-assisted operator evolution method for capturing hydrodynamic transport”. In: *arXiv preprint arXiv:2004.05177* (2020).
- [205] Tibor Rakovszky, Frank Pollmann, and CW von Keyserlingk. “Diffusive hydrodynamics of out-of-time-ordered correlators with charge conservation”. In: *Physical Review X* 8.3 (2018), p. 031058.
- [206] Ji-Gang Ren et al. “Ground-to-satellite quantum teleportation”. In: *Nature* 549.7670 (2017), p. 70.
- [207] Mark Riebe et al. “Deterministic quantum teleportation with atoms”. In: *Nature* 429.6993 (2004), pp. 734–737.
- [208] Daniel A Roberts, Douglas Stanford, and Alexandre Streicher. “Operator growth in the SYK model”. In: 2018.6 (2018), p. 122.
- [209] Daniel A Roberts, Douglas Stanford, and Leonard Susskind. “Localized shocks”. In: *Journal of High Energy Physics* 2015.3 (2015), pp. 1–27.
- [210] Daniel A Roberts and Beni Yoshida. “Chaos and complexity by design”. In: 2017.4 (2017), p. 121.
- [211] J. E. Roman et al. *SLEPc Users Manual*. Tech. rep. DSIC-II/24/02 - Revision 3.7. D. Sistemes Informàtics i Computació, Universitat Politècnica de València, 2016.
- [212] Aurelio Romero-Bermúdez, Koenraad Schalm, and Vincenzo Scopelliti. “Regularization dependence of the OTOC. Which Lyapunov spectrum is the physical one?” In: *J. High Energy Phys.* 2019 (2019), p. 107. DOI: 10.1007/JHEP07(2019)107. arXiv: 1903.09595.
- [213] Elliott Rosenberg et al. “Dynamics of magnetization at infinite temperature in a Heisenberg spin chain”. In: *arXiv preprint arXiv:2306.09333* (2023).
- [214] Shinsei Ryu and Tadashi Takayanagi. “Holographic derivation of entanglement entropy from the anti-de sitter space/conformal field theory correspondence”. In: *Physical review letters* 96.18 (2006), p. 181602.

- [215] Phil Saad, Stephen H Shenker, and Douglas Stanford. “A semiclassical ramp in SYK and in gravity”. In: *arXiv preprint arXiv:1806.06840* (2018).
- [216] Yousef Saad. “Analysis of some Krylov subspace approximations to the matrix exponential operator”. In: *SIAM Journal on Numerical Analysis* 29.1 (1992), pp. 209–228.
- [217] Subir Sachdev. “Quantum phase transitions”. In: *Physics world* 12.4 (1999), p. 33.
- [218] Subir Sachdev and Jinwu Ye. “Gapless spin-fluid ground state in a random quantum Heisenberg magnet”. In: *Physical review letters* 70.21 (1993), p. 3339.
- [219] Subir Sachdev and Jinwu Ye. “Gapless spin-fluid ground state in a random quantum Heisenberg magnet”. In: *Phys. Rev. Lett.* 70 (1993), p. 3339. DOI: 10.1103/PhysRevLett.70.3339.
- [220] Olof Salberger et al. “Deformed Fredkin spin chain with extensive entanglement”. In: *Journal of Statistical Mechanics: Theory and Experiment* 2017.6 (2017), p. 063103.
- [221] Roman Schnabel et al. “Quantum metrology for gravitational wave astronomy”. In: *Nature communications* 1.1 (2010), p. 121.
- [222] Thomas Schuster and Norman Y. Yao. “Operator Growth in Open Quantum Systems”. In: (*forthcoming*) (2022).
- [223] Thomas Schuster and Norman Y Yao. “Operator Growth in Open Quantum Systems”. In: *arXiv preprint arXiv:2208.12272* (2022).
- [224] Thomas Schuster et al. “Many-body quantum teleportation via operator spreading in the traversable wormhole protocol”. In: *Physical Review X* 12.3 (2022), p. 031013.
- [225] Yasuhiro Sekino and L Susskind. “Fast scramblers”. In: *J. High Energy Phys.* 2008 (2008), p. 065. DOI: 10.1088/1126-6708/2008/10/065. arXiv: 0808.2096.
- [226] Yasuhiro Sekino and Leonard Susskind. “Fast scramblers”. In: 2008.10 (2008), p. 065.
- [227] Huitao Shen et al. “Out-of-time-order correlation at a quantum phase transition”. In: *Phys. Rev. B* 96 (2017), p. 054503. DOI: 10.1103/PhysRevB.96.054503. arXiv: 1608.02438.
- [228] Stephen H Shenker and Douglas Stanford. “Black holes and the butterfly effect”. In: *Journal of High Energy Physics* 2014.3 (2014), pp. 1–25.
- [229] Stephen H. Shenker and Douglas Stanford. “Black holes and the butterfly effect”. In: *J. High Energ. Phys.* 2014 (2014), p. 67. DOI: 10.1007/JHEP03(2014)067. arXiv: 1306.0622.
- [230] Stephen H Shenker and Douglas Stanford. “Stringy effects in scrambling”. In: 2015.5 (2015), p. 132.
- [231] Stephen H. Shenker and Douglas Stanford. “Stringy effects in scrambling”. In: *J. High Energ. Phys.* 2015 (2015), p. 132. DOI: 10.1007/JHEP05(2015)132.

- [232] Brian Skinner, Jonathan Ruhman, and Adam Nahum. “Measurement-induced phase transitions in the dynamics of entanglement”. In: *Physical Review X* 9.3 (2019), p. 031009.
- [233] J Smith et al. “Many-body localization in a quantum simulator with programmable random disorder”. In: *Nature Physics* 12.10 (2016), pp. 907–911.
- [234] Douglas Stanford. “Many-body chaos at weak coupling”. In: *J. High Energ. Phys.* 2016 (2016), p. 9. DOI: 10.1007/JHEP10(2016)009. arXiv: 1512.07687.
- [235] Robin Steinigeweg, Jochen Gemmer, and Wolfram Brenig. “Spin-Current Autocorrelations from Single Pure-State Propagation”. In: *Phys. Rev. Lett.* 112 (2014), p. 120601. DOI: 10.1103/PhysRevLett.112.120601. arXiv: 1312.5319.
- [236] Vincent Paul Su. “Variational Preparation of the Sachdev-Ye-Kitaev Thermofield Double”. In: *arXiv preprint arXiv:2009.04488* (2020).
- [237] Vincent Paul Su. “Variational preparation of the thermofield double state of the Sachdev-Ye-Kitaev model”. In: *Physical Review A* 104.1 (2021), p. 012427.
- [238] Leonard Susskind. “Complexity and Newton’s Laws”. In: *arXiv preprint arXiv:1904.12819* (2019).
- [239] Leonard Susskind. “Computational complexity and black hole horizons”. In: *Fortschritte der Physik* 64.1 (2016), pp. 24–43.
- [240] Leonard Susskind. “The world as a hologram”. In: *Journal of Mathematical Physics* 36.11 (1995), pp. 6377–6396.
- [241] Leonard Susskind. “Why do things fall?” In: *arXiv preprint arXiv:1802.01198* (2018).
- [242] Brian Swingle et al. “Measuring the scrambling of quantum information”. In: *Phys. Rev. A* 94 (2016), p. 040302. DOI: 10.1103/PhysRevA.94.040302. arXiv: 1602.06271.
- [243] Brian Swingle et al. “Measuring the scrambling of quantum information”. In: *Physical Review A* 94.4 (2016), p. 040302.
- [244] Yi Hong Teoh et al. “Machine learning design of a trapped-ion quantum spin simulator”. In: *Quantum Science and Technology* 5.2 (2020), p. 024001.
- [245] Barbara M Terhal and David P DiVincenzo. “Problem of equilibration and the computation of correlation functions on a quantum computer”. In: *Physical Review A* 61.2 (2000), p. 022301.
- [246] Minh C Tran et al. “Hierarchy of linear light cones with long-range interactions”. In: *arXiv preprint arXiv:2001.11509* (2020).
- [247] Varun D Vaidya et al. “Tunable-range, photon-mediated atomic interactions in multimode cavity QED”. In: *Physical Review X* 8.1 (2018), p. 011002.
- [248] Benoît Vermersch et al. “Probing scrambling using statistical correlations between randomized measurements”. In: *Physical Review X* 9.2 (2019), p. 021061.

- [249] CW Von Keyserlingk et al. “Operator hydrodynamics, OTOCs, and entanglement growth in systems without conservation laws”. In: *Physical Review X* 8.2 (2018), p. 021013.
- [250] Zak Webb. “The Clifford group forms a unitary 3-design”. In: *arXiv preprint arXiv:1510.02769* (2015).
- [251] Ken Xuan Wei et al. “Emergent prethermalization signatures in out-of-time ordered correlations”. In: *Physical review letters* 123.9 (2019), p. 090605.
- [252] J. Wilson et al. “Trapped arrays of alkaline earth Rydberg atoms in optical tweezers”. In: *arXiv preprint arXiv:1912.08754* (2018).
- [253] David J Wineland et al. “Spin squeezing and reduced quantum noise in spectroscopy”. In: *Physical Review A* 46.11 (1992), R6797.
- [254] K. Wright et al. “Benchmarking an 11-qubit quantum computer”. In: *Nat. Commun.* 10 (2019), p. 5464. URL: <https://www.nature.com/articles/s41467-019-13534-2>.
- [255] Jingxiang Wu and Timothy H Hsieh. “Variational thermal quantum simulation via thermofield double states”. In: *Physical review letters* 123.22 (2019), p. 220502.
- [256] T. Xia et al. “Randomized Benchmarking of Single-Qubit Gates in a 2D Array of Neutral-Atom Qubits”. In: *Phys. Rev. Lett.* 114 (2015), p. 100503.
- [257] Tianrui Xu, Thomas Scaffidi, and Xiangyu Cao. “Does scrambling equal chaos?” In: *Physical review letters* 124.14 (2020), p. 140602.
- [258] Zhenbin Yang. “The quantum gravity dynamics of near extremal black holes”. In: *J. High Energ. Phys.* 2019 (2019), p. 205. DOI: 10.1007/JHEP05(2019)205. arXiv: 1809.08647.
- [259] Norman Y. Yao et al. “Interferometric Approach to Probing Fast Scrambling”. In: (). arXiv: 1607.01801.
- [260] Norman Y Yao et al. “Interferometric approach to probing fast scrambling”. In: *arXiv preprint arXiv:1607.01801* (2016).
- [261] Beni Yoshida. “Firewalls vs. scrambling”. In: 2019.10 (2019), p. 132.
- [262] Beni Yoshida. “Observer-dependent black hole interior from operator collision”. In: *arXiv preprint arXiv:1910.11346* (2019).
- [263] Beni Yoshida and Alexei Kitaev. “Efficient decoding for the Hayden-Preskill protocol”. In: *arXiv preprint arXiv:1710.03363* (2017).
- [264] Beni Yoshida and Norman Y. Yao. “Disentangling Scrambling and Decoherence via Quantum Teleportation”. In: *Phys. Rev. X* 9 (2019), p. 011006. DOI: 10.1103/PhysRevX.9.011006. arXiv: 1803.10772.
- [265] Beni Yoshida and Norman Y Yao. “Disentangling scrambling and decoherence via quantum teleportation”. In: *Physical Review X* 9.1 (2019), p. 011006.

- [266] J. Zeiher et al. “Coherent Many-Body Spin Dynamics in a Long-Range Interacting Ising Chain”. In: *Phys. Rev. X* 7 (2017), p. 041063.
- [267] Jiehang Zhang et al. “Observation of a many-body dynamical phase transition with a 53-qubit quantum simulator”. In: *Nature* 551.7682 (2017), pp. 601–604.
- [268] Pengfei Zhang, Yingfei Gu, and Alexei Kitaev. “An obstacle to sub-AdS holography for SYK-like models”. In: *arXiv preprint arXiv:2012.01620* (2020).
- [269] Tianci Zhou and Brian Swingle. “Operator growth from global out-of-time-order correlators”. In: *Nature communications* 14.1 (2023), p. 3411.
- [270] Tianci Zhou et al. “Operator lévy flight: Light cones in chaotic long-range interacting systems”. In: *Physical review letters* 124.18 (2020), p. 180601.
- [271] D. Zhu et al. “Generation of Thermofield Double States and Critical Ground States with a Quantum Computer”. In: *arXiv preprint arXiv:1906.02699* (2019).
- [272] Daiwei Zhu et al. “Generation of thermofield double states and critical ground states with a quantum computer”. In: *Proceedings of the National Academy of Sciences* 117.41 (2020), pp. 25402–25406.
- [273] Guanyu Zhu, Mohammad Hafezi, and Tarun Grover. “Measurement of many-body chaos using a quantum clock”. In: *Phys. Rev. A* 94 (2016), p. 062329. DOI: 10.1103/PhysRevA.94.062329. arXiv: 1607.00079.
- [274] Huangjun Zhu. “Multiqubit Clifford groups are unitary 3-designs”. In: *Phys. Rev. A* 96 (6 2017), p. 062336. DOI: 10.1103/PhysRevA.96.062336. URL: <https://link.aps.org/doi/10.1103/PhysRevA.96.062336>.
- [275] Huangjun Zhu. “Multiqubit Clifford groups are unitary 3-designs”. In: *Physical Review A* 96.6 (2017), p. 062336.
- [276] Shi-Liang Zhu, C. Monroe, and L.-M. Duan. “Trapped Ion Quantum Computation with Transverse Phonon Modes”. In: *Phys. Rev. Lett.* 97 (5 2006), p. 050505. URL: <https://journals.aps.org/prl/abstract/10.1103/PhysRevLett.97.050505>.
- [277] Quntao Zhuang et al. “Scrambling and complexity in phase space”. In: *Physical Review A* 99.6 (2019), p. 062334.
- [278] Chong Zu et al. “Emergent hydrodynamics in a strongly interacting dipolar spin ensemble”. In: *Nature* 597.7874 (2021), pp. 45–50.